DOE/MC/30171 -- 5298
(DE97002037)
Volume I

Recycle Of Contaminated Scrap Metal, Volume I

Semi-Annual Report
September 1993 - January 1996

July 1996

Work Performed Under Contract No.: DE-AC21-93MC30171

For
U.S. Department of Energy
Office of Environmental Management
Office of Technology Development
Washington, DC

U.S. Department of Energy
Office of Fossil Energy
Morgantown Energy Technology Center
Morgantown, West Virginia

By
Molten Metal Technology, Inc.
Waltham, Massachussetts 02154

Disclaimer

DISCLAIMER

DOE/MC/30171 -- 5298
(DE97002038)
Volume I

Recycle Of Contaminated Scrap Metal, Volume I

Semi-Annual Report
September 1993 - January 1996

Work Performed Under Contract No.: DE-AC21-93MC30171

For

U.S. Department of Energy
Office of Environmental Management
Office of Technology Development
1000 Independence Avenue
Washington, DC 20585

U.S. Department of Energy
Office of Fossil Energy
Morgantown Energy Technology Center
P.O. Box 880
Morgantown, West Virginia 26507-0880

By
Molten Metal Technology, Inc.
400-2 Totten Pond Road
Waltham, Massachussetts 02154

July 1996

olten Metal Technology

Molten Metal Technology, Inc. • 400-2 Totten Pond Road • Waltham, MA 02154 U.S.A. • Tel: 617-487-9700 • Fax: 617-487-7870 • http: //www.mmt.com

July 24, 1996

U.S. Department of Energy
Morgantown Energy Technology Center
Attn: Contractor Reports Receipt Coordinator
M/S F07
PO Box 880
3610 Collins Ferry Road
Morgantown, WV 26507-0880

Subject: Contract Number DE-AC21-93MC30171

Please find enclosed the following deliverable under the subject contract:

- Six (6) hard copies of the Interim Report entitled "Recycle of Contaminated Scrap Metal."

Due to software incompatibilities, it was agreed to with Bill Huber that MMT would deliver this report in paper format rather than on CD-ROM. This deliverable is in releasable form in accordance with the terms and conditions of the subject contract.

If you require any additional information, feel free to contact me at (617)768-4521.

Sincerely,
MOLTEN METAL TECHNOLOGY, INC.

KMBeane

Kathleen M. Beane
Senior Contracts Administrator
Government Sector

cc: V. Gatto
L. Ghoniem
B. Payea
J. Zimmerman

PRDA INTERIM REPORT
TABLE OF CONTENTS

List of Figures

List of Tables

List of Frequently Used Acronyms

ALARA	As Low As Reasonably Achievable
APU	Advanced Processing Unit
BDAT	Best Demonstrated Available Technology
C/M/R	Ceramic/Metal/Refractory
CAA	Clean Air Act
CAS	Calcium Aluminosilicates
CEP	Catalytic Extraction Processing
CET	Compensated Embedded Thermocouple
CFCC	Continuous Fiber-reinforced Ceramic Composite
CPU	Catalytic Processing Unit
CSTRs	Continuously Stirred Tank Reactor
CWA	Clean Water Act
DEP	Department of Environmental Protection
DF	Decontamination Factors
ΔG_i	Change in Gibbs Free Energy
DOE	Department of Energy
DRE	Destruction Removal Efficiency
EDX	Energy Dispersive X-Ray
EDXS	Energy Dispersive X-Ray Spectrometer
EPA	Environmental Protection Agency
GC	Gas Chromatography
GHT	Gas Handling Train

GLR	Glass-Liquid-Refractory
HEPA	High Efficiency Particulate
HLW	High Level Waste
HVAC	Heating, Ventilation, and Air Conditioning
ICP	Inductively-Coupled Plasma
ICTF	Integrated Containment Test Facility
IR	Infrared
LADR	Leaching and Dissolution Resistance
LCD	Liquid Crystal Display
LDL	Lower Detection Limit
MLLW	Mixed Low Level Waste
MMT	Molten Metal Technology
MOCP	Molten Oxide Ceramic Phase
MS	Mass Spectrometer
NAA	Neutron Activation Analysis
ODEs	Ordinary Differential Equations
OFT	Optical Fiber Thermometry
OSHA	Occupational Safety and Health Administration
PCB	Polychlorinated Biphenyl
PCT	Product Consistency Test
PDEs	Partial Differential Equations
PFR	Plug Flow Reactor
PICs	Products of Incomplete Combustion
PID	Proportional Integral Derivative

PLC	Programmable Logic Controller
POHCs	Primary Organic Hazardous Constituents
PSR	Perfectly Stirred Reactor
PVC	Polyvinyl Chloride
Q-CEP	Quantum Catalytic Extraction Process
RCRA	Resource Conservation and Recovery Act
RTD	Residence Time Distribution
SEM	Scanning Electron Microscopy
SPC	Statistical Process Control
TCLP	Toxicity Characteristic Leaching Procedure
THC	Total Hydrocarbons
TOX	Total Organic Halides
TRU	Transuranic Waste
TSD	Treatment, Storage, and Disposal
VHMs	Volatile Heavy Metals
VOC	Volatile Organic Constituent
VPR	Variable Pressure Reactor
WAC	Waste Acceptance Criteria
WETF	West End Treatment Facility
XRD	X-Ray Diffraction
XRF	X-Ray Fluorescence

1. Executive Summary

Catalytic Extraction Processing (CEP) has been demonstrated to be a robust, one-step process that is relatively insensitive to wide variations in waste composition and is applicable to a broad spectrum of DOE wastes. Catalytic Processing Unit (CPU) design models have been validated through experimentation to provide a high degree of confidence in our ability to design a bulk solids CPU for processing DOE wastes. Substantial growth in the feed size and composition compatible with CEP has also been achieved in a relatively short period of time, providing the opportunity to substantially reduce the amount of feed characterization and preparation prior to processing. Two commercial CEP facilities have been placed in commission and are currently processing mixed low level wastes. These facilities provide a compelling indication of the maturity, regulatory acceptance, and commercial viability of CEP.

Research and development activities directed at bulk solid feed systems have achieved significant growth in the feed particle size acceptable for Catalytic Extraction Processing. An extensive series of experiments was conducted on feed materials that were surrogates for a typical waste stream that was provided by DOE. Based on R&D completed to date, a CPU can be confidently designed to accept a drum size unit of completely characterized waste and an approximately 15.24 cm (6 inch)/3539.6 cm^3 (216 $inch^3$) cube of completely uncharacterized waste as shown in Figure 1.1. The particle

Figure 1.1
Growth in CEP-Compatible Bulk Solid Feed Particle Size

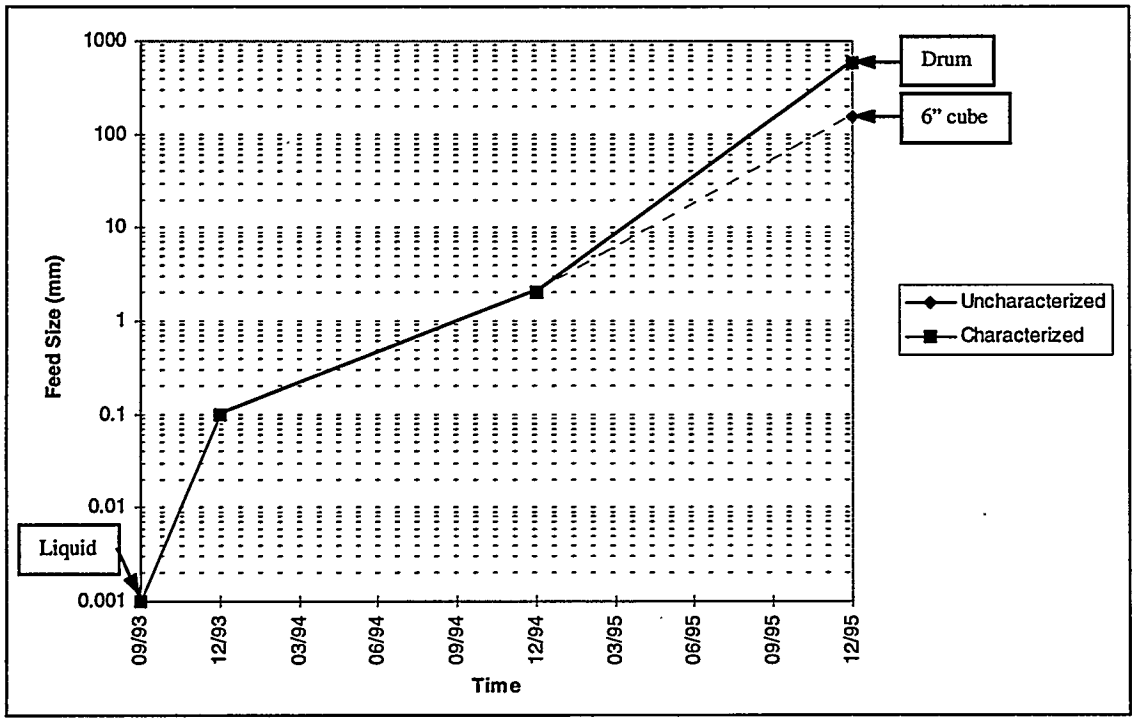

size for completely uncharacterized waste is compatible with commercially available shredder technology. The current factor limiting the size of uncharacterized waste is the uncertainty in the volatile content of the waste stream. This increase in the feed size corresponds to a significant reduction in the amount of waste characterization and feed preparation prior to injection into the Catalytic Processing Unit (CPU). Additional R&D investment is expected to result in developing a high degree of confidence in the ability to design a CPU capable of accepting a drum (and potentially larger) size feed of completely uncharacterized waste. Achievement of this goal will significantly reduce the substantial costs associated with feed characterization and preparation prior to injection into the CPU. Further, eliminating the requirement for feed characterization/preparation is considered to be vital for processing of DOE's substantial inventory of high level waste (HLW) which is packaged in drum size containers.

Catalytic Extraction Processing achieved a major milestone in December 1995 when the two commercial facilities shown in Figure 1.2 were commissioned and subsequently began processing mixed low level waste. These state-of-the-art Quantum-CEP™ facilities were completed on schedule and employ sophisticated automation and control systems for processing of radioactive wastes. The M4 facility was constructed in less than 5 months and is capable of processing up to 1 million pounds per year of heterogeneous liquid and solid mixed hazardous and radioactive wastes. The Westinghouse SEG facility is a robotically-operated plant that is capable of processing 650 High Integrity Containers (approximately 130,000 cubic feet) per year of organic mixed low level wastes. These facilities have demonstrated both the maturity and the economic viability of utilizing CEP for commercial processing of various mixed low level waste streams. Further, these facilities, in combination with previous and on-going research and development activities at MMT, provide important risk reduction for future DOE efforts to apply CEP to site specific requirements and to expand its application beyond MLLW to transuranic (TRU) waste and High Level Waste (HLW).

An important factor to be considered when developing and deploying technologies for the recycle, reuse, and disposal of materials from DOE decontamination and decommissioning activities is the ability to obtain the necessary permits to process these materials. While conventional wisdom may characterize CEP as a thermal treatment system which will likely be permitted as an incinerator, MMT's experience in obtaining permits for CEP facilities indicates otherwise. Four states (Massachusetts, Ohio, Tennessee, and Texas) have characterized CEP as a legitimate recycling process that is a non-combustion, non-incineration technology. Further, the Texas Natural Resource Conservation Commission (TNRCC) has determined that CEP is a recycling technology that is distinct from incineration and can be considered a manufacturing technology because it converts wastes to useful products. The designation of CEP as a recycling technology is significant as it results in the CEP recycling unit being exempt from

Figure 1.2
Commercial CEP Facilities Currently in Operation

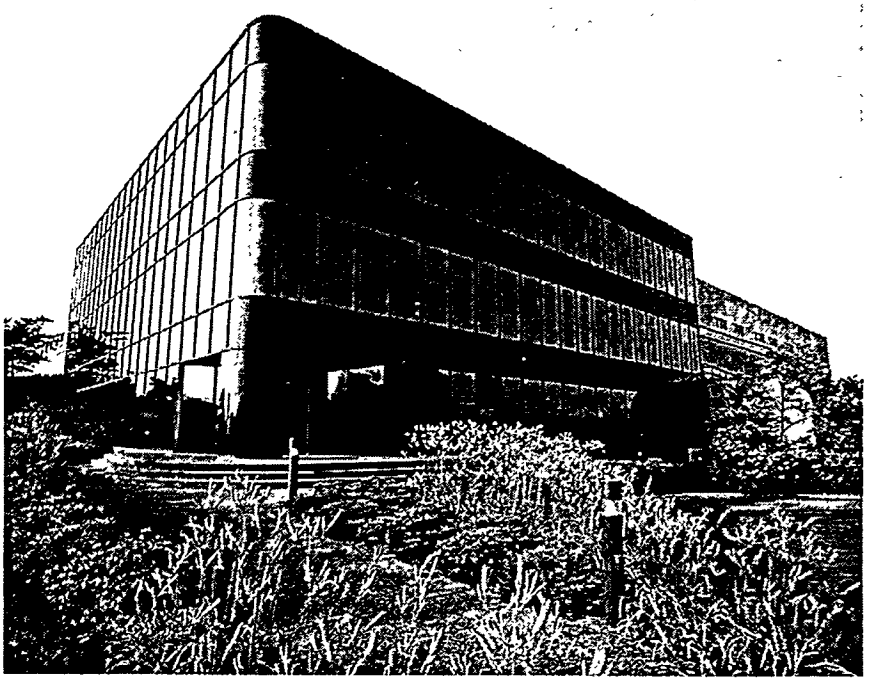

M4 Facility, Oak Ridge, TN

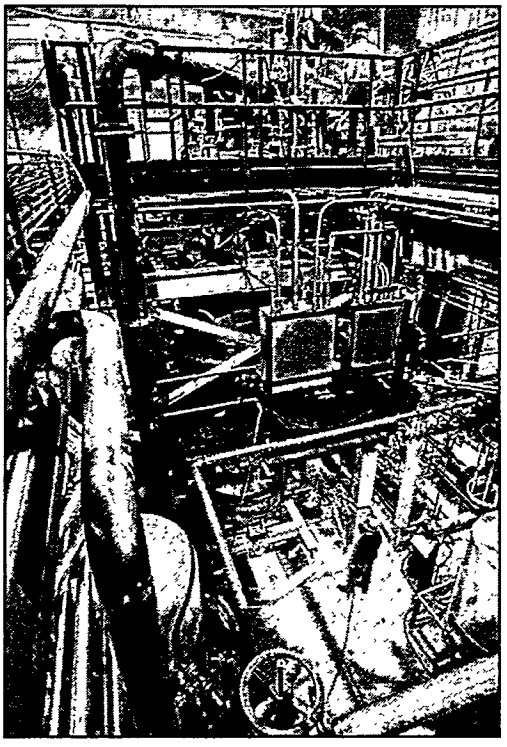

SEG Facility, Oak Ridge, TN

Resource Conservation and Recovery Act (RCRA) permitting requirements. The state of Tennessee has issued permits for the two CEP facilities that are currently in operation for processing mixed low level wastes (MLLW). The U.S. Environmental Protection Agency has also recently recognized CEP as having achieved the Best Demonstrated Available Technology (BDAT) for processing all wastes for which incineration was previously the only approved processing method. EPA's determination reinforces the position that CEP is fundamentally different from incineration, and further confirms EPA's previous conclusions that CEP supports the agency's efforts to reduce the quantity of residuals for land disposal and to minimize cross-media contamination.

The research and development activities performed under this contract have demonstrated Catalytic Extraction Processing to be a robust, one-step process that is relatively insensitive to wide variations in waste composition and is applicable to a broad spectrum of DOE wastes. Substantial growth in the feed size and composition compatible with CEP has been achieved in a relatively short period of time; additional research and development is expected to lead to the ability to accept a drum (and potentially larger) size feed of completely uncharacterized waste. Experiments have also validated our CPU design model, providing a high degree of confidence in our ability to design a bulk solids CPU for processing DOE wastes. Two commercial facilities have been placed in commission and are currently processing mixed low level wastes. These facilities provide a compelling indication of the maturity, regulatory acceptance, and commercial viability of CEP. Additional development work to address the specific requirements of a particular DOE site, and expansion in the application of Catalytic Extraction Processing to transuranic and high level wastes is considered to be the next logical step in the development and deployment of CEP for the recycle, reuse, and disposal of materials from DOE decontamination and decommissioning activities.

1.1. Program Goals and CEP Applicability

The leaders of our nation are under continual and ever-growing pressures to decrease the size of government and decrease spending, while at the same time improve the environment and eliminate the hazardous waste problems plaguing many parts of the country -- seemingly conflicting goals. These are all daunting in their magnitude individually, and when considered together pose a truly monumental task. The U.S. Department of Energy issued a Planned Research and Development Announcement (PRDA) in 1993 with the objective of identifying unique technologies which could be applied to the most pernicious waste streams at DOE sites, and at the same time derive some financial benefit from the application of the technologies.

The DOE identified the problem of Low Level Mixed Wastes as one of the most difficult it faced. The combination of radioactive contamination with additional contamination by hazardous constituents such as those identified by the Resource Conservation and Recovery Act posed an especially challenging problem. Technologies which had traditionally been called upon to solve these problems were coming under increasing attack by regulators and stakeholders. Recent investigations by the EPA had revealed

that many of the byproducts of traditional remediation technologies were considered detrimental to human health at extremely low levels. The DOE searched for technologies which could provide superior regulatory performance, achieve decontamination of the contaminated metals and provide a cost benefit to users.

Specifically, the objective of identifying a process for recycling the metal constituent of the waste streams was identified. The DOE's own stockpiles of contaminated scrap metals amounts to an enormous untapped resource of metals from steel and copper to metals which are in short supply, such as nickel. Millions of tons of metal bearing mild contamination could potentially be brought back to use within the complex, or conceivably to general commerce in the event of the establishment of a deminimis standard. In either scenario, the re-use of the metals would pre-empt the purchase of virgin materials from sources outside the government, thereby decreasing the outflow of capital and conserving precious natural resources. The DOE controls large quantities of radioactive scrap metal as delineated in Table 1.1 below. The DOE's supply of contaminated nickel alone is estimated to have a market value approaching $1,500,000,000.00. By recovering these unexploited resources, DOE decreases U. S. dependence on foreign sources for strategic materials, such as Ni, Nb, and other materials vital to national security.

Table 1.1
Radioactive Scrap Metal Controlled by DOE

Metal	Market Price (US $/ton)[1]	Quantity (tons)	Market Value (US $)
Nickel	6,000	245,000	1,470,000,000
Steel	107	1,300,000	140,000,000
Aluminum	600	195,000	115,000,000
Copper	1,500	38,000	57,000,000

[1]Nominal Prices 1990-91
Annual production estimated at 15,000 tpy
Source: Environmental Restoration Opportunity-Recycle of DOE Contaminated Metal, William Murphie, et al., USDOE 1992.

Desirable recycling technologies were described by the DOE as easily installed, operated and maintained, exhibit superior performance at low cost, generate little secondary waste, remove contaminants to very low levels, reduce worker exposure to contaminants and be readily accepted by the public and regulatory agencies. Molten Metal Technology, Inc., (MMT) was awarded a contract as a result of the PRDA, to determine whether its proprietary technology, Catalytic Extraction Processing (CEP),

could be applied to waste streams the DOE had identified, and meet the exacting requirements of a broad spectrum of evaluators.

Molten Metal Technology Inc.'s (MMT's) Catalytic Extraction Processing (CEP) is a proprietary technology that allows organic, organometallic, metallic and inorganic feeds to be recycled into useful materials of commercial value. CEP is an innovative technology that provides superior environmental performance, no cross-media transfer of pollutants, substantial pollution prevention/waste minimization benefits, and recovery of strategic resources of economic value. CEP can achieve or surpass existing concentration-based BDAT standards while also meeting EPA's goals under important initiatives, such as the Combustion Strategy and the Pollution Prevention Policy.

MMT's goal is to maximize recovery of feed materials on an elemental basis in a safe, efficient, and effective manner. At the core of CEP is a metal bath, operated at temperatures above its liquid state. The liquid metal acts as a catalyst and solvent in the dissociation of the feed and the synthesis of products. Processing of materials in CEP can be conceptually divided into two stages:

- Catalytic dissociation and dissolution: The catalytic effect of the molten metal causes complex compounds in the feed to be dissociated into their elements, which readily dissolve in the liquid metal solution to form elemental intermediates. The formation of dissolved elemental intermediates ensures that only elemental composition--not the physical form or molecular structure of the feed--affects CEP's performance.

- Product synthesis: By adding select co-reactants and/or controlling operating conditions, the dissolved elemental intermediates can be reacted to form desired products of commercial value. Thermodynamics determine product synthesis, while solution equilibria determine partitioning between the metallic, ceramic, and gaseous product streams.

1.1.1. CEP Technology Overview

CEP is a robust chemical process whose performance is based on fundamental chemical principles and engineering design. Given the chemical composition and physical form of the feed, the reaction pathways can be accurately predicted based on thermodynamics and the desired reactions can be carried out under appropriate engineering design. The process robustness while maintaining system performance is in contrast to combustion processes, where competing reactions take place and no accurate predictions of processing results can be achieved. The major technical features that allow CEP to provide significant environmental performance and waste minimization benefits are outlined below:

- CEP feed conversion efficiency is independent of the complexity of the molecular structure of the feed molecule. The liquid metal acts both as a homogeneous

catalyst for the dissociation of complex feed molecules into their elemental constituents and as a solvent of these elemental intermediates. The flexibility and robustness of the CEP process are attributed to the 'singular' dissolved elemental intermediate through which reactions proceed. As a result, CEP feed conversion is independent of the complexity of the molecular structure of the feed molecule. DREs exceeding 99.9999% ('six nines') are typical in CEP regardless of the complexity of feed materials.

- CEP feed conversion efficiency is driven by solvation effects. CEP operates above the metal liquidus point, but does not use temperature as the primary means to change the physical and chemical composition of the feed materials. The carbon concentration in the liquid metal drives feed dissociation and dissolution. The lower the carbon concentration relative to saturation, the higher the forces driving the formation of the dissolved elemental intermediate (i.e., $Fe_3C(\ell)$) and hence more efficient feed conversion per unit time is achieved.

- CEP operates under a highly reducing environment, preventing the formation of undesirable oxidation byproducts (e.g., NO_x, SO_x). The solubility of carbon and oxygen in iron provides CEP with high chemical inertia and allows the system to maintain a highly reducing uniform environment over a wide range of operating conditions. No free oxygen can be found in the system to undergo alternate oxidation reaction pathways which lead to undesirable byproducts, such as NO_x, SO_x, dioxins, and difurans.

- CEP does not provide pathways for the formation of dioxins or difurans. Synthesis via CEP is achieved through specific dissolved intermediates in a highly reducing environment. No viable pathways are allowed for dioxins and difurans formation. Analysis of the CPU off-gas stream in commercial-scale demonstrations of chlorinated waste processing have consistently shown trace levels to be non-detect to the stringent targeted regulatory level of 0.1 ng/Nm^3 (TEQ).

- CEP allows synthesis of high quality products. Synthesis of products is based on manipulation of the reaction pathways for the dissolved elemental intermediate through judicious addition of co-reactants and variation in operating conditions.

The liquid metal bath and the reaction pathway via a singular dissolved intermediate give CEP a number of distinct advantages over conventional thermal processes:

- The liquid metal is a homogeneous catalytic and solvation medium which dissociates the feed into its elements, ensuring no intermediate products of incomplete dissociation. In open flame processes, the extent of dissociation to the intermediate free radicals is dependent on the residence time, temperature, oxygen environment, and system turbulence which are difficult to control. These parameters are readily controllable in CEP.

- The liquid metal solvent has high chemical inertia providing a means of dampening the effect of variations in feed composition, hence allowing for robust control of product quality.

- In CEP, the liquid metal in contact with the liquid ceramic phase can be used to engineer the separation and recycling of inorganics or metal compounds from complex feeds. This multiphase interaction provides CEP with the flexibility to synthesize and recycle desired products of high commercial value.

1.1.2. Material Recovery and Reuse

CEP converts secondary materials into products including synthesis gas, ceramic products and ferrous as well as non-ferrous alloys (carbon steel, stainless steel, nickel, chromium, etc.).

Based upon market analyses, theoretical product modeling, and experimental verification of radionuclide partitioning and resultant product properties, MMT has identified multiple potential uses for Quantum-CEP™ products from the processing of DOE radioactively and RCRA-contaminated scrap metal and other waste forms expected to be generated by the decontamination and decommissioning (D&D) of DOE sites.

Synthesis gas (hydrogen and carbon monoxide) can be used as a low NO_x fuel. CEP product gases usually have a heating value of approximately 300-350 BTU/SCF, or approximately one-third that of natural gas (~1000 BTU/SCF).

Metal alloys containing deminimis radioactivity may be used for containment boxes, for shielding purposes, and with the establishment of a deminimis standard, for release to commerce. Without the establishment of a deminimis standard, multiple opportunities exist within the DOE complex for beneficial use of the recovered decontaminated metal product. Table 1.2 delineates some of these potential metal products. With the establishment of a deminimis standard, such as in Europe, large commercial opportunities for scrap metal recycling would become available. Recovered condensed products from MMT's Fall River facility have been sold for $40-$4140/ton.

Table 1.2
Metal Products for Reuse within the DOE

Product	Material	Total Weight (tons)
Shield Blocks	Carbon or Stainless Steel	300,000
Vitrification Canisters	Stainless Steel	45,000
Universal Dry Fuel Casks	Stainless Steel	282,000
Transportation & Disposal Boxes	Carbon or Stainless Steel	500,000
Transportation & Disposal Drums	Carbon or Stainless Steel	1,250,000
Type A Shipping Casks	Carbon or Stainless Steel	150,000
Reinforcing Bar and Mats	Carbon or Stainless Steel	100,000
Totals:		2,627,000

Source: Workshop on Radioactive Scrap Metal Knoxville and Oak Ridge, TN
University of Tennessee, via SEG 1993

Many radionuclides found in DOE waste, such as U and Pu, will partition to a ceramic phase. MMT is currently exploring potential uses for these products. These materials may be useful as barriers or structural support in repositories. The ceramic composition may be appropriate for use as grouting material for buried high level waste (HLW) tanks. The glass formers found in the CEP product may make it an appropriate substitute for virgin glass to be used in a vitrifier of high level wastes and would be consistent with the objectives of MAWS (Minimum Additive Waste Stabilization). MMT's marketing and regulatory groups are exploring these potential uses to make beneficial use of all product streams from CEP and Quantum-CEP™.

1.1.3. CEP Benefits Lead to Stakeholder Endorsement

MMT has built wide regulatory and community acceptance of CEP as a recycling technology. MMT has successfully obtained approval and acceptance from both state and federal government agencies that CEP is a global solution for environmental protection. This acceptance will expedite siting and permitting, thereby shortening commercialization schedule and lowering overall project cost (Table 1.3).

Table 1.3
Regulatory "Certifications" of CEP

Project	Time
US EPA	
Determination that CEP provides Equivalent Treatment for F024 for which incineration has been mandated Best Demonstrated Available Technology	Approved 7/17/95
Determination that CEP provides Equivalent Treatment for all wastes for which incineration had been mandated Best Demonstrated Available Technology	Approved 3/12/96
EPA Metal Recovery Report to Congress (CEP featured as "Innovative Metal Recovery Technology")	Report to Congress June 1994
MASSACHUSETTS	
MADEP Recycling R&D Permit (Fall River)	Approved 9/17/93
MADEP Application for R&D Recycling Certification (CEP of Biosolids Recycling)	Approved 12/1/93
MADEP Application for R&D Recycling Certification (CEP of Surplus Electronic Componentry)	Approved 5/17/94
MADEP Application for R&D Recycling Certification (CEP of Chlorinated Organic Hazardous Waste, F024, K019 and K020)	Approved 1/24/95
MADEP Application for R&D Recycling Certification (CEP of Toluene Isocyanate Residue K027)	Filed 1/30/95 Approved 3/1/95
OHIO	
OH EPA Preliminary Recycling Analysis (CEP recycling exempt from RCRA-permitting at central hazardous processing facility)	Filed 3/4/94 Approved 6/28/94
TEXAS	
TNRCC Designation as "Innovative Technology"	Approved 8/4/93
TNRCC determination that MMT's Bay City CEP is legitimate recycle/re-use recycling and CEP is a non-incineration, non-BIF technology	Approved 2/27/96
CALIFORNIA	
Acceptance of CEP into California Technology Certification program and finding that CEP is a non-combustion technology	Approved 6/16/95
TENNESSEE	
TNDEC determination that CEP is not combustion and constitutes legitimate recycling	Approved 2/20/96

1.1.4. CEP Benefits Complement DOE Program Goals

The unique processing benefits of CEP combined with the material recovery attributes and broad regulatory acceptance serve the needs of DOE as outlined in the Program goals. The goals of Research Area 5, which specifically address the recycle of contaminated scrap metal, are listed in Table 1.4, with a corresponding listing of CEP's capabilities which meet or exceed the DOE's requirements.

Table 1.4
CEP Meets and Exceeds the DOE's Program Objectives

Research Area 5 DOE Program Goal	CEP's Capabilities
Develop a novel technique that will significantly reduce the potential for spread of contaminants and for worker exposure to radionuclide or hazardous material.	Through reactant addition, radioactive nuclides are engineered into a high density vitreous phase and hazardous components are rendered benign. The tightly-bound ceramic matrix will reduce potential spread and safe operation will assure no worker exposure. A sealed reactor design will prevent fugitive emissions, and up-front automation, protective clothing and monitors will prevent accidental worker exposure.
Develop processes to convert the scrap metal into a form that can be reused.	Reducible metals, such as Fe, Ni, Cr, etc., are captured in a molten metal phase, radionuclides are diverted to a vitreous phase, and hazardous organics are converted to H_2 and CO and liberated as gas. The scrap metal is thus converted to a high-value ferrous alloy.
Minimize secondary waste generation.	The only potential waste material from CEP of scrap metal is the radioactive nuclide-containing vitreous matrix. Because the nuclides are concentrated in this phase, and the volume of this phase is low, waste generation is minimized. Recovery of the radionuclides for potential recycle may be possible in the future.
Comply with existing environmental, health, and safety regulations.	A CEP facility can render RCRA hazardous and TSCA toxic organics benign, capture volatile heavy metals, and concentrate/immobilize radioactive constituents. MMT will meet all EPA, CERCLA, DOE, TSCA, state and local standards.
Develop technologies that produce a reusable form, which is not hazardous under the provisions of RCRA.	CEP of the contaminated scrap metal will form two non-hazardous products: ferro-alloys and syngas. Organic hazardous constituents will be destroyed to form products, CO and H_2. Heavy metal contaminants can be captured and immobilized. The soluble metals, such as Fe and Ni, will concentrate in the metal bath, and other contaminants will be diverted to a ceramic phase.
Develop technologies that produce a reusable form that meets proposed IAEA standards for unrestricted release of bulk contaminated materials.	Preliminary partitioning (thermodynamic equilibrium) studies indicate that the concentrated metal product (ferro-alloy) may contain less than 0.2 Bq/g for alpha emitters and less than 1 Bq/g for high energy beta/gamma emitters.
Develop technologies that remove radioactive and hazardous materials from the scrap metal.	In CEP, the metal is captured as a ferro-alloy, while the radioactive species are reaction-engineered into a ceramic phase. Hazardous organics decompose into elemental constituents and then react to form H_2, CO, etc. Hazardous heavy metals may be captured either in the ceramic phase or condensed from the product gases. Therefore, radioactive, hazardous, and toxic constituents are removed from the metal.
Develop technologies with lower decontamination and recycling costs compared to current technologies.	The chemical inertia and thermal efficiency of the molten metal bath makes CEP processing highly cost-effective. In many commercial applications, the resale of two product streams offsets the processing cost.

1.2. Program Objectives and Accomplishments

The DOE sought to identify technologies which could recycle the valuable constituents of the feed streams and at the same time economically produce a suitable final waste form for disposal while achieving unprecedented environmental performance. While technologies existed to meet individual components of the overall program objectives, no technology had been demonstrated to achieve all components simultaneously.

In concert with the DOE, MMT designed a program which would challenge preconceptions of the limitations of waste processing technologies:

- *Demonstrate the recycling of ferrous and non-ferrous metals* -- to establish that radioactively contaminated scrap metal could be converted to high-grade, ferrous and non-ferrous alloys which can be reused by DOE or reintroduced into commerce.

- *Immobilize radionuclides* -- that CEP would concentrate the radionuclides in a durable vitreous phase, minimize secondary waste generation and stabilize and reduce waste volume.

- *Destroy hazardous organics* -- that CEP would convert hazardous organics to valuable industrial gases, which could be used as an energy source.

- *Recover volatile heavy metals* -- that CEP's off-gas treatment system would capture volatile heavy metals, such as mercury and lead.

- *Establish that CEP is economical for processing contaminated scrap metal in the DOE inventory* -- that CEP is a more cost-effective and complete treatment and recycling technology than competing technologies for processing contaminated scrap.

The execution of this program resulted in all objectives being met and exceeded as delineated in Table 1.5.

Table 1.5
PRDA Objectives Met and Surpassed

Program Objective	Representative MMT Accomplishments
Recycling of ferrous and non-ferrous metals	• 100% metal recovery for surplus metal componentry (64 wt% Ni, Cu, Cr, Fe, Ag, Co, Mo, Mn) • Decontamination of metals > 99.6% (analytically limited) • Recycling certification by MADEP (Recovered condensed phase products sold to local metal recycler.)
Immobilization of radionuclides	• Incorporation of both surrogates and actual radionuclides into stable glass structure proven using neutron activation analysis • All glass compositions passed TCLP
Destruction of hazardous organics	• DREs ≥ 99.9999% for halogenated organics (K019, K020, F024), toxic organics (K027), plastics (PVC, PS), etc. • Negligible trace components, NO_x < 3 ppm, SO_x < 1 ppm, TEQ (2,3,7,8 TCDD) < 0.1 ng/Nm^3 (stringent targeted regulatory limit) -- third-party analysis
Recovery of volatile heavy metals	• Demonstrated partitioning of volatile heavy metals to targeted phase • Volatile heavy metals engineered into durable ceramic product
Cost effective recycling of contaminated metal	• System design established with proven regulatory acceptance • Minimal feed analysis and post-treatment resulted in stream-lined system with low capital and operating costs • No secondary combustion or vitrification required

1.3. Significant Findings and Program Overview

The information and data contained in this report combines the results of studies/experiments performed under this contract with research and development efforts that were funded separately by customers other than DOE. In particular, experimental information addressing radioactive waste was not performed under this contract, but has been included in this final report as it is a major DOE interest item.

Before designing the experiments to verify CEP's applicability to contaminated scrap metal, MMT performed an extensive literature search to establish the existing state-of-the-art in related fields. Previously published studies from numerous sources, including Oak Ridge and Argonne National Laboratories have demonstrated the ability to partition transuranic components, such as uranium and plutonium, from the metal phase into a vitreous phase via melt refining. Residual concentrations ranging from 0.05 ppm to 2 ppm of such radioactive components were achieved using diffusion of oxidizing, vitreous-forming agents to partition the radioactive components. Successful partitioning to less than 10 nCi levels has been demonstrated for uranium- and plutonium-contaminated mild steel, stainless steel, nickel, copper, and aluminum. While melt refining technology can enable partitioning of radionuclides, it can not simultaneously ensure complete conversion of RCRA organic constituents and containment and immobilization of RCRA inorganic constituents. Hence, melt refining is not applicable to DOE mixed wastes which are highly diverse in chemical and physical form, and may contain high concentrations of RCRA and/or metal components.

CEP can offer simultaneous radionuclide partitioning, recovery of RCRA inorganics, and conversion of RCRA organics for a diverse and ill-defined waste feed slate. CEP offers equivalent and potentially better radionuclide partitioning capabilities to melt refining, as the techniques involved are completely incorporated and enhanced in CEP technology. CEP incorporates active radionuclide partitioning through select co-reactant additions and enhanced mass transfer (e.g. convection), while melt refining is based upon "passive" diffusion-based partitioning. For example, CEP can directly add co-reactants into the metal bath. By injecting oxygen directly into the iron bath, oxidation of the radioactive components is greatly enhanced. Thus, significantly better partitioning is achieved with CEP than with traditional melt refining technologies. Bench, pilot, and demonstration-scale tests on common isotopes and DOE-recommended surrogates support these observations. Thermodynamic calculations support the experimental findings and both indicate that pre-contamination radioactivity levels (e.g., virgin metal levels) in the metal can be attained.

Demonstration- and pilot-scale studies have shown that metal decontamination can be achieved simultaneous to RCRA waste conversion. Surplus metal componentry (RCRA characteristic waste, when discarded) doped with radionuclide surrogates (Hf) and common isotopes (Zn) was successfully recycled via CEP. Organic conversion exceeded 99.9999% (DRE), metal recovery exceeded 98 wt% of the feed, and no radionuclide surrogate was detected in the metal (analytically limited). The vitreous product from this demonstration was shown to be durable and chemically stable, passing all criteria for EPA TCLP analysis. Based upon detailed material balance analysis, product analysis, and evaluation of commercial product specifications, the Massachusetts Department of Environmental Protection (MADEP) certified this demonstration as recycling.

The report highlights the comprehensive nature of the efforts and key findings of the program. CEP's capabilities for targeted partitioning of radioisotopes to a stable, non-leachable phase with resultant metal decontamination and RCRA conversion were proven.

1.3.1. Support Facilities and Scope of Expanded Experimental Effort

MMT operates a Recycling-Research & Development Facility in Fall River, MA. The facility houses four bench-scale units, four pilot-scale units, seven physical models, and a commercial demonstration prototype unit, which are shown in Figure 1.3. This state-of-the-art facility is fully permitted by the Commonwealth of Massachusetts for recycling demonstrations using hazardous and non-hazardous materials as CEP feeds. MMT has received recycling certifications from the Massachusetts Department of Environmental Protection for the processing of RCRA and organometallic feeds and has sold the condensed phase products from this facility.

Bench- and pilot-scale experimental units are used to confirm theoretical modeling predictions, establish product quality, determine appropriate materials of construction, assess design parameters and confirm fundamental process chemistry. Many of these systems, including the Advanced Processing Units (APUs) which are appropriate for small commercial-scale operations, are operated round-the-clock for two to three-week experimental campaigns. Physical models are used to study fluid dynamics and transport phenomena, reactor flow patterns, unique reactor configurations, and final design parameters.

The commercial-scale prototype is used primarily for customer and regulatory demonstrations and establishment of commercial design scenarios. MMT has processed a wide range of hazardous, characteristic, and surrogate waste feeds in the commercial prototype. The commercial prototype typically operates round-the-clock during one-week demonstration campaigns, which may include several different feed materials. CEP demonstrations have proven waste recycling into commercially valuable products (>90% of the feed elements) while consistently achieving DREs $\geq$ 99.9999%. Trace components measure non-detect to the regulatory limits.

The demonstration-scale CPU and gas handling unit is equipped with approximately 2,000 monitored variables and 900 control loops linked into the computerized monitoring and control modules. Numerous sampling ports throughout the gas handling train enable full characterization of the product gas quality. Summa canister sampling is performed to enable third-party analysis down to ppb levels via established EPA methods (TO-14). Mass spectrometer samples are drawn on-line and gas composition measurements are taken every twenty seconds for feed-back process control.

Figure 1.3
CEP R&D Units

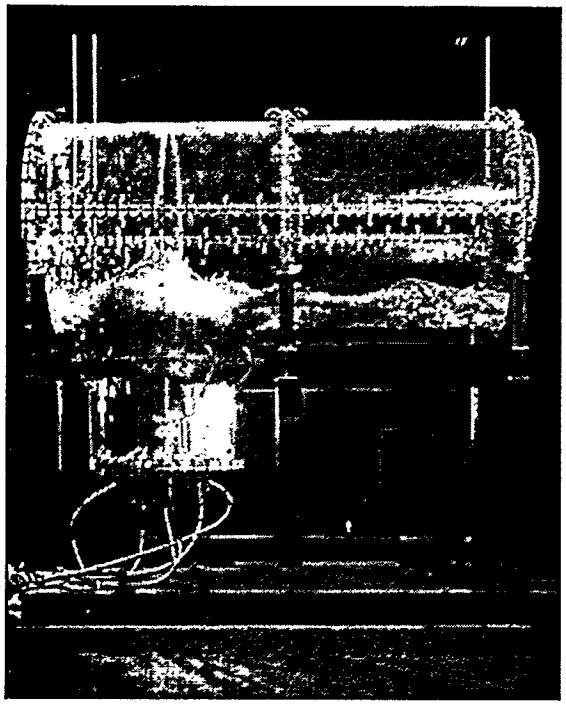

Physical Model

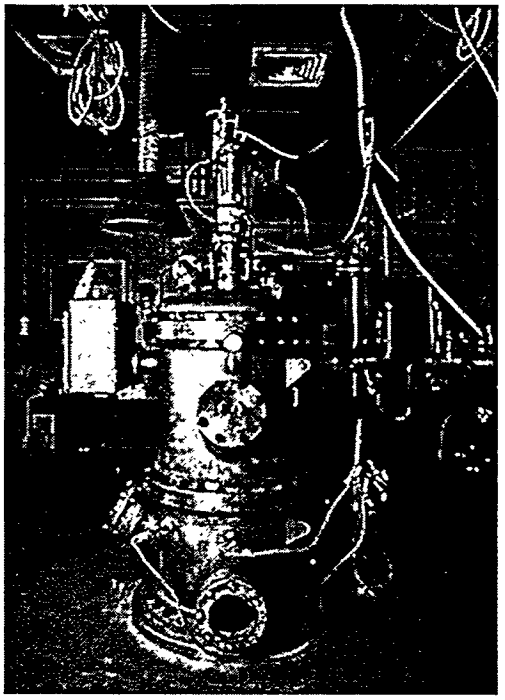

Bench Scale

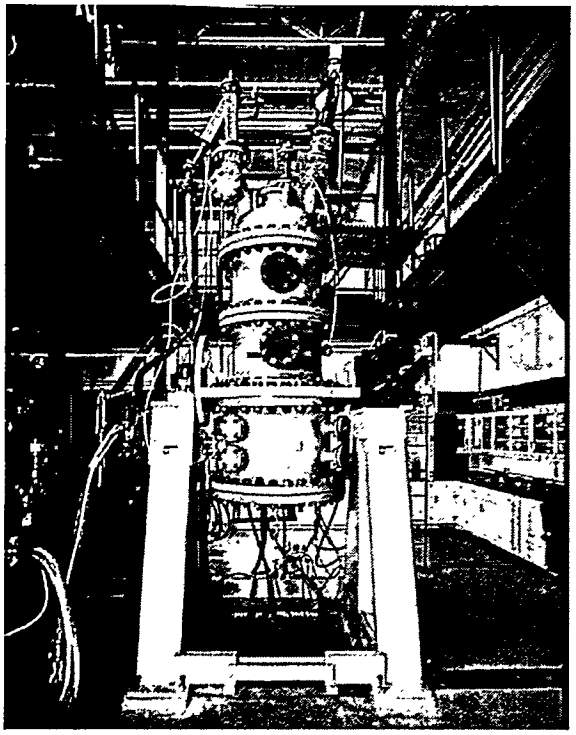

Pilot Scale

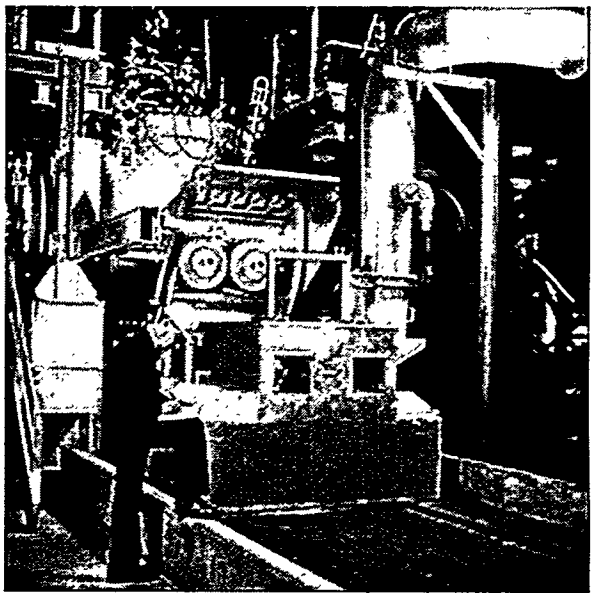

Commercial Scale

1.3.2. Task 1.1 - Design CEP System

1.3.2.1. Bulk Solids Feeding System Design and Analysis

An extensive series of theoretical and experimental studies were conducted on CEP reactor design modeling. Thermodynamics and computational fluid dynamics have been used to characterize the catalytic extraction process to develop a methodology and models for determining CEP reactor design parameters. Several studies were performed on the phenomenology of tuyere operation for injecting feed materials into the reactor. An accretion model was developed to predict the formation of accretions and to evaluate methods for their control. Studies were performed on the absorption behavior of a gas injected into a bath using a tuyere to characterize the various regions surrounding the tuyere plume. These studies provided important reactor design parameters including minimum bath height and maximum tuyere flow rates for effective processing. Extensive theoretical and physical model studies were performed on determining bubble size distributions from tuyere operation in molten metal baths. Calculated bubble size and residence time distributions were determined to be consistent with experimental results. Data obtained from the bubble size distribution study was then applied to a study on the carburization and decarburization of a molten metal bath. The inherent ability of the metal bath to dissolve carbon maintains the quality of the gas phase products by removing any unreacted hydrocarbon species. Finally, the data from these and other reactor-related experiments were used to design and evaluate an innovative, continuous, counter-current reactor which has the potential to yield high quality metal and ceramic products, reduce the volume of the ceramic phase, and reduce overall energy costs.

A critical requirement in DOE's efforts to recycle, reuse, and dispose of materials from its decontamination and decommissioning activities is the design of a robust system capable of processing a wide variety of bulk solid feeds. There are several reactor concepts for bulk feed processing being considered. Common to these concepts is the use of two processing zones: a dissolution/volatilization zone (Zone 1) and a gas polishing zone (Zone 2). A comprehensive series of experiments was performed in the 4-Ton Demonstration Unit using DOE-provided surrogates of typical waste components to obtain data to characterize the dissolution/volatilization zone and to compare that data with predictions based on theoretical calculations. In the continuous treatment of bulk solids in the CEP process, solids are fed into Zone 1 where they are dissolved and/or volatilized at a rate that is dependent on particle size, material properties, and bath conditions. The dissolution process can be mass transfer or heat transfer controlled. The operability range of a reactor can be determined for a given feed material, approximate size range, and specified reactor conditions. The boundaries of the operability range are established by the maximum power capacity of the system, the maximum feedable particle size, the maximum capacity of the gas handling train (GHT), the mass or heat transfer limit, and the volatility of the feed material. A typical reactor operability range for a mass transfer controlled process is shown in Figure 1.4. A high degree of correlation was observed between data obtained during the

experimental test program and theoretically-based Zone 1 design equations, thereby providing a high degree of confidence in our ability to design a reactor for processing bulk solids wastes generated from DOE decontamination and decommissioning activities.

Figure 1.4
Operability Limits for a Mass Transfer Controlled Process

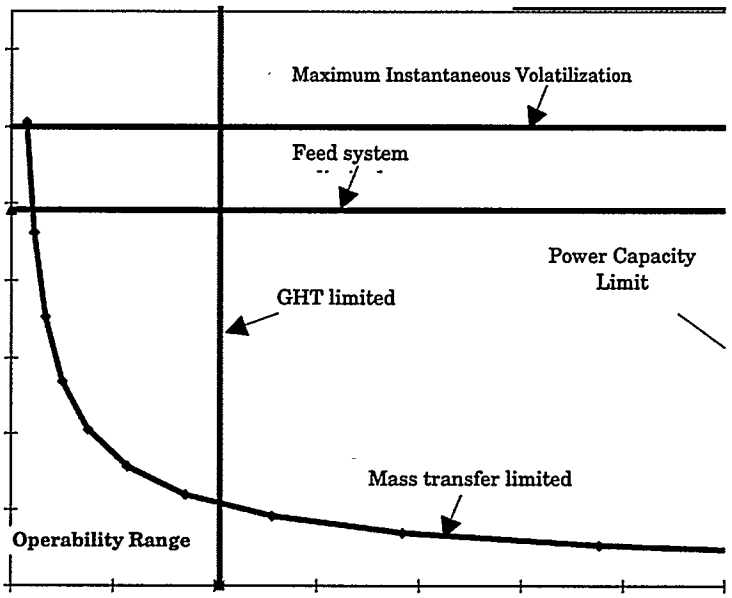

In order to fully realize the benefits of CEP application to DOE wastes, it is necessary to be able to efficiently remove condensed phase products from a reactor, preferably without interrupting the processing of feed materials. MMT has developed and demonstrated an innovative approach to product removal that utilizes an induction coil and susceptor pipe as shown in Figure 1.5. When the valve is in the closed state, the susceptor pipe is plugged with solidified product. The valve is opened by activating the induction coil which melts the solid plug, thus allowing the product to flow through the susceptor pipe into product containers/molds. Metal phase product removal is accomplished through a vertical tapping valve, while ceramic phase product removal is accomplished through a horizontal tapping valve. Remote-controlled, in-process (i.e. reactor tipping not required) product removal using this design has been successfully demonstrated on a pilot scale, providing the basis for continued evolution to commercial-scale product removal system design and development required for processing DOE wastes.

Figure 1.5
Pilot Scale Tapping Valve Design

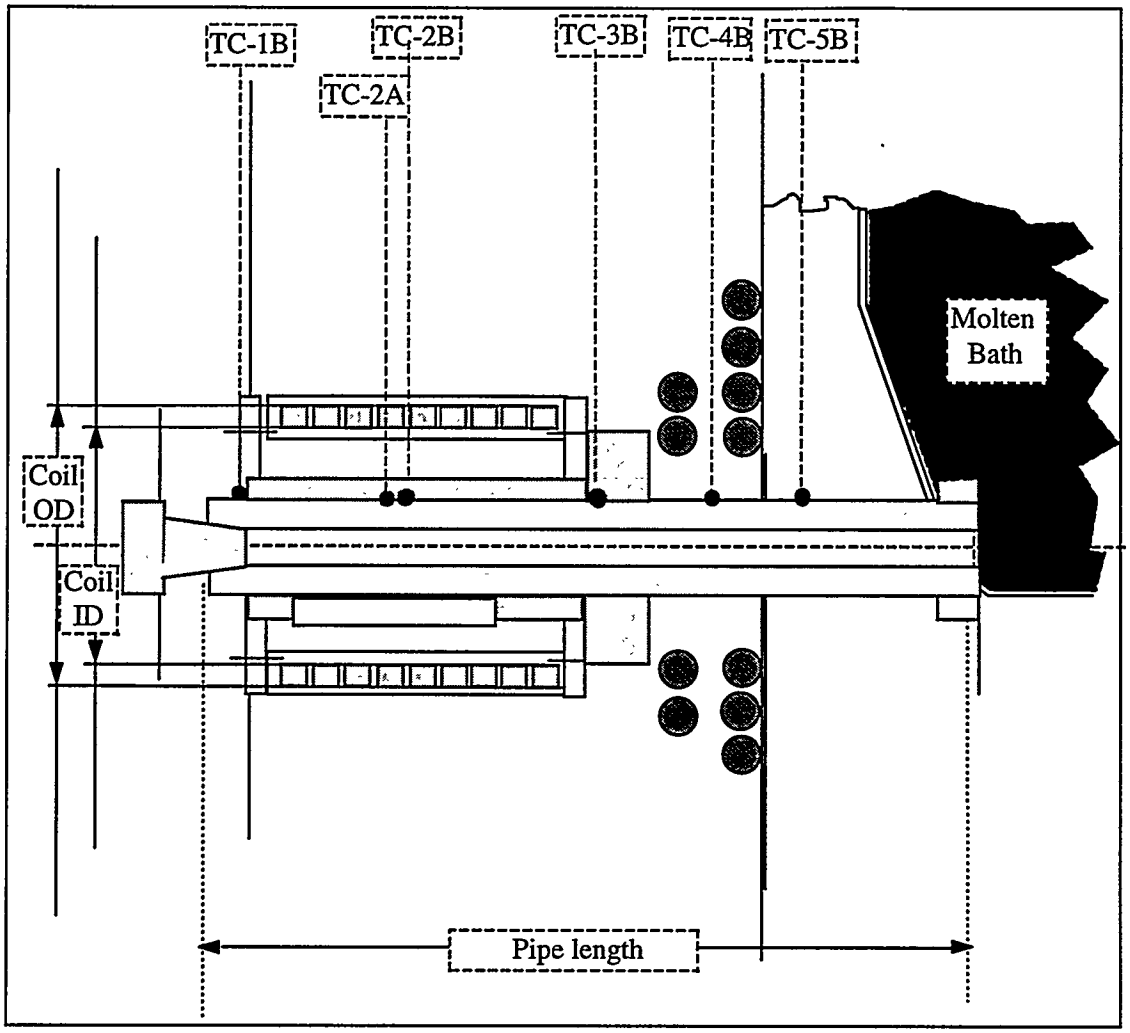

1.3.2.2. On-Line Sensors and Instrumentation

Development of advanced sensors, models, and techniques to monitor key process parameters is critical to robust, automated CEP operation. MMT has successfully a robust reactor control system which utilizes commercial off-the-shelf equipment to the maximum possible extent to monitor critical reactor parameters including bath temperature, headspace temperature, bath composition, bath level, bath pressure, containment system, tuyere injection, and visual observation. Emphasis was placed on the use of non-invasive techniques to minimize both the potential for interruption in the flow of operations and potential delay opportunities for feedback to optimize process control. For example, an IR lightpipe sensor has been successfully demonstrated to provide in-situ, continuous, lag-free, and non-invasive sensing of bath temperature. A 24-hour period of automatic bath temperature control of the 4-Ton Demonstration Unit using a lightpipe is shown in Figure 1.6. Similarly, sensors for the remaining critical reactor parameters and control system hardware/software which integrates the data

provided by these diverse sensors into a robust reactor control system have also been successfully demonstrated. Further, these sensors and their control system have been successfully implemented into the two commercial CEP facilities which are currently processing mixed low level wastes.

Figure 1.6
IR Lightpipe and Automatic Temperature Control Results

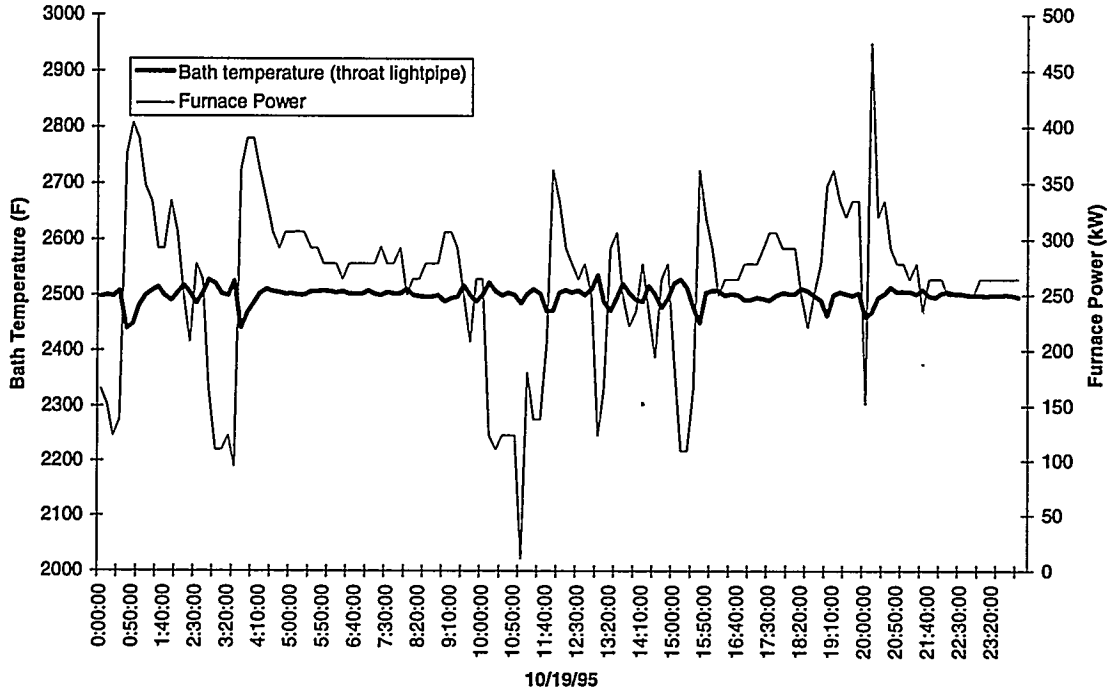

1.3.2.3. Particulate Characterization and Control

CEP has been identified as a technology whose robustness allows the processing of extremely heterogeneous wastes which are likely to contain volatile heavy metals and dust-producing elements. MMT has successfully developed and demonstrated particulate control methods based on the basic mechanisms for dust and particulate generation. Innovations in gas handling train technology and operation have led to both the suppression of dust formation, the recyclability of any dust that may form during processing, and the recovery of volatile heavy metals. Research and development efforts directed at particulate suppression indicate that with the exception of species predicted to volatilize in our system (e.g. lead, mercury), less than 2% will be carried over as dust and can be recycled to the bath (e.g. FeO). Further, the distribution in the particle size is skewed heavily towards the large end of the scale (i.e. greater than 10 microns), which makes them relatively easy to separate from the gas stream. The result is a system which produces a clean gas product that exceeds industrial specifications using proven, reliable technology.

1.3.3. Task 1.2 - Experimental Test Program

MMT developed and executed a comprehensive experimental test plan that was designed to provide performance data on the application of the Catalytic Extraction Process to DOE wastes. The test plan was developed to demonstrate selective radionuclide partitioning and immobilization using surrogates; destruction of hazardous organic constituents; partitioning of non-radioactive recyclable metals, and processing of bulk solids. These experiments also addressed waste feed management, safety management, general operations management, and off gas management. The results of this experimental test plan, which are used throughout this final report, have successfully demonstrated the versatility of CEP to process a broad spectrum of waste materials in the DOE complex. A listing of the experiments performed under this contract have been categorized by major tasks in the statement of work and are presented in a separate appendix. It should be noted that experiments addressing the partitioning of actual radionuclides were not funded by the current contract; therefore, they have not been included in these tables.

1.3.4. Task 1.3 - Experimental Testing

A substantial amount of theoretical work has been performed on the separation of chemically similar metals such as technetium (Tc), uranium (U), and nickel (Ni). It is clearly desirable to separate these long half-life contaminants from short half-life and nonradioactive constituents of the waste material and contaminated metals. With uranium this is more readily accomplished due to the ease of oxidizing its oxide (UO_2) into its dication (UO_2^{2+}). Technetium also forms a dioxide (TcO_2) and it is also possible to form a similar dication (TcO_2^{2+}). If TcO_2^{2+} forms readily, technology can be developed to effect a phase transfer of technetium from its metallic state to an ionic or vitreous phase. High level non-empirical quantum calculations on Tc- and Ni-oxides were performed to derive estimates of the energetics of reactions which can potentially be used for the separation of technetium from nuclear waste or metal surfaces. Theoretical results suggest that oxidation and subsequent migration from the metal phase to the ceramic phase should have a much more favorable equilibrium constant for extraction of technetium oxides (TcO and TcO_2) than for the nickel oxides. Given that the oxidation potential for the uranium oxides (UO and UO_2) are significantly lower than those of technetium, the oxidation of technetium metal into its oxide in the presence of nickel and its subsequent transfer from the metal phase to the ceramic phase is considered to be feasible. The calculated value of the Gibb's Free Energy for oxidation of technetium suggests that the reaction is thermodynamically favorable; however, additional work is required to assess the accuracy of the computational data and to estimate the free energy of the TcO_2 phase transition from available experimental data. This important theoretical work will provide the foundation for a future experimental program which may lead to the ability to recycle and reuse the approximately $1.5 billion of radioactive contaminated nickel in the DOE inventory.

A series of experiments was performed with a divinyl benzene organic combined with either surrogate or actual radionuclides to measure the partitioning of radionuclides in the metallic, ceramic, and gas phases. The radioactive portion of these experiments was not performed under this contract; however, the data has been included in this final report because it is known to be a major DOE interest item. The focus of these experiments was to establish operating requirements to partition radionuclides to the desired phase. MMT has successfully demonstrated that CEP can substantially reduce the volume of radioactive wastes while producing a highly stable waste form for eventual disposal. As predicted, processing conditions enabled complete capture of non-volatile radionuclides into the metallic and ceramic phase. Further, MMT has successfully demonstrated the ability of CEP to control partitioning of radionuclides to either the metal phase which provides a stable waste form with significant self-shielding (the self-absorption of radiation-reducing radiation levels), or to the ceramic phase which also provides a stable waste form and achieves substantial volume reduction. Volatile radionuclides were captured from the gas phase with measured decontamination factors in excess of 10^4. These experiments clearly demonstrate CEP's ability to recycle and reuse radioactive contaminated wastes, effectively control partitioning to the desired product phase, substantially reduce the volume of radioactive wastes, and produce a highly stable waste form for eventual disposal.

1.3.5. Task 1.4 - Optimization of the Vitreous Phase for Stabilization of Radioactive Species

MMT has performed an extensive series of experiments to optimize the ceramic phase for stabilization of radioactive species. While most of this work was performed at MMT's Fall River R&D facility using radioactive surrogates, some experiments have been performed at Oak Ridge, TN using actual radionuclides. Tests using actual radionuclides have successfully verified previously conducted experiments for partitioning their surrogates radionuclides to the ceramic phase. Further, experiments involving the recycle of uranium hexafluoride and West End Treatment Facility sludge were not funded under this contract; however, the results have been included in this final report as they are major DOE interest items.

MMT performed a series of bench scale experiments using radioactive surrogate materials to demonstrate the oxidation and partitioning of radionuclides between the metal and vitreous phases and to identify and optimize the effect of operating conditions on partitioning. The bench-scale experiments were followed by experiments on pilot- and demonstration-scale systems. Hafnium was selected as a radioactive surrogate due to its similarities in thermodynamic behavior (Figure 1.7) and physical properties (Table 1.6) to uranium. Zirconium, although similar to uranium in the thermodynamic properties, was not chosen as the primary surrogate material because of its significantly lower density, but was actually used as a feed material in several experiments and was also proven to effectively partition to the ceramic phase.

Figure 1.7
Identification of Radionuclide Surrogate

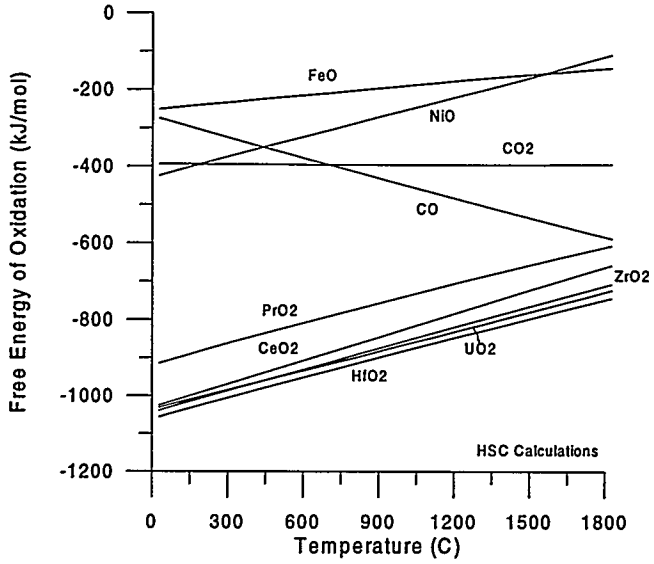

Table 1.6
Physical Properties of Uranium and Surrogates

Element	Oxide		Metal	
	m.p. (°C)	Density (g/cm^3)	m.p. (°C)	Density (g/cm^3)
U	2,878	10.96	1,132	19.05
Hf	2,758	9.68	2,227	13.31
Zr	2,715	5.6	1,852	6.49
Fe	1,369	5.7	1,535	7.86
Ni	1,984	6.67	1,455	8.90

The experimental design parameters evaluated were metal system, gas environment and ceramic phase composition. Radioactive surrogate partitioning was measured using neutron activation analysis (NAA) for non-destructive trace analysis. The hafnium LDL was 0.2 ppm in iron and 2 ppm in nickel. X-ray fluorescence (XRF) was used for analysis of the vitreous phase composition. Metal samples were taken at different positions in the metal bath to ensure uniform decontamination. The contract objective was to demonstrate uniform metal decontamination above 98%. In addition,

backscattered electron imaging and x-ray analysis were used to investigate the nature of the capture and stabilization of the radionuclide surrogate in the vitreous phase.

Average decontamination of the metal samples were > 99% and exceeded the contract's 98% objective in all experimental trials. The calculated decontamination factors were analytically limited with no radioactive surrogate detected in the metals. Table 1.7 summarizes the results. V1 refers to aluminosilicate vitreous compositions while V2 refers to borosilicate vitreous compositions.

Table 1.7
Radionuclide Partitioning

Metal	Vitreous Phase	Decontamination
Iron	V1	≥ 99.62%
Nickel	V1	≥ 99.76%
Iron	V2	≥ 99.08%

Samples taken at different positions in the metal bath demonstrate uniform distribution of any trace amounts of hafnium across the metal (Figure 1.8 and Figure 1.9). This indicates that radioisotope transport to and incorporation in the oxide phase is very efficient under CEP operating conditions.

Figure 1.8
Sampling across Radius of Metal

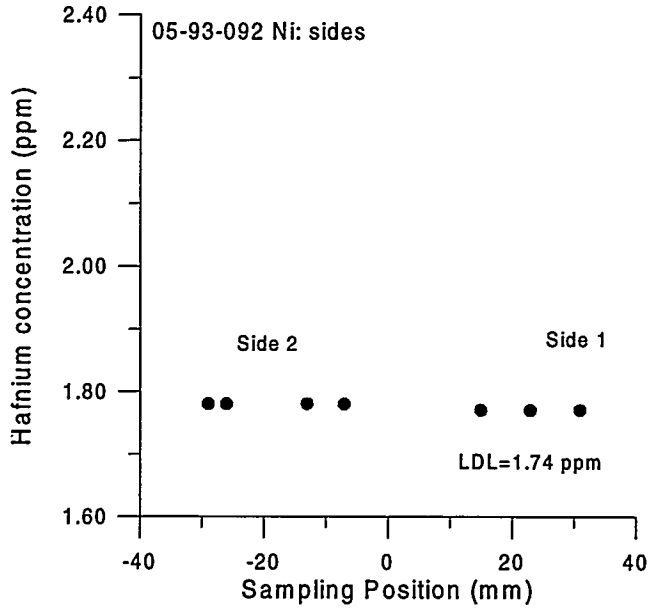

Figure 1.9
Sampling from
Top to Bottom of Metal

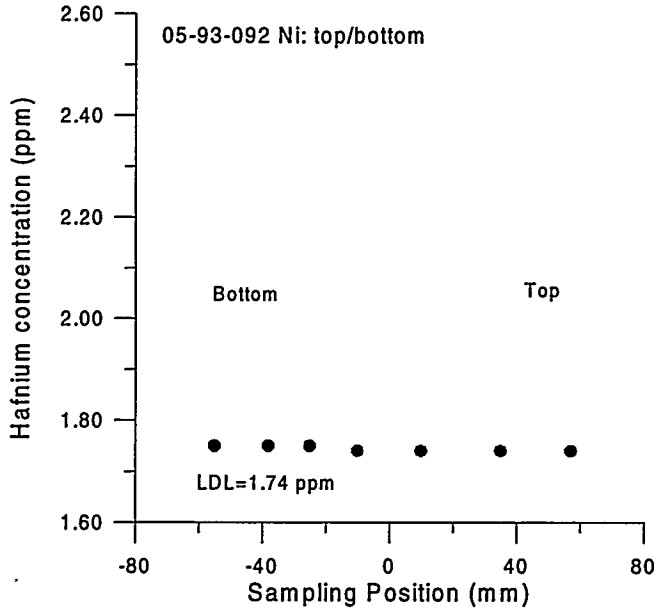

Ceramic samples were analyzed using backscatter electron imaging to identify the nature of the radionuclide capture and stabilization in the ceramic phase. This work indicated that operating conditions and vitreous phase composition can affect

radionuclide capture and stabilization. Figure 1.10 shows the backscatter image of a vitreous sample which has separated into hafnium rich and hafnium poor regions. This is in contrast to the vitreous sample shown in Figure 1.11, where hafnium is uniformly distributed. CEP conditions have been identified to achieve this desired vitreous radionuclide capture and stabilization mechanism.

Figure 1.10
Backscatter Image:
Phase Separation Exhibited

Figure 1.11
Backscatter Image:
No Phase Separation Exhibited

MMT has successfully demonstrated the ability of CEP to partition radionuclides to the ceramic phase, thereby achieving substantial volume reduction of the radioactive waste and producing a highly stable waste form for eventual disposal. Uranium (U) and cerium (Ce) radionuclides were successfully partitioned to a ceramic phase composed of either calcium aluminosilicate or lithium boron calcium aluminosilicate. A glass synthesis experiment was also conducted using known quantities of UO_2 and CeO_2 to evaluate high levels of waste loading and incorporation of these elements into ceramics. The partitioning experiments were performed using two different ceramic phase compositions to evaluate operability, waste loading, and leach resistance. Calcium aluminosilicate was selected for its relatively low viscosity and its leach resistance. Lithium boron calcium aluminosilicate was selected to increase waste loading and decrease viscosity. Both ceramic phase compositions exhibited minimal chemical interaction with the containment system. Four types of analyses were performed on the samples obtained from these experiments: neutron activation analysis (NAA), gamma spectroscopy, a Tennelec (Oxford) $\alpha\beta$ counting system, and a frisker (Geiger counter) for gross initial measurements. Alpha, beta, and gamma activity were measured as a function of ceramic phase sample mass, which was then used to calculate activity/gram of sample and activity/gram of uranium. A comparison of the alpha, beta, and gamma activities as a function of uranium content in the crushed ceramic phase samples is presented as Figure 1.12. Analysis of the metal samples, presented in Table 1.8, demonstrate metal decontamination in excess of 99%, which is consistent with the data obtained from the ceramic phase samples. The data obtained from these experiments conclusively demonstrate CEP's ability to partition actual radionuclides to the ceramic

phase, thus achieving a high degree of metal decontamination which is necessary for the recycle, reuse, and disposal of materials from DOE decontamination and decommissioning activities.

Figure 1.12
Comparison of Alpha, Beta, and Gamma Activity as a Function of Uranium Content in Crushed Glass Samples

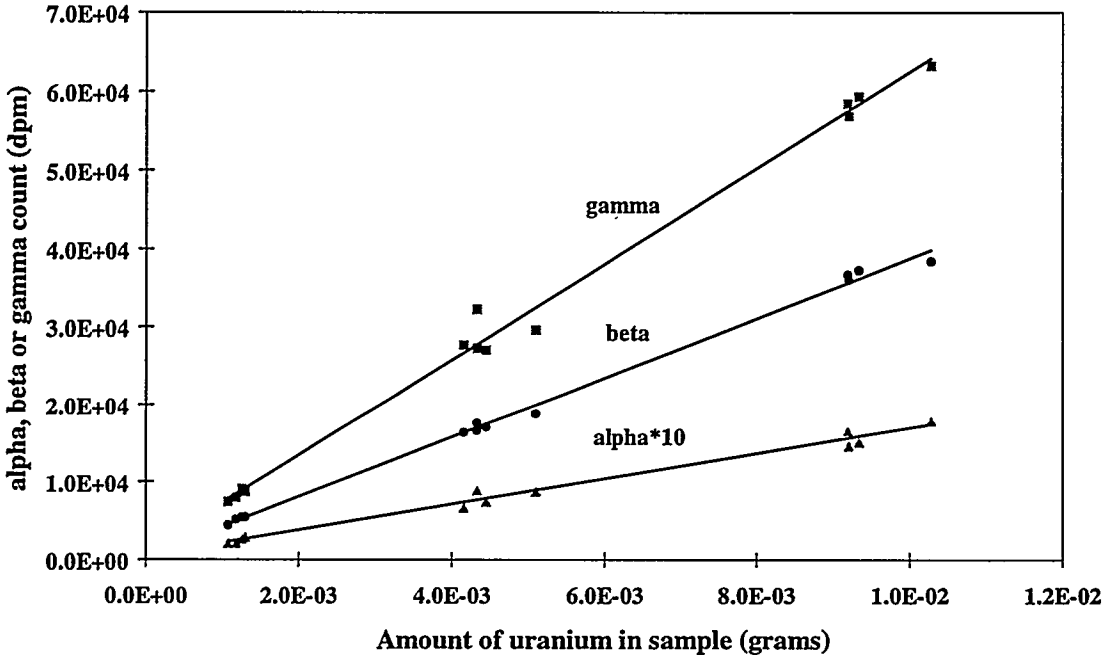

Table 1.8
Uranium Concentration in Metal Samples

Sample	Uranium Concentration (ppm)	Decontamination (%)
M7	0.28	99.97
M8	0.62	99.93
M9	0.69	99.93

MMT has performed a comprehensive series of experiments that have successfully verified the previously established thermodynamic feasibility of using catalytic extraction processing as an efficient and cost-effective means of converting uranium hexafluoride (UF_6) to uranium oxide (UO_x) and anhydrous hydrogen fluoride (HF). These experiments were not funded under this contract, but the results have been included in this final report as it is a major DOE interest item. Uranium hexafluoride is

one of the most widely used chemical compounds of uranium. Over one billion pounds of UF_6 have been produced over the past 50 years in support of the U.S. uranium isotope enrichment enterprise. There is a growing concern regarding the long-term environmental risks associated with continued storage of large UF_6 inventories. DOE currently stores approximately 610,000 metric tons of UF_6, with an additional 22,000 metric tons stored by the U.S. Enrichment Corporation (USEC). MMT has successfully demonstrated the ability of CEP to safely and reliably process UF_6 to produce a more stable uranium compound for recycle within the DOE complex or nuclear industry while producing valuable, high quality anhydrous HF which can be recycled to the commercial chemical market. In the two tests performed to date, no residual UF_6 was detected in either the process off-gas or the chemical traps to a Lower Detection Limit (LDL) of 100 ppm. Safety programs for UF_6 processing have also been demonstrated, confirming the functionality of the facility design including safe handling of the UF_6 and HF, effective chemical trapping of HF product, containment of carbon monoxide and hydrogen, environmental monitoring, and on-line instrumentation. These experiments have successfully demonstrated the applicability of catalytic extraction processing to effectively and economically recycle an important waste form that exists in a large quantity within the DOE complex.

MMT has also performed a series of experiments to optimize the ceramic phase for CEP processing of mixed-waste sludge. These experiments were also not funded under this contract, but the results have been included in this final report as it is a major DOE interest item. The sludge used in these experiments is a byproduct of industrial waste water treatment and was obtained from DOE's West End Treatment Facility (WETF) in Oak Ridge, TN. The WETF sludge contains a significant amount of water and is contaminated with residual organics, chlorine, phosphorous, RCRA metals, nickel, and radionuclides including uranium (1.2×10^{-3} μCi/g), technetium (18.7×10^{-4} μCi/g), and cesium (1.8×10^{-6} μCi/g). The objective of these experiments was to engineer a ceramic phase that is operable (i.e. workable viscosity and minimum containment corrosivity), functional (i.e. accommodates major ceramic-forming components and captures any hazardous and/or radioactive components in a non-leachable form), stable during long-term storage, and maximizes volume reduction. Fifteen bench-scale experiments and a 27 hour pilot-scale experiments were performed during this test program, as well as a series of potential-driven neutralization tests, recipe development tests for cement product development, and slurry injection system development. This test program has successfully developed and demonstrated an operable, functional and stable ceramic phase that achieves a significant amount of volume reduction. Experimental results included the ceramic phase product meeting all Envirocare Waste Acceptance Criteria requirements including passing the toxicity characteristic leaching procedure (TCLP), achieving a mass balance closure of 100±5%, demonstrating uranium capture in the ceramic phase, and meeting market specifications of targeted products for DOE on-site reuse (ceramic product development). Further, this experimental program also successfully demonstrated the versatility of CEP for processing DOE wastes including highly aqueous waste streams such as WETF sludge.

1.3.6. Task 1.5 - Experimental Testing of Resource Conservation and Recovery Act (RCRA) Wastes

The investigation of CEP's conversion and immobilization capabilities for RCRA components of contaminated scrap metal feeds has been well proven during the experimental campaign of this contract. MMT brought to the contract a solid foundation of understanding of the behavior of toxic and halogenated feeds in CEP, and proceeded to optimize the chemistry of the system for the feeds anticipated. Efforts began on bench-scale apparatus, and subsequent prototype trials validated bench-scale results.

Table 1.9 demonstrates CEP's environmental and waste minimization performance for a wide range of heterogeneous wastes, encompassing practically every chemical and physical form. These diverse waste forms span the chemical compositions and physical forms which are encountered throughout the DOE complex. A recent benchmarking procedure developed by DOE for evaluating mixed waste treatment technologies identified naphthalene, dichlorobenzene, and monochlorobenzene as being representative of DOE wastes. CEP environmental performance on these species, surpassing current EPA standards, is presented herein. This same benchmarking procedure identified Cr, Ni, Pb, and Cd as RCRA constituents in DOE wastes. These metals have been successfully recovered as commercial products as part of the surplus metal componentry recycling and biosludge processing. DOE-recommended and MMT identified radioisotope surrogates (Hf, Zr) have been successfully partitioned to a stable, non-leachable phase, also as part of the surplus metal componentry recycling

CEP has robustly recycled a variable and chemically diverse feed slate as represented by the feeds in Table 1.9. High molecular weight aromatics were converted to synthesis gas with a conversion efficiency > 99.9999% with no products of incomplete conversion detected (chemically analagous to benzene and naphthalene, DOE-recommended surrogates). Complex chlorinated organics including aromatics, aliphatics, plastics (PVC), and heavily-chlorinated RCRA listed wastes K019/20 and F024 have been successfully converted to products such as synthesis gas or condensed phase chlorinated products (chemically analagous to PCBs). Trace components such as dioxins and difurans were not detected to the targeted regulatory limit of 0.1 ng/Nm^3 (TEQ 2,3,7,8-TCDD) as shown in Table 1.10. Organically-bound nitrogen and highly toxic isocyanates (RCRA listed waste K027) were synthesized into nitrogen (N_2), hydrogen (H_2) and carbon monoxide (CO) with no detection of NO_x formation to 1 ppm. Highly heterogeneous wastes including surplus metal/weapon componentry (chemically and physically analagous to decommissioning materials) and biosludge

Table 1.9
Major Feeds Processed at the Demonstration Prototype

			Waste Minimization Performance			Environmental Performance		
Feed	**Key Elements**	**Chemical Structure**	**Product Recovery**	**% of feed Recycled**	**Residual**	**DRE**	**TCLP**	**Trace**
Representative Surrogate Feeds								
Polystyrene/ graphite	C, H	High molecular weight aromatic	Syngas	99% to syngas	Dust Negligible	≥ 99.9999%	N/A	PICs < LDL[1] of 1 ppm CO_2<1% NO, SO_2 < LDL of 100 ppm
Chlorotoluene/ heavy organics	C, H, Cl	Halogenated aromatic	Syngas Ceramic	87% to syngas 12% to ceramic	Dust Negligible	≥ 99.9999%	Passes TCLP	PICs < LDL of 1 ppm CO_2 < 1% NO, SO_2 < LDL of 100 ppm
Dimethyl Acetamide/ heavy organics	C, H, N	Organically-bound nitrogen	Syngas Nitrogen	96% to syngas 3% to nitrogen	Dust Negligible	≥ 99.9999% (based on THC)	N/A	PICs < LDL of 1 ppm CO_2 < 1% NO, SO_2 < LDL of 100 ppm[2] NO_x, SO_x < LDL of 1 ppm[3]
Representative Hazardous Waste Feeds								
Industrial Biosludge waste	C, H, N, S, Ash (P, Na, Ca, Mg)	Highly variable heterogeneous organic and inorganic sludge	Syngas Nitrogen Ceramic Ferroalloy	70% to syngas 8% to nitrogen 20% to ceramic 1% to ferroalloy	Dust Negligible	≥ 99.9999% (based on THC)	Passes TCLP	PICs < LDL of 1 ppm CO_2 < 1% NO, SO_2 < LDL of 100 ppm
Surplus Metal/Weapon Componentry	80% of Non-radioactive elements	Precious, volatile (Pb, Zn), and reducible metals (Cr, Ni), plastics, exothermic inorg. uncharacterized solids	Syngas Ceramic Ferroalloy	25% to syngas 8% to ceramic 63% to ferroalloy	Dust Negligible	N/A	Passes TCLP	PICs < LDL of 1 ppm CO_2 < 1% NO, SO_2 < LDL of 100 ppm
K019/K020[4]/ chlorobenzene/ Fuel oil	C, H, Cl	Residuals from PVC mfr; unsat'd Cl-organics	Syngas	76% to syngas 23% to ceramic	Dust Negligible	≥ 99.9999%	Passes TCLP	PICs < LDL of 1 ppm CO_2 < 1% NO, SO_2 < LDL of 100 ppm
K027[5]	C, H, N	Isocyanates, highly toxic	Syngas Ferroalloy (Fe - Ni)	93% to syngas 5% to nitrogen <1% to ceramic <1% to ferroalloy	Dust Negligible	≥ 99.9999%	Passes TCLP	PICs < LDL of 1 ppm CO_2 < 1% NO, SO_2 < LDL of 100 ppm
F024[6]/ Fuel oil/ chlorotoluene	C, H, Cl	Halogenated aliphatics	Syngas HCl gas	82% to syngas 13% to HCl gas <1% to ceramic	Dust Negligible	≥ 99.9999%	Passes TCLP	PICs < LDL of 1 ppm CO_2 < 1% NO, SO_x < LDL of 3 ppm and 1 ppm respectively

[1] LDL = Lower Detection Limit.
[2] As measured by on-line mass spec.
[3] As measured by third party analytical equipment placed on-line.
[4] EPA listed hazardous waste stream: ethylene dichloride/vinyl chloride heavy ends.
[5] EPA listed hazardous waste stream: toluene diisocyanate distillation residues.
[6] EPA listed hazardous waste stream: chlorinated aliphatic hydrocarbons.

Table 1.10
Trace Component Off-Gas Concentrations during CEP of Chlorinated Wastes

Description:		Aromatics - 20% PVC	Biosludges - 2% PVC	Biosludges - 2% PVC	F024	F024
Time	Initial:	15:10	18:34	10:02	0:54	2:50
	Final:	15:40	19:12	11:02	2:18	4:03
Gas Meter Volume (ft^3)	Initial:	619.67	296.70	303.59	319.26	339.35
	Final:	639.67	303.59	313.61	339.35	360.65
Gas Meter Outlet (°F)	Initial:	66	70	70	70	70
	Final:	67	70	70	70	70
Total Sample Volume	SCF:	20.13	6.89	10.02	20.09	21.30
	Nm^3:	0.53	0.18	0.26	0.53	0.56
Analytes (ng)						
Total TCDD:		ND	ND	ND	ND	ND
Total PeCDD:		ND	ND	ND	ND	ND
Total HxCDD:		ND	ND	ND	ND	ND
Total HpCDD:		ND	ND	ND	ND	ND
Total OCDD:		ND	ND	ND	ND	ND
Total TCDF:		ND	ND	ND	ND	ND
Total PeCDF:		ND	ND	ND	ND	ND
Total HxCDF:		ND	ND	ND	ND	ND
Total HpCDF:		ND	ND	ND	ND	ND
Total OCDF:		ND	ND	ND	ND	ND
2,3,7,8-TCDD toxicity equivalents (ng/Nm^3)						
EPA-1989		ND	ND	ND	ND	ND
NATO		ND	ND	ND	ND	ND
Nordic		ND	ND	ND	ND	ND
UBA		ND	ND	ND	ND	ND
BUS		ND	ND	ND	ND	ND

ND = Not Detected to targetted regulatory standard of 0.1 ng/Nm^3.

wastes (chemically and physically analagous to DOE sludges) from wastewater treatment (both potentially RCRA characteristic wastes when discarded), which contained from 0 to > 60% metals, were successfully recycled into commercially valuable products as confirmed by MADEP (Massachusetts Department of Environmental Protection) Recycling Certifications. In all cases environmental standards were met and surpassed. Table 1.11 shows that all ceramic material generated in CEP passed TCLP forming a safe, non-leachable potential final form for radionuclides.

Table 1.11
CEP Ceramic Products Form Non-Leachable Matrices

Waste Processed	TCLP Metals Regulated Limits (mg/l)							
	As 5.0	Ba 100	Cd 1.0	Cr 5.0	Pb 5.0	Hg 0.2	Se 1.0	Ag 5.0
K019/K020[1]	ND	ND	ND	0.3[2]	ND	ND	ND	ND
PVC and Polystyrene	ND	ND	ND	0.3[2]	ND	ND	ND	ND
Spent Metal Componentry with Cl-plastics[1]	ND	ND	ND	0.5[2]	ND	ND	ND	ND
PVC and Polystyrene[3]	NA	NA	ND	ND	ND	NA	NA	NA
Biosludge with 1% Cl	ND	ND	ND	ND	ND	ND	ND	ND
F024	ND	ND	ND	ND	ND	ND	ND	ND

ND = Not Detected; NA = Not Applicable
[1] The full TCLP was run for these samples. All other regulated species were ND.
[2] Cr_2O_3-Al_2O_3 refractory bricks were present during these runs which provided a source of Cr_2O_3. Total Cr has been measured and no hexavalent Cr^{+6} was detected. The refractory has been optimized to eliminate Cr.
[3] A partial TCLP test was performed for Cd, Cr and Pb

1.3.6.1. Mass Balance Closure on Materials Representative of DOE Feeds

MMT has successfully processed and recovered products from multiple materials of direct interest to DOE. Materials such as surplus metal componentry, biosludge, and chlorinated RCRA wastes are analogous to metal, sludge, and organic wastes within the DOE complex. Of particular interest to DOE are radionuclides such as uranium, plutonium and organic contamination originating from sources such as lubricating oils, cutting fluids, solvents, and PCBs. All material which may potentially contaminate scrap metal or be contained in the debris are candidates for processing by CEP. Mass Balance results for a variety of feeds processed via CEP are shown in Table 1.12.

Table 1.12
Demonstration-Scale Mass Balances for RCRA and RCRA-like Feeds
Analagous to DOE Wastes

Components (lbs.)	F024 RCRA Chlorinated Waste	Biosludge Waste	K019/20 RCRA Chlorinated Waste	Surplus Metal Componentry
Waste Feed[1]	666	4684.00	238	496.19
Methane[2]	32	175.58	13.54	10.71
Oxygen[2]	668.13	2022.92	275.70	205.74
Carbon Added to Bath		380.00	70	110
Iron Melt[3]	3510	3180.00	3838	3838
Flux Additions	65	218.00	438.4	176.87
Ceramic in Bath	800	NA		
Total Input	5741.13	10660.50	4873.64	4837.51
Hydrogen[4]	73.27	379.02	28.36	15.71
Carbon Monoxide[4]	1097.69	5846.31	561.13	386.38
Carbon Dioxide[4]	29.47	936.58	9.90	30.59
Hydrogen Chloride[4]	84.88		16.06	
Ferro alloy Product[5]	3505	3225.00	3829.29	4200
Ceramic Product[6]	905	410.00	450.70	312
Total Output	5695.31	10256.92	4895.44	4946.61
Closure	99.20%	96.2%	100.45	102%

[1] Feed composition based on third party elemental feed analysis; total amount of feed injected was calculated based on change in feed tank weight data installed in the 20-second data log program.
[2] Co-feeds measured by on-line flowmeters (20-second datalog program)
[3] Amount of metal added was recorded in the operator book. Carbon concentration in metal was determined by on-site LECO analysis. Pre-injection metal analysis (third party analysis) were used in some cases.
[4] Argon was used as tracer gas to determine the total off-gas flow. Individual product gas flow was determined by mass spectrometer results (20-second datalog program)
[5] Usually a tracer like nickel was used to determine the total weight of metal in bath. The calculation was confirmed by the tapped metal weight. Post-injection metal analysis determined the composition.
[6] Usually a tracer like hafnium was used to determine the total ceramic phase amount. Post injection ceramic analysis determined the composition.

1.3.6.2. Material Recovery

Following the dissolution process characteristic of CEP, the addition of co-feeds and engineering of process variables results in targeted product formation. Very high

conversion of waste feeds has been demonstrated. Demonstrations verify that all organic materials in CEP feed materials are converted to synthesis gas; non-reducible metals such as aluminum, calcium, silicon, etc. are recovered as a ceramic product; reducible non-volatile metals such as copper, iron, cobalt, chromium, vanadium, etc. are recovered as metal product; volatile reducible metals such as zinc and lead are captured and collected in the gas handling train (GHT). The potential of each of these product phases to meet specifications for on-site use as raw materials or commercial market usage has been demonstrated. MADEP has certified CEP as recycling for heterogeneous organic, metallic, and organometallic wastes. The following tables summarize the recovery results in various product phases for CEP.

Table 1.13
Experimental Recovery for Synthesis Gas

	Synthesis Gas Formers (wt% feed)			% Feed	% Recycled	% Recovered
	C	H[1]	O			
RCRA Waste F024	72.50	9.46	0.1	82.06	80.84	**98.51**
RCRA Waste K019/020	68.1	8.07	0.9	77.07	76.3	**99.0**
Surplus Metal	32.09	3.46	23.37	58.86	57.46	**97.62**
Surplus Metal Surrogate	19.11	1.76	4.22	25.09	23.76	**94.691**
Biosludge (1)	45.43	6.57	26.98	78.98	73.57	**93.151**
Biosludge (2)	45.43	6.57	26.98	78.98	74.29	**94.921**

Note: The % Feed represents the potential amount of feed that could form the product. The % Recycled represents the amount of the elements present in the actual product formed based on treatability study results. The % Recovered is the ratio of % Recycled to % Feed which shows the efficiency of the CEP for waste recycling.
[1]Attributable in part to feed variability

Table 1.14
Experimental Recovery for Ceramic Product

	Feed Composition Elemental wt%												% Feed	% Recycled	% Recovered
	Al	Ca	Si	Mg	Ba	O	Cl	S	P	Na	K	Ti			
Biosludge(1)	0.05	0.81	0.35	0.20	-	4.44	0.06	0.36	0.17	1.76	0.48	-	8.69	8.69	100
Biosludge(2)	0.05	0.81	0.35	0.20	-	4.44	0.06	0.62	0.01	1.76	0.24	-	8.54	8.54	100
Actual SMC	8.69	-	7.48	0.23	0.53	-	0.68	0.54	-	-	-	0.70	18.5	18.5	100
Component SMC	7.61	-	-	-	-		-	-	-	-	-	-	7.61	7.61	100

Note: The % Feed represents the potential amount of feed that could form the product. The % Recycled represents the amount of the elements present in the actual product formed based on treatability study results. The % Recovered is the ratio of % Recycled to % Feed which shows the efficiency of the CEP in actual recovery performances.

Table 1.15
Experimental Recovery for Metal

	Feed Composition Elemental wt%								% Feed	% Recycled	% Recovered
	Fe	Cu	Ni	Cr	Co	Mn	Ag	Mo			
Actual SMC	6.97	5.16	1.93	0.61	0.4	0.18	0.15	0.1	15.5	15.5	100
Component SMC	22.53	37.14	1.68	1.97	-	-	0.61	-	64	64	100

Note: The % Feed represents the potential amount of feed that could form the product. The % Recycled represents the amount of the elements present in the actual product formed based on treatability study results. The % Recovered is the ratio of % Recycled to % Feed which shows the efficiency of the CEP in actual recovery performances.

1.3.6.3. Environmental Performance and Regulatory Standards

1.3.6.3.1. Destruction and Removal Efficiency (DRE) Results

Destruction Removal Efficiency (DRE) has been the standard method in the regulatory environment to determine the effectiveness of waste treatment. The amount of principle organic hazardous constituent (POHC) before and after treatment is compared using the formula:

$$(In - Out) / In * 100\%$$

where In = Amount of hazardous constituent in the waste feed

Out = Amount of the same hazardous constituent in the off-gas

In CEP, feed constituent composition is determined by third party analytical laboratory results. SUMMA canisters are filled with off-gas samples at the baghouse outlet during the injection period. Consistently, the hazardous waste materials processed in the feed were not detected in the off-gas down to the lowest detection limits in the range of ppb, resulting in DREs of ≥99.9999% far surpassing the current regulated standard 99.99%.

Table 1.16 shows the results of a chlorinated organic material (PVC/Polystyrene mixture) processed via CEP. Both polyvinyl chloride (PVC) and polystyrene are polymeric molecules that did not volatilize and therefore, would not be detected in the off-gas. An alternative approach for calculating DRE values was based on the assumption that PVC could be modeled as vinyl chloride (CH_2CHCl) or as chloroethane (CH_3CHCl), which are very similar structurally to the PVC monomer (-[CH_2CHCl]-). Similarly, polystyrene (-[CH_2-$CH(C_6H_5)$]-) can be modeled as styrene (CH_2=$CH(C_6H_5)$) or as ethyl benzene ($CH_3CH_2(C_6H_5)$). The modeled compounds were analyzed by EPA Method TO-14. The model compounds were not detected in the off-gas, resulting in DREs of ≥99.9999%.

Table 1.16
DREs for PVC and Polystyrene

Sample No	Sampling Time	Tracer	Compound	DRE
DRE-16-BO	1:49-2:33	Vinyl chloride	PVC	≥99.99998%
DRE-16-BO	1:49-2:33	Chloroethane	PVC	≥99.99998%
DRE-17-BO	4:14-4:50	Vinyl chloride	PVC	≥99.99998%
DRE-17-BO	4:14-4:50	Chloroethane	PVC	≥99.99998%
DRE-16-BO	1:49-2:33	Styrene	Polystyrene	≥99.99994%
DRE-16-BO	1:49-2:33	Ethyl benzene	Polystyrene	≥99.99993%
DRE-17-BO	4:14-4:50	Styrene	Polystyrene	≥99.99994%
DRE-17-BO	4:14-4:50	Ethyl benzene	Polystyrene	≥99.99994%

Trace molecules not detected in the CEP product gas. DREs limited by the lower detection limits

Another example of effective DRE performance was demonstrated in F024 processing. The POHC of the feed (defined by EPA methods), chlorobenzene; and the major hazardous organic (the high concentration in the feed), trichlorobenzene was used to perform DRE calculations. Both of the constituents were not detected to the lowest detection limit in the range of ppb, resulting a DRE of ≥99.9999%. A summary of the F024 test results are presented in Table 1.17 through Table 1.20.

Table 1.17
DREs for Chlorobenzene and Trichloroethene

Sample No.	Sampling Time	DRE for Chlorobenzene (POHC)	DRE for Trichloroethene
1T-94-009-BO-12	0:39	≥99.9999	≥99.9999
1T-94-009-BO-13	1:39	≥99.9999	≥99.9999
1T-94-009-BO-14	1:39	≥99.9999	≥99.9999
1T-94-009-BO-15	2:42	≥99.9999	≥99.9999
1T-94-009-BO-16	2:42	≥99.9999	≥99.9999
1T-94-009-BO-17	3:50	≥99.9999	≥99.9999
1T-94-009-BO-18	3:50	≥99.9999	≥99.9999

Note: Chlorobenzene and trichloroethene were non-detectable in the off-gas. DRE's were limited by the lower detection limit (LDL)

Table 1.18
Off-Gas Performance of F024 Processing
(Based on TO-14 Data)

Constituents	Feed Composition (mg/l)	CEP Product-gas (ppm)
1,1,2-Trichloroethane	18,000	ND (0.00037)
Chlorobenzene	12,000	ND (0.00037)
1,2-Dichloroethane	6,800	ND (0.00044)
1,1,2,2-Tetrachloroethane	11,000	ND (0.00029)
Trichloroethene	24,000	ND (0.00038)

ND = Not Detected (lowest detection limit)
Off-gas regulations are based on the performance of thermal oxidizers; regulations not available for specific organic constituents.

Table 1.19
CEP Performance under Non Wastewater Regulations
(Based on F024 Processing)

Constituents	Feed Composition (mg/l)	CEP Ceramic Product (mg/kg)	CEP Metal Product (mg/kg)	EPA Non Wastewater Regulation (mg/kg)
1,1,2-Trichloroethane	18,000	ND (0.0075)	ND (0.0075)	6.0
Tetrachloroethene	9,700	ND (0.0075)	ND (0.0075)	6.0
Chlorobenzene	12,000	ND (0.018)	ND (0.018)	6.0
1,2-Dichloroethane	6,800	ND (0.0075)	ND (0.0075)	6.0
1,1,2,2-Tetrachloroethane	11,000	ND (0.005)	ND (0.005)	6.0
Trichloroethene	24,000	ND (0.005)	ND (0.005)	6.0
Xylenes	610	ND (0.005)	ND (0.005)	3.0
1,1,1,2-Tetrachloroethane	1,000	ND (0.025)	ND (0.025)	6.0
Hexachlorobutadiene	3,600	ND (0.025)	ND (0.025)	5.6
Naphthalene	900	ND (0.025)	ND (0.025)	5.6
ND=Not Detected (Detection limit)				

Table 1.20
CEP Performance in Wastewater Regulations
(Based on F024 Processing)

Constituents	Feed Composition (mg/l)	Scrubber Water (mg/l)	EPA Wastewater Regulation (mg/l)
1,1,2-Trichloroethane	18,000	ND (0.0015)	0.054
Tetrachloroethene	9,700	ND (0.0015)	0.056
Chlorobenzene	12,000	ND (0.0035)	0.057
1,2-Dichloroethane	6,800	ND (0.0015)	0.21
1,1,2,2-Tetrachloro ethane	11,000	ND (0.001)	0.057
Trichloroethene	24,000	ND (0.001)	0.054
Xylenes	610	ND (0.001)	0.32
1,1,1,2-Tetrachloroethane	1,000	ND (0.001)	0.057
Hexachlorobutadiene	3,600	ND (0.001)	0.055
Naphthalene	900	ND (0.001)	0.059
ND=Not Detected (Detection limit)			

1.3.6.3.2. Best Demonstrated Available Technology (EPA) Standards

One of the main goals at MMT is to provide an environmental solution to waste treatment by converting hazardous materials to uniform and consistent products of high quality in a safe, efficient, and effective manner. Currently the effectiveness of waste treatment is regulated by the concentration of hazardous materials in the after-process waste water and non-waste water residuals. All processes have to ensure that organic constituent concentrations in individual waste water and non wastewater streams are lower than the regulated limits set by EPA. CEP demonstrations surpass the current limits even when comparing with the Best Demonstrated Available Technology (BDAT) for various classes of waste streams.

Consistent with this aim, CEP was recently approved by EPA on 3/12/96 as a non-combustion Best Demonstrated Available Technology equivalent for all wastes for which incineration was previously the only approved processing method. EPA's determination reinforces that CEP is fundamentally different from incineration.

1.3.6.4. Toxic Characteristic Leaching Procedure Results

TCLP (Toxicity Characteristics Leaching Procedure) bas been performed on the CEP ceramic material. All the ceramic samples from CEP runs were subjected to TCLP tests for RCRA metals and all of them passed the tests. Full TCLP analysis including testing for Acid/Base/Neutral Extractables, Pesticides/Herbicides in addition to RCRA metals were carried out on selected feeds. All samples passed TCLP as shown in Table 1.21.

Table 1.21
Full TCLP Results for Major Feeds at CEP

Parameter	Surplus Metal	K027	Biosludge	K019/20
RCRA Metals (mg/ℓ)				
Arsenic	ND	ND	ND	ND
Barium	ND	ND	ND	ND
Cadmium	ND	ND	ND	ND
Chromium	ND	ND	ND	0.3[1]
Lead	ND	ND	ND	ND
Mercury	ND	ND	ND	ND
Selenium	ND	ND	ND	ND
Silver	ND	ND	ND	ND
Acid/Base/Neutral Extractables (mg/ℓ)				
Total Cresol	ND	ND	ND	ND
2,4-Dinitrotoluene	ND	ND	ND	ND
Hexachlorobenzene	ND	ND	ND	ND
Hexachloro-1,3-butadiene	ND	ND	ND	ND
Hexachlorobenzene	ND	ND	ND	ND
Nitrobenzene	ND	ND	ND	ND
Pentachlorophenol	ND	ND	ND	ND
2,4,5-Trichlorophenol	ND	ND	ND	ND
2,4,6-Trichlorophenol	ND	ND	ND	ND
Pyridine	ND	ND	ND	ND
Pesticides/Herbicides (mg/l)				
Chlorodane	ND	ND	ND	ND
Endrin	ND	ND	ND	ND
Heptachlor	ND	ND	ND	ND
Heptachlor epoxide	ND	ND	ND	ND
Lindane	ND	ND	ND	ND
Methoxychlor	ND	ND	ND	ND
Taxaphene	ND	ND	ND	ND
2,4-D	ND	ND	ND	ND
2,4,5-TP	ND	ND	ND	ND

ND=Not Detected
[1] Cr_2O_3-Al_2O_3 refractory bricks were present during these runs which provides a source of Cr. Total Cr was measured in the ceramic phase. Cr^{+6} is not formed under CEP operating conditions. Cr within the CEP system has been analyzed and no hexavalent Cr^{+6} has been detected. The detected concentration was a full order of magnitude below the regulatory limit 5 mg/ℓ.

1.3.6.5. Operability and Reliability for Commercial Applications

Extensive demonstration runs at commercially applicable processing rates (up to 15,000 tons per year) have been successfully performed verifying the long-term operability of the CEP system with respect to on-stream factor, steady-state operation, product quality and consistency, and reliability. MMT has applied over 40 operational performance criteria for verification of efficient and effective processing. Steady-state operation have consistently been demonstrated. On-stream factors > 90% have been achieved (Figure 1.13).

Figure 1.14 and Figure 1.15 demonstrate representative steady-state operation during a chlorinated waste (F024) recycling campaign.

Figure 1.13
Biosludge Injection

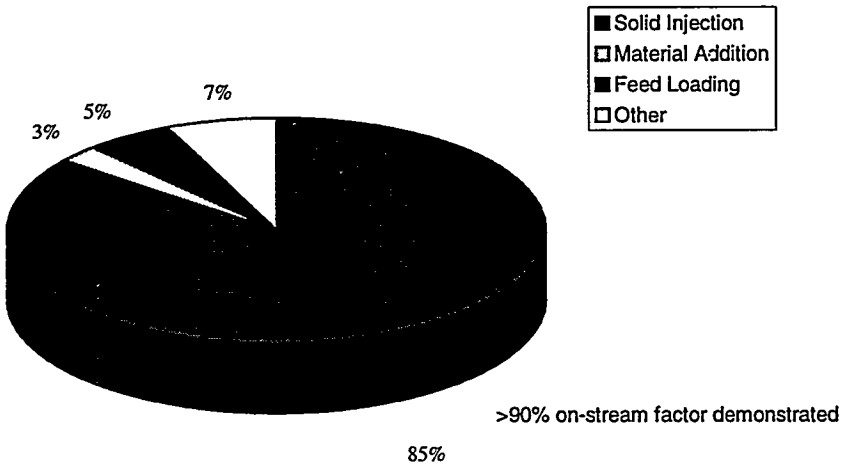

Figure 1.14
F024 Heavily-Chlorinated Liquid Feed Rate

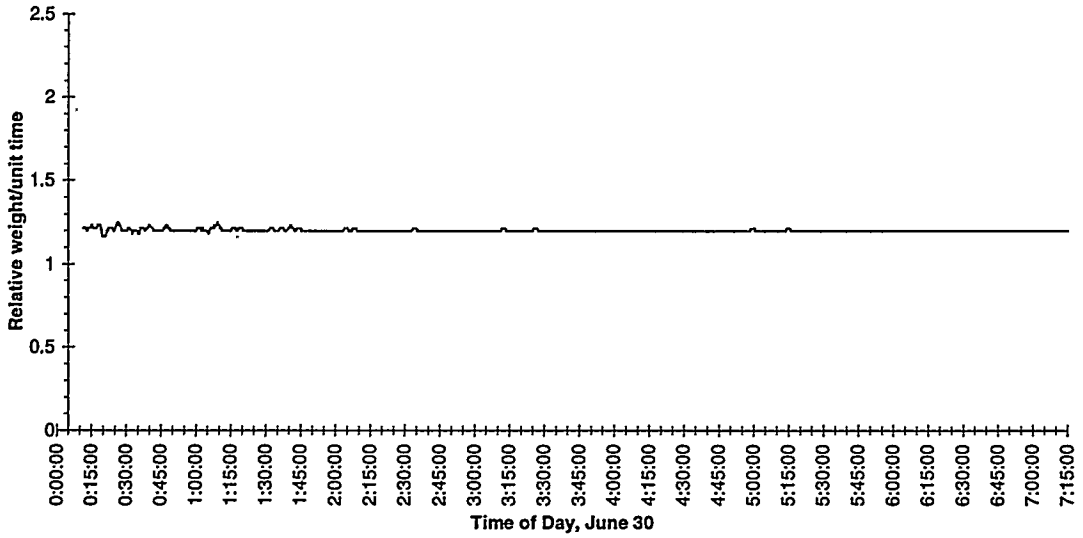

Figure 1.15
F024 Heavily-Chlorinated Liquid Feed - Off-Gas Composition

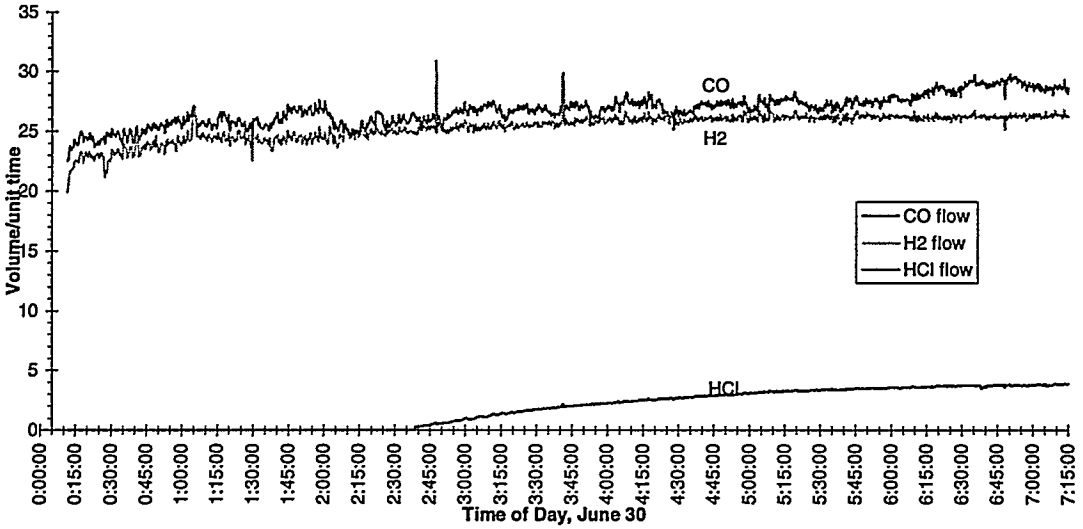

1.3.7. Task 1.6 - Conceptual Design Development for a CEP Processing Facility

MMT has developed a conceptual design of a CEP system in which organic sludges, inorganic sludges, scrap metals, soils, construction debris, and organic debris could be processed through the reactor at feed rates compatible with the natures of the various waste compositions, and in such a manner to provide valuable information that will be

required for the subsequent scale-up to a full-scale CEP system. This conceptual design integrates the myriad of data collected and processed during performance of this contract with the experience and lessons learned obtained from designing, constructing, and operating the two commercial CEP facilities currently in commission.

The CEP system components are arranged into three general areas: feed handling, reactor systems, and the gas handling train. All systems or components used in these areas reflect transportability requirements by incorporating multiple features into modules or skids.

The feed handling area is comprised of equipment required to off-load and handle incoming containers, safely remove their contents, and condition the feed for delivery into the reactor. Each step in the feed handling process contains design features to isolate and protect the operating staff in accordance with MMT standards which meet or exceed all applicable health and safety requirements.

The reactor systems design is based on operating reactor units and incorporates the latest innovations and improvements. The reactor will contain approximately 1,100 lb (as determined during the design phase) of molten iron and a proportional amount of ceramic in the horizontal section. The reactor is equipped with a 600 kW induction coil power supply and additional heat capacity required to preheat the vessel and to supplement heating the horizontal section during product removal operations, lance operations, or to deskull the reactor's interior surfaces.

The capability to sample the metal and ceramic phases, observe key parts of the bath during reactor operation, and to monitor all aspects of the reactor's performance are included in the conceptual design. Upon shutdown, an automatic injection of purge gases will occur to ensure that safe conditions are maintained throughout the system. Ancillary systems for the reactor include a means for discharging the bath contents into a closed container and a system for discharging accumulated ceramic product during extended operations. All reactor components are based on modular concepts to facilitate future alterations that may be required for feed streams other than those currently identified.

The gas handling train (GHT) is capable of safely handling a broad spectrum of gas compositions generated from the incoming feeds. The GHT has the capability to filter or scrub carryover particulate, safely collect potentially reactive dusts and volatile heavy metals, and condition gases for potential reuse. All off-gas passes through a series of absorbents and filters to ensure that no radioactive or hazardous component is discharged into downstream systems. The entire process is fully instrumented and monitored to ensure safe operation for employees and the community.

CEP typically generates hydrogen and carbon monoxide product gases during operations. MMT has combined its numerous years of experience with handling these gases with practices established by the Government and other industries to develop a

safe GHT design. GHT components are designed to minimize the generation of secondary wastes and include the option to recycle most of the secondary waste streams generated through CEP.

Table 1.22 outlines the expected staging of waste streams with their respective functional requirements. This table was used to establish the boundaries for the conceptual design.

The following list of priorities were used while performing tradeoff studies to establish this conceptual design based on the boundaries established in Table 1.22:

1. Safety
2. Environmental Integrity
3. Availability (Reliability)
4. Maintainability
5. Schedule
6. Operating Cost
7. Capital Cost

The conceptual design groups equipment in a logical manner into a module, skid, or prefabricated unit that can be easily installed in the field. The building layout features radiological controlled-access and uncontrolled-access work and support areas for highly effective management of surface/airborne contamination and radiation sources. Confinement systems, including primary and secondary confinement barriers and associated ventilation systems, provide a controlled airflow pattern from the environment into the confinement building, and then from the non-contaminated areas to the potentially contaminated areas to the normally contaminated areas of the building. Figure 1.16 presents a high level process flow diagram of the conceptual design.

Table 1.22
System Functionality by Waste Stream

Waste Stream	Functionality
Soil	• Screening/sizing of clay material with organic and radionuclide contamination • Blending of soil with co-feeds • Tuyere feeding at average 125 lbs soil per hour[1] • Destruction of PCBs/organics • Non-continuous ceramic phase removal during run • VHM capture in GHT • Capture of radioactive and reactive particulates in GHT • Safe containment of radionuclides, VHM, H2/CO • Demonstrate potential for reuse of syngas[2] • Process instrumentation and control • Analytical support equipment
Sediment	In addition to above: • Screening/sizing of sandy materials with high mercury and radionuclide contamination • Significant VHM capture
Inorganic Sludge	In addition to above: • Removal of excess water in presence of organics and mercury • Processing of wastes with high water content (>20 wt%)
Organic Sludge	In addition to above: • Filtering of organic sludges with high solids content • Chlorine capture in ceramic phase • Adequate refractory lifetime for chloride wastes
Scrap Metal Processing Equipment	In addition to above: • Bulk feeding of metal pieces up to 6-8 inches • Non-continuous bulk feeding of metal pieces • Non-continuous metal tapping during run • Sufficient residence time to flux minor radionuclide contamination • Sufficient power to reactor to process 50 lbs/hr
Construction debris	In addition to above: • Sizing/sorting sufficient for bulk feeding (2-4 inches) • Sufficient residence time for formation of ceramic phase with desired properties
Spent Activated Carbon	• Tuyere feeding of dusty solids with high gas generation • Feeding of bulk solids with high gas evolution rates
Personal Protective Equipment	• Shredding/sizing of clothing, plastics, etc.

Figure 1.16
CEP Facility Conceptual Design Process Flow Diagram

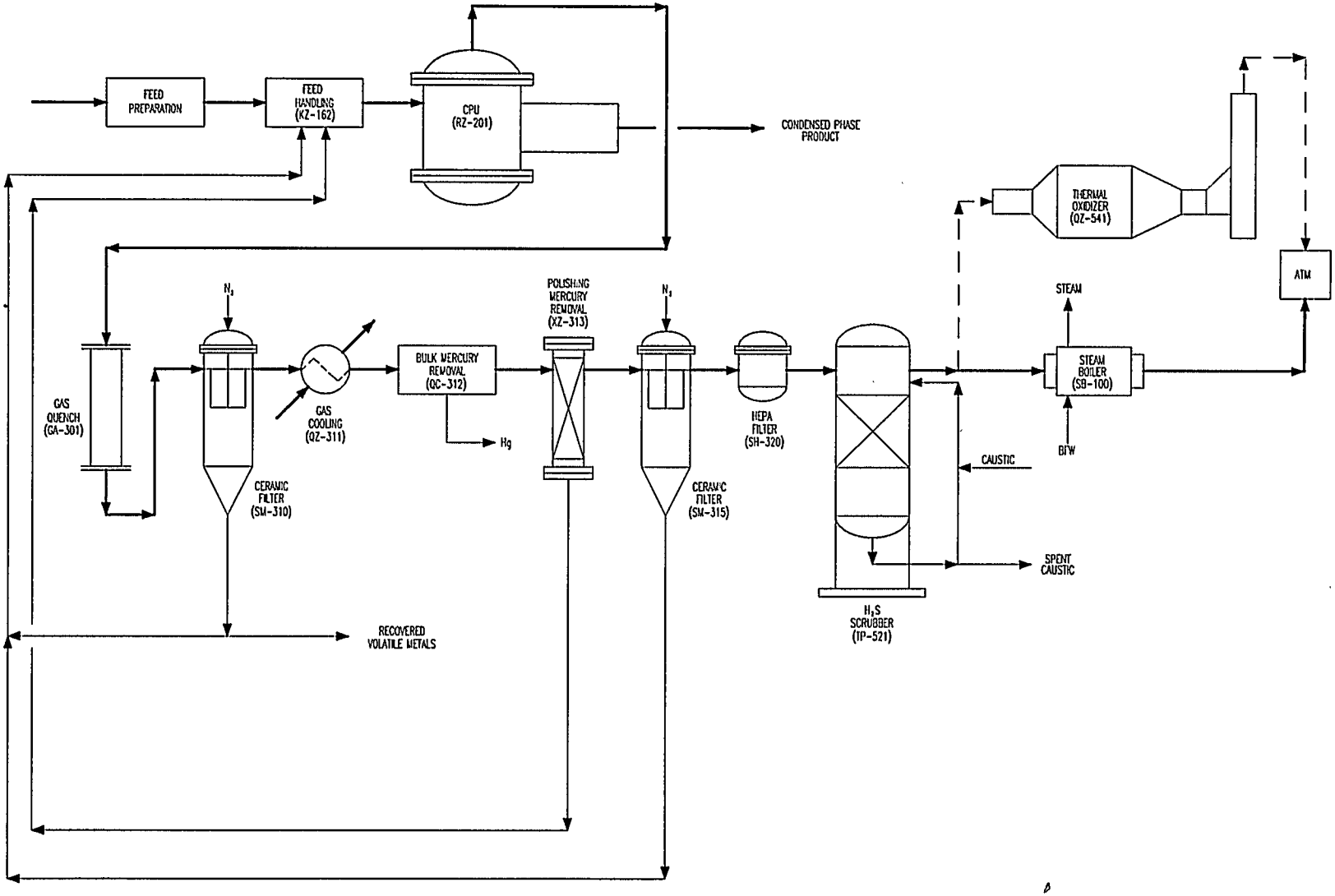

1.4. Conclusions and Recommendations

1.4.1. Conclusions

The research and development activities performed under this contract have convincingly demonstrated Catalytic Extraction Processing (CEP) to be a robust, one-step process that is relatively insensitive to wide variations in waste composition and is applicable to a broad spectrum of DOE wastes. Substantial growth in the feed size and composition compatible with CEP has been achieved in a relatively short period of time, providing the opportunity to substantially reduce the amount of feed characterization and preparation prior to processing. Additional research and development is expected to lead to the ability to accept a drum (and potentially larger) size feed of completely uncharacterized waste. Experiments have also validated our Catalytic Processing Unit (CPU) design model, providing a high degree of confidence in our ability to design a bulk solids CPU for processing DOE wastes. CEP has successfully demonstrated its ability to partition radionuclides to the ceramic phase, thereby achieving a significant reduction in the volume of radioactive waste while attaining metal decontamination factors in excess of 99.9%. CEP has also successfully demonstrated its ability to recycle RCRA hazardous wastes and achieve destruction removal efficiencies exceeding 99.9999% for organic wastes. Two commercial facilities have been placed in commission and are currently processing mixed low level wastes, which provides a compelling indication of the maturity, regulatory acceptance, and commercial viability of CEP.

1.4.2. Recommendations

The efforts concluded under this initial phase of the contract have shown conclusively that CEP is an effective means for decontaminating scrap metal for recycling. It provides superior environmental performance in a cost effective manner, yielding very high metal decontamination factors due to its unique process chemistry. Continued studies in select areas within CEP's operating scheme will allow its designers to optimize systems and advance the progress of CEP's commercialization and minimize the time to actual implementation of a full scale system. Further, future development work should include studies that address the specific needs of particular DOE processing sites in preparation for establishing CEP facilities to process waste streams located at those sites.

This contract has provided the means to evaluate several concepts proposed for the addition of bulk solids to CEP systems to provide the most cost-effective alternative for recycling of DOE's contaminated scrap metal. The experiments proved that the techniques will work, and further refinement could allow the addition of whole drums or similar-sized materials to the bath. Additional funding could accelerate the development of the most promising alternatives and eliminate the need for most size-reduction feed pretreatment systems, thereby achieving a substantial savings in the total cost for decontamination and decommissioning of DOE sites. Future studies

should also address areas to further improve CEP's demonstrated cost-effectiveness for processing a broad spectrum of DOE wastes, including multi-zone processing, process control, energy addition, product removal, and final product quality.

This contract has provided the means to verify the theoretically predicted separation of uranium and transuranics (TRU) from contaminated scrap metal making use of the well-controlled operating chemistry of CEP. Future development work should continue studies on the application of CEP to TRU, including the processing of actual TRU radionuclides, and expand studies on its application to high level wastes (HLW) in the DOE inventory. Progressing beyond these isotopes, the DOE has a long-standing interest in the separation of metals of similar thermochemistry (e.g., Tc and Ni) which are not easily separated using classical techniques (e.g., oxidation). MMT has performed preliminary investigations into several promising methods for separation of similar metals. Further funding would provide for the scale-up of the investigation to molten metal test systems, which is expected to lead to developing the ability to recycle and reuse the approximately $1.5 billion of radioactive contaminated nickel in the DOE inventory.

MMT has processed RCRA-listed wastes, and has proven CEP's ability to provide complete destruction of the hazardous constituents while maintaining high regulatory integrity and producing a useful gas phase product. Due to the unique set of regulations governing the processing of RCRA listed materials, the disposal of a stable final form containing radionuclides but not exhibiting any RCRA characteristic would benefit from delisting. Delisting would provide increased flexibility in terms of disposal destination and cost. Under a further enhancement to the contract, MMT would pursue an aggressive delisting program with the appropriate regulatory agencies, to ensure the possibility for re-use of the metal and gas phase products.

The DOE is pursuing an aggressive schedule for the processing of many of its most hazardous wastes. CEP has been proven to be a viable solution to many of the waste problems, providing recycling, environmental integrity and dramatic volume reduction of radionuclide-containing waste forms. To meet the DOE's aggressive schedule, waste recycling facilities need to be constructed in an equally aggressive timetable. To avoid any delays in implementation of CEP, further funding of the conceptual design for a CEP facility dedicated to processing contaminated scrap metal would be necessary.

2. Task 1.1: Design CEP System

This section follows the systematic approach used to advance the design of a CEP system optimized for processing materials contaminated with radionuclides and organics consistent with the statement of work. A comprehensive series of theoretical and experimental studies were performed to increase overall understanding of the CEP system from feed systems to the reactor to the gas handling train. The results of these and other studies have been applied to the conceptual design for a CEP processing facility presented in Section 6 of this final report, as well as to our designs for CEP facilities including the two facilities currently in operation and processing mixed low level wastes at Oak Ridge, Tennessee.

An extensive series of theoretical and experimental studies were conducted on CEP reactor design modeling. Thermodynamics and computational fluid dynamics have been used to characterize the catalytic extraction process to develop a methodology and models for determining CEP reactor design parameters. Several studies were performed on the phenomenology of tuyere operation for injecting feed materials into the reactor. An accretion model was developed to predict the formation of accretions and to evaluate methods for their control. Studies were performed on the absorption behavior of a gas injected into a bath using a tuyere to characterize the various regions surrounding the tuyere plume. These studies provided important reactor design parameters including minimum bath height and maximum tuyere flow rates for effective processing. Extensive theoretical and physical model studies were performed on determining bubble size distributions from tuyere operation in molten metal baths. Calculated bubble size and residence time distributions were determined to be consistent with experimental results. Data obtained from the bubble size distribution study was then applied to a study on the carburization and decarburization of a molten metal bath. The inherent ability of the metal bath to dissolve carbon maintains the quality of gas phase products by removing any unreacted hydrocarbon species. Finally, the data obtained from these and other reactor-related experiments were used to design and evaluate an innovative, continuous, counter-current reactor which has the potential to yield high quality metal and ceramic products, reduce the volume of the ceramic phase, and reduce overall energy costs.

A critical requirement in DOE's efforts to recycle, reuse, and dispose of materials from its decontamination and decommissioning activities is the design of a robust system to process a broad spectrum of bulk solid feeds. MMT has developed several reactor concepts for bulk feed processing that consist of two zones: a dissolution/volatilization zone (Zone 1) and a gas polishing zone (Zone 2). Theoretical calculations confirmed by an extensive test program have determined the reactor size, range of operability, and conditions for various top-charged bulk feed materials. Additional design studies and experiments were performed on a slurry system for tuyere injection.

Remote-controlled tapping devices for removal of molten metal and ceramic phase product from stationary CEP reactors have been designed and successfully tested. Testing has also been performed on a plasma arc torch as an energy addition system for CEP reactors.

A comprehensive investigation of sensing and monitoring devices was performed to develop a robust reactor control system. Selected sensors were installed and tested to evaluate their ability to accurately and reliably monitor critical reactor operating parameters. These instruments have been integrated into control system hardware and software to provide robust reactor control for various reactors, including the two CEP facilities currently in operation and processing mixed low level wastes at Oak Ridge, Tennessee.

An extensive series of experiments has also been performed to characterize off-gas products from various feed materials in order to size the gas handling train. These studies have focused primarily on particulate characterization and control, and recovery of volatile heavy metals. The data obtained from these experiments has also been incorporated in the design of the gas handling trains installed in the operational CEP facilities.

In summary, this comprehensive series of studies has addressed all of the critical elements of a CEP system, from feed systems to the CEP reactor to the gas handling train. The results of these studies have been incorporated into a conceptual design of a CEP system for processing feed materials contaminated with radionuclides and organics. Further, many of these designs have been implemented into operational commercial-scale processing facilities. While CEP is currently processing a few specific DOE and commercial mixed low level waste streams, the results of these studies indicate that CEP is a robust system capable of handling a broad spectrum of DOE waste streams.

2.1. CEP Reactor Design Modeling

2.1.1. Thermodynamics Calculations

2.1.1.1. Solution Thermodynamics

At the core of the CEP system is a liquid metal that acts as a homogeneous catalyst for the dissociation of complex feed molecules into elements. The flexibility and robustness of the CEP process is attributed to the 'singular' dissolved elemental intermediate through which reactions proceed. The metal bath ensures that in the dissociation of an organic feed, carbon (C) in dissolved form is the only carbon intermediate. This is in contrast to open flame systems where multiple free radical intermediates can be formed leading to hard-to-control side reactions. Given the key role of the metal bath as a solvent, the thermodynamic forces governing the solubility of elements in liquid metal

baths are important in understanding how the operating conditions of the CEP system can be manipulated to synthesize desired products of commercial value.

Solubilities of elements in metal vary depending on temperature, bath composition and metal substrate. For example, the solubility of carbon in iron at 1153°C is 4.27% by weight while in aluminum it is only 0.2% at 1900°C. Hydrogen solubility is low for both metals. Therefore, a hydrocarbon feed injected into an iron bath will form a dissolved carbon intermediate while hydrogen will be released in the product gas stream. However, if aluminum is used as the molten metal substrate, carbon will not form a dissolved intermediate but will be entrained in the gas product stream.

The solubility thermodynamics of metallic solutions of varying concentrations and compositions will be outlined below followed by specific examples of iron solutions (e.g., Fe-C, Fe-O) that are particularly relevant to CEP processing of waste feeds. In addition to the primarily iron-based data outlined below, MMT has thermodynamic solubility data for an extensive range of other metallic and inorganic solutions.

2.1.1.1.1. Characterizing Metallic Solution Properties

At low concentrations (less than 1% by weight), the thermodynamic properties of binary metallic solutions are assumed to obey Henry's law, which states that the activity of dilute solute i (denoted as α_i) is proportional to its concentration. Therefore, the Gibbs Standard Free Energy ($\Delta G°_i$) of solution for a component i in iron at low concentrations is given by:

$$\Delta G°_i = RT \ln(0.5585\, \gamma°_i / M_i)$$

where $\gamma°_i$ is the activity coefficient and M_i is the atomic weight of the solute. The activity coefficient of solute i is defined by the ratio of the activity (α_i) to the mole fraction (N_i):

$$\gamma°_i = \alpha_i / N_i$$

Gibbs Standard Free Energies of solution for selected components in liquid iron at low concentrations are given in Table 2.1. $\Delta G°_i$ functions with a negative slope and intercept are thermodynamically favored, particularly at high temperatures. Therefore, at typical CEP operating conditions (i.e., 1700K), the $\Delta G°_i$ of solution is negative for carbon (-11770 cal/g-atom) and oxygen (-29173 cal/g-atom) and positive for nitrogen (+10567 cal/g-atom) and hydrogen (+21096 cal/g-atom). This indicates that when an organic feed is dissociating into its constituent elements on contact with the molten metal solvent, carbon will form a dissolved intermediate while hydrogen and nitrogen, with their low solubility, will be recovered in the gaseous product stream.

Table 2.1
Gibbs Free Energy of Solution in Liquid Iron
for Concentrations Less Than 1 Weight %

Element	ΔG° (cal/g-atom)	ΔG° at 1700K
Carbon (gr)	5,400 - 10.10T	- 11,770
Hydrogen	8,720 + 7.28T	+ 21,096
Nitrogen	860 + 5.71T	+ 10,567
Oxygen	-28,000 - 0.69T	- 29,173
Silicon	-31,430 - 4.12T	- 38,434
Sulfur	32,280 + 5.60T	+ 41,800
Phosphorous	-29,200 - 4.6T	- 37,020

Dilute solutions with solute concentrations higher than 1% by weight deviate from Henry's law. The departure from ideal behavior, even in relatively dilute solutions, is well characterized and supported by extensive experimental data from the metallurgical industry. Specifically, the departure from ideal behavior is demonstrated in Figure 2.1 where log $(\gamma_x/\gamma_x^\circ)$ is plotted against the atom fraction N_x of the solute x on the top scale and $(1-N_x)^2$ on the bottom scale. The ratio $(\gamma_x/\gamma_x^\circ)$, symbolized by the fugacity (f_x), is a measure of the departure of the solution from Henry's Law. Therefore, in Figure 2.1 solutes with a $\log(\gamma_x/\gamma_x^\circ) \approx 0$ behave ideally (e.g., Cd, Zn), while solutions where $\log(\gamma_x/\gamma_x^\circ) \neq 0$ deviate significantly from ideal behavior (e.g., Cs, Pb). For solute 2 in a dilute solution, a good approximation for γ_2 is:

$$\ln(\gamma_2/\gamma_2^\circ) = \varepsilon_2^{(2)} N_2$$

or

$$\log(f_2) = e_2^{(2)} x_2$$

where $\varepsilon_2^{(2)}$ and $e_2^{(2)}$ are known as the interaction coefficients, and x_2 is the concentration of solute 2 in weight percent. The relationship between $\varepsilon_2^{(2)}$ and $e_2^{(2)}$ for the limiting case of $N_2 \rightarrow 0$ is given by:

$$\varepsilon_2^{(2)} = 230\,(M_2/M_1)\,e_2^{(2)} + (M_1-M_2)/M1$$

where M_1 and M_2 are the atomic weights of the solvent and the solute, respectively. Values for the interaction coefficient ε_x are documented in the literature.

Figure 2.1
Activity Coefficient of Solute X in Dilute Liquid Amalgams at 25°C

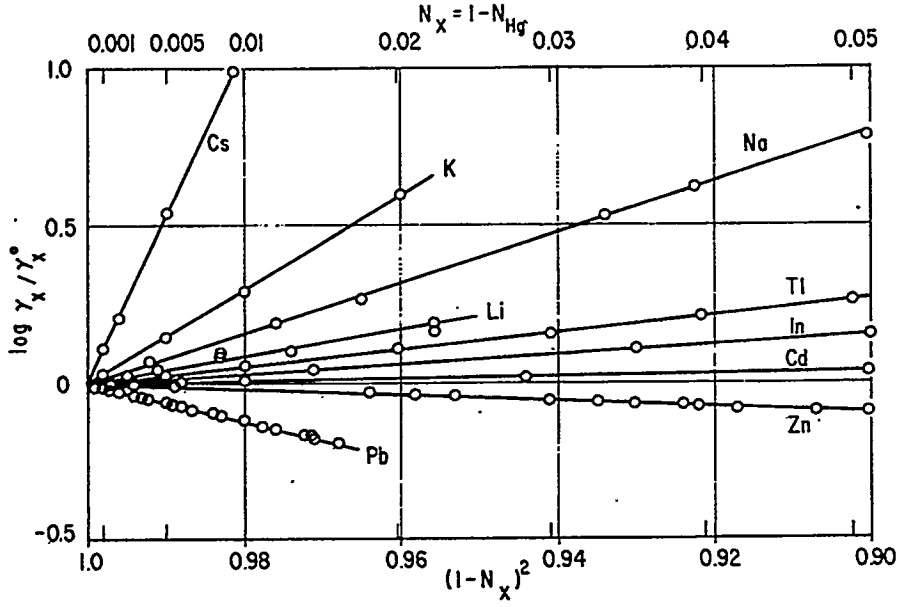

In the terminal regions of binary metallic solutions, a quadratic formalism can be used to describe the composition dependence of the activity coefficient. Specifically, in the terminal region, which may extend to as much as 50 atom percent, the logarithm of the activity coefficient ($\log \gamma_x$) is a linear function of $(1-N_x)^2$. This quadratic relationship for a binary system can be expressed as follows:

$$\log(\gamma_1) = \alpha_{12}(1-N_1)^2$$

$$\log(\gamma_2/\gamma^\circ_2) = \alpha_{12}(N_1^2-1)$$

Figure 2.2 shows the logarithm of the activity coefficient of selected iron alloys at 1600°C.

Figure 2.2
Activity Coefficient of Solute X for Fe-X Solutions at 1600°C
(Except for Fe-Cu at 1,550°C)

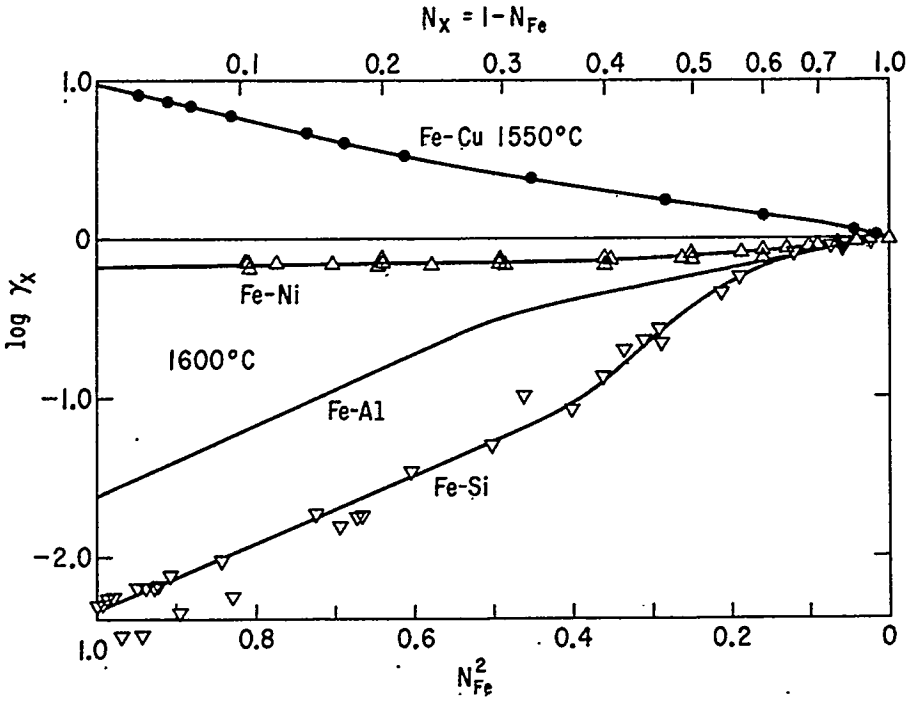

For ternary solutions, activity coefficients are described in terms of interaction coefficients. For a dilute solution of N_i and N_j in solvent N_1 :

$$\ln(\gamma_i/\gamma_i^\circ) = \ln(f_i) = \varepsilon_i^{(i)} N_i + \varepsilon_i^{(j)} N_i$$

or

$$\log(f_i) = e_i^{(i)} x_i + e_i^{(j)} x_j$$

where x is the weight fraction for the solute indicated by the subscript. The relationship between ε and e for dilute solutions ($N_i \to N_j \to 0$) is given by:

$$\varepsilon_i^{(i)} = 230\,(M_i/M_1)\, e_i^{(i)} + (M_1 - M_i)/M_1$$

and

$$\varepsilon_i^{(j)} = 230\,(M_j/M_1)\, e_i^{(j)} + (M_1 - M_j)/M_1$$

where M is the atomic weight of the component indicated by the subscript. The values of the interaction coefficients for ternary systems relevant to CEP are outlined in Table 2.2. In more detailed analyses carried out for recycling of specific feeds and for optimization of the reactor design, the impact of temperature on the interaction parameter is taken into consideration. Also, more complex models have been developed to characterize the behavior of multi-component solutions in liquid metals.

Table 2.2
Interaction Parameters for Ternary Alloys at 1600°C
(Fe-X-H, Fe-X-C, Fe-X-N, Fe-X-S, Fe-X-O)

Solute j	$e_H^{(j)}$	< j wt%	$e_c^{(j)}$	< j wt%	$e_n^{(j)}$	< j wt%	$e_s^{(j)}$	< j wt%	$e_o^{(j)}$	< j wt%
Al	0.013	2	0.064	2	0.002	0.5	0.035	1	-3.90	0.2
B	0.050	1	-----	-----	-----	-----	0.134	0.5	-2.6	0.05
C	0.060	1	0.22	1	0.25	0.5	0.114	0.5	-0.13	1
Co	0.002	14	0.062	10	0.011	12	0.003	10	0.007	5
Cr	-0.002	2	-0.024	25	-0.045	7	-0.011	5	-0.037	20
Cu	0.0005	12	0.018	10	0.009	10	-0.008	8	-0.016	15
H	0	-----	(0.72)	-----	-----	-----	(0.26)	-----	-----	-----
Mn	-0.001	11	-0.007	10	-0.02	6	-0.026	3	0	-----
N	-----	-----	(0.11)	-----	0	-----	(0.03)	-----	(0.057)	-----
Nb	-0.002	2	-0.06	2	-0.061	10	-0.013	5	-0.14	3
Ni	0	-----	0.012	5	0.010	10	0	-----	0.006	20
O		-----	(-0.097)	-----	0.05	-----	(-0.18)	-----	-0.20	
P	0.011	0.5	-----	-----	0.051	-----	0.029	1	0.07	0.5
S	0.008	0.1	0.057	2	0.013	-----	-0.028	1	-0.091	-----
Si	0.027	1	0.113	2	0.047	3	0.063	0.5	-0.14	1
Ti	0.08	0.5	-----	-----	-0.53	0.2	-0.072	1	-1.150	0.3
V	-----		-0.038	20	-0.093	2	0.016	5	-0.14	5.0
W	-----		-0.033	20	-0.002	15	0.001	10	0.008	5
Zr	-----		-----	-----	-0.63	0.1	-0.053	2	-----	-----

Values in parentheses are derived from the corresponding values of ε_j^i.

2.1.1.1.2. Carbon-Iron Solutions

The solubility of carbon in iron is key to CEP's processing of organic and organo-metallic feeds. Specifically, carbon from the dissociation of organic compounds in the

feeds, readily dissolves maintaining a highly reducing environment in the molten metal solvent. Dissolved carbon is an effective reducing agent for a large number of compounds including carbon dioxide and sulfur dioxide, water and a wide range of metal oxides. The reducing strength of dissolved carbon is an important factor to CEP's flexibility in recycling waste streams. Specifically, CEP provides the flexibility to recycle organics to synthesis gas, recover metals and inorganics such as halides, sulfur and phosphorus and separate and concentrate transuranic compounds. The dissolution of carbon in the liquid iron solvent ensures a homogeneous reducing environment and hence, robust control of product composition and quality.

The phase equilibrium behavior of carbon dissolved in iron can be derived from the activity coefficient correlations and is shown in Figure 2.3. There are three invariants in the system; peritectic at 1499°C, eutectic at 1152°C, and the eutectoid at 738°C (Note that the iron undergoes two polymorphic transformations; α-Fe is called the ferrite phase and is body centered cubic while γ-Fe is called the austenite phase and is face-centered cubic). In equilibrium, a graphite phase will separate from the liquid iron (γ-Fe) phase at carbon weight concentrations over 4.27% and temperatures above 1152°C. To avoid graphite formation from an organic feed, the CEP system must be operated at carbon concentrations less than 4.27%. At carbon concentrations above saturation, a dissolved carbon intermediate will not form. As a result, graphite and possibly, products of incomplete dissociation, can be entrained in the off-gas stream with the potential of undesirable reformation reactions taking place downstream.

Figure 2.3
Fe-Carbon Phase Equilibrium Diagram

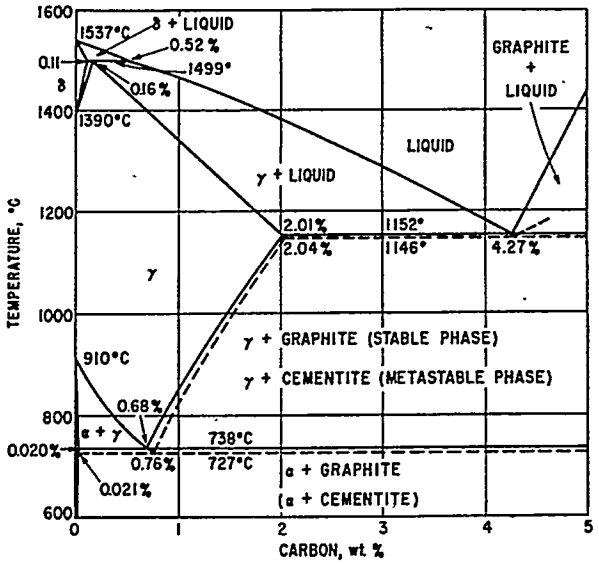

The activity of carbon in α-Fe is given in Figure 2.4 for two different standard states. The composition dependence of the activity of carbon (relative to graphite) may be approximated by the following equation:

$$\alpha_c = \gamma_c^\circ \, e^{0.385 \, x_c^2}$$

where x_c is the weight fraction of carbon in the solution and γ_c° is a temperature dependent activity coefficient of carbon (relative to graphite) when $x_c \rightarrow 0$ represented by:

$$\log (\gamma_c^\circ) = (2336/T) - 2.288$$

The heat of solution of graphite in γ-Fe for dilute solutions is 10.7 kcal/g-atom C. The composition dependence of the activity coefficient is given by the following quadratic formalism:

$$\log (\gamma_c/\gamma_c^\circ) = -2.38 \, (N_{Fe}^2 - 1)$$

Figure 2.4
Activity of Carbon in Austenite for Two Different Standard States

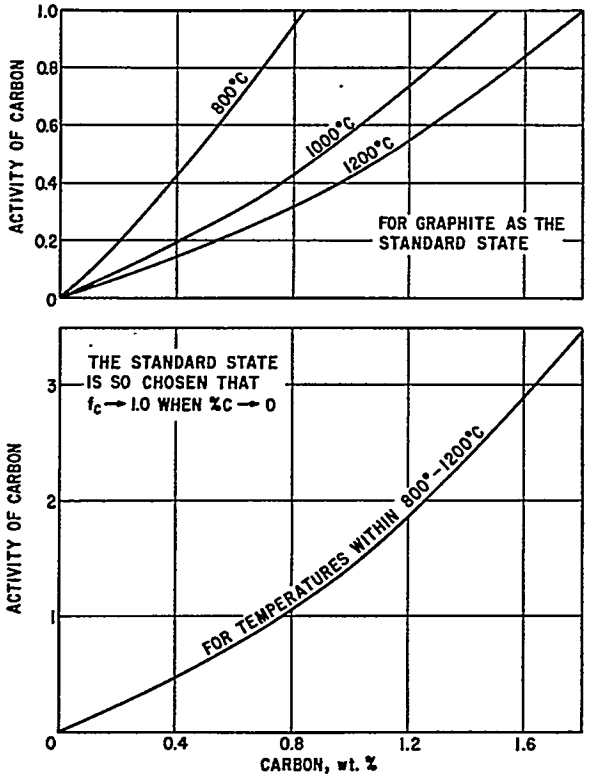

The variation of fugacity ($\gamma_i/\gamma_i°$) with carbon content of liquid iron is shown in Figure 2.5. The solution deviates from ideal conditions at higher carbon concentrations and higher temperatures, indicating that at typical CEP operating conditions, the molten metal bath will deviate from ideal behavior. The effect on the fugacity of carbon of other solutes is shown in Figure 2.6, indicating that the presence of some solutes in the molten bath will increase carbon activity while others will decrease it. Specifically, the presence of chromium or manganese in the molten bath increases carbon solubility while the presence of aluminum, silicon, sulfur and phosphorus decreases carbon solubility. Important to note is the presence of alloying materials in the melt which can impact carbon solubility significantly causing it to vary from 2 to 6 wt%.

Figure 2.5
Fugacity of Carbon in Liquid Iron for the Standard State
$f_c \rightarrow 1.0$ when [C] $\rightarrow 0$

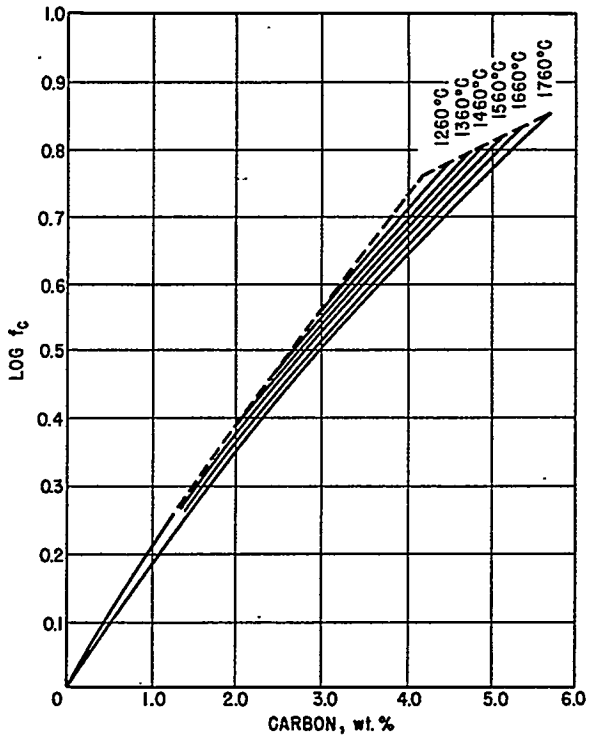

Figure 2.6
Solubility of Carbon in Alloyed Iron Melts at 1500°C

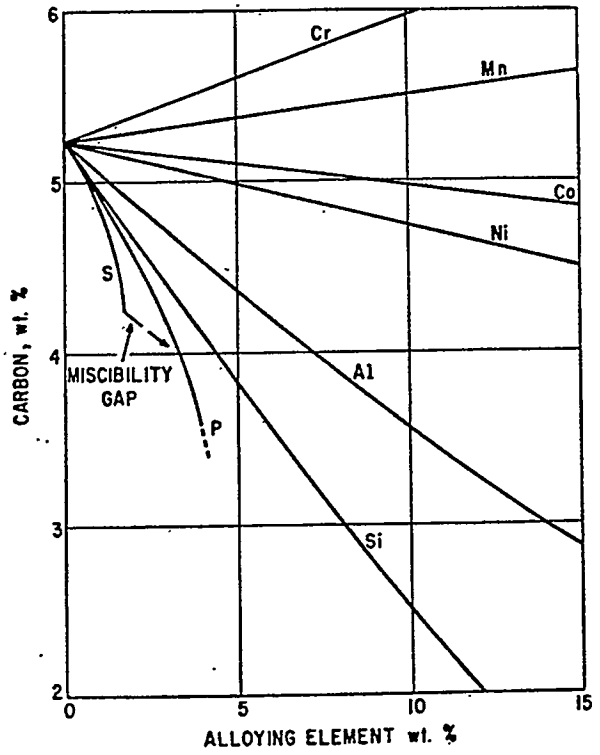

Understanding carbon solubility in iron in the presence of other components and being able to model thermodynamic properties of these multi-component solutions is important to optimizing the CEP process. The formation of a dissolved carbon intermediate ensures complete destruction and conversion of the feed materials. If carbon is not dissolved in the molten metal it can be entrained in the gaseous stream and can lead to undesired gaseous phase reformation reactions.

2.1.1.1.3. Oxygen-Iron Solutions

Oxygen solubility in iron is key to CEP's processing of organic feeds and their conversion to synthesis gas. Specifically, elemental oxygen has relatively low solubility in iron but reacts rapidly with iron to form wustite. The low solubility and high reactivity of oxygen in iron ensures that oxygen added to the CEP system will react as follows:

- High carbon concentration: At dissolved carbon concentrations of [C] > 3 wt %, added oxygen will react to form carbon monoxide since this is the oxidation reaction favored thermodynamically. (See Section 2.1.1.2.)

- Low carbon concentration: At carbon concentrations of [C] < 0.5 wt %, when the carbon is depleted from the system, oxygen will react to form wustite.

Therefore, the CEP system can operate as a reducing atmosphere over a wide range of operating conditions. Addition of excess oxygen to the CEP system will be absorbed as wustite in the metal bath, therefore, eliminating the potential of higher oxygen partial pressure and the potential of formation of compounds such as carbon dioxide or other oxidation by-products such as SO_x, NO_x, dioxins and furans.

The pure oxygen-iron system phase diagrams are shown in Figure 2.7. As noted above, a characteristic feature of this system is that oxygen is soluble in iron only to a limited extent; at the eutectic temperature 1527°C, the maximum solubility is 0.16% O above a liquid oxide phase containing 22.6% O (note that wustite has a variable composition. For example, within the temperature range of 800°C to 1371°C, the wustite in equilibrium with iron has the composition corresponding to $Fe_{0.95}O$). Correlations exist to characterize the activity of oxygen in iron melts as a function of composition and temperature. However, detailed discussions of these correlations are beyond the scope of this report.

Figure 2.7
Oxygen-Iron Phase Equilibrium Diagram

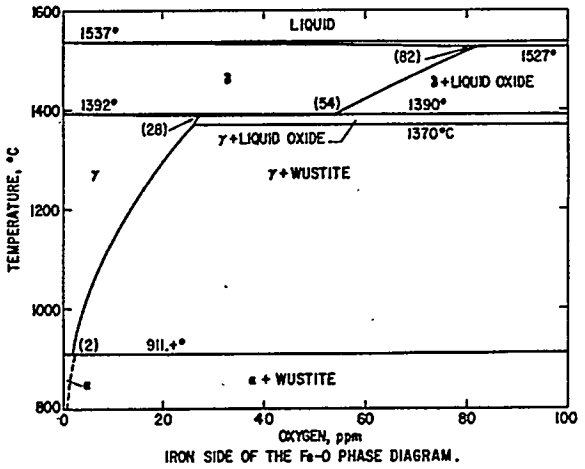

IRON SIDE OF THE Fe-O PHASE DIAGRAM.

The solubility of oxygen in molten iron is affected by the presence of other dissolved compounds. Specifically, most solutes, including carbon, lower the activity coefficient of oxygen in iron (Figure 2.8). The logarithm of activity coefficient of oxygen in iron is highly depressed in the presence of even small amounts of aluminum, titanium and boron indicating significant deviation of these solutions from ideal behavior.

Figure 2.8
Effect of Other Solutes on the Activity Coefficient of Oxygen in Iron

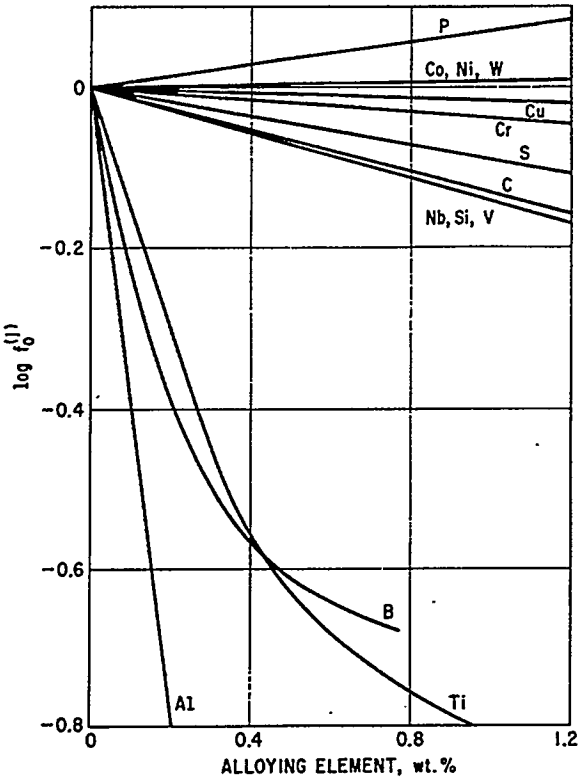

2.1.1.1.4. Sulfur-Iron Solutions

The CEP technology allows for processing and recycling of sulfur-containing compounds without providing reaction pathways for formation of SO_x (Section 2.1.1.3). Key to this attribute of the CEP technology is the complete miscibility of sulfur in iron at high temperatures up to concentrations of 50 weight % (Figure 2.9). A sulfur-containing compound injected into the CEP reactor will dissociate into its elemental constituents. The solubility of sulfur in the molten iron bath ensures that particles of sulfur are not entrained in the off-gas with the subsequent possibility of further reaction with products in the gas stream and production of undesired contaminants. In fact, as will be discussed later (Section 2.1.1.3), sulfur can be recovered and recycled by partitioning to either the ceramic or gaseous phase.

Figure 2.9
Sulfur-Iron Phase Equilibrium Diagram

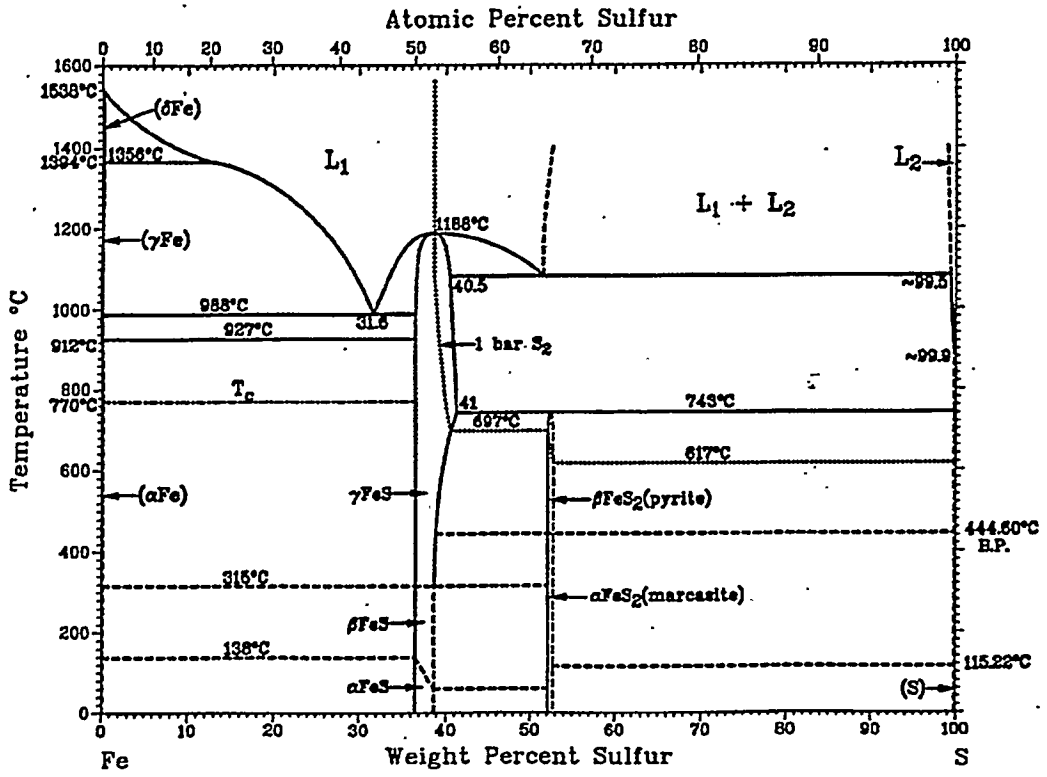

2.1.1.1.5. Hydrogen-Iron Solutions

The low solubility of hydrogen in iron solutions is important in the processing and conversion of organic feeds into synthesis gas. Specifically, organic feeds dissociate to elemental intermediates with carbon dissolving in the iron and subsequently reacting with oxygen co-reactant to form carbon monoxide. Hydrogen is released in its diatomic gaseous state in the product stream. Figure 2.10 shows that at 1,592°C, hydrogen solubility in molten iron is only 24 ppm by weight. Further, addition of even small amounts of carbon further reduces hydrogen solubility.

Figure 2.10
Solubility of Hydrogen in Binary Iron Alloys at 1,592°C and 1 atm

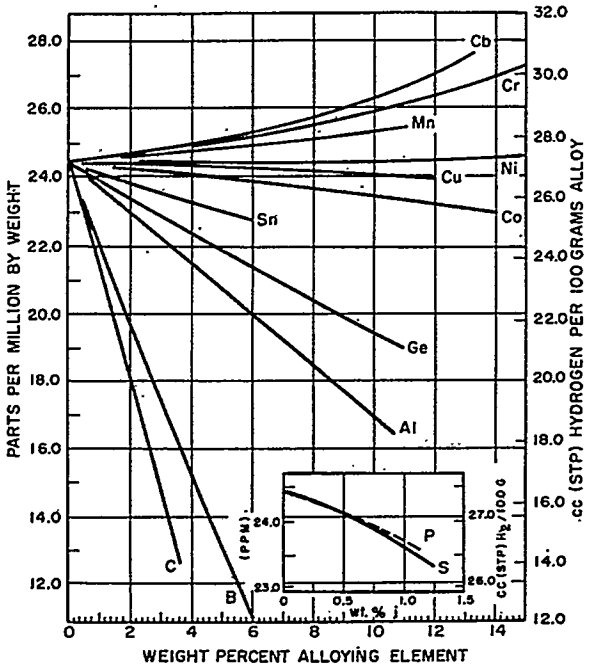

2.1.1.1.6. Nitrogen-Iron Solutions

The CEP technology allows for processing and recycling of nitrogen-containing organic compounds without providing reaction pathways for formation of NO_x or the release of fuel bound nitrogen. Key to this attribute of the CEP technology is the low solubility of nitrogen and the highly reducing environment in the molten iron solvent. Specifically, the nitrogen-containing organic feed to the CEP dissociates into its elemental constituents. Oxygen will react with dissolved carbon to form carbon monoxide (or wustite at low carbon concentration). Nitrogen, which is not soluble in iron, is released in its diatomic gaseous state in the off-gas stream. The highly reducing environment of the CEP ensures that oxidation of nitrogen to NO_x does not occur and that no fuel bound nitrogen is released in the off-gas stream.

2.1.1.2. Reaction Thermodynamics

As outlined above the molten metal bath in the CEP system ensures dissociation of the feed into elemental constituents and the formation of 'singular' dissolved elemental intermediates. The flexibility and robustness of the CEP system in synthesizing products of commercial value is dependent on manipulating the reaction pathways of the dissolved elemental intermediates through select addition of co-reactants and variation in operating conditions. Therefore, reaction thermodynamics are important in understanding the control of potential reaction pathways. The general thermodynamic characterizations of oxidation/reduction reactions are outlined below. In

Section 2.1.1.3, specific examples of feeds relevant to typical CEP commercial applications are discussed.

The starting point for this discussion is an overview of the Standard Gibbs Free Energy ($\Delta G°$) changes accompanying typical reactions relevant to the CEP. Although this data has its limitations because it is for pure (not multi-component) systems it is a helpful tool in determining which of the possible reactions in the CEP system will be thermodynamically favored. Table 2.3 summarizes $\Delta G°$ data drawn from the literature. Of note is the fact that $\Delta G°$ is approximated as a linear function of temperature. Specifically, the Gibbs Free Energy change is defined as:

$$\Delta G° = \Delta H° - T\Delta S° = A + BT$$

where $\Delta H°$ = Standard Enthalpy change, $\Delta S°$ = Standard Entropy change, T = Temperature, and A, B = Constants defined by the equation: $R \ln K = -B - (A/T)$. The error involved in approximating the free energy change to a linear function is small and within the margin of error of the high temperature empirical measurements. For many metallurgical reactions at high temperatures, ΔC_p is small and can be approximated to zero with little loss of accuracy.

Since reactions leading to the largest declines in Gibbs Free Energy are thermodynamically favored, a number of key observations relevant to CEP can be drawn from Table 2.3. Specifically, reactions where A and B have large negative values tend to be thermodynamically favored, especially at high temperatures. For example, the Gibbs Free Energy change at 1700K for the oxidation of carbon to carbon monoxide is -575 KJ/mol O_2, while the oxidation of carbon to carbon dioxide is -400 KJ/mol O_2. Therefore, in a CEP system containing dissolved carbon and oxygen, carbon monoxide formation is thermodynamically favored over carbon dioxide formation.

The reaction thermodynamics outlined above can also be summarized graphically with the Gibbs Free Energy change plotted versus temperature (Figure 2.11). Such diagrams will be used in Section 2.1.1.3 below in considering the thermodynamic forces driving separation and recycling of key components in a typical CEP feed stream. Furthermore, these diagrams can be used to determine how operating conditions (temperature, pressure, bath composition) can be varied to synthesize desired products.

These correlations are for pure systems and provide only approximation to the reaction thermodynamics guiding the process chemistry. Although beyond the scope of this report, MMT has in-depth understanding of the thermodynamic properties of higher order, non-ideal solution reaction chemistry. This knowledge is drawn upon by MMT for refining the CEP process chemistry and reactor design to meet specific customer needs.

Table 2.3
Standard Free Energies of Reaction Encountered in Metallurgical Systems

Reaction	-A	B	Temp. Range (°C)
$C(s) + 2H_2(g) \rightarrow CH_4(g)$	21,550	26.16	25 - 2,000
$C(s) + 1/2O_2(g) \rightarrow CO(g)$	26,700	-20.95	25 - 2,000
$C(s) + O_2(g) \rightarrow CO_2(g)$	94,200	-0.20	25 - 2,000
$Fe(s) + 1/2O_2(g) \rightarrow$ 'FeO'(s)	62,050	14.95	250 - 1,371
$Fe(l) + 1/2O_2(g) \rightarrow$ "FeO"(l)	55,620	10.83	15,370 - 1,700
$H_2(g) + O_2(g) \rightarrow H_2O(g)$	58,900	13.10	25 - 1,700
$H_2(g) + 1/2S_2(g) \rightarrow H_2S(g)$	21,580	11.80	25 - 1,500
$3/2H_2(g) + 1/2N_2(g) \rightarrow NH_3(g)$	12,050	26.70	25 - 700
$1/2S_2(g) + 1/2O_2(g) \rightarrow SO(g)$	15,400	-1.4	25 - 1,700
$1/2S_2(g) + O_2(g) \rightarrow SO_2(g)$	86,620	17.31	25 - 1,700
$1/2S_2(g) + 3/2O_2(g) \rightarrow SO_3(g)$	109,220	38.67	25 - 1,500

2.1.1.3. Feed Conversion and Products Synthesis

Reaction thermodynamics and solution equilibria drive feed conversion and product synthesis in the CEP system. These fundamental physical chemistry principles for key feed components relevant to commercial waste streams are outlined in this report. Specifically, processing of organics, metals, halides, sulfur and transuranics are discussed.

2.1.1.3.1. Organic Feed Conversion to Synthesis Gas

When an organic feed is injected into a CEP reactor, it dissociates and dissolves into elemental intermediates on contact with the molten iron solvent. Hydrogen will not dissolve in the metal solvent but will be released as a gas in the product stream. Addition of oxygen as a co-reactant will lead to the formation of synthesis gas. The production of synthesis gas is due to the effectiveness of the dissolved carbon intermediate as a reducing agent. This is best illustrated by the Gibbs Free Energy diagram (Figure 2.11). The oxides for which the free energy lines are above that of CO can be reduced by carbon. Therefore, when oxygen is added to a system containing carbon and iron at 2000°C, three competing reactions take place:

$$2\underline{C} + O_2(g) \rightarrow 2CO(g)$$
$$\underline{C} + O_2(g) \rightarrow CO_2(g)$$
$$2Fe(s) + O_2(g) \rightarrow 2FeO(s)$$

In this system, one can look at Figure 2.11 to identify that at 2000°C, the Gibbs free energy of reaction of carbon to carbon monoxide (-600 kJ/mol O_2) is lower than that involving carbon to carbon dioxide (-400 kJ/mol O_2) and iron to iron oxide (-250 kJ/mol O_2). Therefore, due to thermodynamic forces CO will be formed preferentially to CO_2 and FeO when oxygen is injected into the carbon-iron melt.

A critical attribute of the CEP system is that a reducing environment is maintained and carbon dioxide or steam is not formed. This is because in the presence of excess oxygen, wustite (iron oxide) formation is thermodynamically favored over carbon dioxide or steam formation. Therefore, in contrast to open flame organic feed processing systems such as coal gasification, the synthesis gas produced from CEP is of high quality with a CO/CO_2 ratio of 10,000:1 and an H_2/H_2O ratio of 2,000:1.

Figure 2.11
Gibbs Free Energies of Oxidation

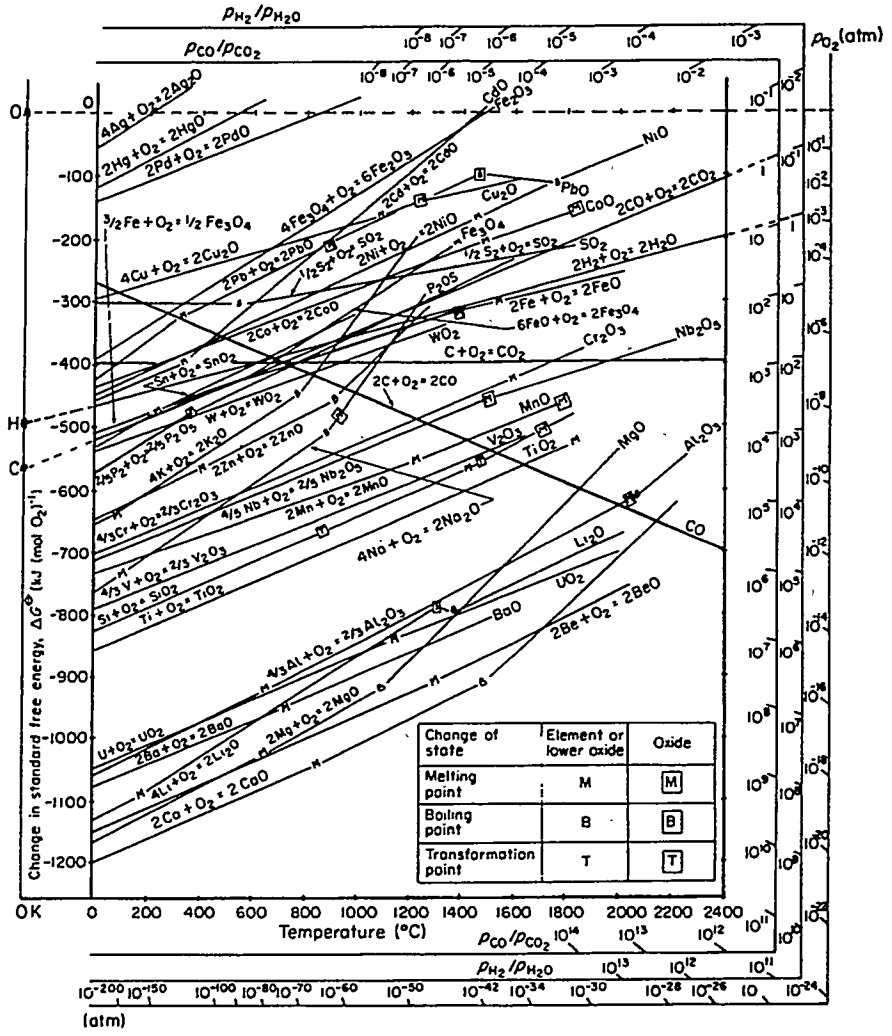

2.1.1.3.2. Metal Recovery

A significant advantage of CEP technology is its ability to recover and recycle metals from organo-metallic feeds. Consider an organo-metallic feed dissociating into its elemental constituents (e.g., C, H, M, where M is the metal) upon injection into the CEP reactor. As outlined above, both the carbon and the metal will readily dissolve in the molten metal solvent. If oxygen is added as a co-reactant, two reaction pathways are possible:

$$\text{(A)} \quad 2\underline{C} + \underline{M} + O_2(g) \rightarrow 2CO(g) + \underline{M}$$

$$\text{(B)} \quad \underline{C} + x\,\underline{M} + y\,O_2(g) \rightarrow M_xO_{2y} + \underline{C}$$

Figure 2.11 indicates which systems will proceed with formation of carbon monoxide (reaction pathway (A)) and which systems will proceed with formation of the metal oxide (reaction pathway (B)). Specifically, carbon monoxide formation is favored in systems containing metals such as nickel, cobalt and copper whose free energy of oxidation is higher than that of carbon. These metals can be recovered as alloys in the iron solvent. Metals with a free energy of oxidation lower than that of carbon (e.g., aluminum, calcium) will form oxides and partition into the ceramic phase. Certain metals can either be recovered as metal alloys or as oxides in the ceramic phase depending on the operating conditions. For example, magnesium is reduced by carbon at elevated temperatures ($T \geq 1800°C$, $p = 1$ atm). However, at elevated pressures, magnesium oxide reduction by carbon, will not be favored.

2.1.1.3.3. Halogen Recovery

Under the Resource Conservation and Recovery Act (RCRA), chlorinated organic compounds of concern include the primary organic hazardous constituents (POHCs) in the waste. Carbon tetrachloride, chloroform, para-dichloro benzene, perchloroethylene, tetrachloroethane, 1,1,1-trichloroethane, trichloroethylene, methyl chloride, polyvinyl chloride (PVC), and polychlorinated biphenyls (PCB) and all their intermediates and derivatives are among the common organic chlorinated compounds.

The CEP technology can recover and recycle halogens from halogenated organic and inorganic feed streams without the formation of undesired by-products (e.g, chlorophenols, dioxins and furans) because in CEP, reaction pathways proceed via dissolved elemental intermediates and are driven by thermodynamic forces.

In order to demonstrate the recovery and recycling of halides in the CEP system, consider the case of a chlorinated organic feed stream. On injection into the molten metal bath, the feed will dissociate into dissolved elemental intermediates. Chlorine can be recovered and recycled as either a metal chloride or hydrogen chloride, or as chlorine gas in the absence of hydrogen. The two reaction pathways are:

- *Formation of Metal Chloride*: Calcium, in the form of calcium oxide, added to the molten iron bath will form calcium chloride. The effectiveness of calcium as a chloride scrubbing agent is demonstrated by the chlorides free energy diagram (Figure 2.12). Calcium chloride is volatile under CEP operating conditions and will distribute itself in the gas product phase where it can be cooled and separated from the other gaseous components as a condensed solid. However, by manipulating the ceramic phase composition, the metal halide can be prevented from distributing into the gaseous phase.

- *Formation of Hydrogen Chloride*: In the absence of calcium, both hydrogen chloride and ferrous chloride will be formed as the free energy of formation for both compounds is of the same order of magnitude (Figure 2.12). If the CEP is

operated at temperatures of 1500°C, the ferrous chloride will volatilize and be recovered as a condensed solid in the gaseous stream. If the CEP is operated at lower temperatures (1000°C) ferrous chloride can be recovered as a liquid in the vitreous phase.

The CEP flexibility in recovering halogens is a major advantage given the technical difficulties and expense associated with processing halogen-containing waste streams in typical open flame combustion processes such as incineration. Halogen containing compounds tend to suppress combustion and are often characterized as non-combustible. Therefore, incineration of these chemicals can result in incomplete combustion leading to formation of highly toxic compounds. The free radical chemistry that occurs during combustion produces radical intermediates which can react to produce dioxins and furans.

2.1.1.3.4. Chloride Partitioning

2.1.1.3.4.1. Thermodynamics of Chloride/Fe/Ni systems

A summary of thermodynamics data associated with the formation of simple chlorinated products is presented in Figure 2.12. The free energy of formation of common chlorides as a function of temperature spanning the entire operating range of CEP is presented. The key comparison to be made here is the relative stability of nickel, iron, and hydrogen chloride. Under thermodynamic control, free energy-based predictions would show a close competition between hydrogen and iron for chlorine, while the formation of nickel chloride is considerably less favored. Thus, one would expect an approximately equal split between HCl and $FeCl_2$ products from injection of chlorinated hydrocarbons into an iron bath, whereas one would expect HCl to largely predominate over $NiCl_2$ from injection into a nickel bath.

In sharp contrast to the aforementioned chlorides, Group I and Group II metal chloride salts have a high degree of stability in a dust or ceramic phase product from a system containing these elements over the entire range of CEP operating temperatures. Therefore, this model will predict predominant generation of their salts (including $CaCl_2$, NaCl, and $MgCl_2$). Any product yield predictions derived from these free energy numbers would indicate virtually all of the injected chlorine being converted to one of these species.

In summary, thermodynamic control would predict a close competition between iron and hydrogen for bonding with chlorine in the final product. This is in contrast to the nickel bath, where the HCl product should largely predominate over metal chlorides. When a ceramic layer is introduced during CEP operation, thermodynamic control predicts predominant retention of chlorine in the ceramic phase over the range of conditions for which unit activity and calcium availability are good assumptions.

Figure 2.12
Chloride Free Energy Diagram

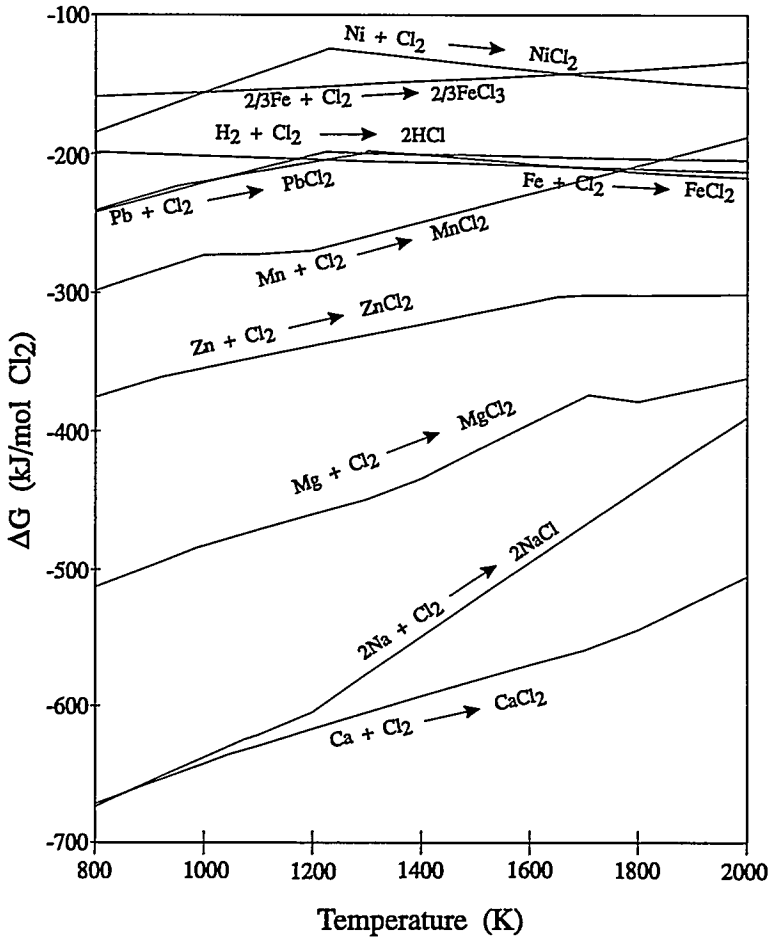

2.1.1.3.4.2. Chlorinated Ceramic Phase

Partitioning of chlorides in a metal/gas system, as discussed above, can be modeled at high temperatures using thermodynamics with standard state conditions. Partitioning of chlorides in a metal/gas/ceramic phase system, however, must take into consideration the effects of mass transfer issues within the ceramic phase. Even though the free energy of reaction can be treated as a true measure of the driving force for the reaction, mass transfer issues can limit the extent of the reaction such that thermodynamic equilibrium is not achieved. In the case of chloride processing with a metal/CaO-Al_2O_3-SiO_2 ceramic phase, the formation of '$CaCl_2$' in the ceramic phase is not only dependent on the activities of the constituents, but also influenced by ceramic phase viscosity, reaction-rate, and residence time of the gas in the ceramic phase.

The CaO-Al_2O_3-SiO_2 ternary system has been studied extensively by the steel making industry and in some detail by the glass industry. While the glass forming region in this system is very large, interest by the steel industry has focused on high CaO- containing

compositions. High basicity (high lime) ceramics are commonly utilized due to their high efficiency for desulfurization and dephosphorization of the metal bath. CaO-Al_2O_3-SiO_2 systems are of primary interest to MMT for potential capture of chlorides as $CaCl_2$.

2.1.1.3.5. Sulfur Recovery

Another important attribute of the CEP technology is its ability to recover and recycle sulfur products without the formation of SO_x. Again, this is due to the fact that in CEP reactions proceed via a dissolved elemental intermediate and are driven by thermodynamic forces. The preferential formation of carbon monoxide over sulfur dioxide is highlighted in Figure 2.11. Specifically, the Gibbs free energy of oxidation of carbon is significantly lower than that of sulfur. Formation of FeO is also thermodynamically favored to sulfur dioxide formation indicating that even if carbon is depleted in the molten metal solution, excess oxygen will form wustite.

Figure 2.13 shows the sulfide Gibbs free energy diagram and highlights the fact that a large number of sulfides can be formed in the CEP system depending on the operating conditions and the addition of co-reactants. For example, addition of calcium (in the form of calcium oxide) will ensure that sulfur in the feed stream is recovered as calcium sulfide which partitions to the ceramic phase. If calcium is not added as a co-reactant, the majority of sulfur will partition between the metal phase (dissolved sulfur S) and the ceramic phase (FeS) with small amounts being released as hydrogen sulfide in the gaseous stream. Again, this demonstrates the operating flexibility of CEP to control the product rate of the sulfur.

Figure 2.13
Gibbs Free Energy Diagram for Sulfides

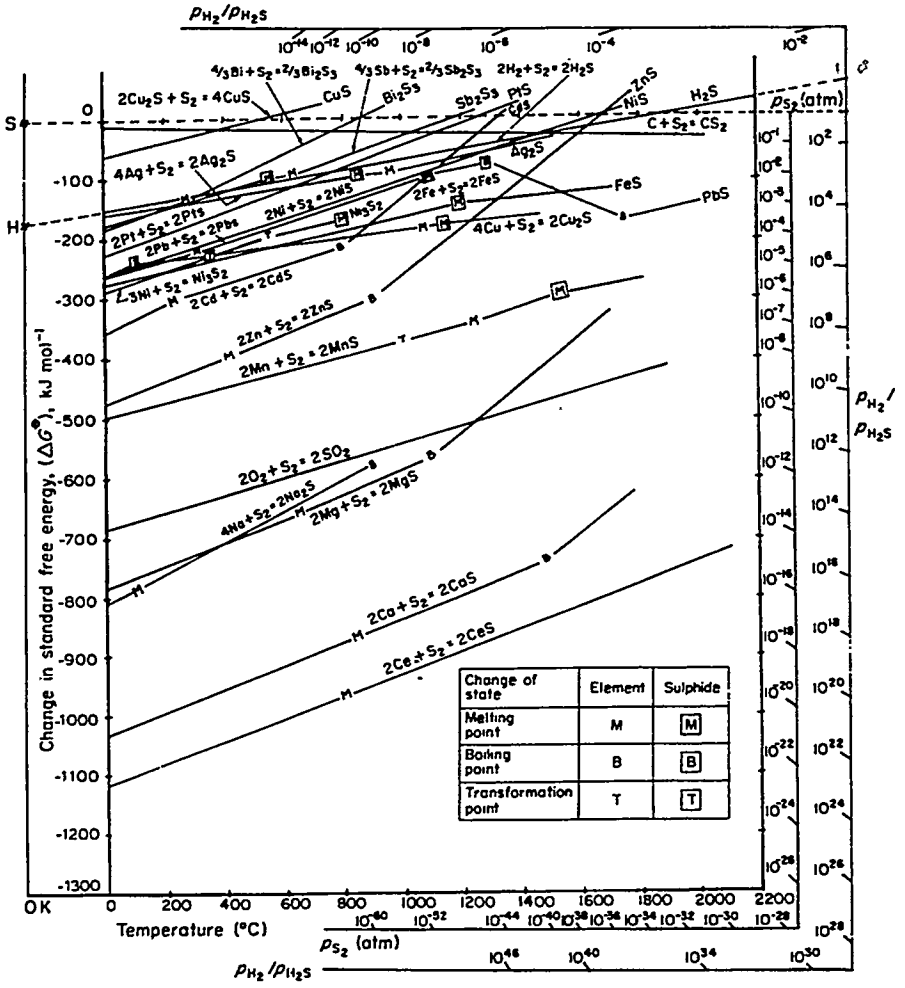

2.1.1.3.6. Transuranic Recovery

An important advantage of the CEP technology is that it can separate and concentrate radioactive compounds from complex contaminated feeds while also recovering and recycling the non-radioactive components of the feed. This attribute of CEP has important implications in the decommissioning of nuclear weapons as well as the decontamination of radioactive sites. This implies that the radioactively-contaminated components of nuclear weapons can be separated, highly concentrated and immobilized in a small volume that can be safely disposed of. Furthermore, feed components such as reducible metals (e.g., nickel, chromium, manganese) can be recovered as alloys while hazardous organic components can be effectively converted to a stable final form.

Table 2.4 shows that the Gibbs Free Energies of reduction by carbon of transuranic oxides are positive indicating that the reactions are not thermodynamically favored. It is this oxide stability that provides a mechanism for the partitioning of these radioactive species into the ceramic phase. Data collected from the literature demonstrates the partitioning of transuranic components from the metal to the vitreous phase. Specifically, residual concentrations ranging from 0.05 ppm to 2 ppm of such radioactive components were achieved by others using diffusion of oxidizing, vitreous-forming agents to partition the radioactive components.

Table 2.4
Free Energies of Reduction of Transuranic Oxides

Reaction	ΔG (kJ/mol) at 2000K
$UO_2(s)+2C(s) \rightarrow 2CO(g)+U(l)$	167.104
$PuO(s)+C(s) \rightarrow CO(g)+Pu(l)$	100.305
$PuO_2(s)+2C(s) \rightarrow 2CO(g)+Pu(l)$	111.377
$Pu_2O_3(s)+3C(s) \rightarrow 3CO(g)+2Pu(l)$	463.122
$ThO_2(s)+2C(s) \rightarrow 2CO(g)+Th(s)$	283.740
$ZrO_2(s)+2C(s) \rightarrow 2CO(g)+Zr(s)$	156.339

2.1.1.4. Experimental Feed Conversion Demonstrations

The processing and conversion of organic, organo-metallic and inorganic compounds in mixed waste streams into stable materials has been demonstrated theoretically in the discussion above. In addition to the theoretical analysis, MMT has collected extensive experimental data in bench-scale and pilot plant units and in commercial-scale metallurgical systems which are presented throughout the balance of this report. The experimental data validates the theoretical predictions and confirms CEP's capabilities to generate high quality products.

The physical chemistry of CEP, specifically the solution equilibria and the formation of a 'singular' dissolved intermediate in the reaction pathway, ensures that complete dissociation of feed streams occurs and that product synthesis and recycling can be controlled and manipulated. Therefore, the molten metal, acting as a homogeneous catalyst and solvent with high chemical inertia, renders CEP a highly flexible and robust recycling technology.

2.1.2. CEP Reactor Design

2.1.2.1. Introduction

A theoretical model has been developed to elucidate the governing chemistry and physics of a CEP reactor. Based on theoretical findings, computer models were developed to assist in reactor design and optimization. Moreover, important design parameters governing reactor performance were identified, which would enable systematic design, optimization, and operation of CEP reactors. This theoretical approach provided a framework for conducting experimentation.

The most important governing equations are summarized, and the implications of the model that has been developed explained.

2.1.2.2. Method

The overall method of approach used for reactor design is a combination of specifying a logical set of input parameters and constraints, and solving a set of equations which govern the hydrodynamics in the reactor.

2.1.2.2.1. Reactor Geometry

Strictly speaking, the full Navier-Stokes equations including the effects of multiphase flow, reaction, compressibility, and turbulence are necessary to describe the conditions that occur in CEP reactors. However, uncertainties concerning interphase momentum transfer, turbulence of multiphase flows, and the inconvenience of using a full 3-dimensional computational fluid dynamics (CFD) code provided the motivation for using a set of governing equations which capture the dominant physics. Therefore, approximations have been made resulting in a set of one-dimensional conservation equations which describe CEP reactors. A conservation-of-mass equation for the gas phase, and a total conservation-of-mass equation for the combined gas-liquid plume were solved simultaneously with a combined conservation-of-momentum equation in order to describe the plumes that form above each tuyere in a molten metal bath.

2.1.2.2.2. Headspace Geometry

Headspace geometry is defined by a combination of spout height above the plumes (H_{spout}), required ceramic/metal settling lengths, and the required mean residence time of off-gases in the head space. Spout height is determined by setting the specific potential energy of the peak of the spout equal to the specific kinetic energy at the centerline of the base of the spout (at the nominal bath surface), with the result:

$$D_{HS} = f\{SF_{HS}, \langle U_S \rangle, k_R, H_b, Q_g\}$$

where $\langle U_S \rangle$ is the mass-averaged velocity at the bath surface, D_{HS} is the headspace (horizontal section) diameter, H_b is the bath depth, Q_g is the off-gas flow rate, k_R is the empirical entrainment coefficient, and SF_{HS} is the safety factor for the height of the horizontal section above the top of the spout.

2.1.2.2.2.1. Length

The headspace length is determined by the largest of the following: 1) ceramic-metal separation distance; 2) gas-particulate separation distance; 3) distance required to provide a specified minimum gas-phase residence time.

2.1.2.3. Reactor Design Case Studies

Examples are presented for CEP reactor design given case-specific criteria consistent with DOE requirements, including: waste feed composition and physical form, plant throughput capacity, desired CEP final phase, and other specific operating constraints. The design results were calculated using computer modeling software developed by MMT using the reactor design method described above.

- **Case I: PCB-Contaminated Oil**

  PCBs are among the most difficult to treat toxic wastes, with a significant stockpile within the DOE complex. The following CEP reactor design simulation has been run for 0.1 wt % PCB in #2 fuel oil. The design feed basis is 11,000 tons/year and the simulation was run for a reactor operating pressure of about 10 bar, within the limit of successful CEP experimentation. The resultant simulation showed the bath mass at 7.3 tons, and the required power level at 200 kW.

- **Case II: Contaminated Scrap Metal (1 atm)**

  A second example of the reactor design simulation was run for uranium contaminated scrap metal. The chemical composition of the feed utilized for this simulation was as follows:

  > 63 wt% C, 2 wt% H, 7 wt% O, 1 wt% N, 12 wt% Cu, 9 wt% Al, 1 wt% Ni, 1 wt% Si, 1 wt% Pb, **0.1 wt% U.**

  The plant design capacity was for over 30,000 tons/year of waste feed material, with CEP to be run at atmospheric pressure. The effect of reduced operating pressure (and to a much lesser extent increased capacity) was dramatic, causing the molten metal bath mass to be 62 tons for this simulation, and the required power level to be over 5000 kW.

2.1.2.4. Leveragability of Reactor Design Model

2.1.2.4.1. Splashing in CEP Reactors

Molten liquid splashing in CEP reactors causes a phenomenon called *skulling*, defined operationally as the solidification of molten metal or ceramic on internal reactor surfaces. This can reduce optimal operability due to run-to-run contamination from the skulled material. Reactor design modeling was applied to determine appropriate relationships to reduce splashing, thereby maintaining a high degree of reliable operability in CEP units.

Splashing in CEP reactors is approximately governed by conversion of the buoyancy driven kinetic energy at the bath surface into potential energy of the spout height. Equating kinetic energy at the bath surface to potential energy at the peak of the spout leads to an estimate of the spout height above the nominal bath surface (H_{sp}):

$$H_{sp} = f\{u_{max}, g\}$$

where u_{max} is the velocity at the center of the gas/liquid plume at the nominal bath surface, and g is acceleration due to gravity. The velocity at the bath surface may be reduced by increasing the bath depth (H_b) to allow increased entrainment of metal into the gas/metal plume that exists within the metal bath, or by reducing the volumetric gas flow through the melt. However, as bath depth increases beyond a critical value, the total spout height above the tuyere (h_{sp}), defined as the sum of the bath depth (H_b) plus the spout height above the surface (H_{sp}), first decreases to a minimum value and then increases. Using results from the one-dimensional mass and energy balance model described earlier, the total spout height can be described by:

$$h_{sp}/H_b = f\{k_R, Fr_{sp}\}$$

or

$$h_{sp} = f\{H_b, k_R, Q_g, g\}$$

where h_{sp} is the total height of the spout above the tuyere (m), and Fr_{sp} is the froude number for splashing. The bath depth at which h_{sp} is a minimum is described as H_b^{min} and can be determined from the second equation above.

The above findings have implications on splashing and operational stability of the bath. splashing in a given reactor becomes excessive, in general, when total spout height increases since more metal is projected at the reactor ceiling. Normally, to reduce splashing, either off-gas flow rate (Q_g), or bath depth (H_b) is reduced. However, bath depth should be reduced only to the point at which the minimum spout height occurs,

plus some safety factor to account for bath sloshing and transient slugging. Below this depth, the system becomes unstable. This phenomenon has been confirmed qualitatively using the physical model.

Determining the exact rates at which splashing occurs requires additional knowledge of the energy balance and mass flow rate of metal at various heights above the bath. The present study provides simple guidelines for controlling splashing and stability in a CEP reactor.

In addition to the operability issues described above, the minimum stable bath depth implies a minimum stable residence time that increases with off-gas flow rate. The minimum stable liquid metal phase residence time is given by:

$$<\tau_{min}> = f\{k_R, Q_g, g\}$$

Since specific utilization is a function of residence time, the minimum residence time possible is generally desired to minimize reactor molten metal mass. Moreover, for feeds that do not require the minimum stable residence time, the required reactor mass may be substantially increased relative to the size dictated by the feed.

The simplest way of increasing throughput per tuyere is by operating the reactor above atmospheric pressure. Another approach for circumventing the limitations imposed by the minimum stable residence time is to operate the reactor in the unstable regime. This requires that the reactor be designed and operated so that despite the intense splashing that will occur, all metal will return to the bath.

2.1.2.5. Conclusions

Computer simulation models have been developed for designing and optimizing CEP reactors. The modeling studies allowed identification of process design parameters governing reactor performance. Two feed waste streams relevant to DOE waste were simulated using user-specified input parameters.

The reactor models have also been used to develop design strategies to reduce splashing in CEP reactors. Stable operating regimes have been established that enable CEP reactors to be operated with minimal splashing, though imposing a limitation of reactor specific utilization. Alternatively, reactor modeling can also be used to allow reactors to be designed and operated such that splashing metal returns to the bath.

2.1.2.6. Nomenclature

Fr_{sp} = Froude number for splashing.
g = Acceleration due to gravity (9.81 m/s^2)
H_b = Bath depth above tuyere (m).

h_{sp} = Total height of spout above tuyere (m).
H_{sp} = Height of spout above bath surface (m).
k_R = Empirical entrainment coefficient (approximately = 1.6).
Q_g = Off-gas flow rate (m^3/s).
t = residence time in liquid metal phase of plume (s).
u_{max} = Maximum plume velocity at the bath surface (m/s).

2.1.2.7. Redesign of Demonstration-Scale CEP Unit

A significant culmination of CEP reactor design modeling and improvement endeavors was the redesign of the demonstration-scale CEP unit at MMT's Fall River Recycling R & D Facility. The basic objectives of the project were to:

- reduce refractory wear in the throat area of the reactor,
- increase reactor throughput,
- reduce splashing, and
- minimize dust carryover.

The previous demonstration unit limitations were overcome mainly by assessment of the complex transport phenomena occurring inside the CEP reactor vessel. The gas plume from tuyere injection typically intersected the reactor wall, thereby limiting metal entrainment in the plume and causing excessive splashing for a given off-gas flow rate. The plume hitting the wall and high mass transfer rates resulted in aggressive refractory deterioration rates in the throat section of the reactor.

Computational fluid dynamics, splashing considerations, and reactor design modeling studies were considered together to enable a reactor redesign which was implemented to allow reactor operation without the gas plumes intersecting the reactor walls. The new demonstration-scale unit was designed to hold as much as 4.1 metric tons of molten metal inside the reactor, increasing the gas throughput by 100%.

Preliminary results from the demonstration-scale experiments indicated the redesign accomplished all its objectives. The data with the reconfigured demonstration reactor qualitatively confirmed design improvements. The refractory showed a very small amount of material loss, too small (i.e., < 0.25") to measure accurately. Operator observations during the run also documented minimal bath splashing, even at a throughput, as measured by reactor gas evolution, more than 50% higher than the throughput demonstrated prior to reactor redesign. The reduction of bath splashing, consistent with expectations, provided further indication that the new bath dimensions have successfully eliminated the plume effect at the reactor walls.

2.1.3. Computational Fluid Dynamics

Predictability of flow conditions inside a CEP vessel may be safely and efficiently modeled using computer simulations, provided the model has the ability to account for the dominant physical variables and chemical reactions. Simulation results can be used to improve the design of CEP reactors and test new vessel configurations without the expense of construction and experimental testing.

Molten Metal Technology has worked in close cooperation with Los Alamos National Laboratory, in utilization of a numerical method useful for solving problems in multiphase flow, known as the ICE scheme (Implicit, Continuous-fluid, Eulerian). This method is generically applicable to a wide variety of fluid systems spanning a range of technologies. The computational code that Los Alamos has developed utilizing this method is called MFICE.

The main objective is to assess the effect of process variables and reactor configuration changes on the residence time distribution of feed materials and reactants in the molten metal bath of CEP. The first step has been to modify and test the MFICE code to fully model the CEP system. This has been accomplished by the following series of steps:

1. verify that the universal design of the computational method was indeed applicable for CEP materials and operating conditions;

2. modify the algorithm in the code to more efficiently solve heat and mass transfer equations for the unique flow conditions found in CEP;

3. test the computational modifications against other numerical methods and/or verify the additions with known physical systems simple enough to be accurately described mathematically;

4. add models of physical interactions to the code to account for chemical reactions, particular fluid flows (e.g., molten ceramic), and inter-fluid exchange;

5. a) determine an applicable experimental result from the literature which can be used to verify physical applicability of the numerical model representing parts of a complex, multiphase CEP system, b) run simulations on such a set of simplified process conditions to generate numerical results, such as property contour fields, and c) compare simulation results with experimental system to verify physical accuracy of the numerical simulation; and

6. combine experimentally verified parts of the model to develop an understanding of complex material flows in the CEP system.

Computational fluid dynamic methods are approximate numerical solutions of partial differential equations (PDEs) that describe the flow of fluids (and related heat and mass

transfer phenomena) as a continuum, as opposed to discrete elements. Modeling a particular physical system requires solving the appropriate continuum equations in space and time subject to initial and boundary conditions particular to that system (describing vessel shape, location of heat sources, flow inlets and outlets, reaction boundaries, etc.). The initial conditions describe the physical state at each position in the domain and at an initial point in time, while boundary conditions describe the system at the domain boundaries at any point in time.

The most widely used nonlinear PDEs governing continuum mechanics are the Navier-Stokes equations. Common techniques applied for a solution involve a model which allows approximating the PDEs with a larger set of nonlinear ordinary differential equations (ODEs), which are then approximated by a system of algebraic equations by performing similar approaches in the time domain. The time dependence is determined by repeatedly computing the solution of the algebraic equations at consecutive time steps.

A computer readily solves these algebraic equations using a model which mathematically describes the physical geometry of the system, or domain. The domain is apportioned into a network of grids called a *mesh*. The mesh size must be defined small enough to adequately describe the transport phenomena at each location, requiring smaller mesh sizes in regions of rapidly-changing properties. Every piece of the mesh has its own associated algebraic equations describing fluid properties (such as velocity, temperature, pressure, concentration, etc.), which are interdependent on each other; consequently, the entire set of equations must be solved simultaneously.

Computational models of physical systems often utilize assumptions invoked to simplify solutions or eliminate the effect of unimportant variables. These models may therefore be limited to certain ranges of material properties or operating conditions for which its assumptions are valid. CEP temperatures, pressures, velocities, fluid conditions, multiple fluids, and chemicals on the other hand, vary widely over regions of the reactor vessel. Particularly, CEP involves blowing large volumes of gas into molten metal at high velocities through a small inlet, with density ratios between the fluids in the 1000's. This code was determined to be numerically stable for such typical CEP conditions, whereas other codes might not be able to handle such conditions.

The MFICE code accommodates input for multiple fluid properties, vessel geometry, computational volume size (or *mesh*), boundary conditions, control variables, and the simulated physical run time of the modeled system. Extension of the code was required for accurate modeling of CEP systems to include effects of chemical reactions. The set of reactions has been initially simplified to minimize computational difficulties.

The code was modified for CEP to improve computer processing time by changing the methodology for solving the governing Navier-Stokes equations for certain variables. Explicit solution techniques utilized by the ICE method are conditionally stable and

effectively limit the computational time intervals. CEP feeds can be relatively viscous and may have high velocities (100's of meters/second) flowing through a tuyere having a very small cross-sectional area (on the order of square millimeters). This wide range of parameters requires very short time steps to meet the numerical stability criteria.

The modification of existing code to meet the needs of MMT involved changing the methodology from explicit solutions to iterative implicit solutions for the parameters limiting computational processing. This change to implicit technique enabled stability to be maintained for the limiting parameter on a similar timescale to the others, overcoming this rate-limiting step and maximizing computational efficiency for modeling flow in CEP systems. Simulation run time was reduced by up to an order of magnitude; for example, those runs requiring 10 hours of computation time with the supplied code were solved in about 1 hour with the modified code.

Changing the code required verification that the new method was numerically and physically valid. A first step check might be performed by assessment of a simple dependent variable, such as the resulting sum of the volume fractions of each fluid within a mesh. This, of course, requires a value of unity, within 7-8 decimal places. Numerical verification was then accomplished by comparing results from the modified code with other numerical results. This normally would include those resulting from the same physical conditions: 1) simulation run with the original code, 2) simulation run with another numerical model, or 3) from known exact mathematical results for a simple physical system.

Examples are given for computer simulations of CEP fluid dynamics to portray two sets of flow conditions: (1) simple feeding of materials through a tuyere at high velocity into a water bath (in a cylindrical vessel of known bath height), and (2) the effect of a molten ceramic layer on splashing and sloshing as a function of time. The intent of the first example was to illustrate verification of the code modifications made by MMT by comparison with a numerical model for similar conditions which had proven its validity through its correspondence with experimental data. The second example was put forth to demonstrate the practical utility of the model for predicting flow patterns during CEP operation.

The process conditions and reactor confirguration utilized as inputs for a simulation run of the MMT-modified MFICE code for air injected into water were entered into the model. The intent of this simulation was to match it with numerical results from Davidson in his model of two-phase flow, resulting from bottom injection of gas into a liquid bath, this would verify the fluid interaction models used in the code development. Davidson verified his numerical method through comparison to actual experimental data of Castillejos and Brimacombe for air injected into water. Therefore, to verify the modified MFICE code's numerical accuracy and physical validity, a comparison with Davidson's results was undertaken.

Figure 2.14 to Figure 2.16 illustrate graphically-represented results from the simulation and their counterparts from Davidson's work. Figure 2.14 shows steady-state void fraction contours as a function of radial position (r) and height (z) in the bath. Figure 2.15 symbolizes centerline void fraction as a function of height (z), and Figure 2.16 represents centerline vertical gas velocities as a function of height (z). Comparison of the results from these two numerical methods could be performed only graphically, as the numerical data solutions for Davidson's work were not available. The shapes and trends observed for each figure generated by the MMT simulation (modified MFICE code) were consistent with Davidson's results, thereby confirming the numerical validity of the model. The validity of Davidson's results was proven through its consistency with the experimental results of Castillejos and Brimacombe, therefore, the validity of MMT's modified model representation of physical systems was established.

Figure 2.14a

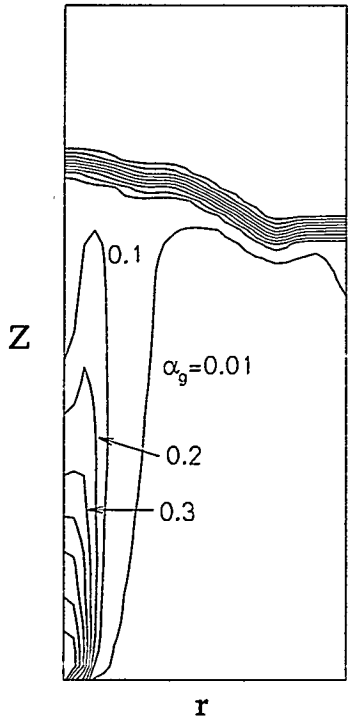

Figure 2.14b

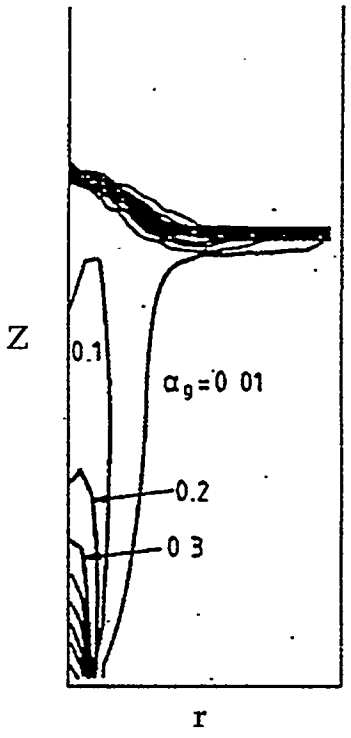

Figure 2.15a

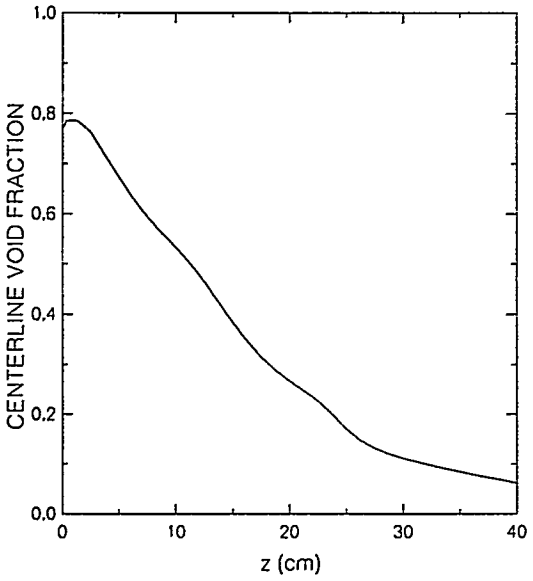

Figure 2.15b

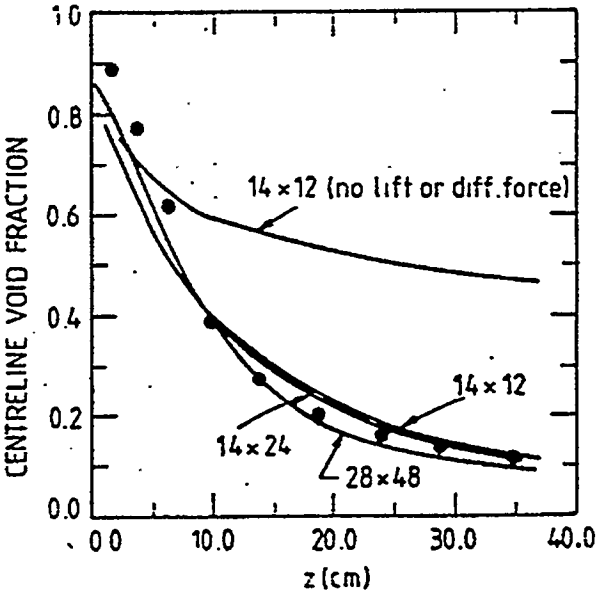

Figure 2.16a

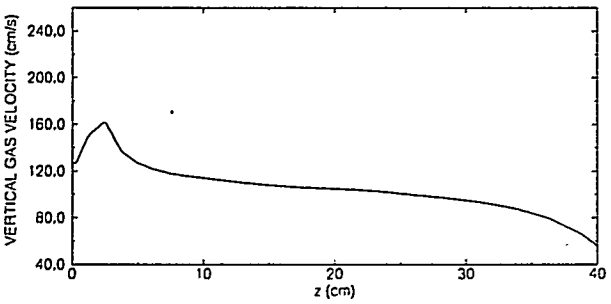

Figure 2.16b

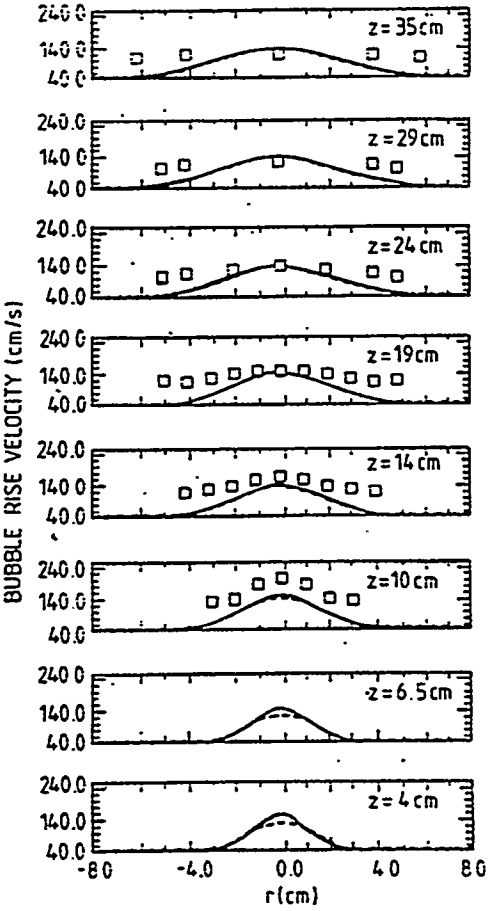

Once verified, application of the method to a system of liquid ceramic and metal was undertaken. The results illustrate the benefits of a molten ceramic layer atop the metal bath in a CEP vessel to help predict and control splashing and sloshing.

Computational Fluid Dynamics provides a means to study a variety of CEP concepts for new CEP reactor designs as well as extending modeling application capabilities. These simulations can save time and money during optimization of reactor design by significantly reducing the number of experimental iterations necessary.

2.1.4. Accretion Model

2.1.4.1. Introduction

An operational accretion model has been developed for modeling of both capped accretions from simple tuyeres and of pipe-like accretions from shrouded tuyeres. Accretion is defined as metal solidification in the bath area surrounding the bottom tuyere, due to local cooling effects. Accretions are desirable because they prevent melting of the tuyere metal pipes by the high-temperature molten metal. However, accretion growth must be controlled to avoid tuyere blockage by excessive metal solidification. The model provides a method for predicting the size and shape of the accretion as well as the temperature profile inside it. This model was developed for radially symmetric accretions and assumes steady-state conditions. Unlike the model described in Ohguchi and Robertson, the accretion model's code has been written in multi-block form so that it could easily model a variety of complicated geometries (i.e., a triple concentric tuyere) without modification. The model provides complete solutions for equations for gas flow in tuyeres and for heat and mass transfer in accretions. Material properties can be either temperature dependent or constant.

2.1.4.2. Modeling

In the multi-block form, complex problems are modeled by combining simple blocks which communicate across their common boundaries. Each block may have different properties or solve different equations. For MMT's accretion model, blocks have been developed for:

- gas flow through tuyeres,
- simple heat conduction for pipes and refractory, and
- accretion growth in the bath.

By combining them, a model was developed for capped accretion from a simple tuyere as illustrated in Figure 2.17. Four blocks were required to model this accretion formation: one gas flow block for the tuyere, one conduction block for the refractory,

and two bath blocks. With additional blocks, a model for the pipe-like accretion from a shrouded tuyere was developed, as shown in Figure 2.18.

Figure 2.17
Illustration and Corresponding Computational Set-Up of a Simple Accretion

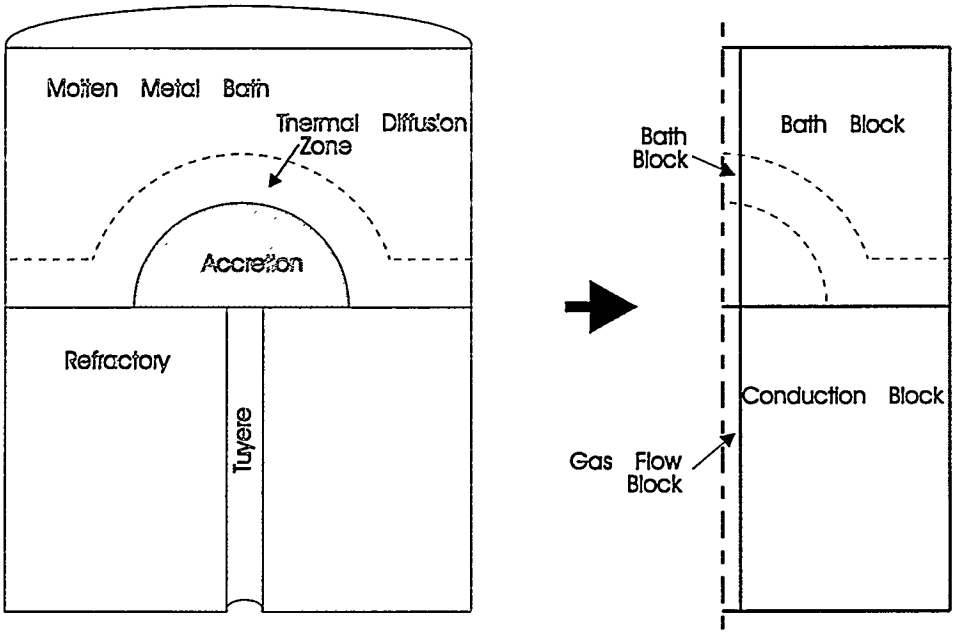

Figure 2.18
Illustration and Corresponding Computational Set-Up of a Shrouded Tuyere and Accretion

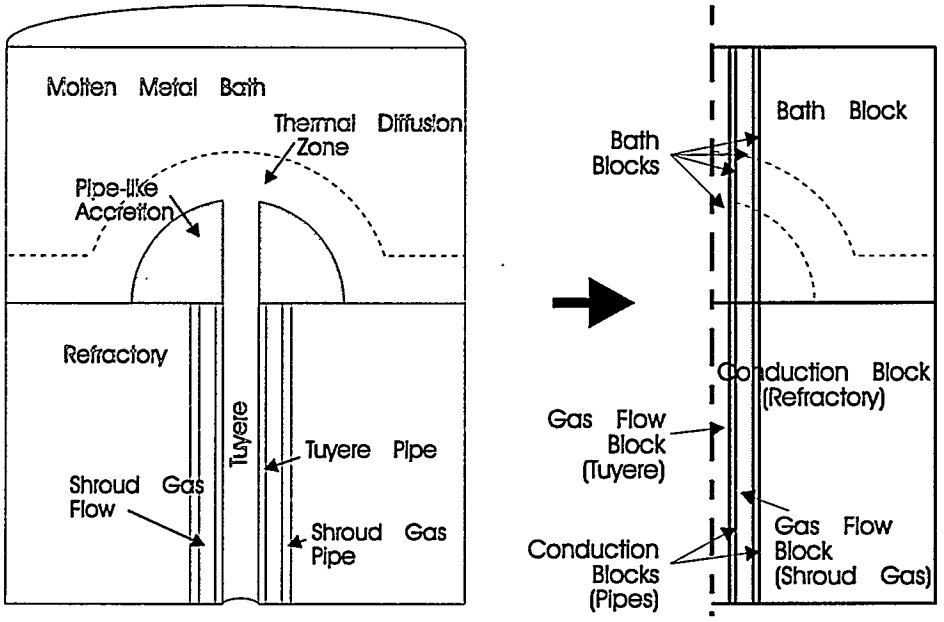

For capped accretions, the gas flow in the tuyere was modeled as 1-D compressible pipe flow with heat transfer and friction. Boundary conditions would carry heat to and from the refractory or pipe next to it, based on empirical formulations.

In the bath, the accretion was assumed to be made of homogeneous porous media. Its size and shape were determined from a contour through the metal temperature field, at the accretion surface temperature. Heat was transferred from the metal to the gas inside the accretion through a volumetric heat transfer coefficient. As shown in Figure 2.17 and Figure 2.18, a thermal diffusion zone was used to model the heat transfer from the accretion to the surrounding bath, as in Ohguchi and Robertson. Outside this zone, the bath temperature was assumed to be constant.

Modeling the pipe-like accretion from a shrouded tuyere was achieved through special boundary conditions, as illustrated in Figure 2.18. In this case, the 1-D pipe flow solution from the central flow of the tuyere into the bath above it was extended with appropriate boundaries. The height of this extension was set by the accretion in the neighboring block. For the time being, no gas flows were assumed to exist through the boundary between the pipe extension and the accretion.

Chemical reaction and radiation heat transfer models were also added for the special situation of a shrouded tuyere with oxygen as the central gas. Oxygen could react exothermically with the iron in the bath, creating a significant amount of heat, some of which would radiate down the pipe-like accretion and inner tuyere.

2.1.4.3. Formulation

Calculation of the accretion size and shape and the corresponding thermal diffusion zone is a moving boundary problem, requiring an iterative solution as demonstrated by the computational flow chart shown in Figure 2.19. This scheme involved alternating the solution of each of the block types, and updating the material properties and the boundary conditions that were used to communicate information between the blocks, until a steady-state convergence criterion was met. In addition, an inner iterative loop for bath blocks was employed to resolve the accretion boundary, assuring agreement between the gas and metal temperature fields.

Figure 2.19
Computational Flow Chart

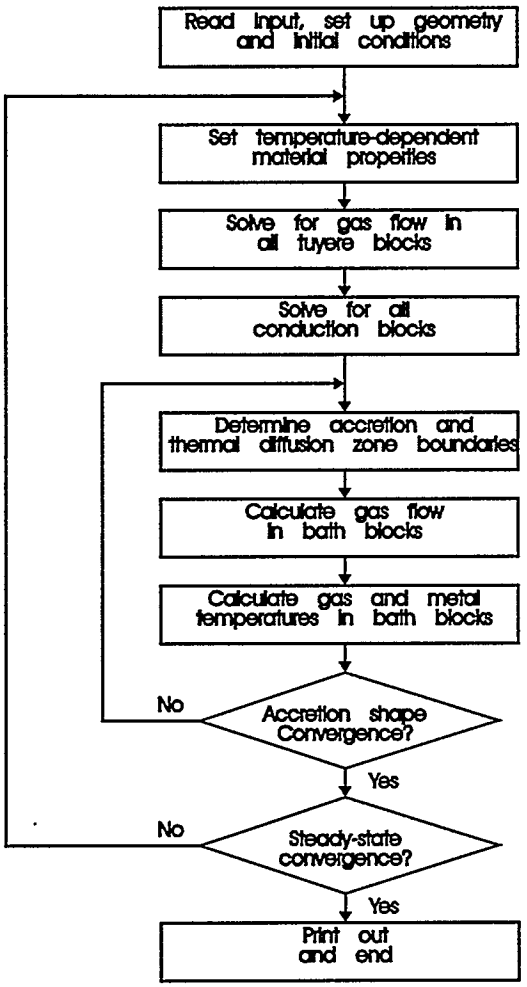

2.1.4.4. Conclusions

A model for simulating accretion in a CEP reactor has been developed and successfully tested. The model was used to calculate the accretion size and shape and the thermal diffusion zone. Simulation results from the MMT accretion model were consistent with data from Ohguchi and Robertson's work, hence verifying the model's accuracy. Simulation results from a shrouded tuyere example run are graphically illustrated in Figure 2.20. The figure shows temperature and pressure contours in the bath as a function of bath height (h) and radial distance (r) from the tuyere central pipe. The metal bath temperature is observed to decrease as r→0 and h→0 due to the cooling effect of the shroud gas as it exits the tuyere. The input parameters for this example included tuyere inside and outside diameter, cooling gas flow rate, thermal conductivity of the refractory and metal bath physical properties. As an illustration of the effect of the oxygen/iron chemical reaction and corresponding radiation heat transfer, similar results using this model are presented in Figure 2.21.

Figure 2.20
Results from a Shrouded Tuyere Example Run

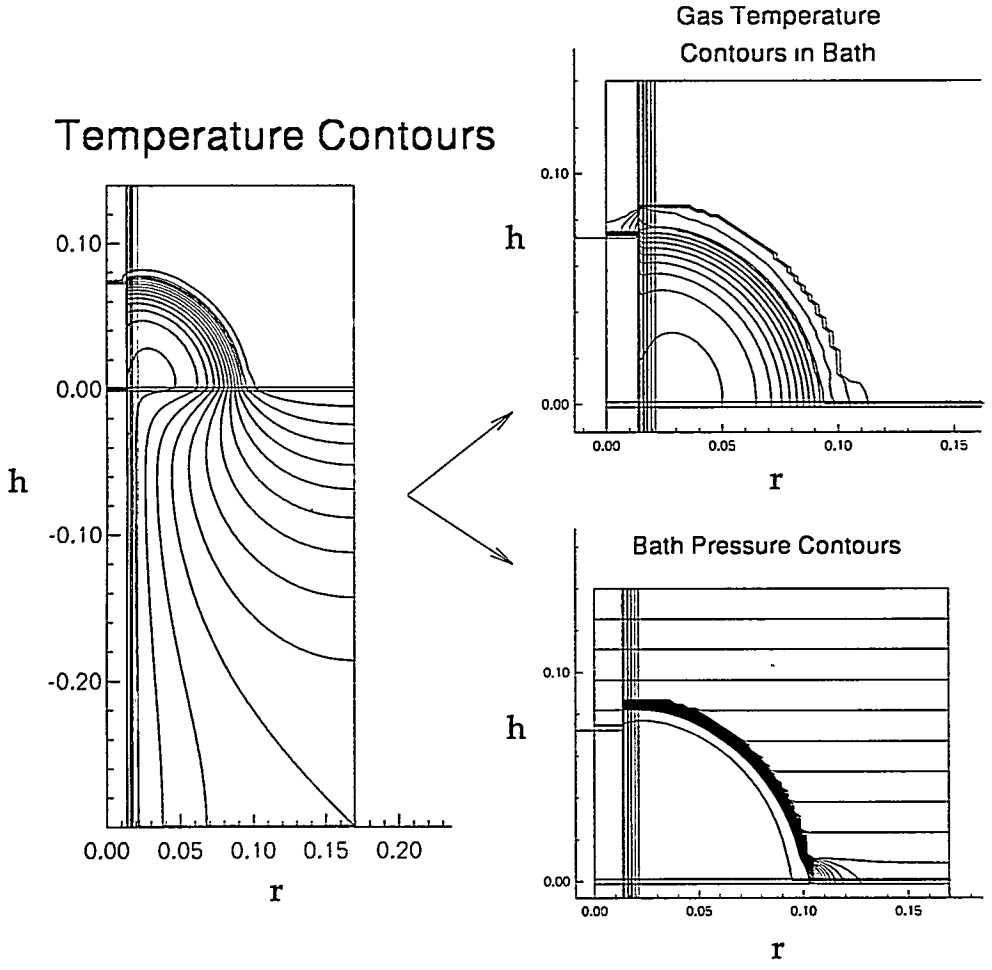

Figure 2.21
Results from a Shrouded Tuyere Example Run with Oxygen/Iron Reaction and Radiation Effects Included

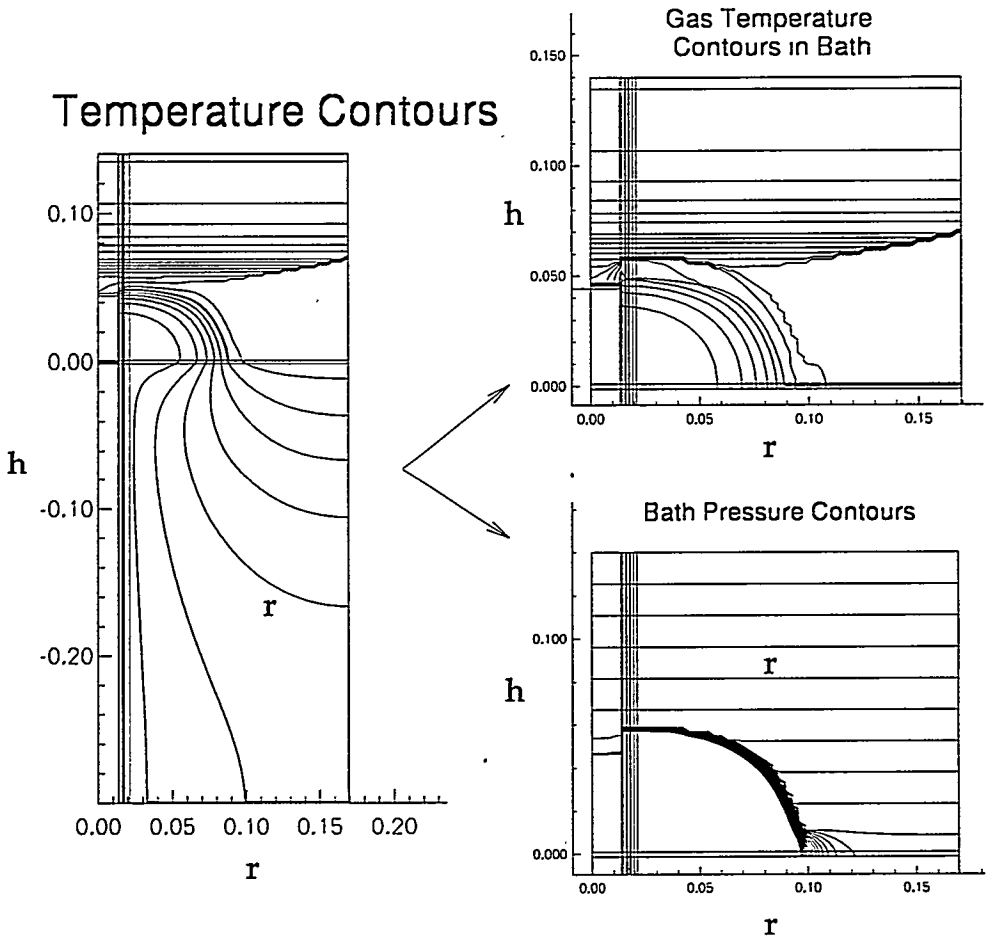

2.1.5. Bulk Solids Feed Literature Search

MMT conducted a literature search of solid injection techniques for metallurgical and other high temperature processes to determine their applicability to CEP processing of bulk solids. These papers provided insight into injector design, reactor geometry, process conditions, operational requirements, materials of construction, and cooling methods. A list of the pertinent papers identified during the search is presented below:

1. The EPRI Center for Materials Production, "Application of Plasma Technology in the Environmental Waste Processing Industry", CMP Report No. 92-5, July 1992.

2. US Patent No. 4,405,365, 9/20/83, "Method for the Fabrication of Special Steels in Metallurgical Vessels", E. J. Robert.

3. US Patent No. 4,750,716, 6/14/88, "Injection Lance", Michael C. Reeve-Parker.

4. WO Patent No. 91/05214, 4/18/91, "Top Submerged Injection with a shrouded Lance", Floyd, J. M.

5. US Patent No. 4,783,060, 11/8/88, "Immersion Lance", Erich Struzik.

6. US Patent No. 3,833,209, 9/3/74, "Apparatus for Refining of Steel", Yi-Chung Chang.

7. WO Patent No. 87/03010, 5/21/87, "Top Submerged Lancing Reactor and Direct Smelting of Zinc Sulphide Materials Therein", John Millice Floyd.

8. US Patent No. 4,854,553, 8/8/89, "Self-Shielding Lance", Michael D. Labate.

9. Brew, R. B. M. "The Britannia Bottom Blown Oxygen Converter." MIM Technology Marketing Ltd. (1992):

10. Engh, T. A., K. Larsen, and K. Venas. "Penetration of Particle-Gas Jets into Liquids." 6 (1979): 268-273.

11. Guthrie, R., H. Lee, and Y. Sahai. "On the Formation of Thermal Accretions ('Mushroom') in Steelmaking Vessels." (1992): 445-462.

12. Irons, G. A., and L. R. Farias. "The Influence of Lance Orientation and Gas Evolution on Particle-Liquid Contact During Submerged Powder Injection." 25.4 (1986): 297-306..

13. Irons, G. "Fundamental Design Issues For Gas and Solids Injection Into Molten Metals." I (1993): 261-272.

14. Irons, Gordon A. "Fundamental and Practical Aspects of Lance Design for Powder Injection Processes." (submitted for publication, 1991):

15. Jenkins, T. W., N.B. Gray, and H.. K. Worner. "Application of the Levenspiel Dispersion Model to Metal Flow in Pilot Plant WORCRA Continuous Steelmaking Furnace." 2.April (1971): 1258-1259.

16. Kandell, P. "Program Sizes Pipe and Flare Manifolds for Compressible Flow." .June 29 (1981): 89-93.

17. Koria, S. C., and K. W. Lange. "Development of Blowing Practice for Combined Top Blowing and Bottom Stirred Processes."

18. Kuzmin, A. L. et al. "Resistance of Oxygen Lances for Blowing Through Metals." 7 (1978): 603-605.

19. Kuznetsov, A. F., and L. Y. Nazyuta. "Role of the et in the Emulsification Process When Melting Steel in Basic Oxygen Converters." 5 (1976): 42-46.

20. Lakatos, T., L. G. Johansson, and B. Simmingskold. "Viscosity Temperature Relations in the Glass System SiO2-Al203-Na2O-K2O-CaO-MgO) in the Composition Range of Technical Glasses." 13.3 (June) (1972): 88-95.

21. Lee, C. K., J. H. Neilson, and A. Gilchrist. "Effects of Nozzle Angle on Performance of Multi-Nozzle Lances in Steel Converters." 6 (1977): 329-337.

22. Lee, C., H. Neilson, and Gilchrist A. "Scaling Effects in Model Testing of Efflux Characteristics of Steel Converter Lances." .No. 6 (1979): 274-284.

23. Levenspiel, O., Kunii, D., Fitzgerald, T. "The Processing of Solids Changing Size in Bubbling Fluidized Beds." (1968)" 87-96.

24. Madorsky, S. L. "Rates of Thermal Degradation of Polystyrene and Polyethylene in a Vacuum." 2.18 (1952): 133-156.

25. Okane, K. et al. "Process for Gasification of Solid Carbonaceous Material." U.S. Patent #4,388,084 (1983):

26. Pickering, S. J. et al. "New Process for Dry Granulation and Heat Recovery from Molten Bast-Furnace Slag." 12.1 (1985): 14-21.

27. Pickering, S. J. et al. "New Process for Dry Granulation and Heat Recovery from Molten Bast-Furnace Slag." 12.1 (1985): 14-20.

28. Prosvirin, K. S. et al. "Structure of the Reaction Zone When a Molten Mixture of Iron and Carbon is Blown with Oxygen from Below." 2 (1976): 57-60.

29. Ravella, A. "Use a Spreadsheet for Preliminary Reactor Design." .February (1993): 68073.

30. Sahai, Y., and R. I. L. Guthrie. "The Formation and Growth of Thermal Accretions in bottom Blown/Combination Blown Steelmaking Operations." I&SM .April (1984): 34-38.

31. Schnurenberger, E., and P. Gerber. "Steel Treatment in the Ladle by Injection Through a Slide Gate Nozzle." (1977): 22.

Area: Bulk Solids Feeding
Total No. of Abstracts Obtained: 149
Total No. of Papers Obtained: 29

2.1.6. Absorption Behavior of a Gas Jet Injected Vertically into a Metal Bath

2.1.6.1. Scope

This set of experiments was designed using the water-based physical models to perform gas breakthrough measurements. As has been established earlier, the physical models use water as a means to investigate hydrodynamic and thermodynamic effects of different variables in the molten metal system using a medium which allows feedback from visual and other means in an expedient and simple manner. Gas absorption in the bath was investigated using a combination of gas flow rates, tuyeres, and bath heights in the water models, with ammonia in water proving to be an excellent surrogate for the behavior of absorptive gases, such as oxygen, in a molten metal system.

The ammonia gas was found to break through a water bath when the level approached the momentum region of the tuyere-induced jet. This bath level is thought to mark the line of demarcation between the momentum and buoyancy regions of the ammonia absorption plume. Co-injection of nitrogen did not increase the required bath level to stop ammonia gas pass-through. The residence time distribution (RTD) of ammonia was found to move to the right in a non-linear fashion with increasing bath heights.

2.1.6.2. Apparatus and Procedures

Ammonia injections were performed in a 56 gallon water model with a given tuyere size and a triple concentric tuyere. Ammonia gas breakthrough was detected by an ammonia probe located at the bath's center axis. The bath RTD was measured by a conductivity probe submerged just below the surface of the bath. The conductivity probe, located in the center of the bath, was movable in a vertical direction.

The analog signals from both probes were measured and recorded by a LabView data acquisition system for post-injection analysis.

2.1.6.3. Results and Discussion

2.1.6.3.1. Absorption Behavior

The complete absorption of ammonia in water involved three distinct regions characterized by: the penetration of the ammonia jet, evolution of dissolved gas due to heat of absorption, and kinetic energy transfer to the water. This interaction is schematically shown in Figure 2.22.

Figure 2.22
Absorption of Ammonia in Water

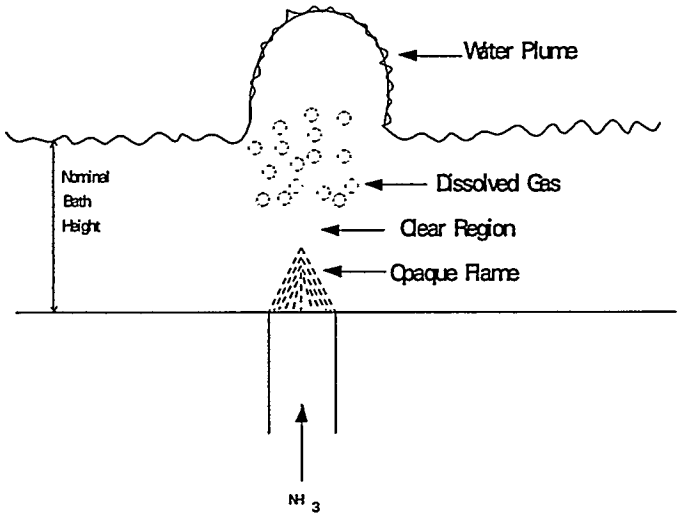

As the bath height was increased, the water plume decreased in height. A decrease in the bath height, however, caused a break up of the water plume on the surface, until surface sputtering subsequently resulted in ammonia breakthrough. Injections above an experimentally determined velocity (with sufficient bath height) produced an elongated reaction zone and a decrease in back attack by a factor of eight, relative to injections at fractionally lower velocities.

2.1.6.3.2. Breakthrough

Figure 2.23 shows the minimum bath height needed to prevent ammonia gas breakthrough as a function of tuyere injection pressure for a 1/4" tuyere. Note the discontinuity in the slope of the data after sonic conditions were established. Injections in the second annulus of a triple concentric tuyere (nearly the same cross-sectional area) had similar results.

Figure 2.23
Breakthrough vs. Gas Flow

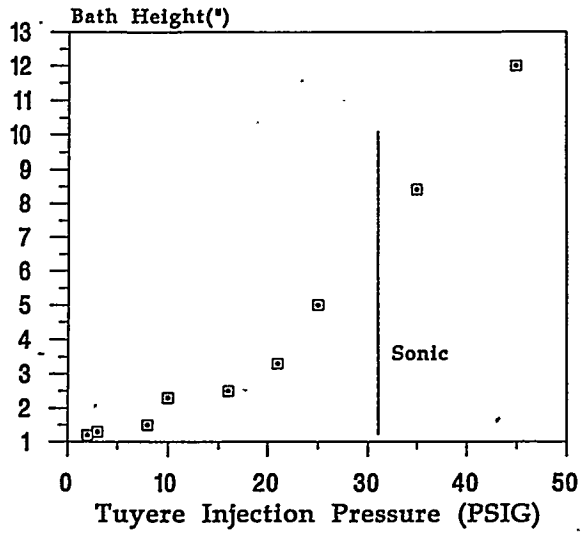

Continuing injections with a triple concentric tuyere (with ammonia in the second annulus), nitrogen was injected in the outer annulus and then in the inner annulus. Two ammonia flow rates were studied (sub-sonic and sonic conditions), with four nitrogen co-injection rates. Plotted in Figure 2.24 are the results. Analysis of the anomalies between the two flow rates indicated that there was no gas shrouding (from the outer annulus injection) or rapid absorption of ammonia (from the center annulus injection). Therefore, the rate of absorption of ammonia into the bath was not affected by the nitrogen flow injection point. However, up-stream (prior to injection) mixing of ammonia with nitrogen showed that 60% of the injections had a higher bath height than the annuli data as illustrated in Figure 2.25. Note the annuli data are the averaged data of both the inner and outer injections.

Figure 2.24
Outer vs. Inner Annulus N_2 Flow

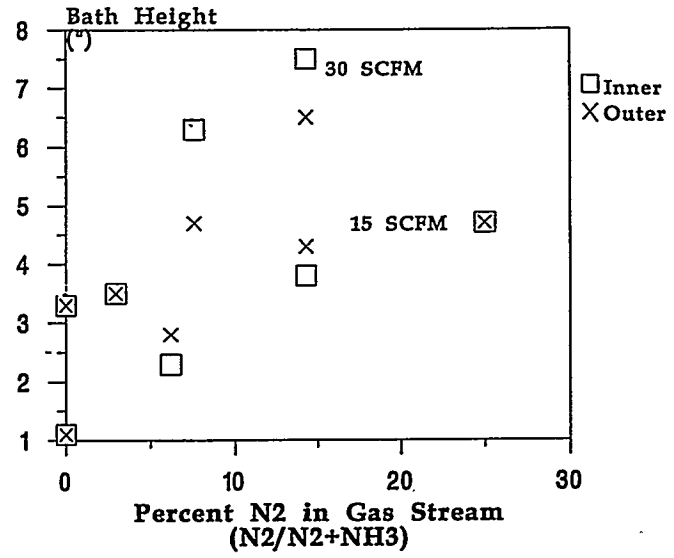

Figure 2.25
Annulus vs. Pre-Mixed N_2

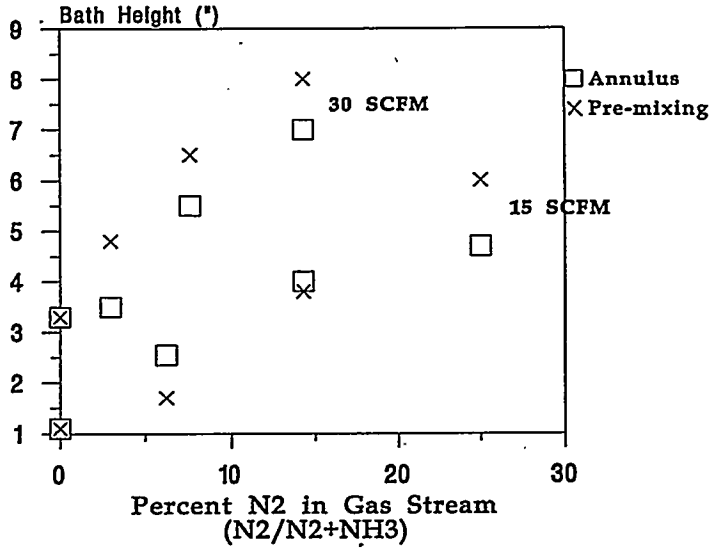

Figure 2.26 shows the combined results of Figure 2.23 to Figure 2.25 non-dimensionally. Plotted in Figure 2.26 is the percent of nitrogen in the gas stream versus the co-injection bath height divided by pure ammonia injection bath height. Under sonic conditions, there was little difference in the minimum bath height between N_2 annuli flow and pre-injection mixing. At sub-sonic conditions, the required water level to prevent breakthrough was approximately four times higher relative to sonic conditions. The

effect of pre- versus post-injection mixing of N_2 with ammonia was a function of the nitrogen fraction in the gas stream.

Figure 2.26
Relative Breakthrough

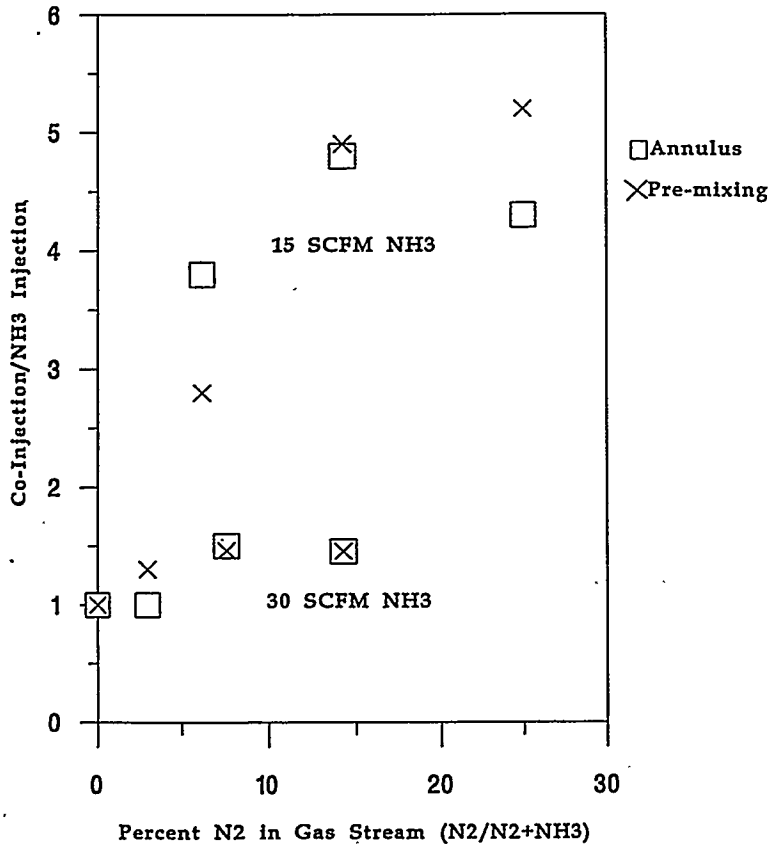

The length of the ammonia absorption zone was compared with the reaction zone of oxygen in a bottom-blown converter. Baptizmanskii developed mathematical relationships between the length of the reaction zone and the Archimedes criterion. The relation for the primary reaction zone in a bath with a carbon content of 1 to 3% is:

$$L = 1.66 Ar^{0.394} d$$

where L is the reaction zone, d is the tuyere diameter and Ar is the Archimedes criterion. The Archimedes criterion is the inertial force of the jet divided by the gravitational force of the water. Baptizmanskii used the Archimedes correlation:

$$Ar = \frac{4}{\pi} \frac{I}{\rho_\ell g d^3}$$

where I is the jet pulse (kg.m/s^2), ρ_ℓ is the density of the liquid (kg/m^3), g is the acceleration constant (m/s^2). This definition of the Archimedes criterion is equivalent to the modified Froude number divided by two. Making use of MMT's tuyere design models, where the Froude number was computed, the Archimedes number was experimentally determined for the absorption of ammonia in water.

A comparison of the experimental results with Baptizmanskii's relation is shown in Figure 2.27. The curve represents calculation results from Baptizamskii's empirically derived equation. The trends in the molten metal were similar to the water model results.

Figure 2.27
Archimedes Criterion Comparison

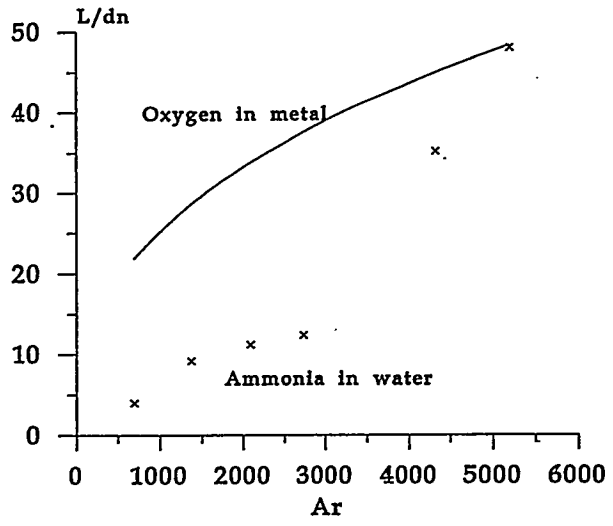

In addition, a comparison was made to an equilibrium relation at sonic flows developed by Faushe. He showed that the required length for complete ammonia absorption is:

$$Z = 12.5\,d\left(\frac{\rho_g}{\rho_\ell}\right)^{1/2}\frac{\Delta h}{\Delta T\,C_p}$$

where Δh is the heat of solution (J/Kg), ΔT is the temperature change (K), and C is the specific heat capacity (J/Kg.K). The flow dependence term in this relation cancels with the jet mass entrainment term. For the sonic injection of ammonia in water, the resulting distance for complete absorption was determined to be 4.23d.

2.1.6.4. Relevance to Molten Bath Processes

The water model results indicate that annular co-injection and pre-injection mixing (at sonic conditions) of nitrogen did not affect the absorption of ammonia into the bath. Therefore, molten bath breakthrough is dependent on shroud gas flow rate or position. Reaction with the bath cannot be mitigated by co-injection conditions. In addition, comparison of the ammonia interaction zone with that of oxygen in molten metal showed consistent trends, thus confirming the validity of water physical modeling.

2.1.6.5. Conclusions

1. Bath height needed to prevent breakthrough increased as injection flow rate was increased.

2. At sonic conditions in the tuyere, the type of nitrogen co-injection did not affect the reaction zone.

3. The length of the ammonia absorption zone was similar to the length of the oxygen reaction zone in metal, using an Archimedes criterion as a comparison.

4. RTD increases with bath height.

NOTE: pages 2-51 through 2-106 were removed because they contained proprietary information

2.2. Bulk Solids Feeding System Design and Evaluation

2.2.1. Dissolution/Volatilization Zone Characterization Studies for the Treatment of Bulk Solids

2.2.1.1. Introduction

A critical requirement in DOE's efforts to recycle, reuse, and dispose of materials from its decontamination and decommissioning activities is the design of a robust system to process a wide variety of bulk solid feeds. The capability to process bulk solids will increase the range of materials and broaden the application of CEP. The term bulk solids refers to materials that are more economically fed into the top of a molten metal bath than by submerged injection through a tuyere.

There are several reactor concepts for bulk feed processing being considered. Common to these concepts is the fact that they include multiple zones. A dissolution/volatilization zone (zone 1) and a gas polishing zone (zone 2). The reactor concepts differ primarily on the gas polishing zone, whereas the dissolution/volatilization zone is analogous for all the different reactor concepts. It is necessary to first characterize the dissolution/volatilization zone common to all the concepts. This characterization will allow us to determine the requirements for the second zone to be able to evaluate the potential success of the different designs. Thus, the efforts will initially be concentrated on characterizing zone 1. In addition, hardware development to test zone 2 for different concepts will be performed in parallel. A pilot-scale reactor at Fall River was utilized to perform this campaign.

Several experimental investigations have been performed in the past to study some of the reactor concepts for the gas polishing zone. The water model was utilized to study key parameters of zone 2 for the treatment of bulk solids. The reactor concepts investigated are the baffle, the reinjection of gases, and the lance.

Lance studies in the water model were performed to study the effects of process variables on system residence time, bubble characteristics and lance strains. Nitrogen, ammonia, and solid CO_2 pellets were used as feed materials in these tests. In the ammonia tests, the tuyere flow was the dominant factor affecting the time of residence; whereas for the solid CO_2 tests, the lance flow was the dominant factor. For the reinjection concept, the effect of eductor size and tuyere flow on the entrainment ratio (lb CO_2/ lb N_2) were studied. It was concluded that eductor size and tuyere flows determined the entrainment ratio. A preliminary study on the baffle concept was also performed. The objective of this test is to determine system parameters that allow the quickest processing of a bulk solid, with a steady bath level on both sides of the baffle.

2.2.1.2. Theoretical Background

In the continuous treatment of bulk solids in the CEP process, solids are fed to the molten metal bath (zone 1) where they are dissolved and/or volatilized at a rate that depends on their particle size, material properties and the conditions in the bath. The dissolution process can be mass transfer or heat transfer controlled. To characterize the volatilization/dissolution zone, it is important to determine the operability range of the reactor for a given feed material type, approximate size range and reactor conditions. The operability range is enclosed by the following limiting curves:

1. MAXIMUM POWER CAPACITY OF THE SYSTEM. In addition to the energy required by the operation of the reactor, the power source has to supply the sensible, latent and dissolution heat required to treat bulk solids. Thus, for a given power supply available, there is a maximum bulk feed rate possible.

2. MAXIMUM FEEDABLE PARTICLE LIMIT. This is a physical limitation based on the dimensions of the reactor and on the feeder system.

3. MAXIMUM GHT CAPACITY LIMIT. The maximum flow rate in the gas handling train (GHT) limits the bulk solids feed rate. The off-gas rate includes the stoichiometric amount of oxygen required to maintain a constant concentration (along with the natural gas required for cooling and the operational gas flow) and the off-gas generated from the volatilization of the feed material.

4. MASS OR HEAT TRANSFER LIMIT. During steady-state operation of the reactor, a given mass fraction of solids will be present in the system (i.e., loading). The loading depends on the feed rate, the mass of metal in the bath and the dissolution and/or volatilization time. The loading of the system increases when the feed rate is increased. To design a reactor to treat bulk solids, it is necessary to determine the maximum loading for a given set of operating conditions and feed types. In this section the relationship of the loading with the feed rate, the mass of the bath and the dissolution time will be obtained for mass and heat transfer controlled processes. The experimental portion of this study will provide information on the maximum loading and its dependence on the properties of the feed material and bath conditions.

2.2.1.3. Experimental Test Program

A series of experiments was conducted to determine the maximum feed rate for a given set of operating conditions and feed types. The campaign utilized feed materials which were surrogates of typical DOE waste components to determine the operability range for various CEP reactors. The operability range for a reactor can be represented in a diagram of mass flow rate versus feed size as shown in Figure 2.65. The diagram includes the operability limits discussed in section 3.2.1.2. The mass transfer limit is represented in this diagram. The operability limits have been determined through experimental testing. The GHT limit and the instantaneous volatilization limits depend on the fraction of volatile content in the feed.

Figure 2.65
Operability Limits for a Mass Transfer Controlled Process

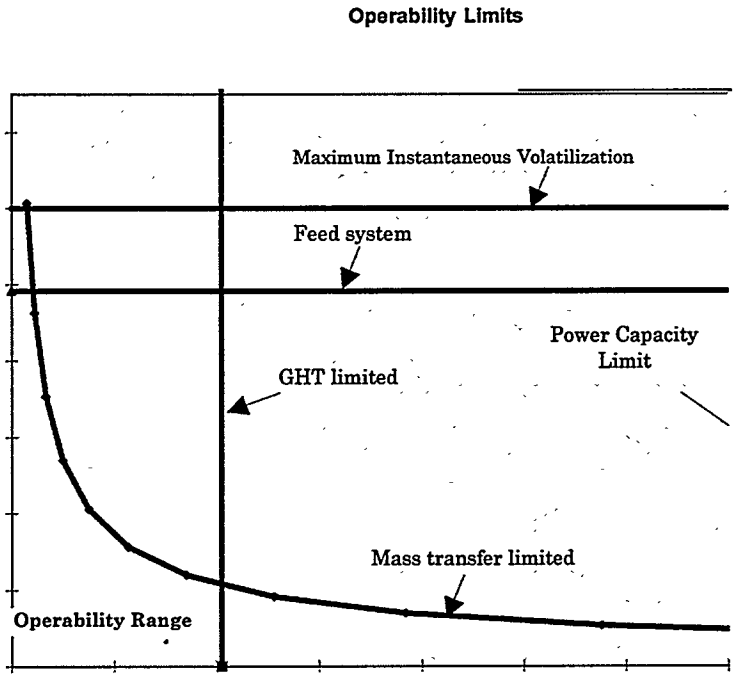

During steady-state reactor operation, a given mass fraction of solids will be present in the system (i.e. zone of influence), and the dissolution and/or volatilization time. The loading of the system increases as the feed rate is increased. Thus, the experimental campaign included a series of tests which determined the dissolution/volatilization time and the dependence of loading on feed rate.

2.2.1.3.1. Zone 1 Reactor Design Strategy And Application To DOE Surrogate Waste

The Zone 1 design equations have been correlated with experimental data and can now be utilized to determine the operating limits of a given reactor for different feed particle sizes. The operating window includes the mass transfer, power supply, feeding system size, instantaneous volatilization rate and maximum gas handling capacity limits. In Figure 2.65, the mass transfer limit is a function of the feed particle size. The GHT limit is obtained from the volatilization of the material.

Zone 1 design equations can also be utilized to determine the size of a given reactor for a required throughput. Table 2.27 contains a description of typical components of DOE surrogate waste that have been used to size various reactors. The materials are representative of the components of these waste materials.

Based on the dissolution results, the materials controlling the rates of metal dissolution ceramic phase dissolution have been identified. The highly volatile materials determine the gas handling train capacity. The larger size material determines the feeding system size and all the elements are included in the calculation for the power requirement for the processing of this feed.

Table 2.27
Typical DOE Surrogate Waste Components

Waste Component	Wt %	Characterization Size
Activated Carbon	5	~ 3"
Wood (4 x4, random lengths to 4 ft., simulated pellets)	15	4"
PVC (Pipe, Sch 40, 2-4" OD, Random lengths to 4 ft)	10	1/4"
Neoprene Rubber	3	N/A
Glass Beads (1/4" diameter)	5	1/4"
Sheet Metal, galvanized (crushed desks, ducts, cabinets)	15	5"
Mild Steel (4" width, random length up to 4 ft)	15	4"
Stainless Steel (Pipe, 3 to 4 ft long, 1 to 4 inch OD)	8	1/2"
Alumina Crucibles	7	N/A
Leaded Gloves	3	N/A
Water	4	N/A
Cement (Chunks: 4-12" diameter)	5	12"

2.2.2. Slurry System Design

The most efficient means to add certain physical forms to a CEP system is expected to include the use of a slurry system. Soils, sludges and ashes are among the types of feeds which may be mixed with some sort of slurrying liquid (contaminated fuel oil, alcohols, etc., partly chosen on a liquid waste availability basis) to form a suspension which can be pumped into a reactor via a tuyere or submerged lance. MMT designed a slurry injection test system consisting of an agitated tank with a grinder pump in a recycle loop. The grinder pump breaks up the agglomerates in the feed resulting in uniform suspension of particles in liquid.

2.2.2.1. Background

To determine the optimum conditions for slurry preparation and injection into a CEP® unit, the following experimental progression will be carried out with the finished test equipment:

- Bench scale slurry preparation tests
- Grinding pump tests
- Hot metal tests

2.2.2.2. Experimental Plan

Table 2.28 lists various aspects of the proposed bench-scale testing to be determined using the feed slate presented in Table 2.29. In this project, a solids loading range of 10-40% solids will be tested. As solids fraction is increased, the viscosity of the slurry increases, which is an advantage to CEP addition. The use of additives in order to stabilize the suspension will be assessed on an as-needed basis.

The combination of solids and liquids is dependent upon their compatibility. A guideline, should be obtained from the bench scale experiments. The criteria for solid-liquid combination should be:

- the chemical interaction between the solid and liquid components should be absent or minimum
- heat release due to mixing should be negligible
- total water content of the slurry should be minimized.

Table 2.28
Expected Information from the Bench-Scale Slurry Tests

Data	Method	Purpose/utility
a. Settling Rate	Moving Interface in a measuring jar	Stability of the suspension and how long the slurry can be stored
b. Agglomeration	Visual observation and/or particle size analysis	nature and stability of the suspension
c. Surfactants etc.	Use surfactants with a polar head and a hydrocarbon tail	Obtain the minimum concentration for stable suspension
d. Slurry Viscosity	Viscometer (as a function of RPM, i.e., shear rate)	Rheological behavior of the slurry; helps in estimating the transportation pressure drops

Table 2.29
Feed Slate

Description
Solids
polymers (15 %) water
60% water, 40% filter-pressed solids from wastewater treatment facility. 75% of solids is ash (30% of total weight).
Liquids
hexamethylene diisocyanate in 8-10% o-dichlorobenzene.
diisocyanateodicycloheyl methane in 15% o-dichlorobenzene.
75% methanol, 10% aniline, 15% water
ortho-2,3-toluenediamine
2,3 & 2,4 toluenediamine with 4% dichlorobenzene

Some of the issues to resolved and the assumptions made are shown in Table 2.30

Table 2.30
List of Assumptions and the Rationale

Issue	Assumption	Rationale
Feed Conditioning: Wet/Dry	Feed solids will be used as-is, i.e., wet.	Some volatiles may escape during drying
Mixing of Feed Streams	Do not intra-mix the solid streams and liquid streams.	The composition is not fixed and therefore characterization could be difficult if the streams are intra-mixing is allowed.
Wastewater sludge as the Benchmark	Sludge will be used in all the parametric sensitivity tests	Representative of wide variety of feed types.
Surrogate Liquid	Diesel will be used as the surrogate liquid.	Easy to handle.

Viscosity of the liquid is one of several factors that determines the need of additives; for the case of significant settling velocities, viscosity-enhancing agents may have to be added:

The stability could depend upon several variables. One of them is the thoroughness of mixing or dispersion. This variable could be dependent on the scale of experiments also. In fact, a comparison of the bench scale results with the slurry skid experiments can provide insight into possible scale-up effects. In a case of poor dispersion, the slurry tends to be less stable and may settle out quickly. This parameter, i.e., the characteristic time scale for this settling process, can be characterized by taking a sample and measuring the sedimentation rate. Stability of the slurry is also going to depend upon the agglomeration rate which could be sensitive to the composition of the surrounding liquid phase. Agglomeration rate tends to be reduced by non-polar liquids, because of low cohesion forces (surface tension) and low ionic strengths. If the suspension is the agglomerating type, stabilizing/emulsifying agents may need to be added. Stability of the suspension could also depend upon its wetting characteristics. If the liquid is non-polar and the solid-liquid system is non-wetting, surfactants may be required in order to stabilize the dispersion. If there is water present in these solids wetting of particles by diesel cannot be taken for granted, in which case emulsifiers, surfactants and/or stabilizing agents should be added. Both anionic type and non-ionic type surfactants need to be tested. These experiments focus on determining the optimum concentrations of surfactants for slurry stabilization and for cleaning purposes. These experiments should be preceded by chemical compatibility tests.

These answers should be determined from the bench scale tests and no significant scale-up effects are anticipated in this regard.

2.2.2.3. Slurry Skid Tests

A set of experiments will be conducted to demonstrate the capability to generate stable slurries that can be pumped through pipes without significant 'silting'.

For this purpose, the most suitable solid-liquid combination based on the bench scale data will be tested in the test skid. The system is basically a tank with a recycle loop with a grinder pump. The grinder pump helps in breaking up the solid agglomerates and in suspending the particles in the liquid. This pump is not expected to size reduce hard particles. The design is such that the grinder pump runs for about 15 min., achieving 3-6 passes; this time is expected to be sufficient to break up the agglomerates. If longer times are desired, a heat exchanger can be added to the circuit.

In order to determine the dependence of particle size distribution (i.e., a measure of the ease of solid agglomerate break-up), samples should be collected after 1,3, 5, 10 and 15 minutes of operation. Same samples can be used for sedimentation tests also. The other parameter that needs to be tested is the speed of the pump. These tests should generate a particle loading-grinding time-RPM-particle size-sedimentation rate matrix of experimental data.

These focus on slurry preparation aspects. The next issue is the slurry storage. Given enough time, the density difference between the solids and the liquid will result in phase separation. After turning the grinder pump off, under agitation and circulation, samples should be collected as a function of time. This data will help in designing injection skids for CEP® units; this experimental data will aid in determining the agitator power requirements in order to keep the solids suspended. This power requirement can be empirically estimated using published correlations such as the one suggested by McCabe and Smith[1]:

$$\frac{P}{g\rho_{sl}V_{sl}u_t} = \left(1-\varepsilon_{sl}\right)^{2/3}\left(\frac{D_t}{D_a}\right)^{1/2} e^{4.35\beta}$$

$$\beta = \frac{H-E}{D_t} - 0.1$$

where

P = power required

[1] McCabe, W.L. and J.C. Smith, 1976, "Unit Operations in Chemical Engineering, McGraw Hill, NY.

H = height (from the bottom) of the liquid column

E = Clearance between impeller and the vessel floor

D_a,D_t = diameters of the agitator and the tank respectively

ρ_{sl}, V_{sl} = density and total volume of the slurry

u_t = terminal velocity, cm/s (from sedimentation experiments)

ε_{sl} = volume fraction of liquid

The duration of each experiment will be limited by the heat accumulation effects. Both the grinder pump and the agitator dissipate heat continuously; in addition, heat may come from heat of mixing also. Based on the liquid medium volatility, an upper limit for slurry temperature should be set.

A brief description of the sample collection trap is given below.

2.2.2.4. Sampling

To understand the stability of the suspension and to obtain particle size distribution data, samples of the slurry need to be taken at various stages of the batch preparation process. For this, an on-line, simple trap design has been adopted; the sample collecting trap is basically a 2" pipe section of 50 cm length with two swagelok® fittings at each end. This trap is provided with two leak-tight quick-connects. A part of this sample will be sent for particle size analysis and the remaining will be used in settling tests. The data obtained will be compared with the data obtained from the bench-scale experiments described in the previous section.

The diameter of the trap should be such that particle deposition should be negligible. The two parameters that control this phenomenon are the residence time and the diameter of the trap. These parameters should be adjusted such that the settling length ($v_t\tau_r$), based on the particle deposition velocity, should be much smaller than the trap diameter: $D/(v_t\tau_r) \sim 100$. The settling velocity measured for feed particles is < 2 mm/min. in a medium of 0.05 g/cm-s viscosity. Based on a flow rate of 2 gpm, the diameter is 1.35 cm.

2.2.2.5. Slurry Feed Preparation Grinder Skid Program

The CEP system is designed to feed a wide range of heterogeneous waste materials. Liquid feeds can be injected via tuyere; solid materials, that can be milled into powders, have been pneumatically conveyed with an inert gas (nitrogen) for simplicity. Both methods have been successfully demonstrated on the commercial-scale CEP in Fall River Recycling-Research and Development Center for the variety of feeds.

Although pneumatic conveyance of solids is effective, MMT's experience has shown that tuyere-feeding of solids in a liquid slurry provides the most reliable syngas delivery. Previous injection trials at the MEFOS development facility in Sweden proved that MMT tuyeres are well-suited for reliable commercial-scale throughputs of slurries. The objective of this program is to demonstrate the commercial-scale preparation of slurries for tuyere injection into a CPU. The injectibility of the slurries will be verified by hot tuyeres injections into the Tuyere Testing Unit (TTU).

The solids selected for this test include:

- sludge (filter-pressed solids from wastewater treatment facility that are 60% water, 30% soil components, and 10% organic matter).
- toluene diisocyanate residue (polymer urea with 15 % water)

Diesel will be used in these tests as a surrogate for blendable hydrocarbon liquid wastes. Table 2.31 summarizes the grinder skid experimental plan aimed at optimizing slurry preparation conditions.

Table 2.31
Grinder Pump Experiments

Liquid	Solid		Grinding Time (min)	RPM
		%		
1. Diesel	Biosolids	10	15	6000
2. Diesel	Biosolids	20	15	6000
3. Diesel	Biosolids	40	15	6000
4. Diesel	Biosolids	Best	15	4000
5. Diesel	Biosolids	Best	20	6000
6. Diesel	TDI Residue	Best	15	6000

The grinder skid system is shown in the attached diagram Figure 2.66. The solids are manually charged into the holding tank and the liquids are pumped into the vessel. The slurry is pumped around a recycle loop with a grinder pump. The grinder pump helps break up the solid agglomerates and suspend the particles in the liquid. This pump is not expected to size reduce hard particles. The grinder pump will run for 15 to 20 min, achieving 3-7 passes. The grinding time is limited by the heat build-up in the liquid from the pump.

Figure 2.66
Slurry System Development Module Piping & Instrument Diagram

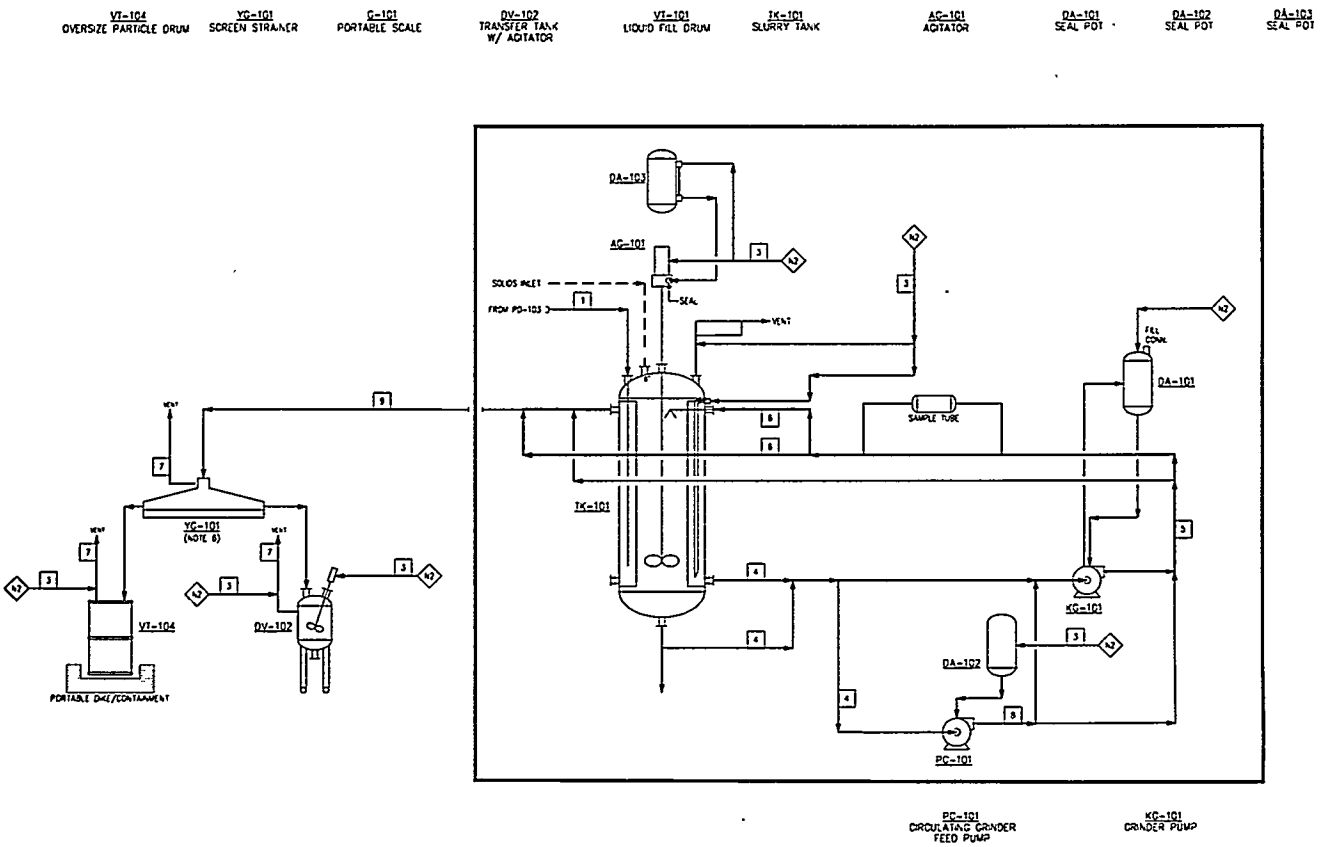

2.3. Bottom Tapping Pilot Studies

In order to fully realize the benefits of CEP application to DOE wastes, it is necessary to be able to efficiently remove the condensed phase products from the reactors. This report covers the development status of remote controlled tapping devices for removal of molten product from stationary CEP reactors. The tapping devices each comprise an induction coil and a susceptor pipe connecting the molten bath with a receptacle for the product. When the valve is in the closed state, the susceptor pipe is plugged with solidified product. Valve opening is achieved by activating the induction coil and melting the solid plug. Bottom tapping of metal using a tapping valve of this type has been successfully demonstrated on a semi-commercial scale.

2.3.1. Background And Objectives

The objectives of the Bottom Tapping Pilot Studies Campaign are the following:

- Demonstrate the operability of hot metal tapping on a semi-production scale, using an existing design for horizontal bottom tapping comprising an

inductively heated susceptor pipe containing a metal plug mounted horizontally at the bottom of the reactor.

- Provide tapping valve characteristics - timing and power - for the specific design.
- Provide data for tapping at various bath temperatures.

The intention was to demonstrate complete metal drain capability through the bottom valve mounted on the pilot scale reactor in a first phase. The results obtained in this phase of the work, comprising complete bottom drain of an 800 lb bath at 2,990°F and a 300 lb bath at 2,700°F are discussed below.

Based on the first phase work, the next step will be to demonstrate intermittent tapping of ceramic phase horizontally and metallic phase vertically on the pilot-scale reactor. The reactor will be equipped with two tapping valves allowing the reactor to be operated in the vertical position with a bottom drain capability and intermittent horizontal ceramic phase tapping capability. Tapping will be interrupted by using a slide gate system on the upper tapping valve. Placing the reactor in the horizontal position will allow testing of intermittent vertical metal tapping. This will provide characterization of valve-to-OPEN and valve-to-CLOSED transients for both valves.

2.3.2. Apparatus

The current-design bottom tapping valve installation is shown in Figure 2.67. The existing Fall River pilot-scale reactor design and bottom clearance dimensions are such that vertical bottom tapping is undesirable. The experimental valve was installed horizontally, which requires that the tapping pipe penetrate the APU-1 reactor main coil. This also led to the selection of a short coil and thus a low coil/pipe length ratio. The pipe extends through an eyebrow arrangement in the water cooled main reactor coil, creating a cold spot in the pipe and plug between the coil and the bath. The amount of power required to open the valve was precalculated and the procedure for opening the valve at the chosen bath temperature was established based on these calculations. The tapping pipe was equipped with six thermocouples as shown in Figure 2.67. The thermocouples were intended to provide on-line information on the temperature development from the steady state temperature profile to valve OPEN status.

Figure 2.67
Sketch showing the bottom tapping valve on the pilot-scale reactor.

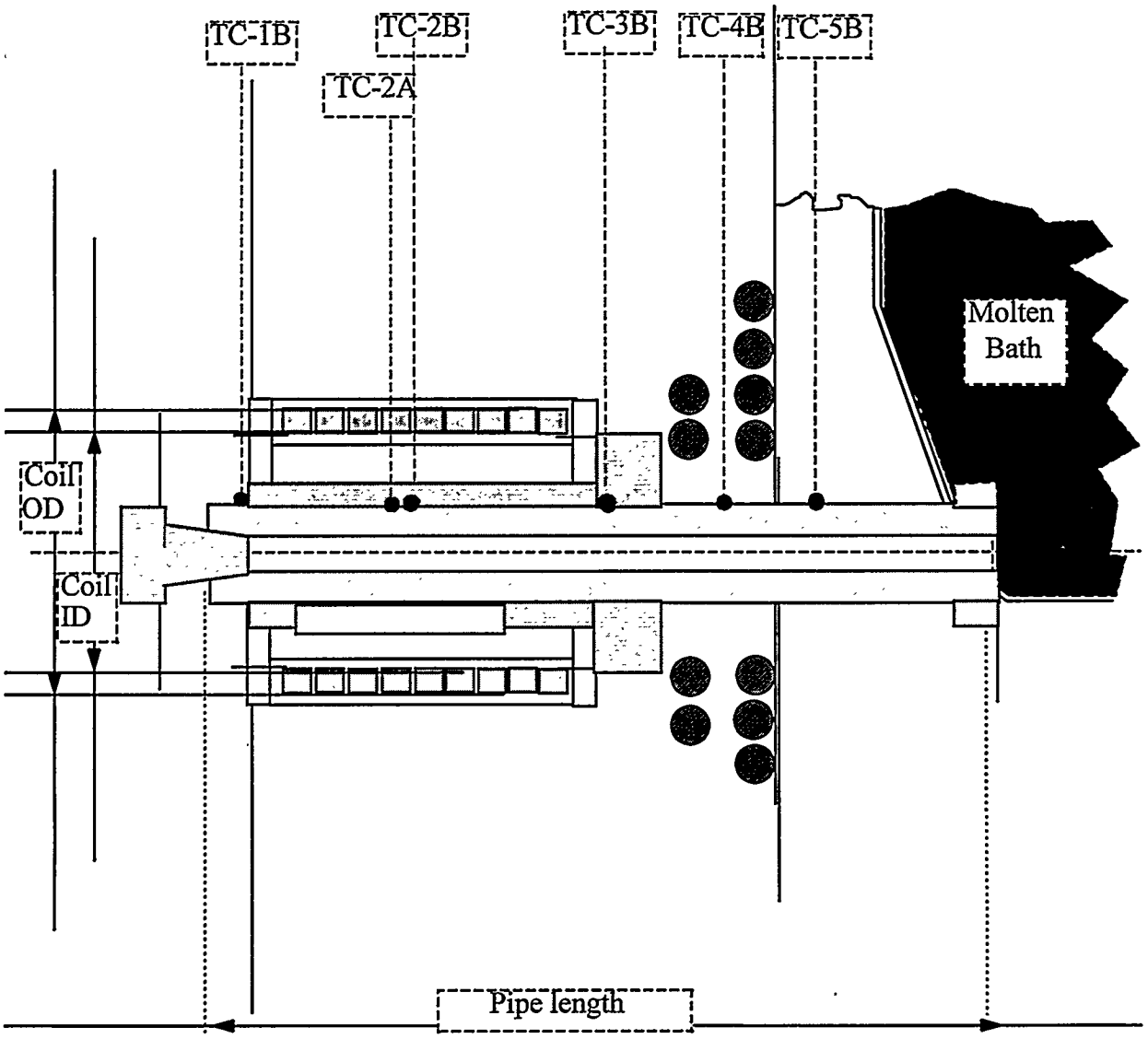

2.3.3. Tapping Procedure

The first run had two objectives. First, to verify findings from the 80 lb. Bottom Tapping Unit (BTU) on a scale of 800 lb. of molten metal (iron bath at 2,800°F, 3% carbon); second, to obtain data on the valve performance as a function of time and power applied to the valve induction coil.

The procedure for opening the valve was based on sequential activation of the valve coil. The susceptor pipe was slowly brought close to its maximum operating temperature of 3,200°F, at which point the power was switched off to allow the generated heat to dissipate axially before the next coil activation. The relatively slow heating was intended to protect the thermocouples.

The experimentally critical temperature readings were given by TC-2B located at the hottest point under the induction coil and TC-3B which provided reliable readings and gave information on the steady state temperature profile in the absence of accurate readings from TC-4B and TC-5B. The latter thermocouples were expected to monitor the coldest temperatures along the pipe but, owing to the thermal conductivity of the grout used to secure the pipe in place, in reality reflected the cooling effects of the main reactor coil.

Bottom tapping was accomplished after four heating cycles at a bath temperature of 1570°C. The metal was completely drained, leaving no residue in the reactor. The valve assembly and the seals between the crucible and tapping pipe were inspected after the run and found to be intact.

The second run aimed to verify that the tapping valve could be opened at a lower bath temperature and that the reactor could be fully drained starting from a lower metal level. The reactor was charged with 300 lbs of iron, 3% carbon, and tapping was initiated at a bath temperature of 1460°C. Based on heat transfer calculations, this bath temperature represented the lower bound for successful tapping, given the induction heating limitations and estimated thermal losses of the system. It was estimated that tapping could be achieved at a temperature 70 degrees below the metal liquidus temperature in the coldest portion of the pipe.

The induction coil was fired at full power, in five on/off cycles. Immediately after the fifth burst of power, hot metal started trickling out, indicating that the entire plug was molten and communicated the pressure differential to the pipe opening. The stopper was retracted and the 300 lbs of metal completely drained from the reactor. The tapping pipe was clean and free of metal after the tap.

The power delivered to the coil during the runs was estimated following two different routes. Estimate I was based on calculations of expected coil performance at assumed current levels ranging from 400 to 700A, the known useful energy delivered and estimated thermal losses. Estimate II was based on calculation of heat flows under the coil based on linearized approximations of dT/dt in the susceptor pipe during the power ON/OFF cycles.

2.3.4. Discussion

The pilot scale bottom tapping tests were successfully carried out at two bath temperatures and two metal charge weights. Remotely controlled bottom tapping of liquid metal without tilting the reactor was demonstrated on a pilot scale. In-house experience in the design and operation of induction heated tapping valves has been established.

2.4. Energy Addition Systems

2.4.1. Introduction

The standard method of energy addition to CEP reactors has relied exclusively on induction heating. In addition to being a non-contact source of energy, induction heating has been found to offer controllability and efficiency. Gas burners and resistance heaters have also been used for pre-injection operations such as pre-heating and initial metal charge melting. These systems have been optimized for use in R&D purposes, and thus may not prove to be the most economical in a commercial environment. A preliminary literature survey and analysis of energy addition systems have revealed the suitability of alternative sources of energy for specific CEP applications.

Plasma arc torches have been considered to offer an alternative heating method for CEP, but have not yet been developed. Potential uses of the plasma torch include primary heating of metal bath charges, pre-heating of the refractory brick materials, and the addition of supplemental heating to the horizontal extension section of a multi-zone CEP reactor. Before they can be applied to CEP systems, plasma arc torches have to be characterized with respect to controllability, efficiency, electrode component lifetime, and effect on refractory wear.

2.4.2. Objectives

The primary goals of the initial phase of the test plan are as follows:

1) Install a plasma arc torch system on a testing unit and complete hardware shakedown tests. The electrical, cooling, and torch gas systems will be installed, in addition to control logic and software development;

2) Define the operating envelope of the plasma torch system using nitrogen working gas. The impact of varying furnace conditions on the torch operating envelopes will be determined to improve its operability and controllability; and

3) Perform characterization and optimization tests after establishing the operability of the plasma torch. The goal of these tests will be to define how the torch should be operated to maximize operational stability and overall heating efficiency, while minimizing flow rate and excessive localized heating.

2.4.3. Experimental

Figure 2.68 shows the plasma torch test unit. The plasma torch was mounted vertically and aimed into a crucible containing a suitable metal charge to be melted. The off gas is from the test unit is directed to the tap/ceramic baghouse.

Figure 2.68
Plasma Torch Test Unit

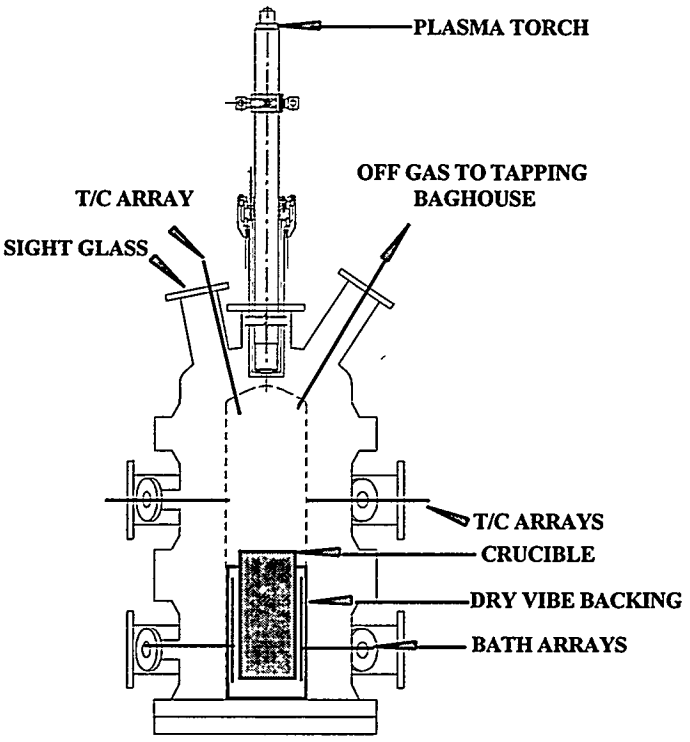

2.4.3.1. Preliminary Run Description

A commercial 150 kW plasma torch was acquired and installed on the test unit. The control software was also tested. After the operability of the PEC plasma torch had been established, preparations were made for the torch characterization and optimization phase. Because the plasma torch operates at high voltages, proper electrical grounding was practiced to prevent accidental electrical shocks. The torch was only operated in the non-transferred mode during this campaign. Proper grounding procedures and suitable electrical isolation and shielding were in place prior to start-up.

2.4.3.2. Torch Characterization Tests

The torch operating envelope (ranges of mass flux and torch current) for nitrogen working gas was explored. A typical torch operating map is illustrated in Figure 2.69. The independent variables are torch current and torch mass flux, which can be controlled by the process operator. Operating maps can be generated for different torch working gases and for different furnace pressures (and for different torch-to-melt distances when the torch is operated in the transferred arc mode).

Figure 2.69
Generic Torch Operating Map

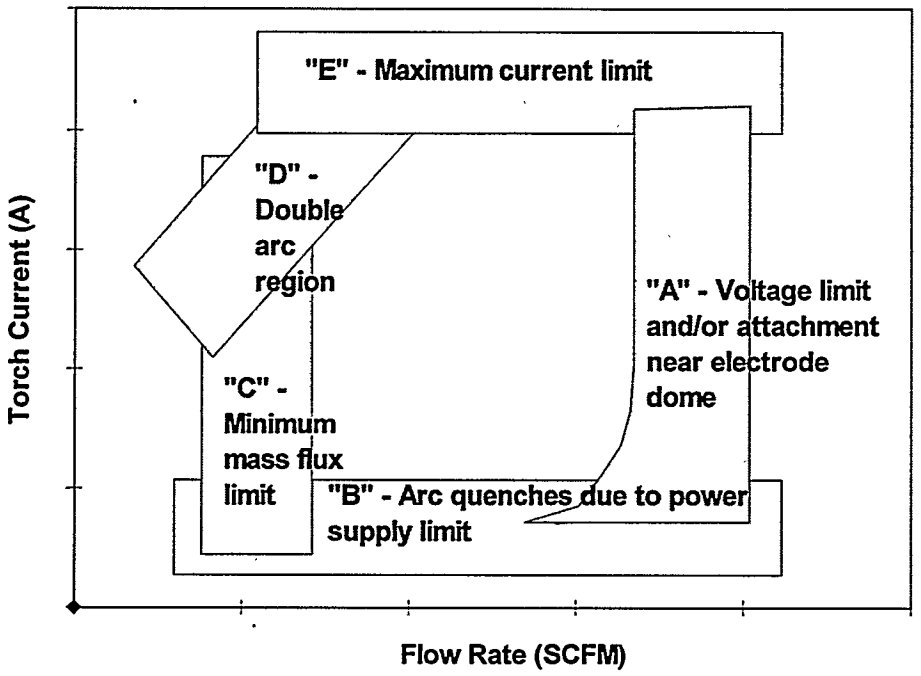

The boundary at the high mass flux end of the operating map (labeled "A" in Figure 2.69) arises from maximum torch-voltage limits. The torch voltage is not a parameter directly controllable by the operator. It is a strong function of the gas flow rate. Voltage also depends on the type of working gas and the furnace pressure. The operating voltage of a transferred-arc torch also depends on the torch-to-work piece distance. In general, the arc attachment location on the inside (dome) electrode moves rearward with increasing mass flux, as the sketch in Figure 2.70 shows. This rearward movement increases the arc length and the resulting arc voltage. The plasma torch maximum operating voltage limits are 500 to 750 volts.

Figure 2.70
Plasma Arc Torch

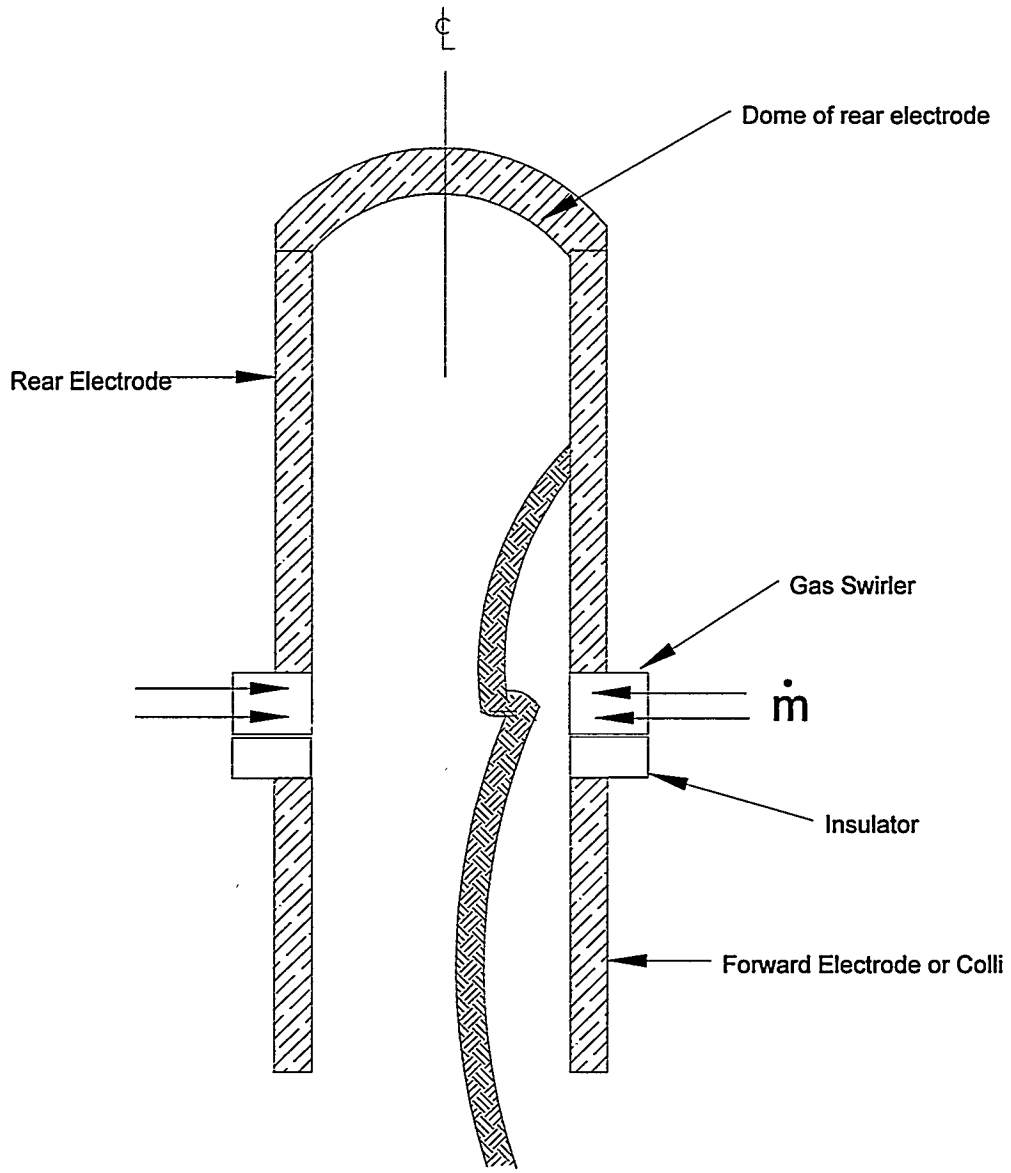

The boundary "A" can be defined by another factor. Under certain torch operating conditions, as the mass flow is increased the arc will reach the dome of the rear electrode before exceeding the maximum allowable torch voltage. When such condition occurs, further increase in mass flux will not result in higher voltage. The torch will start to make a hissing sound when the arc attachment point reaches the electrode dome. Continued torch operation at this condition will result in excessive local wear of the electrode. One can also use this constraint as a criterion to define boundary "A".

At boundary "B", toward the low current side of the operating envelope, arc quenching occurs due to power supply limitations. The current control circuits will stop

functioning at low currents and/or power. This boundary is horizontal if the limit is set for minimum current, while minimum power limit will result in a sloping boundary in Figure 2.69 and Figure 2.70.

The boundary "C," at the low mass flux side of the torch operating envelope, arises from constraints set by the torch developer. The manufacturer limits the mass flux in the 150 kW torches to no less than 2 sf^3/min. This constraint is necessary to prevent the arc-to-rear electrode attachment points from being situated too close to the gas swirler (see Figure 2.70 for torch geometry). This situation is undesirable for several reasons. First, the intense heating from the arc foot can damage the nearby "O"-rings, as well as the gas swirler itself. Second, this can complicate the maintenance and disassembly of the torch. During torch disassembly, a special wrench is inserted into the electrode bore for unscrewing the rear electrode from the electrode holder. The grip of this wrench is not adequate for electrode removal if there is excessive material wear near the lip of the electrode.

Torch operation at high current and low mass flux condition will increase the risk of double arcing. Increasing the arc current increases the diameter of the arc channel, the current-carrying part of the plasma gas. The arc channel is shielded from the metal segments of the torch by the outer (and colder) region of the swirling plasma. The thickness of this gas shroud is reduced at lower mass flow rates. Upon coming closer to the metal segments of the torch, the arc might find it energetically preferable to short-circuit through the torch body, as shown in Figure 2.71. Such double arcing usually destroys the torch elements. Boundary "D" in Figure 2.69 is used to prevent such double arcs from occurring during torch operations.

Figure 2.71
Double Arcing

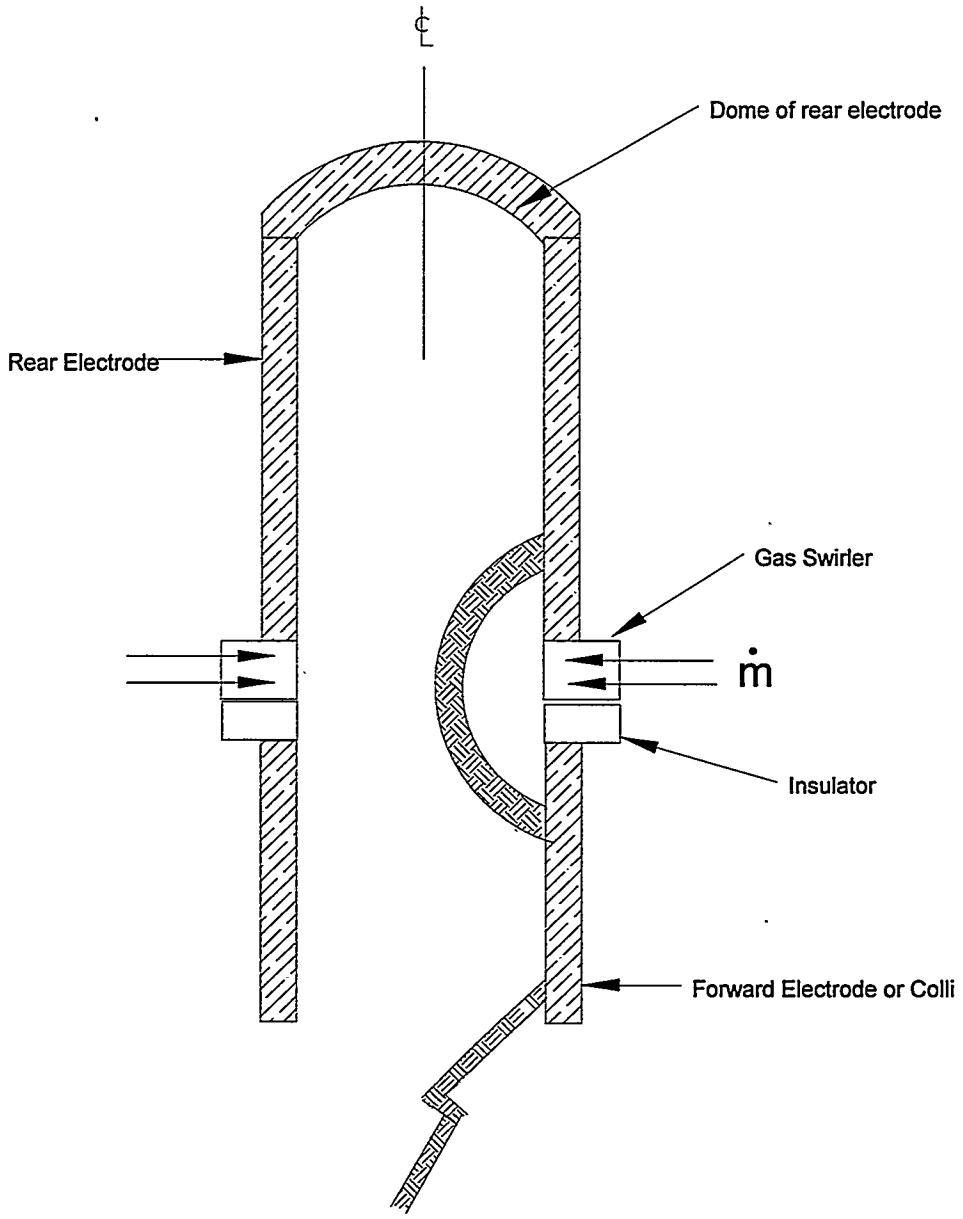

Boundary "E" results from the maximum current limits specified by the torch maker. Maximum current is 250 amps for our torch model.

How the torch operating envelopes vary with furnace operating conditions were to be determined during this experimental campaign. The torch operating boundaries described above will shift as furnace operating conditions are varied. Having a knowledge of how these boundaries translate, prior to adjustments to the furnace pressure or as the working gas is changed, will be invaluable to operate and control the torch during CEP operations. These operating envelopes are also useful for torch

ignition. Arc ignition can occur only under a certain combination of conditions and within a certain range of operating variables. Torch maps can provide the operators with such start-up information.

It is also possible to cross-plot onto these operating maps lines of constant torch voltage, torch power, torch efficiency, or other torch properties that are useful to the operator. This is illustrated in Figure 2.72. As mentioned above, the torch voltage and torch power are not variables directly controllable by the process operator. The torch voltage depends on the torch current (which is set by the operator) and the plasma resistance (which depends on many factors such as the type of working gas, the arc length, the temperature and surface conditions of the electrodes, the current density of the arc, etc.). From the torch maps, one can easily determine which combinations of operating variables to choose in order to obtain the desired voltage and/or power.

Figure 2.72
Generic Torch Operating Map

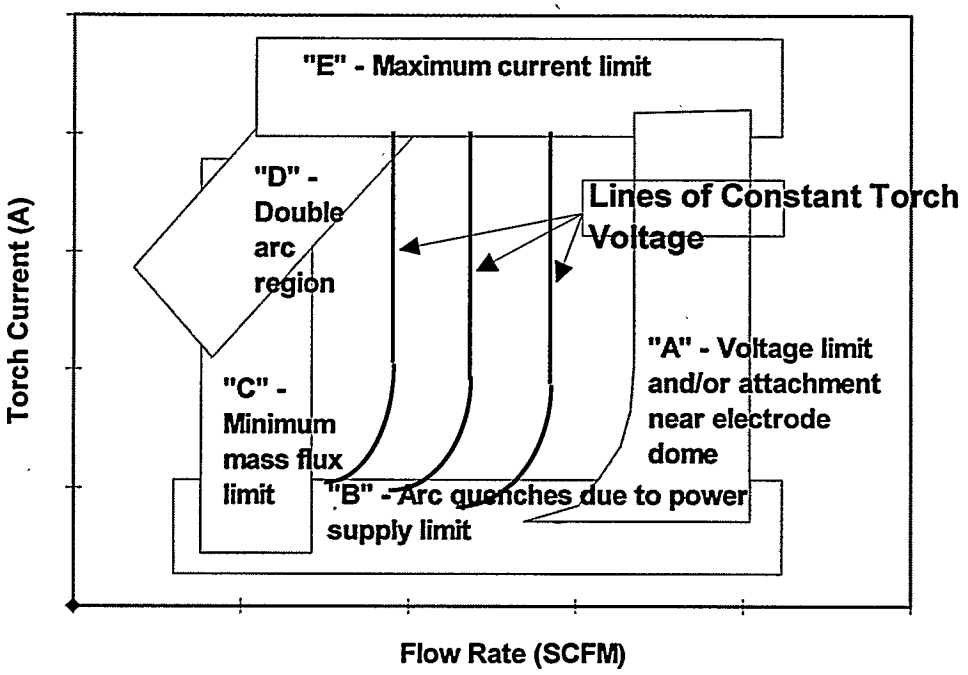

Torch characterization tests for nitrogen gas will be carried out. The torch efficiency and heat transfer efficiency to the metal bath will be determined as a function of operating variables. Instrumentation will be provided in the test unit in order to determine heat transfer from the plasma jet to the reactor walls and to the melt (see Figure 2.72). The power supplied to the torch and the cooling water losses will be determined, allowing a near complete heat balance to be established.

2.4.3.3. Optimizing Dilution Gas Flow

The optimum dilution gas flow will be determined for maximum overall heat transfer to the bath while minimizing localized heating. Special attention will be made to determine the surface temperature distribution on the refractory near the torch exit, as a function of the amount of dilution gas. Dilution gas is required to lower the torch gas temperature. Otherwise, radiation from the plasma jet may cause excessive localized heating. If too much dilution gas is used, then this limits the temperature differential between the gas and the metal bath will be limited, resulting in a lower overall heating efficiency. Excessive gas flow also lowers the gas residence time within the reactor, further reducing the heating efficiency.

2.4.3.4. Torch Efficiency

The factors that influence the torch efficiency will be identified. The torch efficiency (in the non-transferred arc mode) is expected to increase by elongating the arc length. This can be done by increasing the mass flow rate. The length of the rear electrode cavity can be increased and the swirler configuration can be changed.

The tangential component of the injected flow, which is a function of the swirler configuration, can have important influence on the torch efficiency. One of the effects of the swirl flow is to gradually mix cooler gas in with the body of the arc column. This provides a moderately high voltage gradient per unit arc length and tends to increase the total arc length. The vendor typically recommends different swirler configurations for different torch gases. The number of injector holes and the injector cross-section areas are different on the various injector designs to optimize the overall torch efficiency. Based on the manufacturer's recommendations, testing with alternate swirler configurations may be conducted.

Torch efficiency is also expected to decrease with increasing pressure. The sensitivity of torch efficiency to pressure will be addressed after the results from the initial tests at atmospheric pressure are completed

2.4.3.5. Other Torch Operation Issues

The feasibility of introducing powdered ceramic formers into the swirling dilution gas will be determined. Since plasma torches are very effective at heating powders, injecting finely divided ceramic formers into the plasma jet stream will help increase the heating efficiency of this material. In addition, the presence of particulates in the torch exhaust gas will help increase the radiative component of heat transfer to both the reactor bricks and to the crucible. Tests involving transfer arc mode of torch operation are not suitable for the proposed test unit. Torch tests with CO/H_2 as the working gas are planned for future trials.

2.5. Sensing and Monitoring Devices, and Control Methods

2.5.1. Introduction

Development of advanced models and techniques to monitor and control key process parameters is crucial to robust, automated CEP operation. Specifications for methods, equipment, and procedures have been developed for QCEP™ reactor control strategies. These specifications are limited to the Q-CEP™ reactor only, which consists of the molten metal bath and its containment system. Key parameters to be monitored for reactor control include bath temperature, headspace temperature, bath composition, bath level, bath pressure, containment, tuyere injection, and visual observation. Other QCEP™ subsystems have been included to the extent that they may impact reactor control strategies. Commercial, off-the-shelf equipment has been utilized to the maximum extent possible. Emphasis has been placed on the use of non-invasive techniques in order to minimize both the potential for interruption in the flow of operations and potential delay opportunities for feedback to optimize process control. A list of vendors consulted by MMT for this effort is provided a Table 2.32.

Table 2.32
Vendors Contacted for Sensing and Monitoring Devices Studies.

Thermocouples: NANMAC Corporation Heraeus Sensor Heraeus Electro-Nite Hoskins HY-CAL Engineering **Infrared Pyrometers** Williamson Corporation IRCON Accufiber Mikron Omega Quantum Logic Corporation IMPAC **IR Lightpipes** Sapphire General Ruby and Sapphire Co. Crystal Systems Insaco Saphikon Valley Design Quartz glass Heraeus Amersil Fiber Optics Pro-Optical Technologies Schott CeramOptec **High-Temperature Optical Fiber Thermometry** Luxtron/Accufiber **Suction Pyrometer** John Zink NANMAC Corporation Land Combustion	**TV Camera** J. M. Canty LENOX HITACHI IST Bass Electronics Metrovideo **Ultrasonic Thermometry** Thermosonics **Analytical** Extrel Fisons VTI Thermo Environmental Instruments **Dust Loading** Fireye Optimonitor Allen-Bradley Sensidyne MIE **Spectroscopy** American Hollographics Ocean Optics Graseby ALG Hellma **Level** VEGA CASI Magnetron Dynavision Kay-Ray/Sensall

2.5.2. Bath Temperature

2.5.2.1. Requirements

The primary objective of the bath temperature control strategy is to keep the bath molten and above a minimum acceptable temperature. This minimum temperature depends on the liquidus temperature of the bath and on possible accretion growth effects. A secondary objective of the bath temperature control strategy is to minimize changes of the bath temperature and operate at the optimum temperature to minimize containment wear.

In general, temperature should be controlled to ±50 °F. However, it may be important to be able to determine with a higher accuracy (e.g., ±10 °F) if a low or high level limit has been reached.

The bath temperature is controlled by adjusting the power setting of the bath induction coil power supply. Closed-loop control is required, with the controlled variable being the bath temperature and the controller output the power supply setting. The primary concern is to obtain a continuous, accurate, and lag-free indication of the bath temperature.

2.5.2.2. Primary Sensing Method: IR Lightpipe

The infrared (IR) lightpipe sensor is an in-situ, continuous, lag-free, and non-invasive temperature sensing method to measure bath temperature. Unlike embedded thermocouples, this sensor is not affected by refractory wear. Bath temperature measurement using a lightpipe was first demonstrated at MMT during 10 lb unit run in May 1995, and was subsequently demonstrated in the 4-Ton demonstration Unit in June 1995. Since then, bath temperature sensing using a lightpipe has been successfully demonstrated in various MMT units.

The lightpipe provides a path for the IR radiation from the molten metal bath to a dual-wavelength pyrometer. The lightpipe is in direct contact with the bath, which prevents the changing intervening atmosphere from affecting the operation of the top-mounted, dual-wavelength pyrometer. A lightpipe is a solid rod of material with high IR transmission characteristics. Application of a lightpipe to CEP reactor control involves significant material science considerations including IR transmissivity, melting point, chemical stability, and coefficient of thermal expansion. Cost is also an important factor in the selection of the lightpipe material. After extensive consultations with various vendors, MMT developed a design compatible with CEP operations that is shown in Figure 2.73. One end of the lightpipe is in contact with the molten metal; the other end is outside of the containment system.

IR emissions are collected by a reimaging lens or a terminated fiber optic cable and carried via a fiber-optic cable to a dual-wavelength pyrometer.

Figure 2.73
IR Lightpipe Schematic

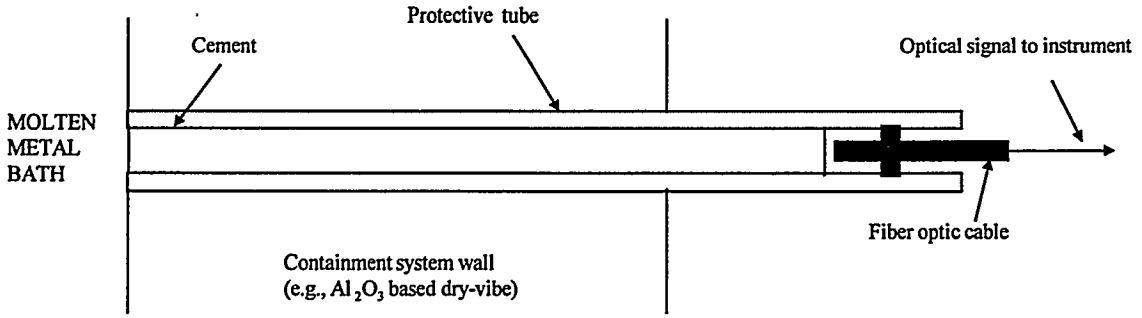

The feasibility of MMT's lightpipe rod was demonstrated in May 1995. Lightpipes were installed in two locations: the throat and the tuyere block.

As a result of the demonstration of the technical and commercial feasibility of this sensing method concept, it was decided to include provisions to install a lightpipe in the castable bottom blocks of the QCEP™ containment system. The location for the lightpipe is between the tuyere pipe and the containment wall. A detailed lightpipe sensor package for QCEP™ has been designed and was successfully tested in the demo unit.

Figure 2.74 shows a 24-hour window of automatic bath temperature control using a lightpipe measurement of the bath temperature for the PID process variable: Table 2.33 summarizes the status of the IR lightpipe sensing technique.

Figure 2.74
IR Lightpipe and Auto Temperature Control Results

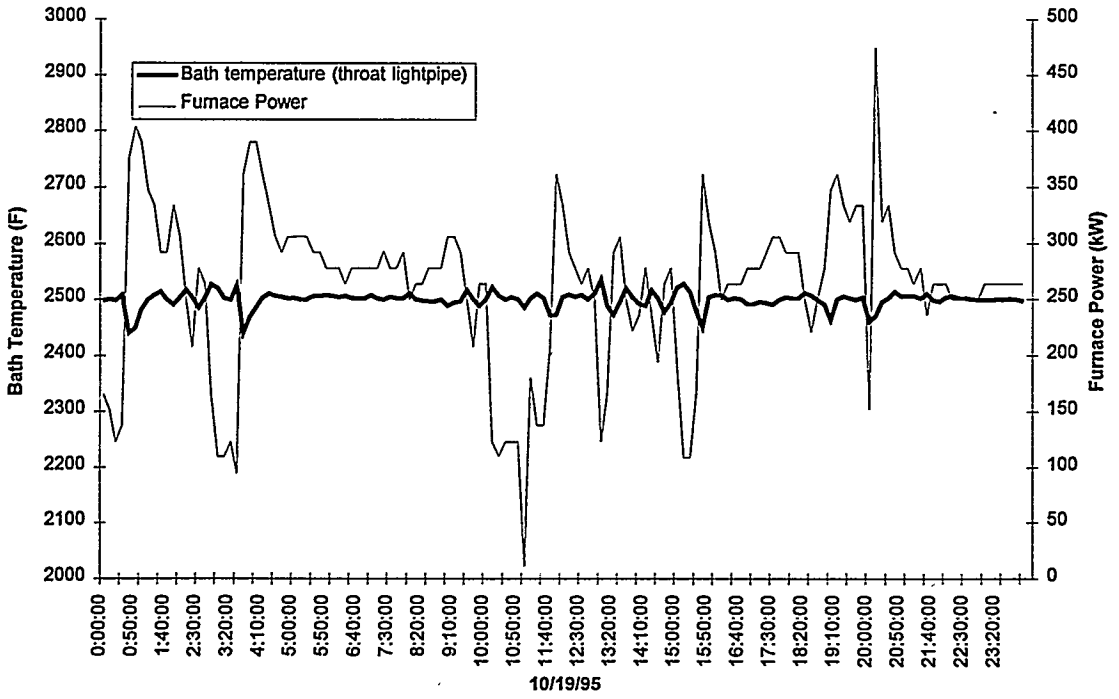

Table 2.33
Summary of IR Lightpipe Status

IR Lightpipe Status
A lightpipe installed in the throat section of the demo unit has provided more than 220 hours of service in a molten metal environment, and has survived three full cooldown/warmup cycles. Automatic bath temperature control using the lag-free lightpipe bath temperature measurement as the process variable has performed very well, providing tight bath temperature control (±50 °F from setpoint) for several days and under the presence of various perturbations (reaction ON/OFF, metal adds, etc.) A lightpipe package has been designed for QCEP and successfully tested in the tuyere block of the demo unit. The QCEP™ lightpipe package installed in bottom blocks will be tested after a redesign of the demo unit bottom plate system is finalized. This redesign was necessary to provide a straight path through the bottom plate for the lightpipe rod.

2.5.2.3. Contingency Sensing Methods

2.5.2.3.1. Embedded thermocouples plus CET model

This is a proven sensing method for bath temperature prediction and has been used successfully several times in Fall River units. The bath temperature is estimated using a embedded thermocouples measurements and a temperature model (Compensated Embedded Thermocouple (CET)).

Figure 2.75 shows a 24-hour window comparison between the bath temperature predicted by the CET model and the bath temperature measured by an IR lightpipe (see section 3.2.1). The CET model prediction "lags behind" the bath temperature by approximately 20 minutes in this example.

Figure 2.75
CET Bath Temperature Results

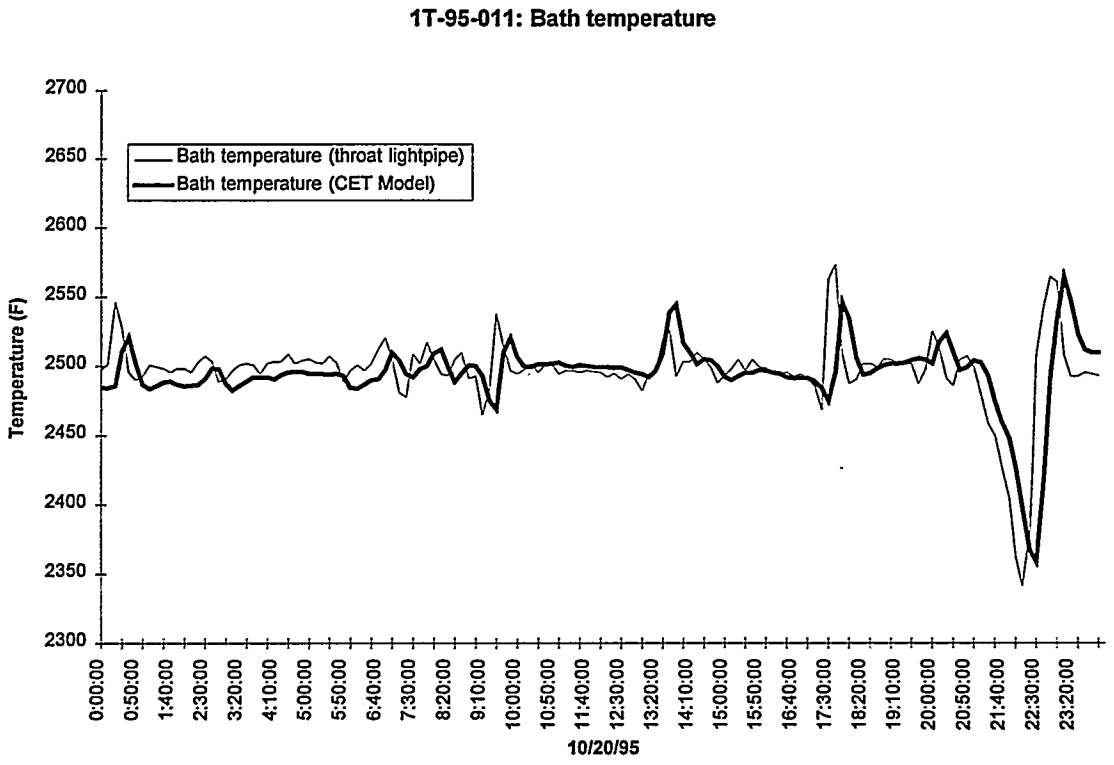

Disadvantages of this method include the need for periodic calibration to compensate for refractory wear, reliability of individual thermocouples, and unavoidable lag between the predicted temperature and the actual bath temperature.

The design basis for QCEP includes two arrays of four thermocouples (B-type) each installed in the castable bottom blocks. Thermocapable spacing is a compromise

between low lag and ability to maintain temperature control after 4" to 5" of refractory wear in the bottom block section. The arrays are 180 degrees from each other. The array radial location is between the tuyere and the crucible wall. This location is expected to minimize unwanted effects such as accretions and end effects. Thermocouples wires exit straight through the bottom plate to minimize failures.

Embedded Thermocouples Plus CET Model Status
The CET model has been tested successfully several times in the demo unit using throat and tuyere thermocouple arrays. A CET software module of commercial quality has been developed. The module includes features such as easy configuration, digital filtering, sensor diagnosis, automatic rejection of bad sensors, self-tuning, and automatic refractory wear correction. Closed-loop temperature control was successfully demonstrated in run 1T-95-001 using tuyere thermocouple arrays. Simulation and open-loop response test was used to tune the PID loop. Embedded thermocouples arrays in bottom blocks will be tested after a redesign of the demo unit bottom plate system is finalized. This redesign is necessary to provide a straight path through the bottom plate for thermocouple wires.

2.5.2.3.2. Dual-Wavelength Pyrometer

A dual-wavelength IR pyrometer with a fiber optic cable and a reimaging lens installed on top of the reactor vessel, looking at the bath surface through the sightglass port, may be used as an independent measurement to calibrate the embedded thermocouple model. The presence of a ceramic phase and/or dust may affect this temperature sensing technique.

Dual-Wavelength Pyrometer Status
The concept has been demonstrated with an IRCON unit in the demo unit several times under no dust conditions. A dual-wavelength pyrometer from Williamson with a fiber optic cable and reimaging lens was tested in run 1T-95-004[52]. The performance of this pyrometer was similar to the IRCON. May provide a reference temperature to calibrate the CET model or the IR lightpipe under purge mode.

2.5.2.3.3. Temperature Sampler

Provisions for high accuracy, discrete temperature sampling system has been made in the QCEP design. The sampler is being designed and will be installed in a 8" penetration on the reactor headspace. This intrusive sensing method allows temperature sampling using a reusable temperature probe. The concept is similar to the Electronite temperature measurements routinely used in Fall River units.

The temperature sampler should provide an accurate reference temperature to calibrate the other continuous temperature sensing methods.

2.5.2.3.4. Energy Balance Model

An energy balance model provides a prediction of the bath temperature based on feed and power input measurements and an accurate estimate of heat losses. The energy balance model can be kept calibrated with the primary continuous temperature sensing method and used as a contingency.

2.5.2.3.5. Other Bath Temperature Sensing Methods Considered

A number of alternate bath temperature sensing methods were considered, including high temperature Optical Fiber Thermometry (OFT), side-wall thermocouple plugs, suction pyrometer, TV camera with image analyzer, millimeter wave pyrometer, ultrasonic thermometry, and optical fiber continuous feed. Evaluation of these technologies will continue as most show promise for potential application to CEP reactor control.

2.5.2.4. Control Strategy and Automation

2.5.2.4.1. Melt Control

The charge temperature during heatup can be monitored by embedded thermocouples arrays, the top-mounted dual-wavelength pyrometer, and the IR lightpipe. The headspace temperature can be monitored by the headspace embedded thermocouple arrays and the upper susceptor dual-wavelength pyrometer. The pyrometers do not start reading until the target temperature exceeds 1700 °F. Below this temperature, the only instruments available are embedded thermocouples.

Power settings will be provided to operators. A melt model will be available to monitor progress of the melting procedure and compare predicted with actual temperatures.

A top-mounted color TV camera will provide images of the charge so operators can observe the onset of melting and perform power adjustments as appropriate to ensure a smooth melt.

As more experience is gained with QCEP™ melting, the melting procedure will be automated. An AUTO MELT module will automatically control the power supply with

a pre-established power sequence and compare expected temperatures with measured temperatures. If the module detects a discrepancy, it will stop the AUTO MELT procedure and issue an alarm so the operator is notified that there could be a problem. The details of the AUTO MELT module are currently being defined.

2.5.2.4.2. Bath Temperature Control

The temperature of the molten bath can be monitored by the IR lightpipe, the CET model, and, when the system is not in reaction mode, by the top-mounted dual-wavelength pyrometer. It is assumed that the temperature sampler will be available to take periodic samples of the bath temperature.

The first choice to monitor bath temperature is the IR lightpipe. This sensor has no lag and requires no adjustment for refractory wear.

In the event that the IR lightpipe is not functional, the second choice is the CET model. This method has a lag and requires periodic adjustments to compensate for refractory wear. The CET model is designed to automatically reject bad thermocouples and for bumpless transfer when the lead model is no longer functional due to thermocouple loss. The reference temperature to periodically calibrate the CET model can be obtained from the temperature sampler. If the system is not in reaction mode, an additional reference temperature can be obtained from the top-mounted dual-wavelength pyrometer.

As demonstrated in the demo run, the bath temperature can be controlled automatically with a PID loop. One PID loop should be implemented in the PLC with the IR lightpipe output as the process variable, and another PID loop should be also implemented in the PLC with the CET model as the process variable. The tuning constants will be different for both PID loops, with the IR lightpipe loop providing tighter control due to its reduced lag.

The temperature setpoint will be established at a predetermined increment above the liquidus temperature. A simple control strategy is proposed, with only two temperature setpoints. The first setpoint corresponds to the liquidus temperature of the charge. The second setpoint corresponds to the liquidus temperature at saturation. This choice of temperature setpoints represents a conservative temperature control strategy.

2.5.3. Headspace Temperature

2.5.3.1. Requirements

The primary objective of the headspace temperature control strategy is to avoid skulling (i.e., solidification of molten metal in headspace walls.)

A secondary objective of the headspace temperature control strategy is to avoid condensation of volatile radionuclides present in the off-gas. However, the condensation temperature of these radionuclides is rather low.

The headspace temperature is controlled by the temperature of the upper section of the reactor crucible. This section heated by an inductive coil. The wall temperature is adjusted by manipulating the headspace inductive coil power supply setting.

2.5.3.2. Primary Sensing Method

2.5.3.2.1. Side-Mounted Pyrometer

A side mounted pyrometer with sight glass and sight tube through induction coil measures the outside wall temperature.

Side-Mounted Pyrometer Status
This sensing method was demonstrated using a dual-wavelength pyrometer and a single-wavelength pyrometer in a 10 lb. unit[17].
A dual-wavelength pyrometer is recommended to minimize effects of changes in target conditions and intervening atmosphere.
A fiber optic link is recommended to minimize radiation damage to pyrometer electronics.

2.5.3.3. Contingency Sensing Methods

2.5.3.3.1. Embedded Headspace Thermocouples

One array of two type-B thermocouples embedded in headspace refractory. This system was designed to allow in-situ removal and replacement of the thermocouple array. This concept has been demonstrated in the 4 ton demo unit.

2.5.3.3.2. Thermal Model

Calculates the headspace temperature distribution based on the wall temperature, the bath temperature, and the bath spout. A preliminary model has been developed.

2.5.3.4. Control Strategy and Automation

The headspace temperature can be monitored by the susceptor temperature indication and the embedded thermocouple array. An on-line model will estimate the headspace surface temperature based on the embedded thermocouple readings. The upper susceptor power supply will be adjusted to maintain the desired headspace temperature. This process may be automated with a PID control loop.

2.5.4. Bath Composition

2.5.4.1. Requirements

Composition control in CEP reactors is typically used to maintain the desired off-gas quality, maintain the desired ceramic phase properties, and to ensure that the bath chemistry is compatible with the containment system.

In CEP reactors with a Fe-C molten bath, composition control is mainly achieved by carbon concentration control. Several non-invasive carbon control methods have been developed at MMT for this binary system and used in Fall River units

2.5.4.2. Primary Sensing Method

The bath composition is controlled mainly by off-gas characterization plus a thermodynamic model. Oxygen flow is adjusted to keep the bath composition within the desired range.

2.5.4.2.1. Off-gas Characterization: Mass Spectrometer

Initially the process gas analysis requirements for Q-CEP™ were defined as requiring only characterization of CO and CO_2 in the offgas. As the design progressed and various alternative operating strategies were introduced to accommodate new containment system designs, it was clear that increased flexibility was needed. This led to the conclusion that a design based on the use of discrete gas analyzers was neither cost effective nor flexible enough to satisfy changing project requirements. As a result the use of a mass spectrometer was considered. A mass spectrometer provides the flexibility to adapt to changing design requirements, and it is therefore the recommended solution.

2.5.4.2.2. Thermodynamic Models: The CO/CO_2 Ratio Model

Conditions of high oxygen potential in the bath lead to FeO formation. To avoid FeO accumulation, enough carbon must be present in the melt so that oxygen will preferentially react with carbon to form CO and CO_2 instead of FeO. In other words, the bath oxygen potential must be kept below that required to form FeO.

The CO/CO_2 ratio model is based on the reaction:

$$\underline{C} + CO_2 = 2CO$$

At very low, relatively constant carbon mole fractions x_c, this ratio is directly proportional to bath carbon based on equilibrium at the bath surface:

$$\frac{P_{co}}{P_{co_2}} = \frac{K(T)\gamma^{*}_{c} x_c P_T}{P_{co}}$$

where P_{co} and P_{co2} are the partial pressures of CO and CO_2, P_T is the total pressure, K(T) is the equilibrium constant, and γ_c^* is the activity coefficient, assumed constant since operation is confined over a very short range of carbon concentrations. P_{co} is assumed constant, since $P_{co2} << P_{co}$ and changes are below 10%. Assuming that all excess oxygen feed goes to CO, a material balance on carbon shows that the change in x_c is proportional to the excess oxygen flow rate. Combining these two effects, the change in the oxygen flow rate is found to be inversely proportional to the change in excess oxygen flow rate.

Assuming thermodynamic equilibrium, the predicted CO/CO_2 ratio or predicted dissolved oxygen depends on carbon percentage as shown in Figure 2.76. According to this thermodynamic relationship, the CO/CO_2 ratio could be used as an indicator of oxygen potential in the bath. As the CO/CO_2 ratio decreases, the likelihood of FeO accumulation increases. A bath composition control strategy could be based on maintaining the CO/CO_2 ratio above a certain value by adjusting the oxygen flow through the tuyere.

Figure 2.76:
CO/CO_2 ratio and dissolved oxygen vs. %C in bath

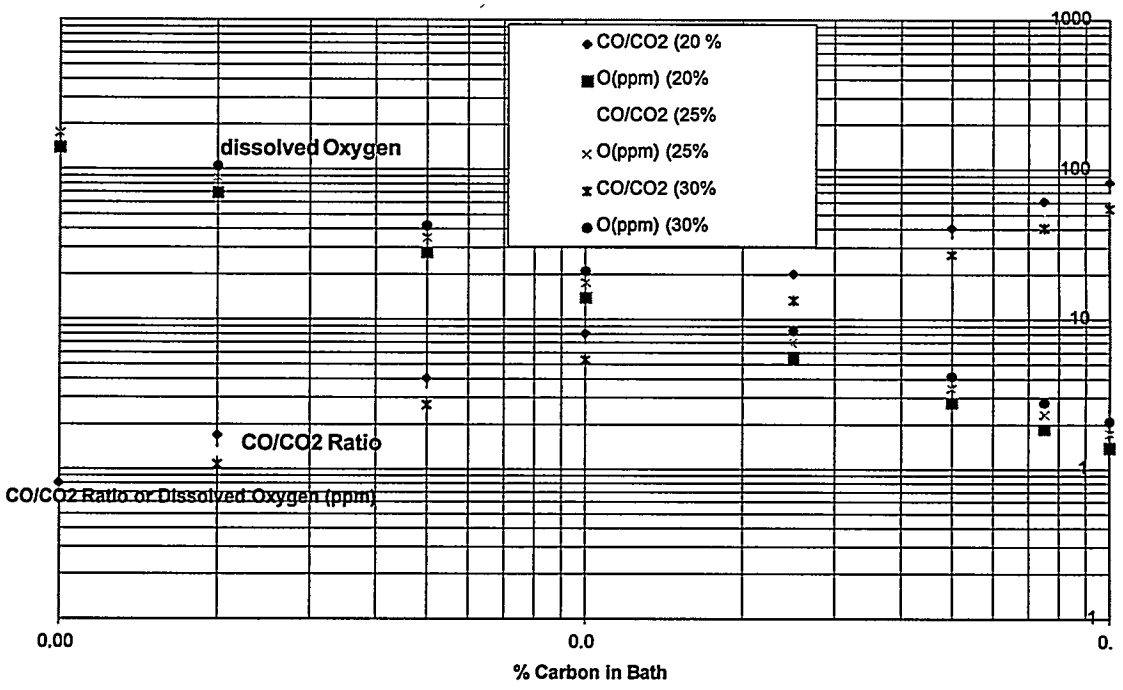

A bath composition control strategy has been developed based on maintaining the CO/CO_2 ratio above a certain value by adjusting the oxygen flow through the tuyere. This control technique has been demonstrated and confirmed with a dissolved oxygen sensor. If at any point the CO/CO_2 falls below the setpoint, the O_2 flow is reduced by a predefined step (e.g., ΔO_2 = 1 scfm). This action is repeated until the CO/CO_2 ratio

exceeds the setpoint. A feedback loop controller for this system has been developed based on an estimate of the rate of change of CO/CO_2 and an estimate of the response time of the CO/CO_2 analyzer to changes in oxygen flow rate. For this system the response time is fast enough that a proportional controller is all that is necessary, with integral action included to avoid offset to disturbances. Figure 2.77 shows the effectiveness of the CO/CO_2 ratio model in maintaining a steady CO/CO_2 ratio. In this run, the bulk carbon concentration was maintained at a steady level of approximately 0.2% by continuous adjustment of the oxygen flow (not shown), leading to the steady off-gas composition shown.

Figure 2.77
CO/CO_2 Ratio at Low Bath Carbon

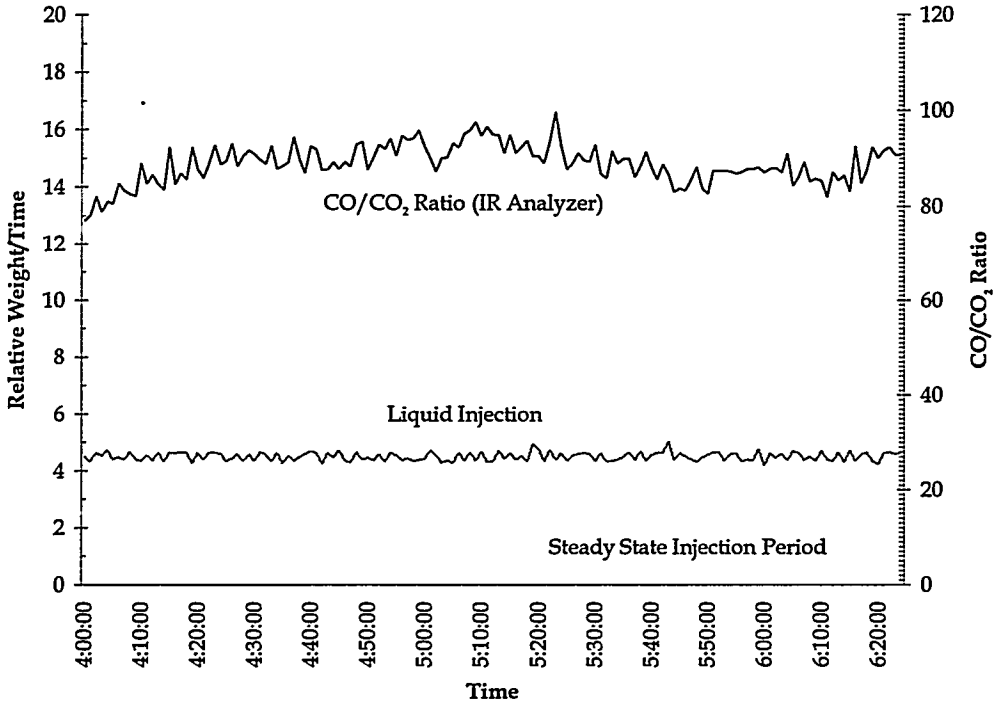

2.5.4.2.3. Thermodynamic Models: Total Hydrocarbons Content

In a Fe-C system, the Total Hydrocarbons Content (THC) Model has been implemented to use measurements of carbon-containing offgas species to infer the activity of carbon in the bath. It is based upon the following equilibrium relationship:

$$\underline{C} + 2H_2 = CH_4$$

$$\Delta G = (-87.657) - T_{bath}(-0.108741)$$

$$In\left(K_{eq,CH4}\right)\Delta G / \left(RT_{bath}\right) = \frac{\Delta G}{\left(RT_{bath}\right)}$$

$$K_1(T) = \frac{P_{CH_4} P_T}{a_c P_{H_2}^2}$$

where K_1 is the equilibrium constant, P_i is the partial pressure of component i, P_T is the total pressure, and a_c is the activity of carbon. The activity of carbon can be determined based on the above relation given the partial pressure of the components are determined from the off-gas characterization and the equilibrium constant calculated based on thermodynamics. The activity of carbon can then be mapped with the bath carbon concentration based on thermodynamics as shown in Figure 2.78. The THC levels can then be correlated with bath carbon composition as shown in Figure 2.79.

Figure 2.78
Carbon Activity (1500°C)

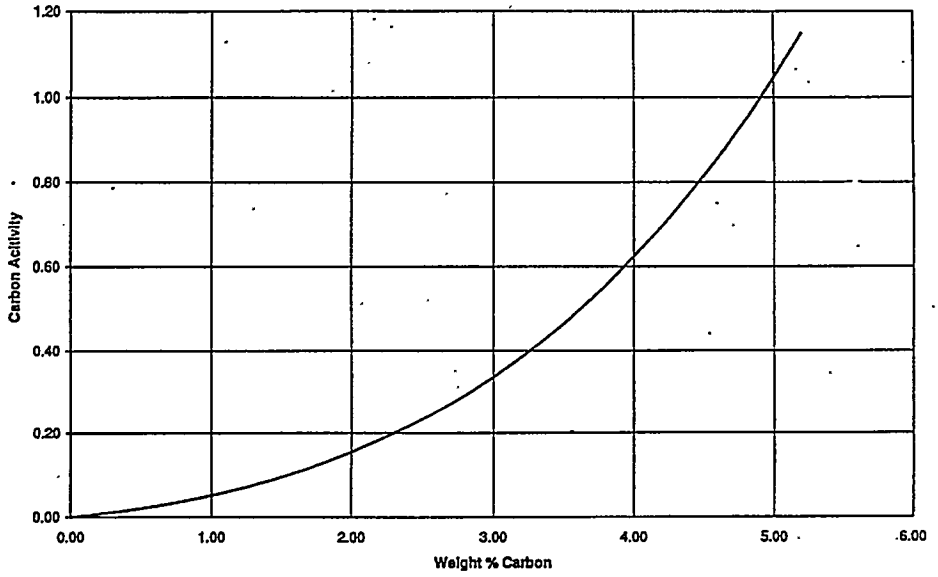

Figure 2.79
THC Readings vs. %C for Different Bath Temperatures

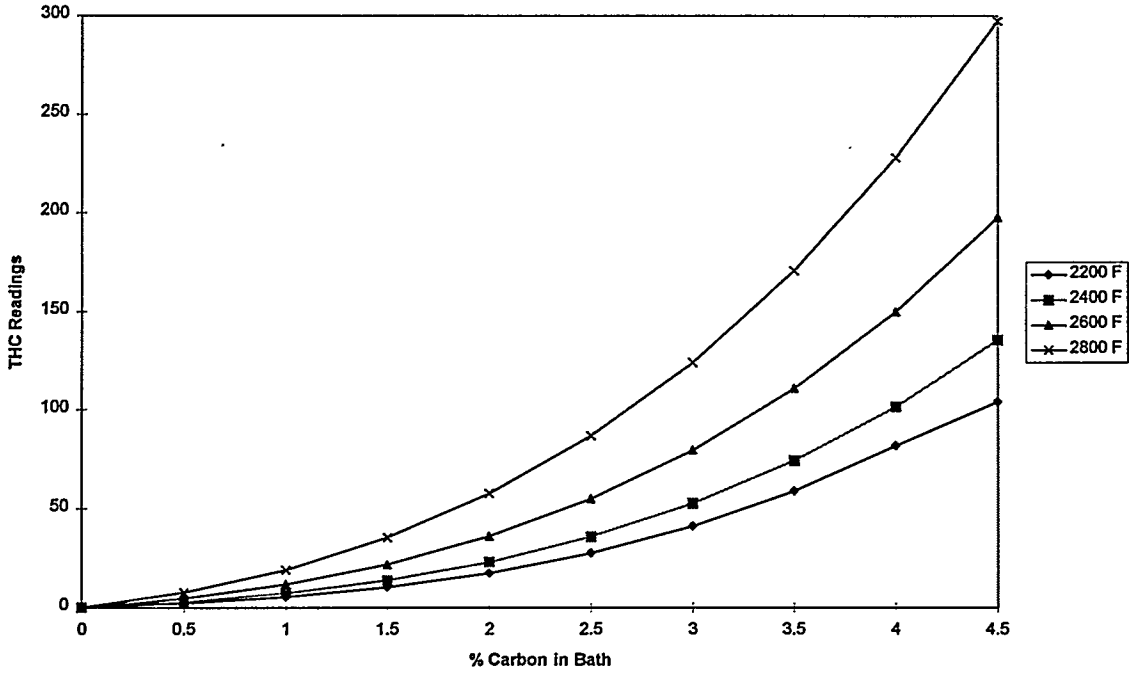

The use of the preceding relationship for the estimation of bath carbon is based on the following assumptions which apply to CEP operation:

1) The kinetics of these reactions are rapid enough to reach equilibrium at bath conditions and the residence time in the reactor is sufficient to raise the feed temperature to bath conditions.

2) After the gas stream leaves the bath, reactions involving the formation or destruction of the offgas trace products are negligible.

Experimental results had demonstrated the consistency of the predicted bath carbon concentration with the actual LECO measurements. Figure 2.80 shows the experimental results during a demo unit run, in which the bath carbon determined by LECO followed the thermodynamic behavior. This THC model demonstrates the sensitivity of bath carbon with the offgas quality at medium to high carbon concentrations. It thus can be used to set up the upper boundary of the bath carbon control operation.

Figure 2.80
Measured vs. Predicted THC Levels - 1T94-004

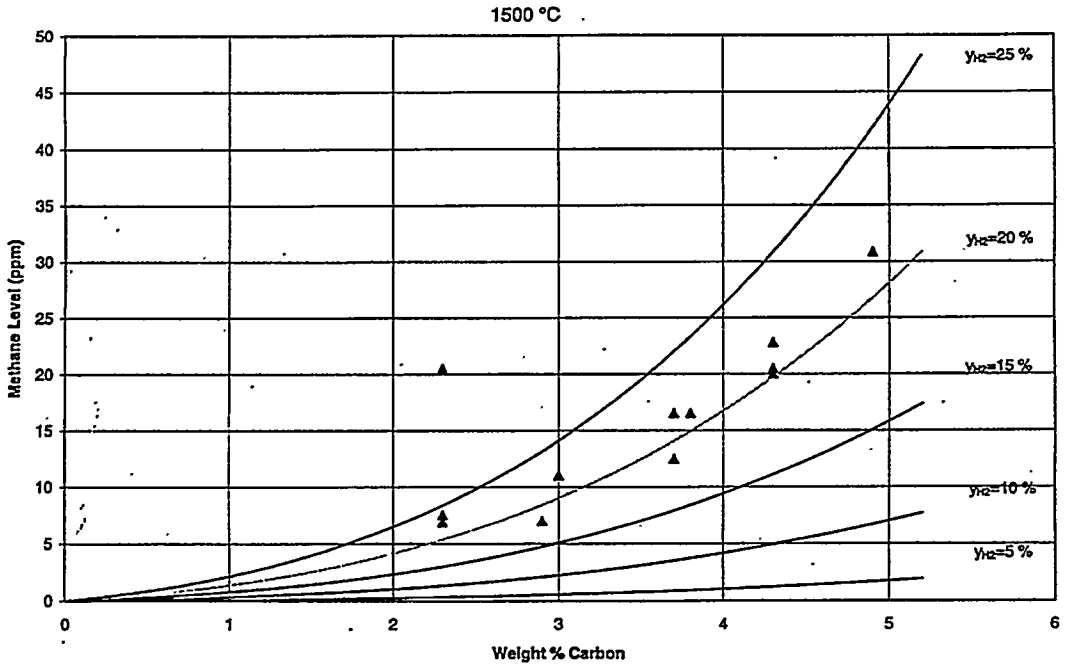

To apply this relation in the control scheme, the CH_4 level was predicted and compared with the actual measurements. The CH_4 level can be predicted based on the following equation:

$$y_{CH_4,measured} = y_{CH_4,bath} \frac{F_{T,bath}}{F_T}$$

Figure 2.81 demonstrates the CH_4 level determined by the model and the actual measurement based on THC analyzer. The THC analyzer reading is a function of the offgas CH_4 concentration (the concentration of C_{2+} hydrocarbons is negligible in comparison). The analyzer represents a fast and economical source of CH_4 measurements independent from the mass spectrometer, which can be used as a check of the THC analyzer. Note the consistency of the correlations.

Figure 2.81
Carbon Prediction via off Gas Correlation

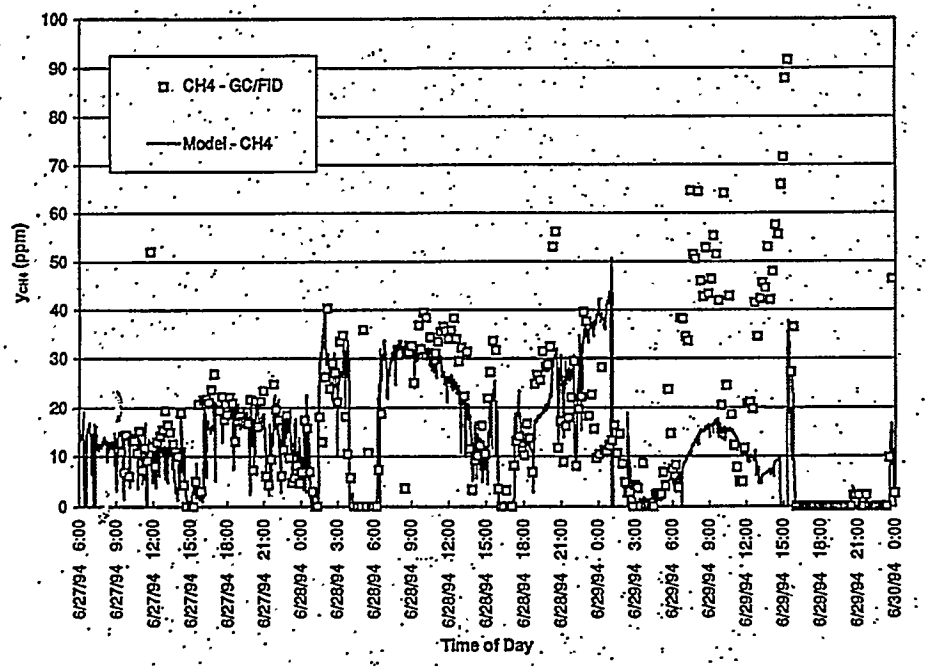

The Total Hydrocarbon Model takes the advantage of the relationship between the equilibrium constant of hydrocarbon reactions and the carbon concentration in the bath. The input parameters included only off-gas characterization and bath T, P, independent of the feed composition. Further, no integration of systematic errors is present because the carbon concentration in the bath is calculated directly from off-gas measurements.

2.5.4.3. Contingency:

2.5.4.3.1. Mass Balance Models

Mass balance models are based on balancing all the species going into the molten metal bath with all the species going out. There are two types of models: the Feed Forward Model and the Mass Spec Model[3]. Mass balance models require a specification of the feed composition and flow, as well as flow of natural gas, oxygen, and inerts into the system. This information is assumed to be available for the mass balance models input. In addition, the feed flow is measured and all flows going into the reactor are independently metered. The offgas flow is also metered, and the offgas composition is measured by a mass spectrometer. The Feed Forward Model predicts the offgas flow

and composition from feed measurements plus thermodynamic models. It does not use the measurements of the offgas flow and composition. The Mass Spec Model uses offgas flow and composition measurements in addition to feed measurements.

The following discussion describes in detail the method of approach. The basis of the calculation is a general steady-state carbon balance on the reactor:

$$\frac{dN_c}{dt} = F_{c,in} - F_{c,out}$$

where $F_{c,in}$ is the carbon flow into the reactor, which is known from feed composition and manual additions, $F_{c,out}$ is the carbon leaving the reactor, which is estimated by the model, and dN_c/dt is the calculated accumulation term.

$F_{c,\,in}$ is determined by the following equation:

$$F_{c,\,in} = F_{c,\,feed} y_{c,\,feed} + F_{c\,hand\,add}$$

Two models were used to determine the value of $F_{c,\,out}$ (1) feed-forward model and (2) mass spec model.

In the feed-forward model, $F_{c,out}$ is estimated using partitioning and thermodynamic models as shown by the following equations:

$$F_{o,in}' = F_{o,feed} + F_{o,other}$$

$$F_{c,out} = f\left(F_{o,in}, F_{ca,in}, F_{al,in}, F_{ss,in}, F_{c,in}\right)$$

$$y_{c,both(t)} = \frac{\left(M_{bath,T}(to)\right)\left(y_{c,bath}(to) + 12'_{to}\int N_{c,net}\,dt\right)}{M_{bath,T(t)}}$$

The output of carbon is determined based on the thermodynamic partitioning of feed material. Factors that affect the partitioning of carbon include the oxygen usage in the bath, the carbon input, etc. (see Equation (14)). The carbon concentration in the bath, (y) is thus the accumulation term between in and out and can be calculated based on the integration of the rate of change of bath conditions.

In the mass-spec model, $F_{c,out}$ is estimated using the mass-spec data as shown by the following equations:

$$F_{c,out} = T_{off,T}\left(y_{co,offgas} + y_{002,offgas}\right)$$

$$y_{c,bath(t)} = \frac{\left(M_{t,bath}(to)\right)\left(y_{c,bat}(to)\right) + 12'_{t0}\int N_c^{net}\,dt}{M_{t,bath(t)}}$$

The carbon exiting the system ($F_{C,\ out}$) is based on the off-gas concentration of carbon monoxide and carbon dioxide, assuming the total hydrocarbon trace levels were negligible to the overall carbon output. Again, the bath carbon concentration is the accumulation term between in and out and can be calculated based on the integration of the rate of change of bath conditions.

Figure 2.82 shows the performance of the mass balance models with self-tuning when compared with discrete bath carbon samples.

Figure 2.82
Carbon Models Prediction

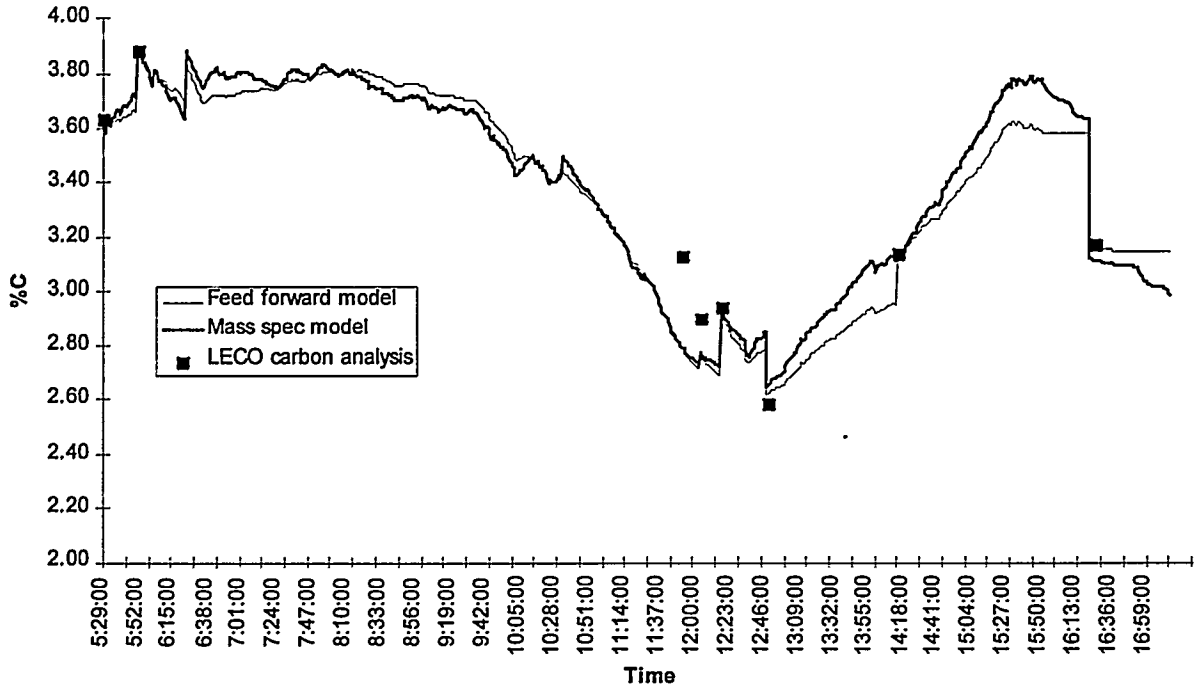

Periodic calibration of model estimates is required due to the inherent integration of sensing errors by the model. Traditional LECO measurements are used to provide this calibration. These models are very useful for a short-term control, instantaneous measurement of bath carbon concentration, and coarse oxygen flow adjustment. The error raised from the model shift may be decreased in commercial applications in which fluctuations in conditions will be minimal.

Ongoing studies for improvements included:

- the application of techniques similar to temperature control, including filtering, self-tuning, and diagnostics control, aiming to improve the accuracy and minimize systematic errors.

- the application of procedural steps such as intermittent samples taking and metal tracing.

2.5.4.3.2. Other Bath Composition Sensing Methods Considered

A number of alternate bath composition sensing methods were considered, including opacity and turboelectric dust loading sensors, oxygen sensor, laser-produced plasma spectroscopy, and molten metal emission spectrometry. Evaluation of these technologies will continue as most show promise for potential application to CEP reactor control.

2.5.4.4. Control Strategy and Automation

The mass balance models indicate the level of O_2 needed to maintain a stoichiometric feed, thus avoiding reaching a high O_2 limit (potential for FeO generation), or a low O_2 limit (potential for excessive offgas dust loading). Actual bath composition will drift over time; therefore, mass balance models are used as a coarse adjustment of the O_2 flow. Fine adjustments of the O_2 flow is provided by the CO/CO_2 ratio and THC models.

2.5.5. Bath Level

2.5.5.1. Requirements

The primary objective of bath level control is to determine whether the bath level has reached the maximum value. The maximum unexpanded bath level should be below the crucible joint to allow removal of this system. Bath growth can be minimized by selecting various compositions of the initial charge according to the type of feed materials.

2.5.5.2. Primary sensing method

2.5.5.2.1. Microwave switch

An off-the-shelf microwave level switch has been identified. It consists of a transmitter and a receiver which are mounted on the side walls of the vessel in two 5" penetrations 180 degrees from each other at a level a few inches above the final melt line. A clearance through the inactive coil section for the microwave beam has been provided for. The microwave beam receiver detects the presence of the microwave beam. If the beam is interrupted by the bath, the receiver issues an alarm signal, indicating that the maximum level has been reached.

A bench-scale test confirmed that the microwave beam can penetrate the expected refractory thickness, and a water model test confirmed that under conditions of low flow the microwave switch can detect when the maximum level has been reached

2.5.5.2.2. Side-Mounted IR Ligthtpipe

This approach is currently under consideration. The total infrared energy collected by an IR lightpipe mounted in the side wall of the containment system is expected to depend on bath level for as long as the lightpipe is exposed. Once the lightpipe is totally submerged in the metal bath, the total IR energy should remain constant and represent the bath temperature.

Changes in injection flow rate should change the bath spout size, thereby changing the view factor of an un-submerged lightpipe. This change in view factor should be reflected as a change in IR energy. This relationship between injection flow and IR energy offers a simple way to detect whether the lightpipe is submerged or not: if the IR signal changes when changing the injection flow rate, it means that the lightpipe is not submerged. If it does not change, it means that the lightpipe is submerged.

Metal splashing is expected to add noise to the measurement. One way to determine when the lightpipe is totally submerged under conditions of a splashing bath is to observe the measurement noise and interpret noise suppression as level above the lightpipe location.

An experiment was conducted on a 10 LB unit to verify the feasibility of this method. Figure 2.83 shows the result. A sensitivity of more than 100 °F with bath level was observed.

Figure 2.83:
IR lightpipe sensitivity to bath level

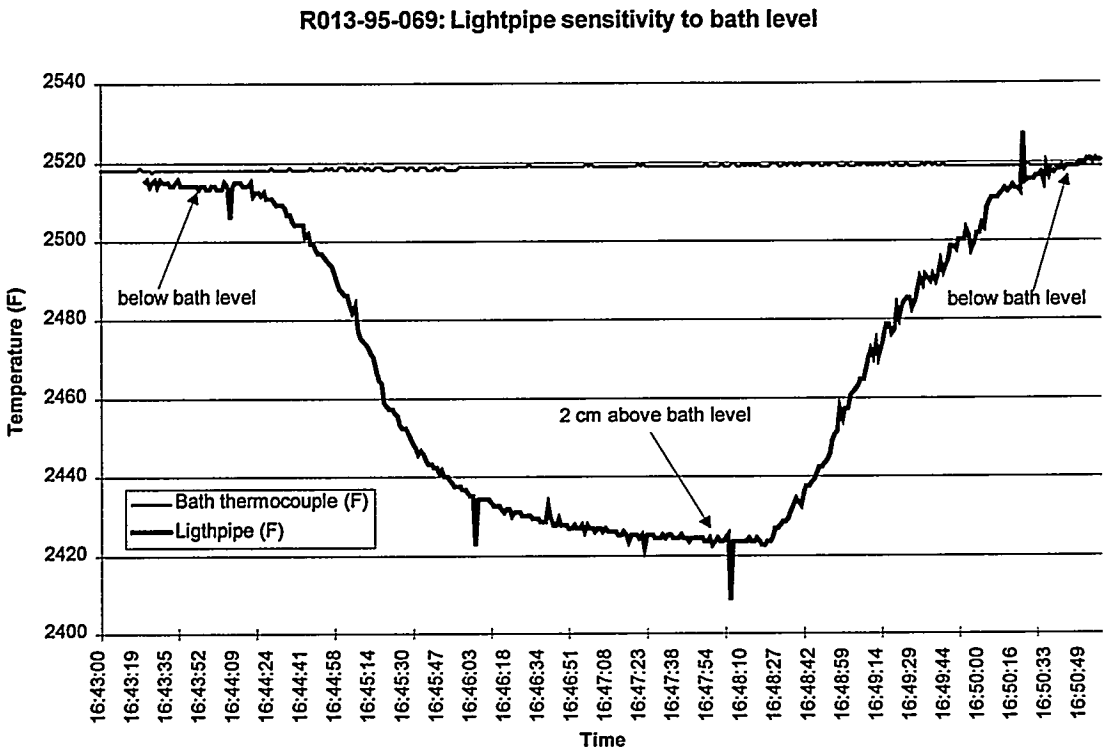

2.5.5.3. Contingency

2.5.5.3.1. Side-Wall Thermocouple Plug ("Krowitz" array)

The concept of using embedded plugs with thermocouples in dry-vibe for temperature measurements was tested in the APU-10. The idea is to install thermocouples very close to the molten metal taking advantage of the excellent wear resistance of the high-density plugs. A sensitivity of the measurement to metal level indicated that the pressurization/depressurization of the reactor caused metal to uncover/cover the plug tip, resulting in temperature changes of 200 to 300 °F. Modeling confirmed the fact that radiation heat transfer generates lower surface temperatures with respect to the same surface in direct contact with the molten metal, and the difference is significant enough to be measurable.

2.5.5.3.2. Other Bath Level Sensing Methods Considered

A number of alternate bath level sensing methods were considered, including microwave radar, radiometric switch, laser, inductance, ultrasound, TV camera with image analyzer, axial temperature, load cells, and conductivity circuits. Evaluation of these technologies will continue as most show promise for potential application to CEP reactor control.

2.5.5.4. Control Strategy and Automation

Level monitoring in the reactor is challenging due to the dynamics of the bath's surface, which reduces the accuracy of bath level measurements. Data provided by the microwave switch is the primary input for the bath level; however, the data is supplemented by thermocouple data and bath level models to compensate for potential measurement errors. The ability to accurately determine when the reactor level has reached its maximum setpoint will improve with the application of sensing technologies currently under evaluation.

2.5.6. Pressure Control

2.5.6.1. Requirements

The primary objective of bath pressure control is to maintain the bath at the desired pressure setpoint. Pressurized operation is desired to increase the system throughput.

2.5.6.2. Primary Sensing Method

2.5.6.2.1. Pressure Transmitters

Two reactor pressure transmitters are provided, one on process gas discharge and one on rupture disk penetration. PLC logic with operator override selects controlling signal. Chemical seals are used to protect sensor. Differential pressure transmitter measures the difference between process gas discharge line and rupture disk line to detect blockage. Pressurized operations have been demonstrated in the VPR and APU 10 units.

2.5.6.3. Contingency

2.5.6.3.1. Redundancy

Redundancy in pressure transmitters provide contingency.

2.5.6.4. Control Strategy and Automation

The reactor pressure is controlled automatically by a PID loop. Reactor inlet flows will to be adjusted according to reactor pressure. An on-line control module is under development to provide automatic tracking of reactor flows with reactor pressure.

2.5.7. Containment Diagnosis

2.5.7.1. Requirements

The primary objective of the containment diagnosis is to provide the operator with an indication that conditions exists that could potentially develop into a potential containment breach in progress. A containment breach includes both permeation and

cracking. This system will afford an orderly system shutdown prior to a breach in containment.

2.5.7.2. Primary Sensing Method

2.5.7.2.1. Grids

Detection grids, which are area sensors based on electrical behavior of the refractory lining, are expected to indicate either pointwise or uniform lining deterioration. Grids indicate the potential for a containment system breach by an increase in current.

The QCEP design includes three grids between the dry-vibe and the shell, and one grid outside of the shell. An additional bottom grid is under consideration. The concept of containment diagnosis using grids has been demonstrated several times in MMT units.

2.5.7.2.2. Tuyere Thermocouples

Thermocouples will be placed on the tuyere pipe which are inserted into drilled holes in a tuyere brick. These thermocouples will be potted with a high-temperature refractory cement. Three tuyere thermocouples have been incorporated in the QCEP design, at various depths from the hot face.

2.5.7.3. Contingency Sensing Method

2.5.7.3.1. Grid thermocouples

Three arrays of two thermocouples each are mounted between grids. Thermocouple indications may be used to differentiate between uniform permeation and metal fins. An increase in temperature or in temperature rate of change would indicate the potential for a containment breach.

2.5.7.3.2. Bottom plate thermocouple

One (1) type K thermocouple installed in the Q-CEP™ reactor bottom plate to detect failure of containment bottom blocks. Additional thermocouples may be added to provide a scanning system for bottom plate temperature.

2.5.7.4. Control Strategy and Automation

The major parameters to monitor are deviation and rate of change for both grid currents and thermocouple temperatures. An on-line software module is provided to calculate both values for each containment-related sensor, and to issue an alarm when corresponding setpoints are exceeded. Most indications will be treated as warnings, with a few providing shutdown indications.

2.5.7.4.1. Shutdown Indications (Preliminary)

When the indication of the last tuyere pipe thermocouple exceeds a setpoint, the outer grid exceeds a setpoint, or the bottom plate thermocouple(s) exceeds a setpoint.

As more experience is gained with this monitoring system, features to reject sensor failures and avoid nuisance alarms will be added to this module.

2.5.8. Tuyere Injection

2.5.8.1. Requirements

Injection of selected feed materials into melts with very little or no tuyere wear has been demonstrated. The major thrust of current efforts is to come up with a well defined start up procedure for iron melts that minimizes the initial accretion removal time with very little or no tuyere wear. Development of a strategy that minimizes injection startup time and provide an appropriate algorithm to automate the injection procedure is anticipated. Efforts are currently underway to automate commencement of feed injection during reinjection (i.e. feed injection after the initial accretion removal). This automation will be attempted in the next demo unit run as an advisory controller. Once fully tested, this model is expected to perform active control.

2.5.8.2. Primary sensing method

Tuyere injection control strategies require pressure and flow rate indication for each component flow in each passage, as well as reactor pressure and temperature indication.

2.5.8.3. Contingency Sensing Method

No contingency is provided for primary instrumentation associated with tuyere injection control strategies. It is assumed that the reliability of pressure transmitters and flow meters is adequate and that no redundancy is required. Enough instrumentation is available for the system to go to a safe-state injection condition after losing a primary instrument.

2.5.8.4. Control Strategy and Automation

Initially, tuyere injection control strategies will be manual procedures. A tuyere diagnostics module is available and predicts pressure drop in each passage. This information is expected facilitate injection control strategies decisions and tuyere wear assessment. Future in tuyere automation efforts include the development and testing of algorithms for an automatic injection start sequence and automatic feed flow tracking of reactor pressure.

2.5.9. Visual

2.5.9.1. Requirements

Visual observation of the bath conditions are required, particularly during the melting procedure. In addition, visual observation could be used during reaction mode to detect changes in the amount of dust loading, and in purge mode it could indicate presence of foam/ceramic and perhaps bath level.

2.5.9.2. Primary Sensing Method

2.5.9.2.1. Top-Mounted TV camera

A top-mounted compact TV camera with remote iris, zoom, and focus control will be provided. This camera will be mounted in a purged enclosure on top of one of the flange with sightglass.

2.5.10. On-line Control Models

2.5.10.1. Requirements

Some reactor control strategies require on-line computer models. These models are in-house FORTRAN modules which are interfaced to the control system via a C++ executive module. This executive, which facilitates the integration of FORTRAN modules with the control system.

The first package of on-line control models will provide basic monitoring and diagnostics information for the reactor. This package includes the following modules:

1. Model executive
2. Melt model
3. CET model
4. Mass balance model
5. Containment diagnosis model
6. Tuyere diagnosis model

The package will include operator interfaces and tagname database compatible with the system, and will be ready for integration with the rest of the control system. An improved control model package includes modules to enhance the control and automation of the reactor, and consists of:

- Enhancements to existing models

- Auto melt model
- Auto injection sequence
- Auto pressure tracking
- Any other on-line model needs identified

2.5.10.2. Primary on-line Models

2.5.10.2.1. Model Executive Module

Previous experience with on-line computer models at MMT Fall River indicates that it is very important to provide a flexible and robust environment for computer models and to minimize the number of interfaces for input/output to the control system. A contract with Bioprocess Automation, Inc. to develop a software executive that coordinates the execution of on-line FORTRAN modules and performs input/output with the control system was completed on July 1995. This software executive is expected to greatly facilitate the maintenance, robustness, and communication of on-line computer models for QCEP and other commercial units. Model developers will be able to modularize control models and concentrate on just the FORTRAN module development. Embedding the FORTRAN module into the control system will be an easy operation. The model has been tested and integrated into the APU-10 unit.

2.5.10.2.2. Melt Module

The melt module performs the following functions:

- Calculates the charge temperature based on available instrumentation input
- Trends the calculated charge temperature with the target temperature during heatup
- Trends future values of charge temperature based on current inputs
- Allows the operator to visualize the impact of changing current power settings on future charge temperatures.

2.5.10.2.3. Compensated Embedded Thermocouple (CET) Module

This CET module performs the following functions:

- Filters embedded thermocouple inputs.
- Calculates a smooth surface (bath) temperature and rate of change from user-specified pairs of embedded thermocouples, taking into account thermal conductivity dependence on temperature.

- Automatically selects one pair of embedded thermocouples as the lead predictor of bath temperature and rate of change. The lead predictor pair can also be selected manually.

- Optional self-tuning automatically adjust all other thermocouple pairs to follow the lead pair predicted temperature.

- Automatically rejects bad thermocouple inputs and issue high noise and/or rate of change alarms. Thermocouple inputs can also be rejected manually.

- If one thermocouple from the lead pair is rejected, it transfers to the next best predictor pair. The transfer is bumpless if the auto-tuning option has been previously selected.

- Automatic calibration for a user-specified reference bath temperature. Provides a set of thermocouple distances to match a user-specified reference bath temperature.

This module allows on-line configuration of models, and automatically rejects bad thermocouple readings for the calculation of the lead bath temperature.

2.5.10.2.4. Mass Balance Module

The mass balance module performs the following functions:

- Calculates the feed composition from lab analysis of feed and dust.

- Calculates stoichiometric O_2 per pound of feed.

- Calculates bath composition from species balance (feed forward and mass spec models)

- Calculates bath level based on bath composition

- Calculates expected offgas rates

- Performs What-if calculations

2.5.10.2.5. Tuyere Diagnosis Module

The tuyere diagnosis module calculates the expected pressure drop in tuyere passages. By comparing the predicted with the actual pressure drop, the operator can obtain useful information for control or tuyere wear assessment purposes.

2.5.10.2.6. Containment Diagnosis Module

This module calculates the rate of change of several containment-related instrumentation, and triggers alarms if deviation or rate of change setpoints are exceeded.

2.6. Particulate Characterization and Control

2.6.1. Dust Formation Studies

2.6.1.1. Summary

CEP has been identified as a technology whose robustness allows the processing of extremely heterogeneous wastes. The ability to partition volatile elements to the gas handling train dictates a need for a thorough understanding of the mechanisms for condensation and deposition of those elements.

An experimental unit was constructed to investigate condensation of zinc vapor in a test pipe. An argon stream saturated with zinc vapor was produced by bubbling a small portion of the hot gas (1200-1300°F) through a molten zinc bath at 1100-1200°F. Test piping of 1.00" to 1.25" nominal ID was used to condense the metal.

The test parameters studied were the wall temperature and the gas velocity. The wall temperature was varied by cooling the test pipe with either air or water. The effect of velocity was evaluated by reducing the pipe diameter at a constant gas flow rate. The effects of these two variables on the tenacity of the zinc deposition were evaluated by sectioning the test pipes and quantifying the weight of zinc deposited.

2.6.1.2. Introduction

Elemental partitioning in an iron bath has been quantified by previous experiments performed in the VPR. The VPR partitioning data for representative metal elements are summarized in Table 2.34. As the data indicate, most of the cobalt and sodium remain in the metal phase at 2500-2800°F. Cobalt stays in the bath because of its high boiling point, while sodium reacts with the sulfur in the feed to form non-volatile sodium sulfide. The majority of the zinc and the cesium partition to the gas phase as volatilized heavy metals which then enter the GHT.

Table 2.34
Volatile Metal Partitioning Data

Element	Boiling Point(°C)	% Retained in Bath
Zinc	907	<30
Cesium	671	<30
Cobalt	2879	>85
sodium	883	>85

Cesium and zinc that enter the reactor off-gas piping will condense if the pipe wall temperature is below the dewpoint of the off-gas. The condensed solids can either be swept away with the gas stream or accumulate on the wall of the pipe. In the latter situation, accumulation can lead to excessive pressure drop and eventual blockage of the off-gas piping.

In addition to physical blockage of the off-gas pipe, the accumulation of radioactive solids is an effect of Q-CEP operation that requires additional investigation, understanding and management.

The dewpoint for a particular element is a function of the system pressure, the vapor pressure of the element, and the concentration of the element in the off-gas stream.

The estimated dewpoints of cesium and zinc in the off-gas are summarized in Table 2.35 for the average and maximum concentration of the element expected in the feedstream. The dewpoint is calculated at 5 bar, assuming that all the metal in the feed is vaporized. The dewpoint calculations assume that for every pound of organic fed per minute, 60 SCFM of off-gas (40 SCFM process and 20 SCFM of dilution) is produced.

Table 2.35
Calculated Dewpoints

Element	PPM Dry Feed	Dewpoint at 5 bar (°F)
Cesium	800	<150
Zinc	800	824
Zinc	5000	950

To minimize the potential problem associated with the condensation of the heavy metals, two approaches can be considered:

- Maintain the pipe wall above the dewpoint, and
- Cool the pipe wall below the dewpoint and somehow prevent dust settling on the walls.

The objective of this study is to investigate the effect of wall temperature and gas velocity on zinc deposition and evaluate alternative cooling surfaces such as a sintered porous tube with radial flow.

2.6.1.3. Experimental Equipment

The equipment required to perform the zinc deposition experiment is shown in Figure 2.88. This equipment is designed to provide 10 SCFM of hot argon at 1200-1300°F with a maximum zinc dewpoint of 900°F. The modular design allows for a variety of test pipes and rapid changes in the equipment setup.

Figure 2.88
Zinc Dust Generator

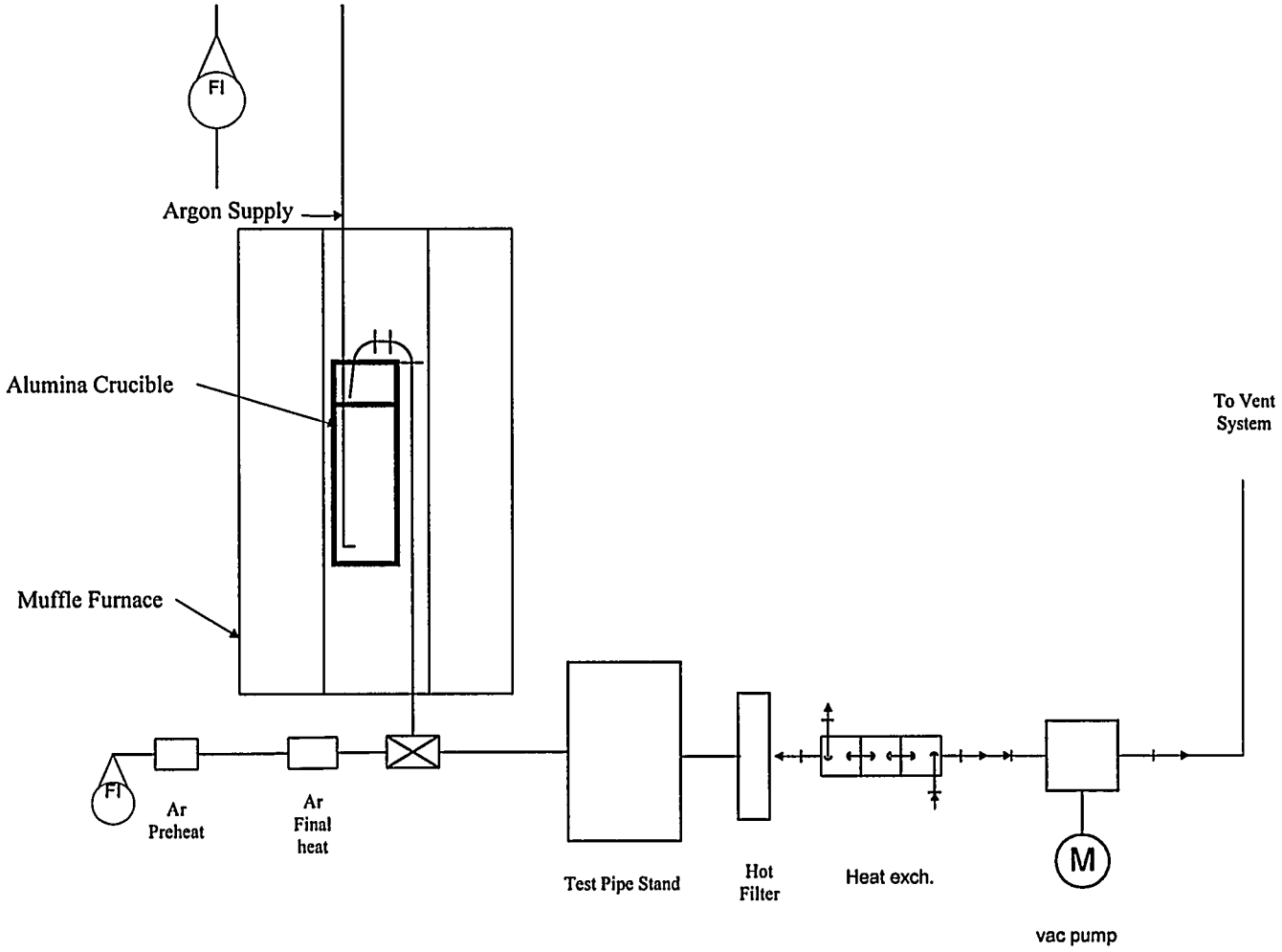

The off-gas piping from the crucible is stainless steel tubing heated with electric heating tape to ensure that condensation does not occur in the off-gas piping or in the mixing tee. The tee was used to mix the saturated off-gas from the generator (0.1-0.5 SCFM) and the heated main argon stream (10 SCFM). The mixed stream is fed to the zinc deposition test pipe; the maximum design temperature of the mix gas is 1200°F.

The zinc deposition test section is stainless pipe that was air cooled by natural convection (no insulation) or water jacketed depending on the specific equipment. The pipe is either 1.0" or 1.25" ID and 10 feet long. Thermocouples were installed to measure the inlet and outlet temperatures and an I/R temperature indicator was used to measure the wall temperature along the length of the pipe for the uninsulated case.

After the test pipe, a high temperature Balston filter was used to collect and weigh the zinc particulate. The maximum gas temperature in the filter inlet is 900°F. A water-cooled heat exchanger or a direct water spray was used to cool the gas to 200°F. The gas flowed into a jet pump to maintain the generator at atmospheric pressure. Compressed air was used to provide the necessary flow to maintain pressure.

2.6.1.4. Theory

In Figure 2.89, the dewpoint of the mixed feed gas is shown as a function of generator temperature and flowrate at a total gas flowrate of 10 SCFM. The graph assumes the zinc generator off-gas is saturated with zinc. The maximum flowrate of the generator off-gas is estimated to be 0.5 SCFM. Assuming a generator temperature of 1200°F and a generator gas flowrate of 0.5 SCFM, this condition corresponds to a mixed gas dewpoint of 900°F with a zinc loading of 60 g/hr. If the generator flowrate is reduced to 0.1 SCFM at a constant temperature of 1200°F, the mixed gas dewpoint is reduced to about 800°F, lowering the zinc loading to 13 g/hr. It should be noted that the melting point of zinc is 788°F. If the dewpoint is higher than the melting point, the deposit may have more of a tendency to coat the wall because it will initially condense as a liquid and then solidify on the surface. If the dewpoint is below the melting point then the zinc will condense as discrete solid particles and have less tendency to coat the wall.

Figure 2.89
Dewpoint vs. Generator Temp and SCFM

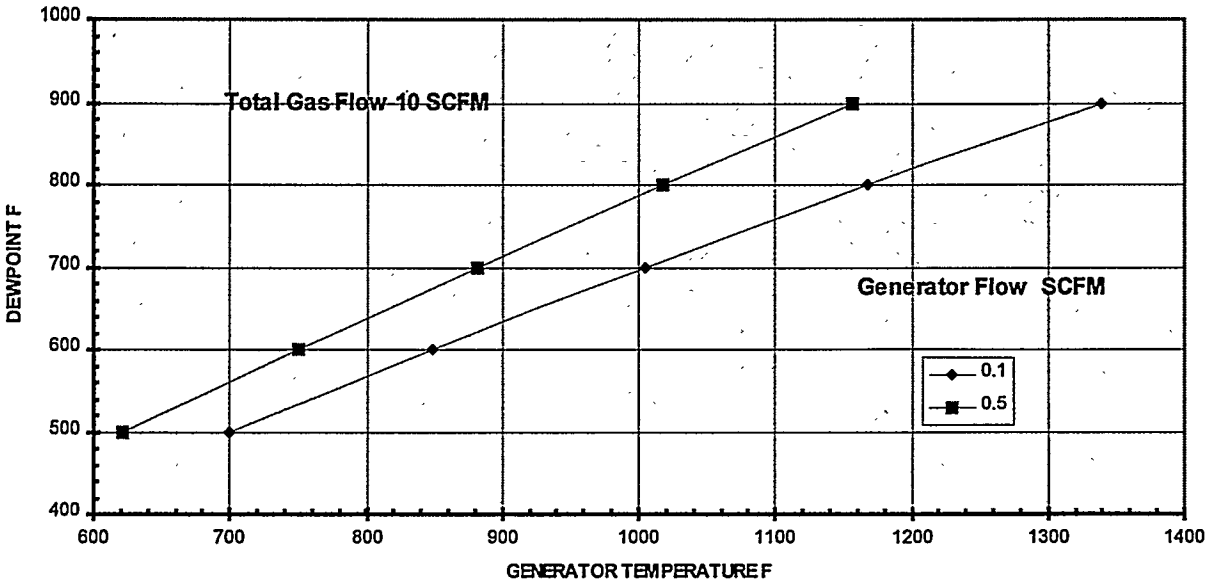

Table 2.36
Zinc Vapor Pressure

Temp(°F)	Vapor Pressure (mmHg)	Normalized to P(800°F)
600	.0043	0.02
700	.0344	0.15
800	.1990	1.00

Table 2.36 shows the dependence of zinc vapor pressure with temperature. This data shows that cooling a gas with an 800°F dewpoint to 600°F condenses approximately 98% of the zinc vapor.

2.6.1.5. Experimental Plan

The initial set of runs is outlined in Table 2.37 below Two parameters were varied: the wall temperature and the pipe diameter. The gas flowrate and the zinc loading were maintained constant. In the second pair of tests, the pipe diameter was decreased to 1.0 inch ID to increase the flow velocity by a factor of four.

Table 2.37
Experimental Runs

EXP #	FEEDGAS			ZINC GENERATOR			TEST PIPE			
	Dew Pt (°F)	SCFM	Inlet (°F)	gms/hr	TEMP (°F)	SCFM	L (FT)	ID (")	Inlet fps	Comment
1	800	10	1200	13	1200	0.1	10	1.25	42	Air Cooled
2	800	10	1200	13	1200	0.1	10	1.0	164	Air Cooled
3	800	10	1200	13	1200	0.1	10	1.0	164	Water Cooled 100F Wall
4	800	10	1200	13	1200	0.1	10	1.25	42	Water cooled 100F Wall

After each experiment, the test pipe was sectioned for microscopic examination. Zinc content of some sections was determined by soaking the test piece in acid and analyzing the zinc concentration.

2.6.2. Dust Formation Mechanisms - Chlorinated Feeds

Particulate control methods in the CEP system have been developed through an understanding of the basic mechanisms for generation of dust and particulates. Innovations in gas handling train technology and operation have led to both suppression of dust formation as well as recyclability of any dust that may form. The result is a system producing a clean gas product exceeding industrial specifications using proven, reliable technology.

Two different mechanisms exist for dust to enter the gas handling train. The first is by entrainment of particles due to the gas velocities exiting the bath. Typically, particles collected by this phenomenon are greater than 10 microns in size. The other mechanism involves vaporization of the material in the bath, primarily in the area surrounding the tuyere. These particles condense in the GHT and are typically smaller in size. Dust formation is therefore a function of the rate of gas generation from the feed and the surface velocity of the gas as it exits the condensed phases of the reactor. Studies have focused on several means of providing added control of dust generation.

High resolution electron microscopy indicates that most CEP dust samples are composed primarily of self-agglomerated submicron particles attached to each other. The mechanism is similar to sintering at high temperatures. Each of these submicron particles is either a single crystal or a single crystal with an external chloride shell. Some isolated alloy particles are also found, imbedded in graphitizing carbon platelets. Detailed chemical analyses and diffraction methods indicate that the composition and crystallography of CEP dusts is directly influenced by the type of injection and metal

addition during operation. Based on the structure of the CEP dusts, they are able to be recycled and recovered through engineering design.

Dust analysis has led to development of hypotheses for the mechanisms of dust formation (as shown in Figure 2.90). With a better understanding of the dust formation mechanism, the operating conditions can be adjusted to minimize it. Materials are injected into the melt from the bottom at high velocity. These materials decompose and continue with high kinetic energy up through the melt in a gaseous state. The gas passes through the molten iron, into the molten ceramic (if present), "dragging" the iron along. Because of the high viscosity of the ceramic, the gas and the metal punch through the ceramic. The chemical potential of the material at this peak is inversely proportional to the radius of the peak. The radius can be as low as 0.02 μm, drastically increasing the chemical potential, μ. This reduces the melting point of the material at this peak, and the metal at this peak is "pinched" off, and escapes from the melt. This reaction can occur at numerous points on the surface of the melt simultaneously. The combination of these actions, as well as with "melt" bubbles at the surface can allow more particles to escape from the melt. The overall series of these separate events bring the melt into a turbulent state.

At very high temperature, this metal particle reacts with the HCl gas to form iron chloride which is a gas at these conditions. The particle, shown in Figure 2.91, shrinks in size as more of the iron reacts with chlorine to form the chloride. Eventually, the particle reaches an intermediate temperature zone where the iron chlorides are in a solid phase. In this temperature region, instead of the iron chlorides evaporating, a solid ash layer of iron chloride is formed around the metal particles. The gaseous chlorides formed in the high temperature zone also condense and are adsorbed to the surface of these particles.

Figure 2.90
Formation of an Iron or Alloy Droplet from Molten Metal Bath

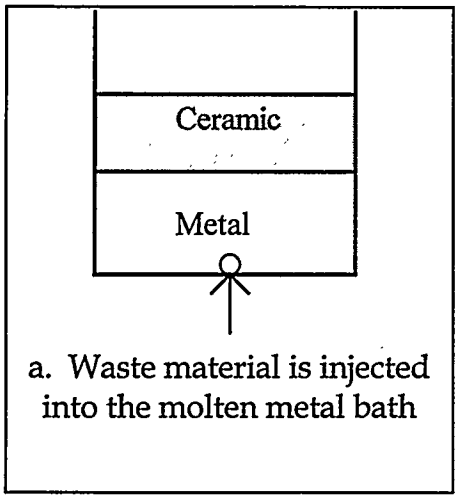

a. Waste material is injected into the molten metal bath

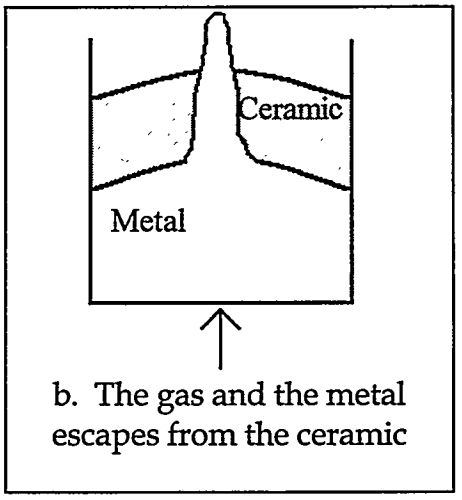

b. The gas and the metal escapes from the ceramic

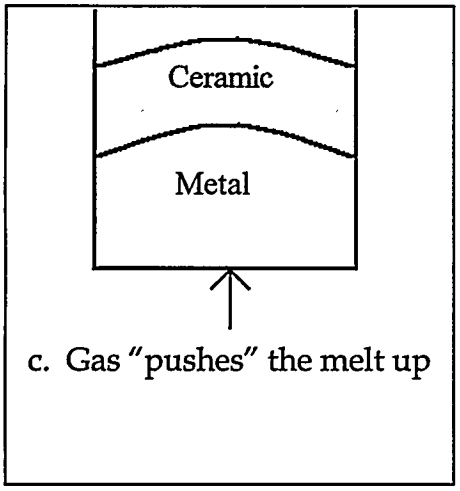

c. Gas "pushes" the melt up

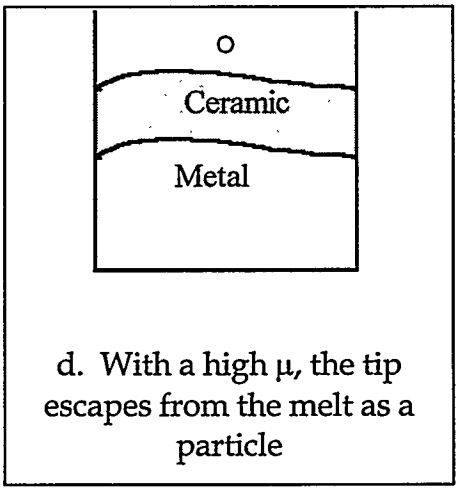

d. With a high μ, the tip escapes from the melt as a particle

Figure 2.91
Formation of an External Chloride Scale on Metal Particles Observed in Dust Samples

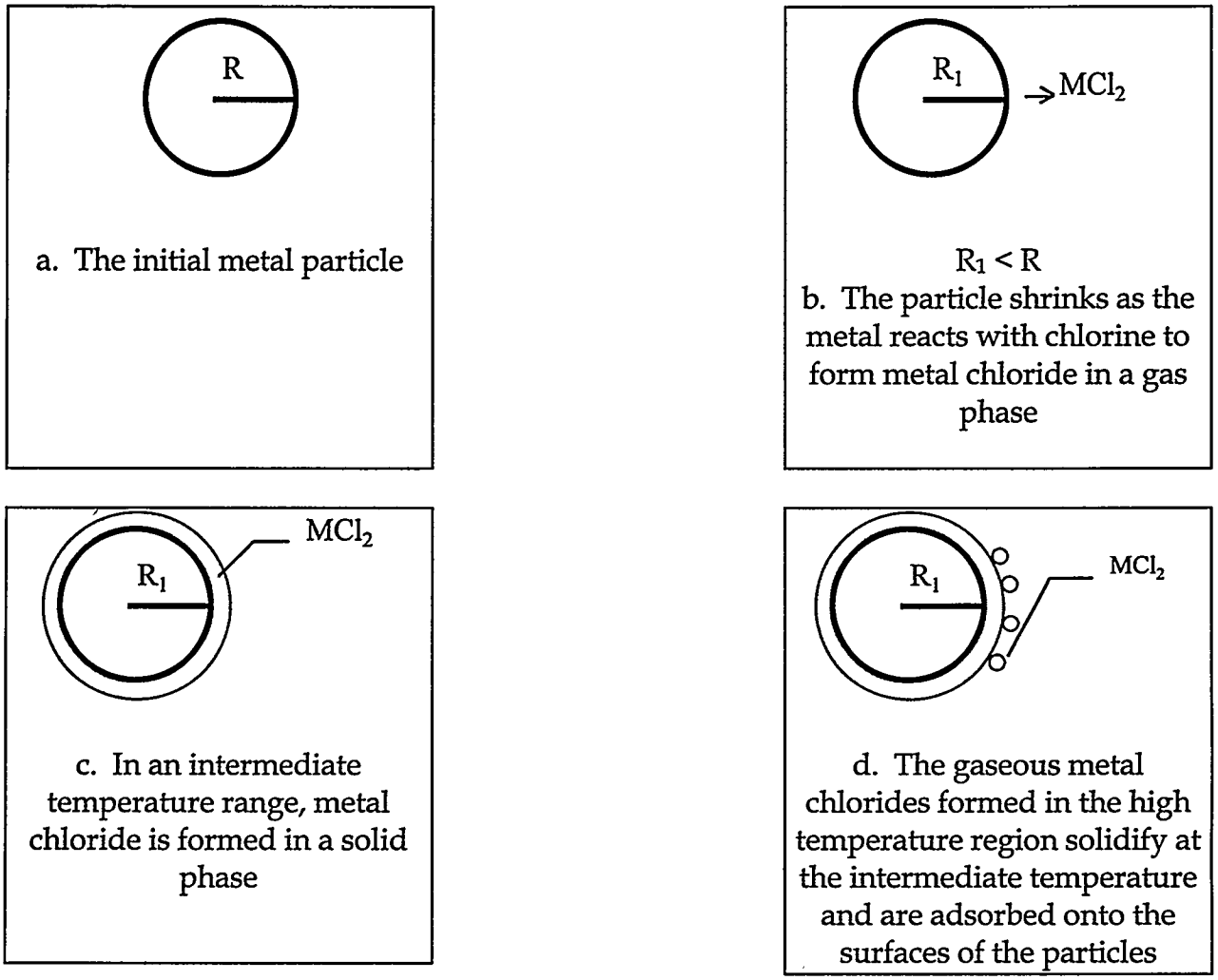

2.6.3. Dust Recyclability in Biosolids Processing

The MMT commercial design for a feed preparation system allows for solid particles (direct-fed or slurry-fed) up to 1000 microns (1 mm) in diameter. The data in Table 2.38 show that at least 98% of the dust analyzed was < 1 mm in diameter and would be acceptable for slurry recycling in a commercial CEP facility. At the Fall River facility, the nominal injection size of the solids feed system is 230 microns. This represents 80% of the dust analyzed. A sieve analysis and elemental composition was performed on biosolids process dust collected at the baghouse. The sieve results are listed in Table 2.38.

Table 2.38
Sieve Analysis of Baghouse Dust

Microns	Wt%
> 850	2.0
> 250	17.3
> 180	9.7
> 150	52.7
< 150	18.3
Total	100.0

2.6.4. Effect of Pressurized Operation - Fly Ash Processing

2.6.4.1. Experiment Summary

The following section describes experiments intended to investigate the effect of pressurized operation on the suppression of component volatilization. MMT has conducted a campaign to investigate the application of CEP to processing of fly-ash to produce synthesis gas and stable ceramic phase product. Several tests with fly-ash have been performed, from single variable investigations on small experimental units to large fully integrated processing runs. These results provided in-depth knowledge of the general characteristics of fly-ash processing including feeding methods, elemental partitioning, ceramic phase characteristics and properties, component volatilization, as well as environmental performance.

Recognizing the effect of secondary dust formation on fly-ash operations costs, MMT performed an experimental run operated entirely at elevated pressures to demonstrate the suppression of volatiles while processing fly-ash. This effect of pressure on dust suppression had already been observed by MMT during previous runs with different feed materials.

This elevated pressure test was performed with the following experimental conditions:

- operating temperature of 1320 °C ± 30 °C;
- operating pressure of 60 psig (4.21 kg/cm^2-g);
- starting metal bath of 36.32 kg of carbon-saturated iron;
- initial ceramic layer of 3.63 kg (CaO-Al_2O_3-MgO-SiO_2-B_2O_3).

A total of 2.8 kg of fly-ash was injected into the bath of a bench-scale reactor over a 5 hour period. No flux co-feed was used. The initial ceramic phase that was utilized in this run better simulates the continuous operation proposed for this type of feed.

The results have demonstrated the effects of pressurized operation on lowering dust formation by achieving a 52% reduction in dust formation. This result maps directly into reduced operating costs associated with secondary dust stabilization and disposal from previous atmospheric pressure results.

Minimization of secondary dust formation is accompanied by incorporating these volatile components (such as Na, K, and Cl) into a stable ceramic phase product. Pressurized test results have produced a ceramic phase composition showing an average composition of 6.95 wt% chlorine, a 107% increase over the previous fly-ash ceramic products that had 3.36 wt% chlorine. Alkali concentrations, represented as NaCl and KCl, in the ceramic phase product were 119% and 50% higher than previous atmospheric tests for NaCl and KCl, respectively. These results are indicative of the CEP ceramic phase's ability to capture increased levels of these volatiles into a stable, durable product.

2.6.4.2. Secondary Dust Formation

2.6.4.2.1. Effect of Pressure on Secondary Dust Formation

According to fundamental physical laws governing liquid/vapor phase equilibrium, an increase in pressure reduces the volatilization of a component within a mixture. This effect can be readily seen by analyzing Raoult's Law for ideal mixtures:

Raoult's Law

$y_a = (Psat/P_t)\, x_a$ where: a = component a
y_a = mole fraction in vapor phase
Psat = vapor pressure of component a
P_t = system total pressure
x_a = mole fraction in liquid phase

At a given temperature, the vapor pressure of component 'a' remains constant. However, as the pressure of the system is increased, the mole fraction of component 'a' in the vapor phase will be decreased, thus reducing volatilization. Also, reducing temperature will reduce the vapor pressure of component 'a', and Raoult's Law also predicts a reduction in volatilization.

This theory can be correlated to the *ceramic phase* formed in the CEP system. The gases evolving from the system will hold a given amount of component 'a' (i.e., NaCl or KCl) in accordance with the vapor pressure of the component, the mole fraction in the liquid

phase, the pressure of the system, and also non-ideal interactions among system components. While Raoult's Law does not account for the effects of non-ideal interactions, it is nevertheless useful for describing the impact of pressure on volatilization.

The results of previous fly ash runs at atmospheric pressure were analyzed to see how well Raoult's Law and ideal solution thermodynamics predicts the resulting volatilization. Utilizing defined run parameters of 1480 °C, effective atmospheric operating pressure, and reported material additions including carrier gas rate, the predicted volatilization of NaCl and KCl was analyzed and shown in Figure 2.92. The effect of increasing the system pressure would have is predicted in Figure 2.92. The actual run result was within 13% of the predicted value. Additional data points would be required to further confirm the correlation.

Figure 2.92
NaCl/KCl Volatilization for Atmospheric Pressure Test

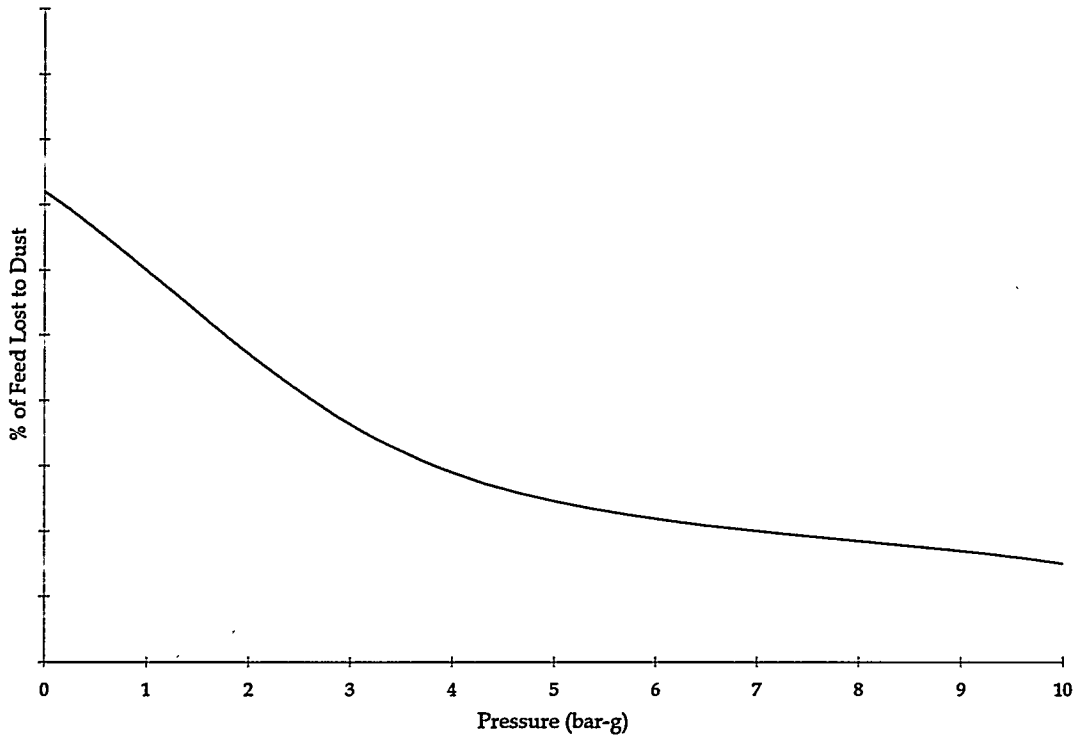

The same analysis for the pressurized test at 1320°C and 60 psig was performed prior to the test and is shown in Figure 2.93. In Figure 2.93, the predicted volatilization for both NaCl and KCl combined and for total dust including other constituents is shown as a function of pressure. The predictions in both Figure 2.92and Figure 2.93 support to a first approximation that pure component vapor pressure data and ideal solution

vapor/liquid equilibrium models can be used to characterize component volatilization (i.e., dust formation) in the processing of fly-ash.

Note: The values shown in Figure 2.92 and Figure 2.93 are not directly comparable to each other as carrier gas flow for fly-ash injection was significantly different between runs. This accounts for the higher volatilization predicted for NaCl/KCl even though the feeds were the same and operating temperatures were reduced from Figure 2.92 to Figure 2.93. These graphs also only predict the operation of the experimental runs and do not correlate to the proposed operation of commercial-scale facilities.

Figure 2.93
Dust Volatilization during Elevated Pressure Test

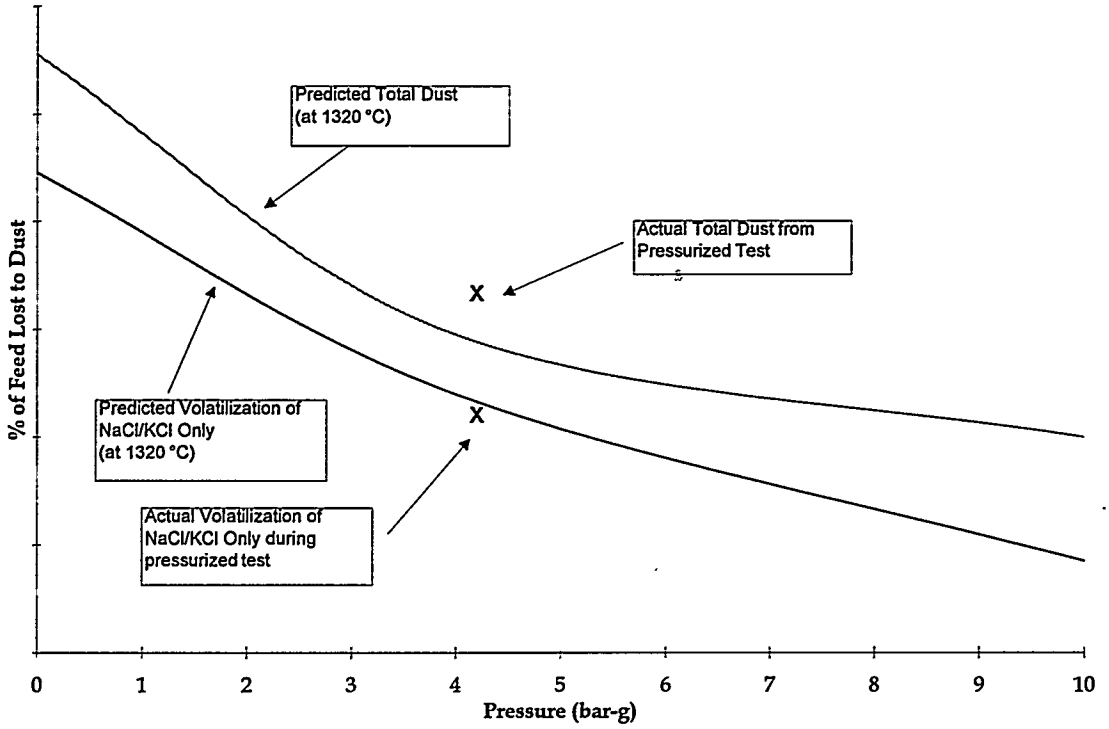

Because this model for predicting dust formation is based upon the physical properties of the fly-ash constituents, it should be valid not only for fly ash but also for other waste feeds. Operation at lower temperatures will reduce dust formation due to the reduction in component vapor pressure. However, CEP's ability to operate at increased pressure will allow even lower dust formation.

2.6.4.2.2. Dust Composition

Secondary dust, or volatile material that exits the bath in the gas phase, is collected in the experimental unit gas handling train filters. A small amount of dust was found in the system piping prior to the filters that was collected and added to the filter-collected dust. The composition of the dust from the system lines and the filters was analyzed and the average values shown in Table 2.39.

Table 2.39
Average Secondary Dust Composition for Processing Fly-Ash at Elevated Pressures (60 psig)

Element	wt%
Ca	6.26
Al	1.24
Si	0.61
Mg	0.23
Fe	2.48
Na	14.25
K	14.22
Cl	54.71
Zn	4.53
Pb	1.32
S	0.15
Total	100.00
These values were normalized to 100% due to the exclusion of C, H, and O. Prior to normalization the above elements constituted 98.03% of the dust composition.	

The material was a fine, gray dust with a consistent appearance to previous runs performed with fly-ash.

2.6.4.3. Ceramic Phase Composition

The final ceramic phase for the elevated pressure fly-ash tests was the product of 2.8 kg of fly-ash feed and 3.86 kg of an initial ceramic layer. A starting ceramic phase simulates a continuous operation where incoming fly-ash feed would see an established

ceramic phase layer and thus benefit from the solution thermodynamics by producing less secondary dust formation. It is expected that after a suitable ceramic phase has been established, flux addition would have begun at approximately 35% of the fly-ash feed. This additional flux will maintain the composition of the ceramic layer and the fluidity of the phase.

Operation at elevated pressure has shown its dramatic effects on reducing volatilization and thus secondary dust formation in Section 2.6.4.2. This correlates to higher levels of these "normally" volatilized materials (such as Na, K, Cl, etc.) remaining in the bath and partitioning into a stable ceramic product. The ceramic phase for the latest pressurized test has shown a significant increase in NaCl, KCl, and $CaCl_2$ concentrations in the ceramic product over previous ceramic product produced during atmospheric operations as shown in Table 2.40.

Table 2.40
Increased Volatile Capture in Ceramic Product while Processing Fly-ash at Elevated Pressure

Constituent	Atmospheric Operation (wt% in ceramic)	Pressurized Operation at 60 psig (wt% in ceramic)	Net Increase in Ceramic Capture (%)
NaCl	0.43	0.94	219
KCl	0.22	0.33	150
$CaCl_2$	4.82	10.00	207
Cl (total)	3.36	6.95	207

This increase in volatile capture due to increased pressure is indicative of CEP's ability to produce a stable ceramic phase product that can accommodate these components. These results confirm previous tests performed by MMT on alkali and chlorine capture in ceramic phases. The stable, durable ceramic phase products containing these components have always passed full TCLP tests. Table 2.41 shows the TCLP results for the ceramic phase product for the pressurized fly ash run with the increased levels of chlorine and alkalis.

Table 2.41
TCLP Results for Fly Ash Processing Ceramics

	Sample ID							
MMT Run	As	Ba	Cd	Cr	Pb	Hg	Se	Ag
Fly-Ash Test Run (pressure = 60 psig)	ND	4.0	ND	ND	ND	0.01	ND	ND
Detection Limits (mg/l)	1.0	0.5	0.1	0.2	0.5	0.005	0.5	0.1
U.S. Regulatory Limits (mg/l)	5.0	100	1.0	5.0	5.0	0.2	1.0	5.0
ND = not detected.								

Table 2.42 shows the average composition of the ceramic product with chlorine represented as metal chlorides.

Table 2.42
Average Composition of the Ceramic Product

Constituent	wt%
CaO	38.87
Al_2O_3	12.54
SiO_2	31.84
MgO	3.12
NaCl	0.94
KCl	0.33
$CaCl_2$	10.00
S	0.60
Total	100.00

The important result of this run is that the increased pressure was instrumental in suppressing the volatilization of the alkalis and chlorides and that the ceramic phase is capable of supporting increased levels of these constituents. Further demonstrations will only determine the limits of the system to optimize the superior performance of CEP in producing minimum secondary dust.

2.7. Volatile Heavy Metals Recovery

2.7.1. Introduction

Volatile heavy metals (VHMs) are present in varying degrees in DOE mixed waste streams being considered for CEP application. An understanding of volatile heavy metals partitioning in the CEP system is critical for effective processing of this waste. Developing the capability to characterize VHMs behavior under different reactor operating conditions will significantly enhance knowledge about VHMs accumulation in the GHT. This knowledge will be invaluable for the design of a gas handling train that ensures VHMs are fully recovered for re-injection or re-use.

Earlier bench- and pilot-scale VHMs partitioning studies, focused on lead, have indicated that at typical CEP temperatures of 1,500-1,550 °C, less than 15 wt% of the lead was recovered in the metal and ceramic phases. Sampling analysis has suggested significant volatility of lead and zinc and potential recovery in the GHT. Despite these findings, the preliminary nature of this early work accentuated the need for a more detailed and definitive study on VHMs behavior in CEP systems.

2.7.2. Objectives

To better understand the behavior of volatile heavy metals in a CEP system, demonstration-scale trial experiments were performed in which lead, zinc, and cesium were injected as co-reactants. In addition, thermodynamic modeling of the system under study was performed to predict VHMs partitioning and to examine the effect of different operating parameters. The primary goals of this study were as follows:

1) Validate earlier VHMs' partitioning data on a large scale unit;

2) Collect experimental data to fully account for VHMs accumulation and deposition in the gas handling train;

3) Improve sampling protocols to increase the level of confidence in the analytical data;

4) Examine the effect of a changing bath chemistry on VHMs final form;

2.7.3. Thermodynamic Analysis

To better explain the findings of the earlier studies, thermodynamic modeling of the system was performed. The components most favored to form were predicted and their volatilities determined for a given set of operating parameters. Phase stability diagrams, free energies of reaction, and vapor pressures were theoretically determined for a system containing the elements lead, zinc, iron, chlorine, and oxygen using thermodynamic analysis. Table 2.43 lists the boiling point for lead and zinc as well as

for oxides and chlorides of both metals predicted to be encountered in the CPU. The vapor pressures, when available, of these components are also presented.

Table 2.43
Boiling Points and Vapor Pressure Data

Compound	Normal Boiling Point (°C)	Vapor Pressure @ 1,500 °C (bar)
Lead (Pb)	1740	0.23
Zinc (Zn)	907	
$PbCl_2$	950	
PbO	1482	0.16
$ZnCl_2$	732	
ZnO		2.53E-5

Although the boiling point of lead (Pb) is quite high (1,740 °C), the high vapor pressures of Pb and PbO combined with the stripping action of the off-gas severely limit the amount of retention in the metal bath. This leads to significant volatilization and condensation in the gas handling train. To maximize VHMs recovery, areas of preferred deposition in the GHT must be identified.

To illustrate which compounds have the highest potential to form under CEP reactor conditions, phase stability diagrams for iron, lead, and zinc compounds as a function of oxygen and chlorine partial pressures have been determined, as shown in Figure 2.94, Figure 2.95, and Figure 2.96, respectively.

Figure 2.94
Phase Stability Diagram of Lead, Oxygen, and Chlorine at 1,500 °C

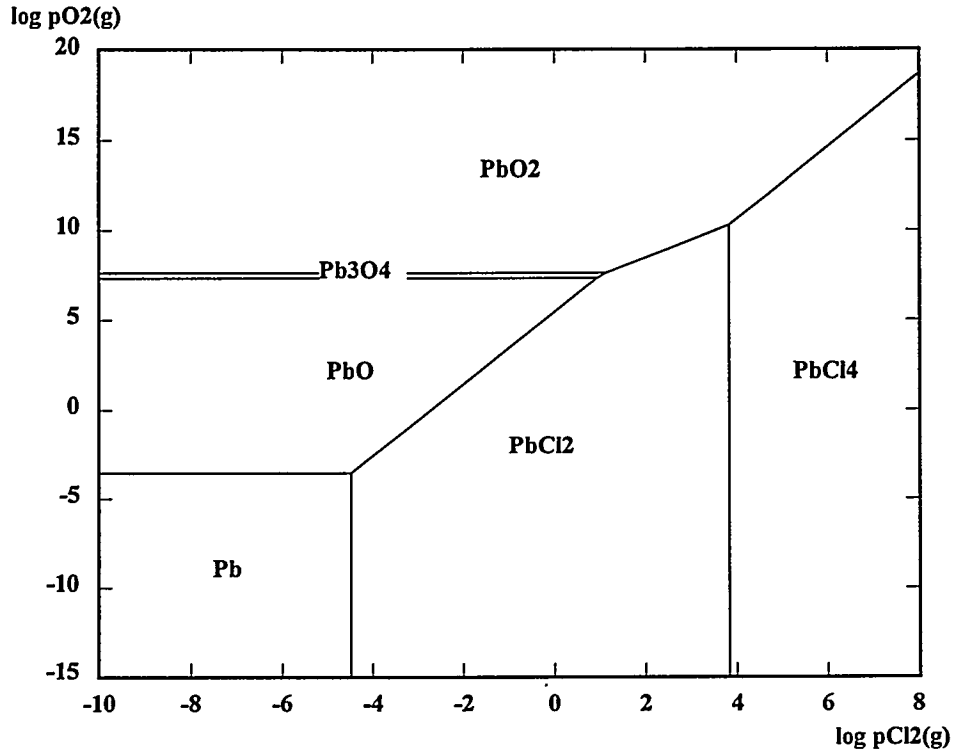

Figure 2.95
Phase Stability Diagram of Zinc, Oxygen, and Chlorine at 1,500 °C

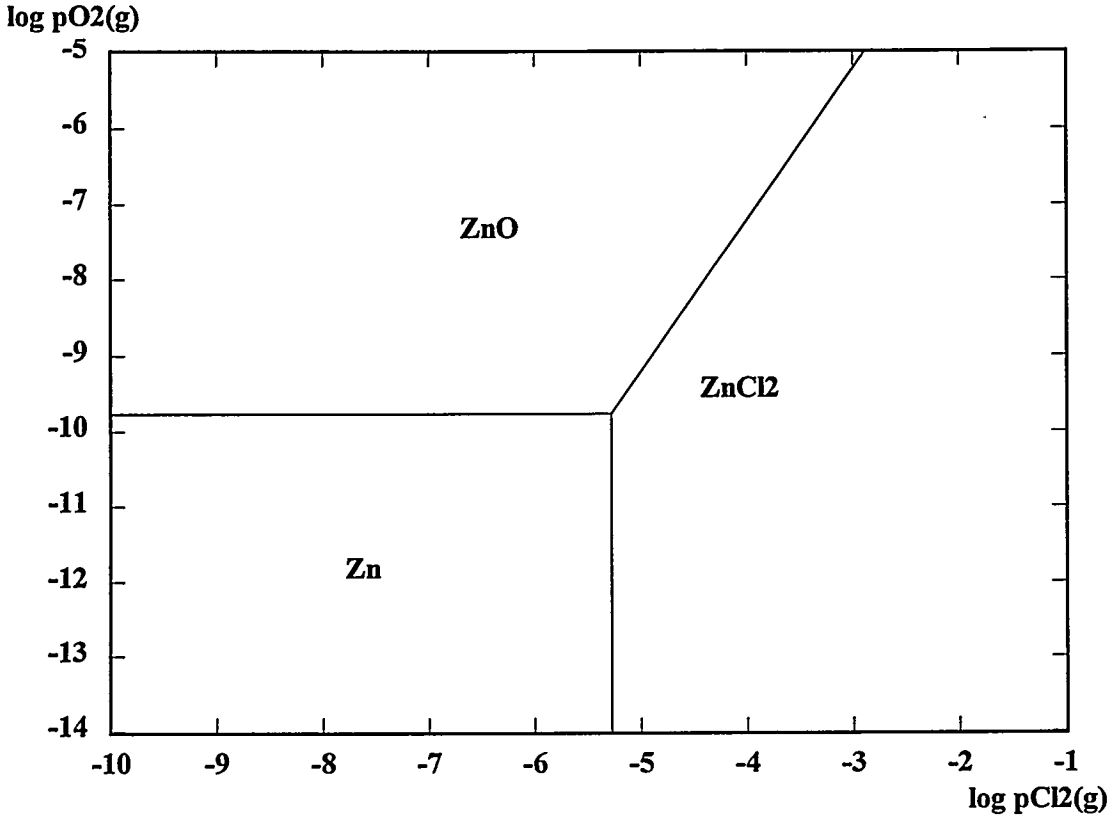

Figure 2.96
Phase Stability Diagram of Iron, Oxygen, and Chlorine at 1,500 °C

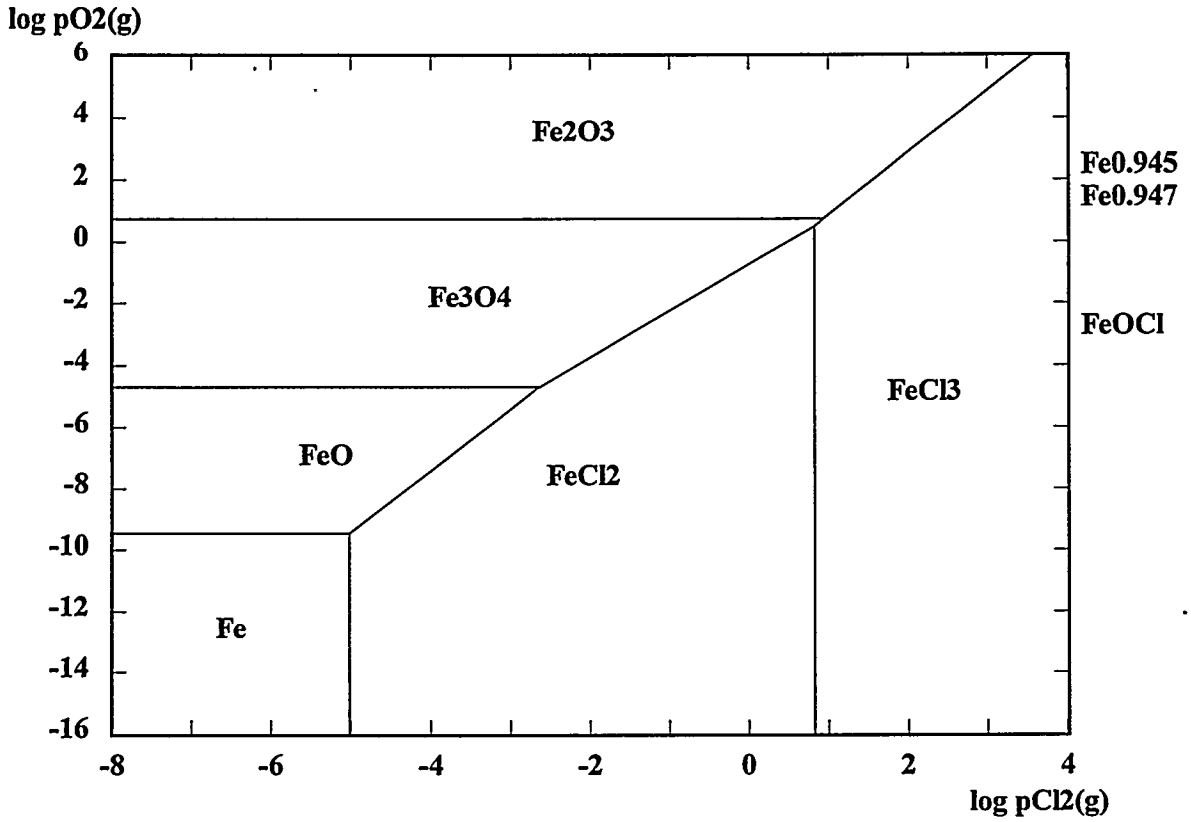

Since iron is present in a molten stable phase, oxygen and chlorine partial pressures were predicted to be less than 10E-10 and 10E-5 atm, respectively, at a reactor temperature of 1,500 °C. However, both FeO and $FeCl_2$ were likely to be present in small amounts. Using a similar analysis, the phase diagrams indicate that PbO, $PbCl_2$, ZnO, and $ZnCl_2$, as well as a significant quantity of the pure elements are predicted to be present.

To substantiate these findings, the Gibbs Free Energy of formation per mole of gas (either chlorine or oxygen) for the above compounds was examined. The diagram is shown in Figure 2.97. As predicted, the components most favored have the lowest free energy of formation. For instance, ΔG_f of PbO at 1,500 °C is approximately -30 kcal/mole, versus -8 kcal/mole and 17 kcal/mole for PbO_2 and Pb_3O_4, respectively. It was also observed that oxides form more readily than chlorides. Therefore, if the partial pressure of oxygen and chlorine in the CPU were identical, volatile heavy metal oxides would be favored over the chlorides'. However, because CEP is operated under strongly reducing conditions, chlorine partial pressure exceeds that of oxygen when chlorine is present in the feed material.

Figure 2.97
Gibbs Free Energy of Formation of VHMs Compounds

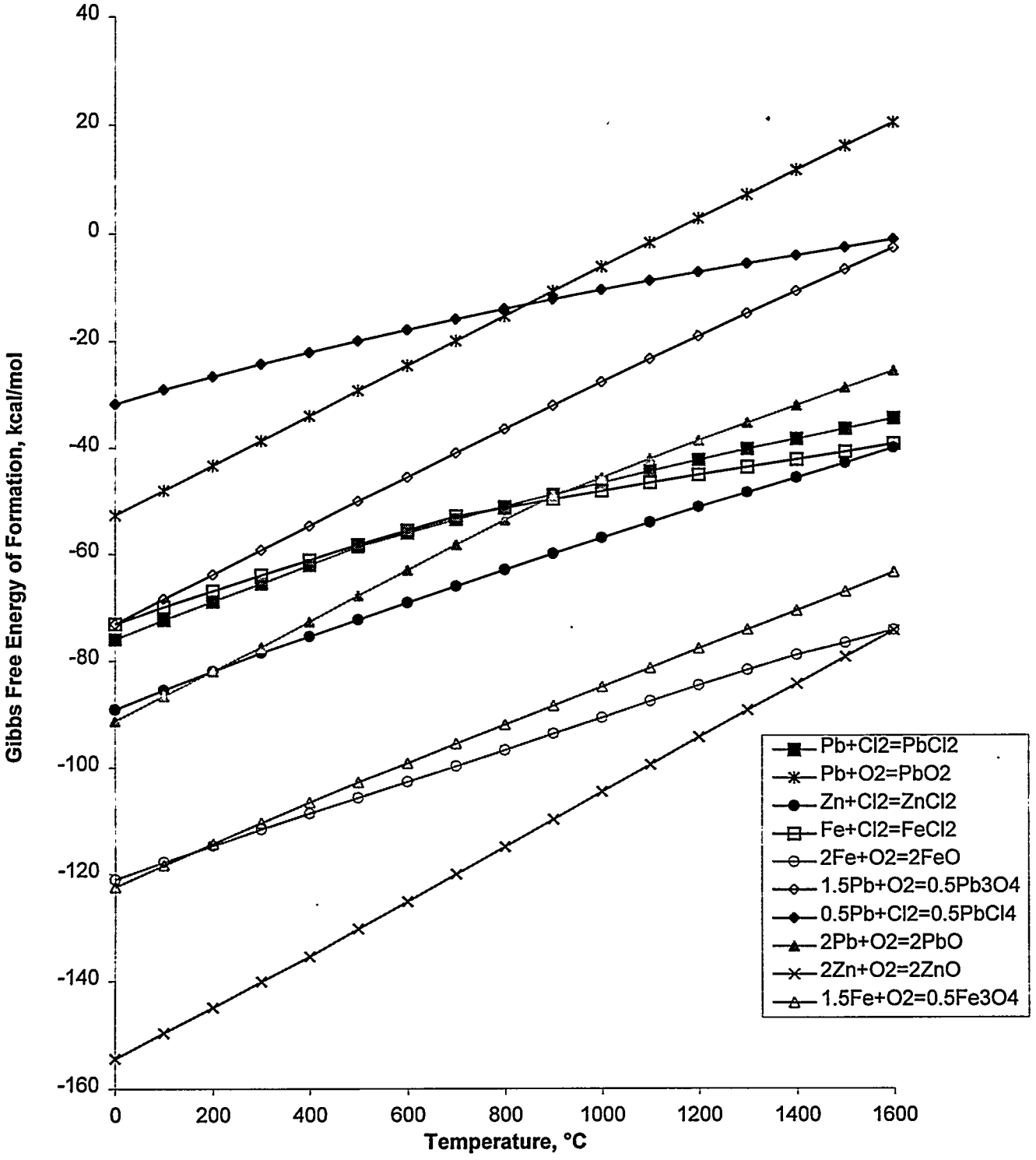

Vapor pressure data for the pure metals (Fe, Pb, and Zn) as well as for their oxides and chlorides were determined in order to predict which compounds would be expected to volatilize. The relationship between vapor pressure and the equilibrium constant can be derived by starting with Raoult's Law, which is valid for ideal mixtures maintained at low total pressures and low vapor pressures. Raoult's Law states:

$$x_i P_i^{vap}(T) = y_i P$$

where x_i and y_i are the mole fraction of component i in the liquid and gas phase, respectively, $P^{vap}(T)$ is the vapor pressure of component i at the given temperature (T), and P is the total pressure. At atmospheric pressure, the relationship between vapor pressure and the equilibrium constant becomes:

$$\log P_i^{vap}(T) = \log \frac{y_i}{x_i} = \log K$$

The vapor pressure curves were generated by calculating the equilibrium constant (K) for component phase transformation from the liquid to the gas phase. The results are shown in Figure 2.98.

Examination of the relative volatilities of these compounds indicated that at a reactor temperature of 1,500 °C, significant amounts would be volatilized from the bath into the gas phase. At 1,500 °C, the vapor pressure of all compounds but Fe, FeO, and ZnO was found to be greater than 0.1 bar. Since the temperature of the off-gas is typically decreased from over 1,200 °C to approximately 550 °C before the inlet to the gas cooler, a significant reduction in the vapor pressure was predicted to occur, leading to materials condensation and deposition on the interior pipe surface. Over the length of the off-gas duct, the vapor pressure was expected to decrease by several orders of magnitude for all compounds. The vapor pressure of the most volatile compound, $ZnCl_2$, was predicted to drop below 0.05 bar at 550 °C. Although much of the condensed material is thought to be entrained in the off-gas flow to the gas cooler, thermodynamic analysis indicated that deposition of volatile heavy metal compounds on the pipe surface is plausible. Demonstration unit experiments should incorporate thorough pre-run and post-run inspection and sampling of the off-gas duct in order to account for VHM collection in this area.

To understand the effect of a changed bath chemistry on VHMs partitioning and final form, experiments were conducted during which zinc and cesium were injected in an Fe-C-S. To illustrate which compounds have the highest potential to form under CEP reactor conditions, phase stability diagrams for iron, zinc, and cesium compounds as a function of oxygen and sulfur partial pressures have been determined, as shown in Figure 2.99, Figure 2.100, and Figure 2.101, respectively.

Figure 2.98
Vapor Pressure of VHMs Compounds

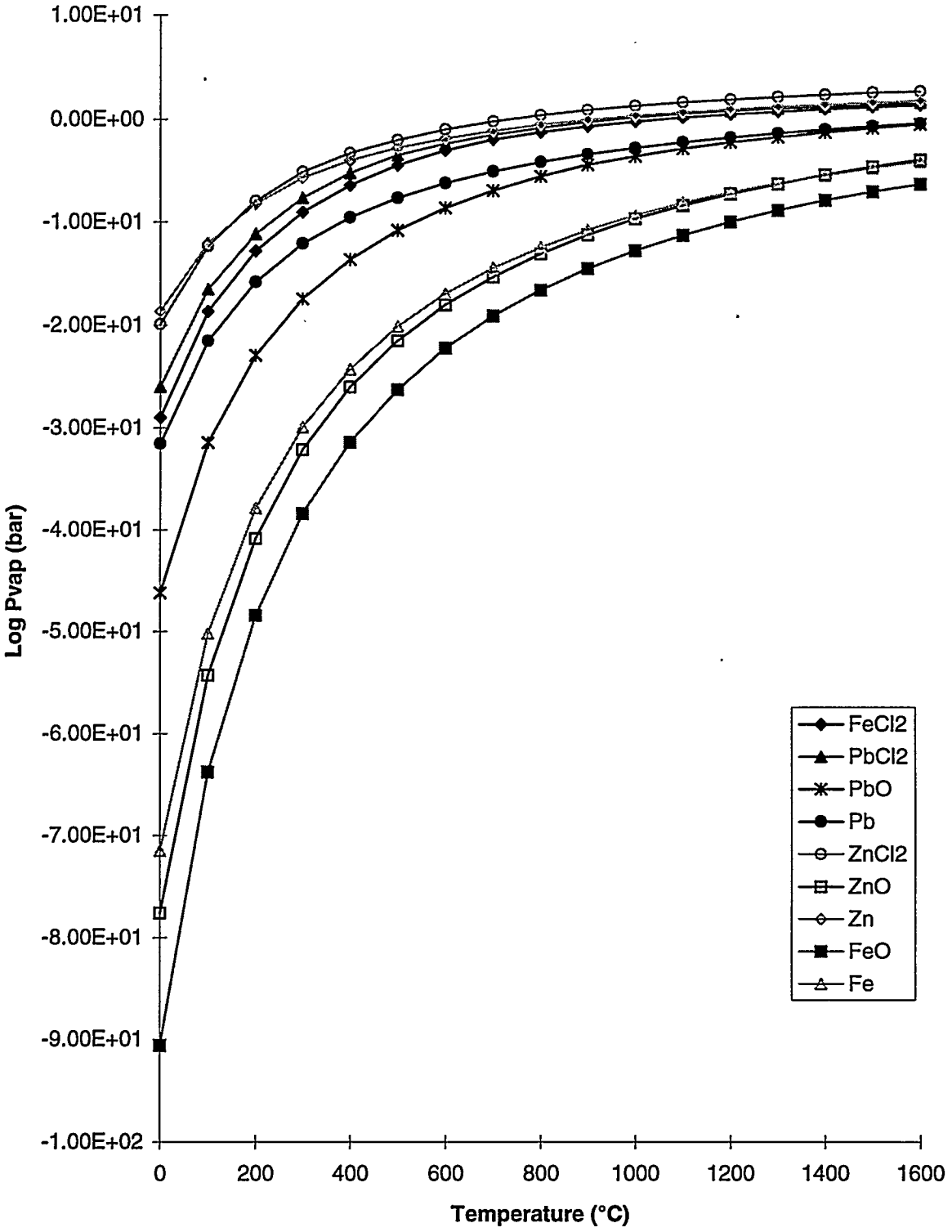

Figure 2.99
Phase Stability Diagram of Iron, Oxygen, and Sulfur at 1,500 °C

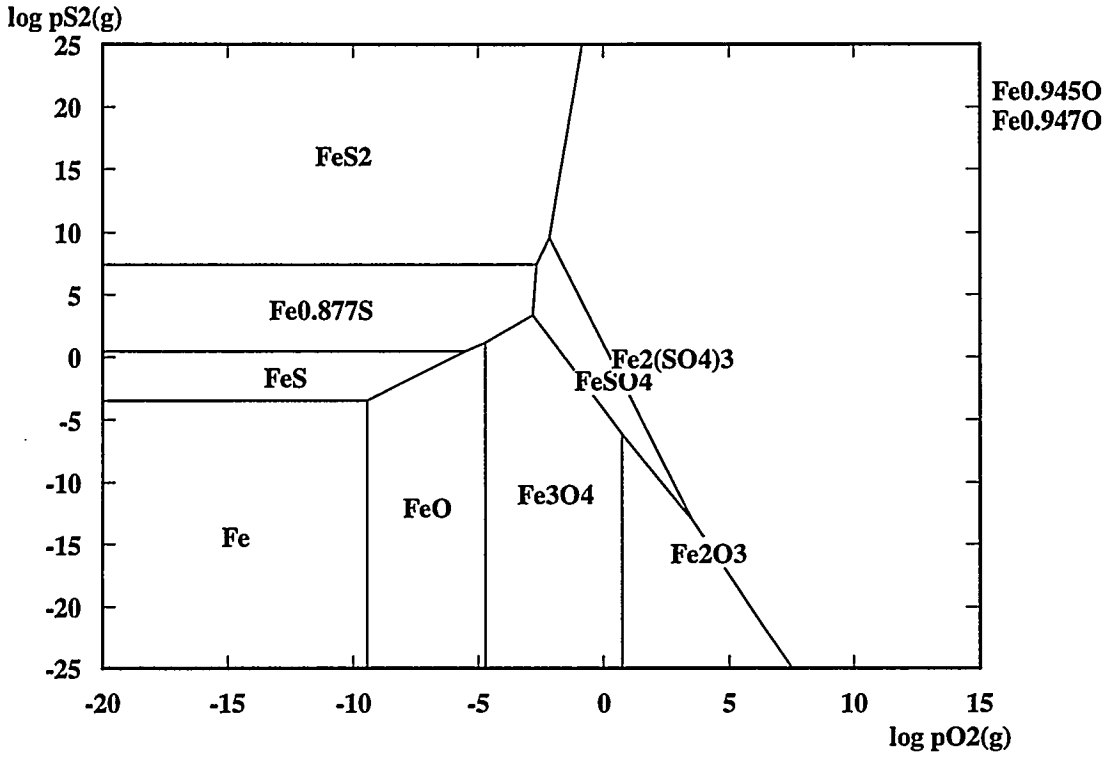

Figure 2.100
Phase Stability Diagram of Zinc, Oxygen, and Sulfur at 1,500 °C

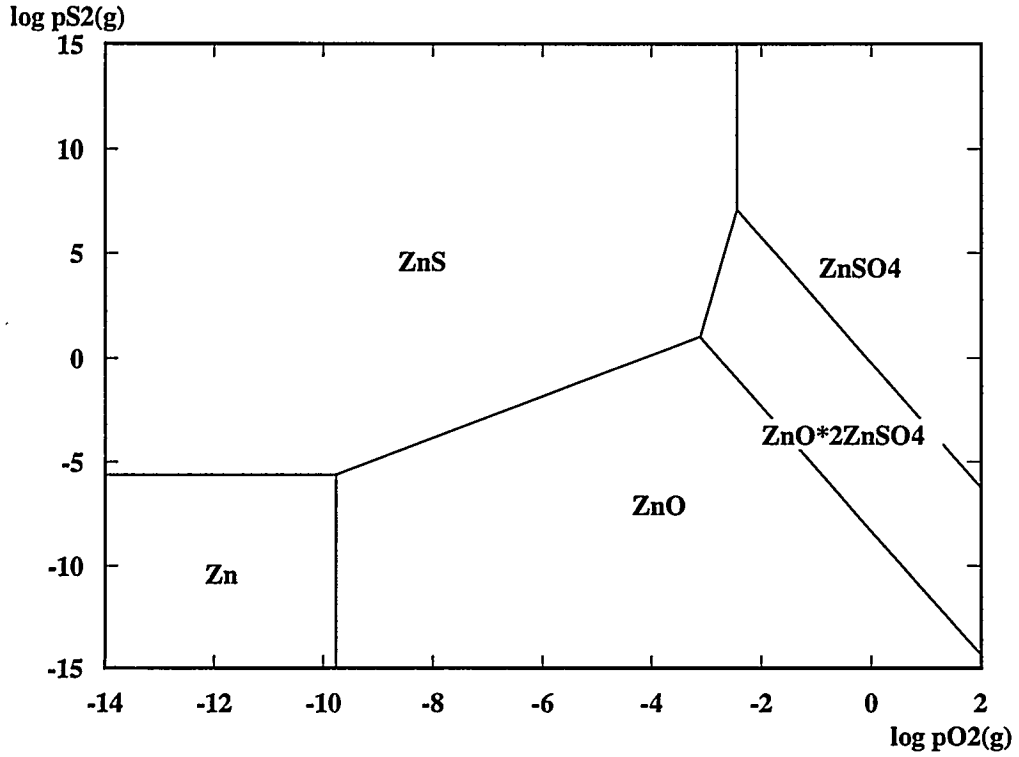

Figure 2.101
Phase Stability Diagram of Cesium, Oxygen, and Sulfur at 1,500 °C

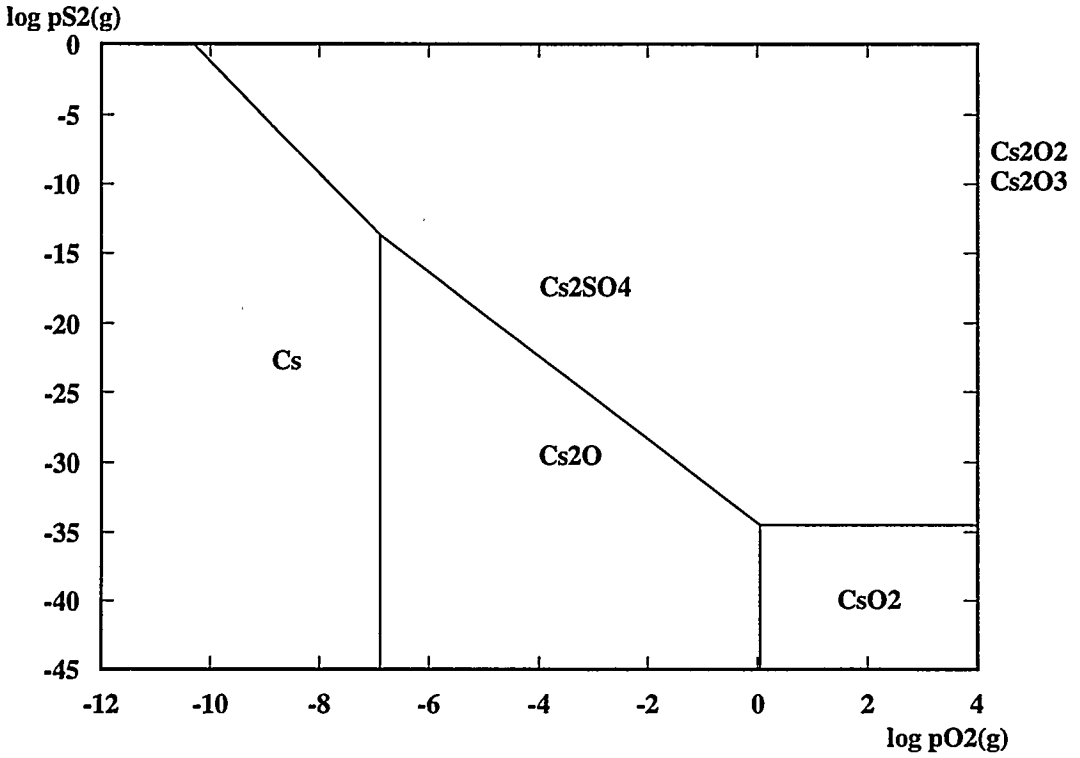

When sulfur is incorporated into the bath, both iron and iron sulfide (FeS) were predicted to be present as stable molten phases. Based on Figure 2.99, the oxygen partial pressure would be less than 10E-10 atm (at 1,500 °C), while that of sulfur would be between 10E-5 atm and 1 atm. Using these limits, the phase diagrams of Figure 2.100 and Figure 2.101 indicate that ZnS as well as a significant quantity of the pure elements (primarily Cs and Zn) would be predicted to be favored.

To substantiate these findings, the Gibbs Free Energy of formation per mole of gas for FeS, PbS, and ZnS was examined. As predicted, FeS was found to be the most stable (has the lowest ΔG_f) compound, as shown in Figure 2.102.

Vapor pressure data for the pure metals (Fe, Pb, Zn, and Cs) as well as for their sulfides were determined in order to predict which compounds would be expected to volatilize under typical CEP operating temperatures. As shown in Figure 2.103, cesium and zinc had the highest volatility, while FeS showed the least tendency for volatilization.

Figure 2.102
Gibbs Free Energy of Formation of VHMs Compounds

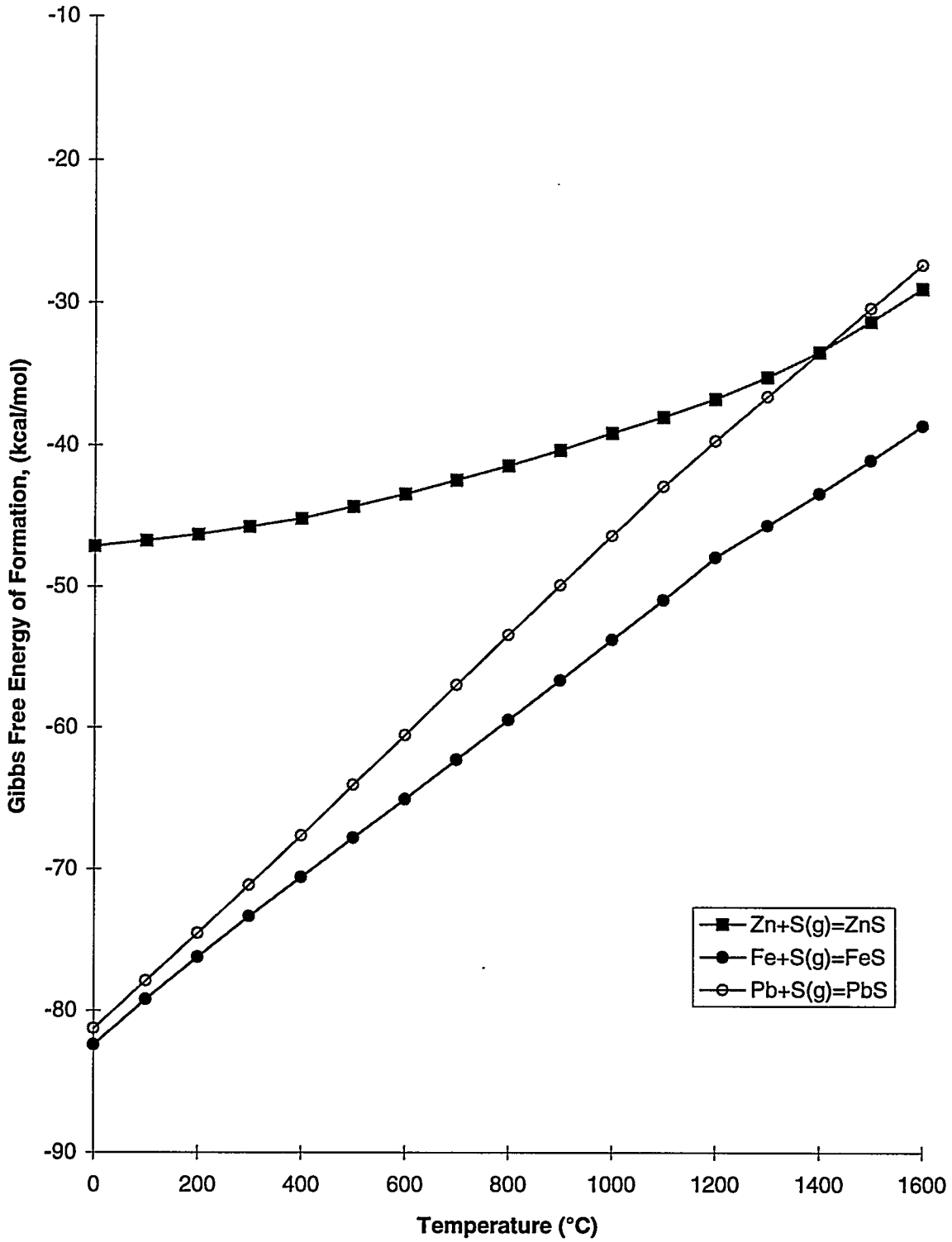

Figure 2.103
Vapor Pressure of VHMs Compounds

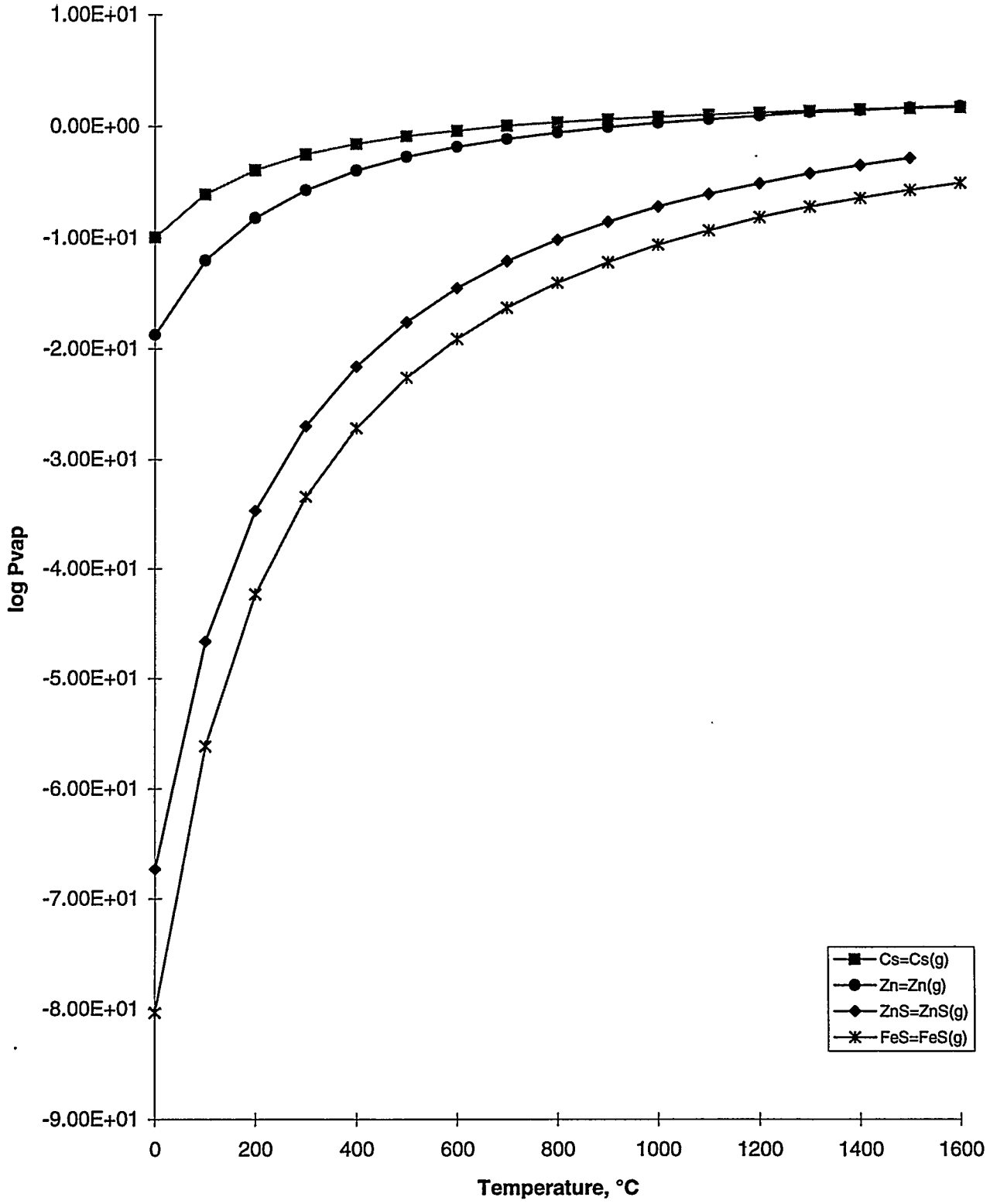

2.7.4. Method of Approach

Volatile heavy metals were mixed with surrogate waste feed materials and injected at varying levels as co-addidants into the CPU. Lead, zinc, and cesium were presumed to represent volatile heavy metals behavior in the CEP system. Depending on the form of the feed stream to be processed, the metals were injected in solid or liquid-dissolved form. methods for VHMs sampling have evolved during the course of the study. For example, on-line isokinetic dust sampling protocols were not utilized initially. These protocols were later implemented in order to obtain on-line measured dust loading data for comparison with post-run analytical results. A new sampling method was used to collect samples from additional areas of the gas handling train.

Dust samples were taken from pre-specified sampling ports installed in various locations on the demonstration unit, as shown in Figure 2.104. Post-run samples were taken from the tapped metal, process baghouse dust, tap/ceramic baghouse dust, gas cooler dust, and tapped ceramic (if present).

Figure 2.104
CEP Demonstration Prototype Unit - Sampling Ports

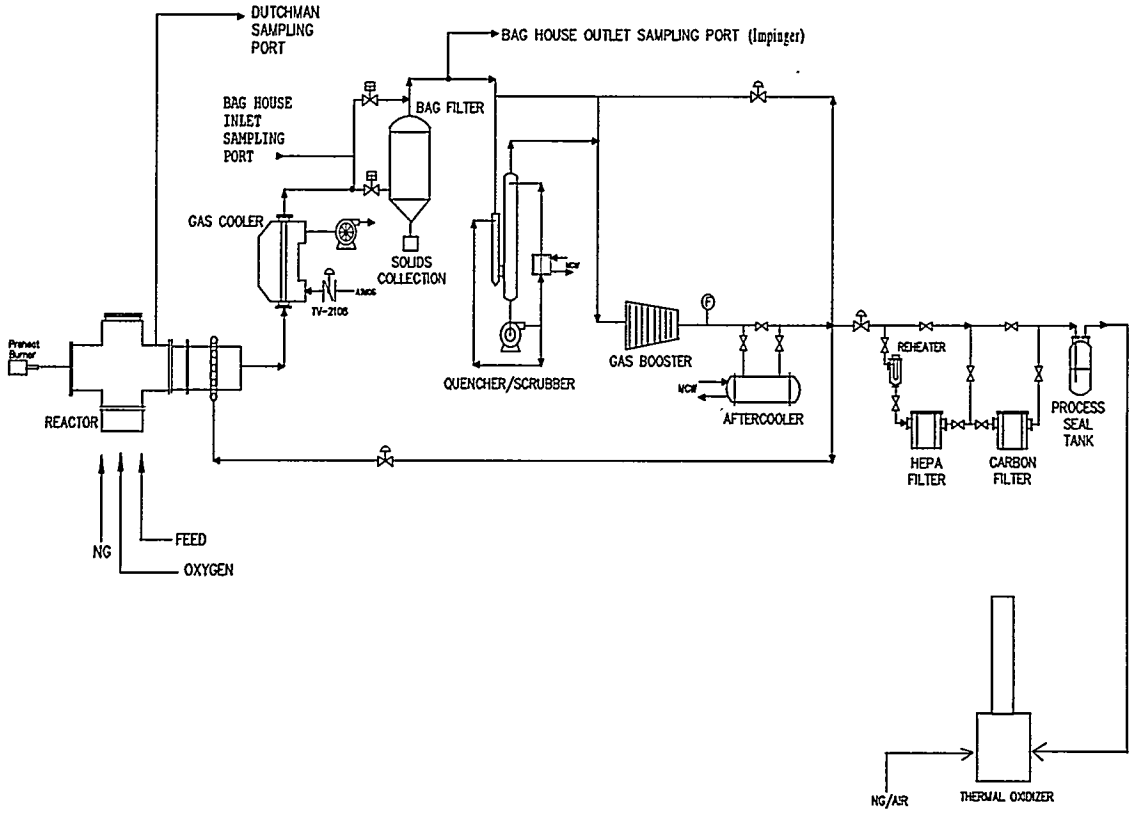

Mass balance calculations were performed by analyzing pre-injection and post-run samples. The inlet mass was calculated from knowledge of the feed composition and

total quantity injected. Outlet mass calculations were based on the total quantity and composition of post-run dust collected from the GHT and the tap/ceramic baghouse, and the quantity and composition of tapped metal and ceramic phases. Additional scraping samples were taken from the interior surface of the off-gas duct to assess the quantity and identity of dust deposition, if present.

2.7.5. Experimental Results

In the first set of experiments, lead and zinc were injected in an Fe-C metal bath. The quantity of metals injected was too small to ensure accurate partitioning data. During a second set of experiments, new methods have been added to the sampling protocol to improve mass balance closure data. The third set of experiments included injection of zinc and cesium in an Fe-C-S system.

2.7.6. Mass Balance Data (1)

The following tables summarize VHMs partitioning and mass balance closure data collected during demonstration-scale experiments. The experimental campaigns included R005-93-015, R005-93-017/018, R005-94-003/004, R005-94-005/006, and R005-94-008/009.

Table 2.44
R005-93-015: VHMs Partitioning

Sample Location	Pb (lb)	Pb Recovery (%)	Zn (lb)	Zn Recovery (%)
Total injected	7.79		7.79	
Tapped metal	ND	0	1.39	17.8
Tapped ceramic	ND	0	0.27	3.5
Gas cooler dust	0.008	0.11	0.01	0.12
Process baghouse dust	0.99	12.73	2.70	34.67
Tap/ceramic baghouse dust	0.0002	0.002	0.01	0.13
Cumulative	1.00	12.84	4.38	56.25
Scrubber - quench tank	0.31	3.98	0.28	3.60
Error - metal detection limits	0.13	1.67	0	0
Error - ceramic detection limits	0.02	0.26	0	0
Cumulative	1.46	18.75	4.66	59.85
Error - missing dust if dust recovery is 70%	1.43	18.33	3.88	49.88
Error - missing dust if dust recovery is 35%	2.85	36.67	7.77	99.77
Cumulative (with range for unaccounted dust)	2.89 - 4.31	37.08 - 55.42	8.54 - 12.43	109.73 - 159.62

Table 2.45
R005-93-017/018: VHMs Partitioning

Sample Location	Pb - lbs	Pb - % recovery	Zn (lb)	Zn Recovery (%)
Total injected	7.616		7.616	
Tapped metal	ND	0	0.38	5.05
Tapped ceramic	ND	0	ND	0
Gas cooler dust	0.92	12.09	0.35	4.61
Process baghouse dust	0.21	2.81	0.24	3.18
Tap/ceramic baghouse dust	0.72	9.40	0.017	0.22
Cumulative	1.85	24.30	0.99	13.06
Scrubber - quench tank	0.10	1.31	0.03	0.40
Error - metal detection limits	0.16	2.14	0	0
Error - ceramic detection limits	0.004	0.05	0.001	0.01
Cumulative	2.11	27.80	1.02	13.47
Error - missing dust if dust recovery is 70%	2.64	34.72	0.87	11.44
Error - missing dust if dust recovery is 35%	5.29	69.44	1.74	22.88
Cumulative (with range for unaccounted dust)	4.75 - 7.40	62.52 - 97.24	1.89 - 2.76	24.91 - 36.35

Table 2.46
R005-94-003/004: VHMs Partitioning

Sample Location	Pb - lbs	Pb - % recovery	Zn - lbs	Zn - % recovery
Total injected	11.52		11.52	
Tapped metal	ND	0	ND	0
Tapped ceramic	0.02	0.21	0.007	0.06
Gas cooler dust	0.10	0.83	0.012	0.104
Process baghouse dust	1.53	13.28	0.84	7.29
Tap/ceramic baghouse dust	1.03	8.98	0.087	0.76
Cumulative	2.68	23.30	0.95	8.25
Scrubber - quench tank	1.87	16.23	1.09	9.46
Error - metal detection limits	0.13	1.12	0.32	2.78
Error - ceramic detection limits	0	0	0	0
Cumulative	4.68	40.65	2.36	20.49
Error - missing dust if dust recovery is 70%	3.80	32.97	1.34	11.65
Error - missing dust if dust recovery is 35%	7.59	65.95	2.68	23.30
Cumulative (with range for unaccounted dust)	8.48 - 12.27	73.62 - 106.60	2.70 - 5.04	32.14 - 43.79

Table 2.47
R005-94-005/006: VHMs Partitioning

Sample Location	Pb - lbs	Pb - % recovery	Zn - lbs	Zn - % recovery
Total injected	22.7		7.43	
Tapped metal	0.53	2.33	1.05	14.13
Tapped ceramic	0.01	0.04	0.02	0.27
Gas cooler dust	0.20	0.88	0.67	9.02
Process baghouse dust	0.38	1.67	0.87	11.71
Tap/ceramic baghouse dust	0.20	0.88	0.03	0.40
Cumulative	1.32	5.80	2.64	35.53
Scrubber - quench tank	0.28	1.25	0.24	3.23
Error - metal detection limits	0	0	0	0
Error - ceramic detection limits	0	0	0	0
Cumulative	1.60	7.05	2.88	38.76
Error - missing dust if dust recovery is 70%	0.34	1.5	0.67	9.10
Error - missing dust if dust recovery is 35%	1.45	6.38	2.68	39.24
Cumulative (with range for unaccounted dust)	1.60 - 3.39	7.05 - 13.43	2.88 - 5.56	38.76 - 78.00

Table 2.48
R005-94-008/009: VHMs Partitioning

Sample Location	Pb - lbs	Pb - % recovery	Zn - lbs	Zn - % recovery
Total injected	0.43		7.51	
Tapped metal	0.34	79.1	0.66	8.8
Tapped ceramic	0.01	2.3	0.01	0.13
Gas cooler dust	0.03	6.9	0.21	2.8
Process baghouse dust	10.06	2339	16.03	213
Tap/ceramic baghouse dust	0.05	11.5	0.01	0.13
Cumulative	10.48	2437	16.92	225
Error - metal detection limits	0	0	0	0
Error - ceramic detection limits	0	0	0	0
Cumulative	10.48	2437	16.92	225
Error - missing dust if dust recovery is 70%	4.31	1002	6.87	92
Cumulative (with range for unaccounted dust)	10.48 - 14.79	2437 - 3439	16.92 - 23.79	225 - 317

The recovery values for both Pb and Zn shown in Table 2.44 through Table 2.47 were low, averaging less than 35 wt% (discounting the low dust collection error assumption). This was caused by the inability to account for all the dust accumulation, either because of ineffective post-run dust collection or because additional areas in the GHT were not examined for dust deposition. A thorough cleaning of the process baghouse following run R005-94-009 (see Table 2.48) revealed the presence of dust and VHMs contributed from earlier experiments. The quantity of dust collected from the gas handling train was estimated to comprise 35 to 70 wt% of accumulated dust. These estimates were used to calculate a range of VHMs recovery values (error in dust collection measurement). In addition, the estimated error due to equipment detection limits in the metal and ceramic layers was included in the mass balance calculations

The lack of retention of Pb and Zn in the metal or ceramic phase was in-agreement with results from earlier heavy metal partitioning studies. In general, the majority of zinc and lead was collected in the form of dust. Figure 2.105 and Figure 2.106 show the

cumulative percent recovery of Pb and Zn observed in the CEP system. It was also observed that for a given component, the percent recovery in each location in the gas handling train (e.g., process baghouse vs. gas cooler) was not consistent. The chemical form of the volatilized metal was thought to affect its condensation profile in the gas handling train. During processing of feed containing a relatively higher concentration of chlorinated components, VHM chlorides were preferentially formed (e.g., $ZnCl_2$). Because the volatility of $ZnCl_2$ is higher than that of ZnO (see Figure 2.98), zinc chloride was expected to travel farther down the GHT, and hence accounting for the difficulty in determining all the areas of deposition.

Figure 2.105
Cumulative Pb Recovery in the Demonstration Unit

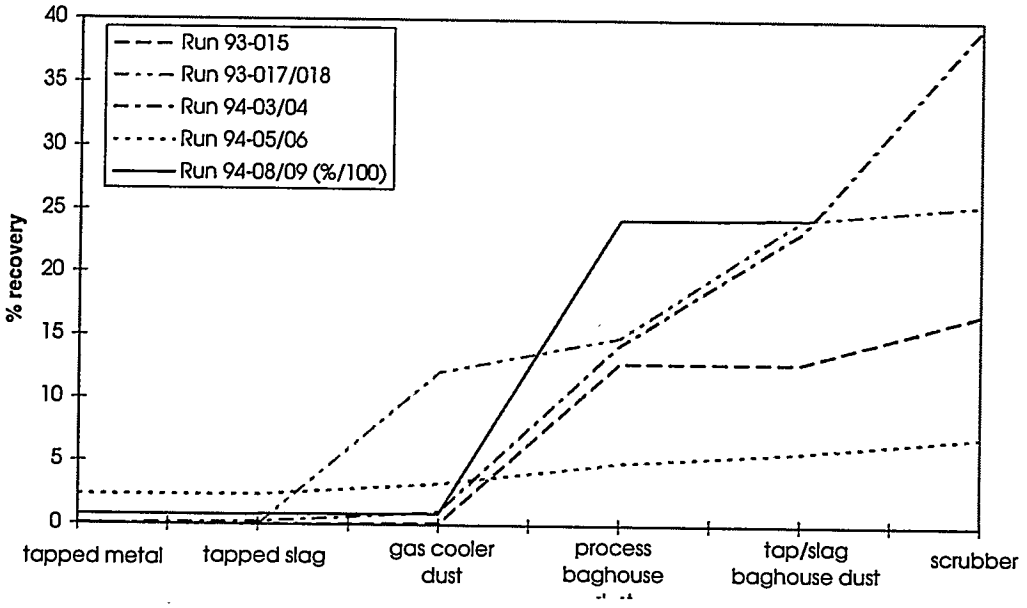

Figure 2.106
Cumulative Zn Recovery in the Demonstration Unit

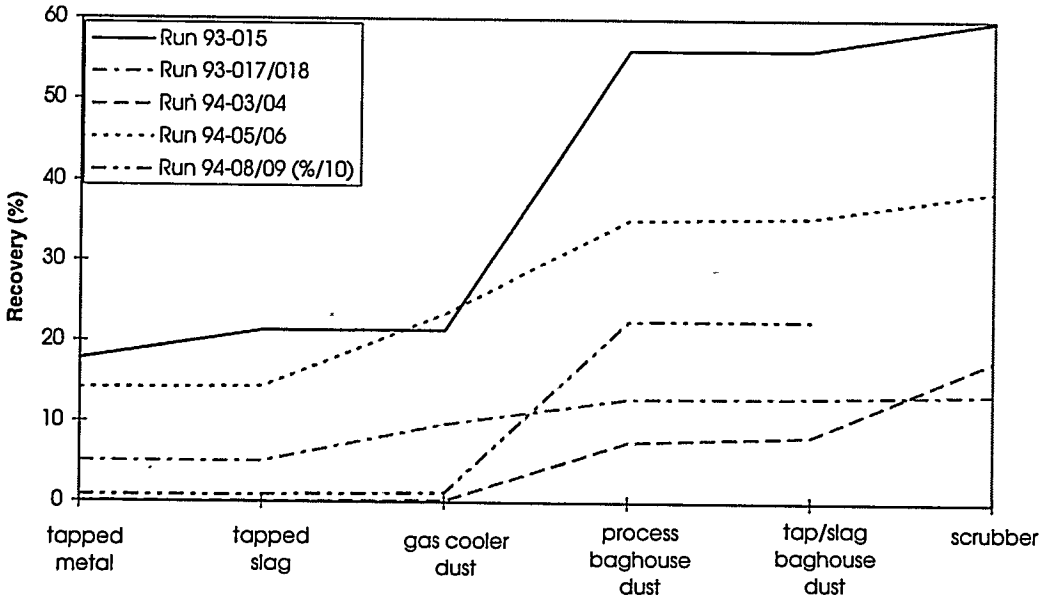

Additional samples were obtained from the off-gas duct in order to determine the extent of VHMs deposition upstream of the gas cooler. Results of the analytical analysis are shown in Table 2.49.

Table 2.49
Off-gas Duct Sampling Analysis

Element	South portion of disconnect flange (Wt%)	6" Downstream of south portion of disconnect joint (Wt%)
Lead	<0.010	<0.010
Zinc	<0.010	<0.010
Iron	56.87	61.25
Sulfur	2.81	2.45
Chlorine	<2.44	3.82
Phosphorus	0.26	0.39
Chromium	0.61	0.69
Sodium	3.31	1.56

No significant quantities of lead and zinc were detected. Although thermodynamic analysis predicted VHMs deposition in the off-gas duct, physical entrainment of dust particulates by the off-gas flow was believed to preclude any significant deposition.

The scrubber material contribution to the mass balance was thought to contain a high degree of error inherent in the measurement techniques. The post-run sampling method of the scrubber/quencher solution did not provide a representative sample of the materials captured in the scrubber. To address this deficiency, a new sampling protocol was used during R005-94-008/009 involving diverting a slipstream from the inlet to the scrubber and sending it through a set of impingers designed specifically for VHMs capture. No difference between the baseline (inert purge mode) concentrations and the majority of the impinger samples, indicating that only trace amounts of VHMs were present upstream of the scrubber. However, the feed concentration of Pb and Zn was very low for this run, which might have contributed to the lack of any detectable concentrations. Sampling from this location was continued in later runs.

2.7.7. Mass Balance Data (2)

To improve VHMs material balance closure, additional injection experiments were performed. Previous sampling protocols had limitations which contributed to some degree of uncertainty in the experimental results. Modifications to the sampling protocol and sampling devices were implemented in order to improve the quality of data collected. Isokinetic dust samples were taken in order to correlate the amount of dust generated with that actually collected. An attempt was made to improve post-run dust removal from the process baghouse and the gas cooler to reduce error associated with incomplete recovery.

A new sampling method was implemented downstream of the process baghouse by diverting a slipstream from the inlet stream to the scrubber and sending it through a set of impingers designed specifically for VHMs capture. The impinger set-up followed standard method 5 (M5) protocol for volatile heavy metal (lead) capture. The impinger train was comprised of 2 impingers filled with 0.1N nitric acid, one knockout impinger (empty), and one impinger filled with silica gel. The nitric acid solutions were analyzed for Pb and Zn. Preliminary impinger samples indicated that the quantity of VHMs present downstream of the process baghouse was negligible. Analysis of samples taken during VHM-enriched feed injection were used to confirm these findings.

Table 2.50 outlines the samples taken during the experimental campaigns (R005-94-010 and R005-94-011) and their purpose.

Table 2.50
VHM Samples During R005-94-010 and R005-94-011

Sample Location	Type of Sample	Purpose
Dutchman	non-isokinetic dust	Determine ratio of VHMs to other species to see if VHMs drop out in lines preferentially relative to other species
Baghouse inlet	isokinetic dust	Determine dust loading and VHM levels
Scrubber inlet	slipstream to impingers	Determine quantity of VHMs that remains in dust stream
Reactor bath	metal	Identify amount of VHMs which remain in reactor

Table 2.51 and Table 2.52 show a summary of the mass balance calculations for lead and zinc.

Table 2.51
R005-94-010: Volatile Heavy Metal Partitioning

Sample Location	Quantity Pb (lb)	Pb Recovery (%)	Quantity Zn (lb)	Zn Recovery (%)
Total injected	20.26		19.45	
Tapped metal	1.04	5.1	1.6	8.22
Tapped ceramic	0	0	0	0
Gas cooler dust	0.34	1.68	1.36	6.99
Process baghouse dust	20.51	101.23	9.51	48.89
Tap/ceramic baghouse dust	0	0	0	0
Cumulative	21.89	108.05	12.47	64.10
Error - metal detection limits	0	0	0	0
Error - ceramic detection limits	0.025	0.15	0.005	0.02
Cumulative	21.92	108.20	12.48	64.12

Table 2.52
R005-94-011: Volatile Heavy Metal Partitioning

Sample Location	Quantity Pb (lb)	Pb Recovery (%)	Quantity Zn (lb)	Zn Recovery (%)
Total injected	3.37		11.34	
Tapped metal	0.38	11.27	0.08	0.67
Tapped ceramic	0.001	0.03	0.0009	0.01
Gas cooler dust	0.039	1.15	0.386	3.41
Process baghouse dust	9.87	292.92	11.09	97.76
Tap/ceramic baghouse dust	0	0	0	0
Cumulative	10.29	305.39	11.55	101.84

Table 2.52 shows lead recovery was close to 100 wt% while zinc recovery was 64 wt%. In R005-94-011, calculated lead recovery was approximately 300 wt% and the zinc recovery was close to 100 wt%. These recovery values are relatively high compared with 25-30 wt% recoveries that were calculated in the earlier runs. The dramatic improvement in the relative recovery values for lead and zinc was attributed to effective cleaning and collection of dust from the process baghouse and other locations in the GHT. The large amount of lead collected from the gas handling train following R005-94-011 may have been contributed by earlier runs, hence accounting for a theoretically unplausible recovery value.

Impinger sampling was also performed at the baghouse outlet to determine the extent of VHMs which were present downstream of the baghouse. The results are summarized in Table 2.53 and Table 2.54.

Table 2.53
R005-94-010: VHM Impinger Baghouse Outlet Sampling

Feed (lb/min)	g Zn/SCF	g Pb/SCF	g Zn/g Zn fed (%)	g Pb/g Pb fed (%)
0	0.0012	0.0012		
1.2	9.69E-06	2.42E-05	0.02	0.06
1.4	0.0028	0.0029	6.91	6.73
1.9	0.0002	0.0001	0.37	0.23
Average	0.0011	0.0011	1.82	1.76

Table 2.54
R005-94-011: VHM Impinger Baghouse Outlet Sampling

Feed Rate (lb/min)	g Zn/SCF	g Pb/SCF	g Zn/g Zn fed (%)	g Pb/g Pb fed (%)
0	0.0007	0.0002		
1.3	0.0003	0.0002	0.77	0.38
2.1	0.0001	3.7E-05	0.19	0.06
Average	0.0002	0.0001	0.48	0.22

The average amount of each element collected at the baghouse outlet per amount fed was less than two percent in run R005-94-010, and less than half a percent in run R005-94-011, indicating that most VHMs were captured upstream of the scrubber.

2.7.8. Mass Balance Data (3)

Mass balance calculations were performed for zinc and cesium injected in an Fe-C-S bath containing varying levels of sulfur. Dust samples were taken from pre-specified sampling ports and analyzed for Zn and Cs, as outlined in Table 2.55.

Table 2.55
VHMs Sampling Protocol

Sample Location	Type of Sample	Purpose
Hot dust port	isokinetic dust	Determine dust loading and VHMs levels downstream of reactor
Baghouse inlet	isokinetic dust	Determine dust loading and VHMs levels upstream of baghouse
Reactor bath	metal	Identify amount of VHMs which remain in reactor

The partitioning data for Zn and Cs for runs R005-95-004/005, R005-95-006, and R005-95-007 are summarized in Table 2.56, Table 2.57, and Table 2.58, respectively.

Table 2.56
R005-95-004/005: Partitioning Data for Zn and Cs

Location	Quantity (lb)	Wt% Cs	Wt% Zn	Quantity Cs (lb)	Quantity Zn (lb)	Wt% Cs Recovery	Wt% Zn Recovery
Final Tapped Metal (run 005)[1]	4463	0.001	0.007	0.045	0.321	0.49	2.66
Gas Cooler	12	0.53	2.24	0.06	0.27	0.69	2.23
Process Baghouse	292	0.80	1.73	2.34	5.05	25.39	41.86
Total Recovery						26.57	46.75

[1] No final metal sample was taken from run 004

Table 2.57
R005-95-006: Partitioning Data for Zn and Cs

Location	Quantity (lb)	Wt% Cs	Wt% Zn	Quantity Cs (lb)	Quantity Zn (lb)	Wt% Cs Recovery	Wt% Zn Recovery
Final tapped metal	3642	0.005	0.0012	0.182	0.044	1.3	0.31
Process baghouse	40	0.67	1.99	0.268	0.796	1.91	5.69
Tap/ceramic baghouse	28.3	0.01	0.03	0.003	0.08	0.02	0.06
Gas cooler	0						
Total recovery						3.23	6.06

Table 2.58
R005-95-007: Partitioning Data for Zn and Cs

Location	Quantity (lb)	Wt% Cs	Wt% Zn	Quantity Cs (lb)	Quantity Zn (lb)	Wt% Cs Recovery	Wt% Zn Recovery
Partial tapped metal	3035	0.021	0.0077	0.637	0.234	2.10	0.77
Final tapped metal	2000	0.022	0.0072	0.44	0.144	1.45	0.47
Gas cooler dust	31	4.84	6.4	1.50	1.984	4.94	6.53
Process baghouse dust	426	4.27	6.24	18.19	26.582	59.84	87.44
Tap/ceramic baghouse dust	28	0.01	0.04	0.003	0.011	0.009	0.037
Total recovery						68.32	95.25

There was a wide variation in the recovery values for zinc and cesium (6, 47, and 95 wt% for Zn, and 3, 27, and 68 wt% for Cs), primarily due to inconsistent post-run dust collection from the gas handling train. Consistent with earlier findings, the majority of dust was collected from the process baghouse. On-line isokinetic dust samples were taken to gain a better understanding of VHMs loading in the gas handling train. The results are summarized in Table 2.59 through Table 2.62.

Table 2.59
R005-95-004: VHM Loadings during Solids Injection

Solids Feed Rate (lb/min)	Hot Dust Port: g Cs/g Cs fed	Hot Dust Port: g Zn/g Zn fed
1.3	0.47	0.30
1.6	0.31	0.25
1.3	0.36	0.26
1.2	0.16	0.14
Average	0.33	0.24

Table 2.60
R005-95-005: VHM Loadings during Liquid Injection

Location	Wt% Zn	g Zn/g Zn fed
Hot dust port	12.07	0.10
Baghouse inlet	2.37	0.07

Table 2.61
R005-95-006: VHM Loadings during Feed Injection

Solids Feed Rate (lb/min)	Hot Dust Port: g Cs/g Cs fed	Baghouse Inlet: g Cs/g Cs fed	Hot Dust Port: g Zn/g Zn fed	Baghouse Inlet: g Zn/g Zn fed
2.2	0.44		0.36	
1.9	0.30	0.26	0.34	0.27
1.5	0.41	0.45	0.51	0.50
2.0	0.37	0.33	0.39	0.40
1.9	0.40	0.38	0.49	0.41
2.4		0.21		0.23
Average	0.38	0.33	0.42	0.36

Table 2.62
R005-95-007: VHM Loadings during Feed Injection

Solids Feed Rate (lb/min)	Hot Dust Port: g Cs/g Cs fed	Baghouse Inlet: g Cs/g Cs fed	Hot Dust Port: g Zn/g Zn fed	Baghouse Inlet: g Zn/g Zn fed
1.6		0.57		1.02
1.8		0.70		1.01
2.3	0.25	0.30	0.38	0.52
2.3	0.96	0.20	1.11	0.30
2.4		0.11		0.20
2.5		0.19		0.21
2.4		0.36		0.43
Average	0.61	0.35	0.75	0.53

Typical loading (wt element/wt element fed) values for Zn and Cs ranged from 0.3 to 0.5 at both the hot dust port (gas cooler inlet) and the baghouse inlet. The metals' loadings in the baghouse inlet were only slightly less than those in the inlet to the gas cooler, indicating that only a small percentage of the volatile metals was deposited in the gas cooler. This is consistent with the fact that the majority of post-run dust was found in the process baghouse.

furthermore, the calculated loading values (wt element/wt element fed) of Zn and Cs indicated deposition of significant quantities of these elements in the off-gas piping upstream of the hot dust port. When samples were scraped off the piping surface and analyzed, small concentrations of zinc and cesium were detected. It was postulated that the observed loading was affected by the amount of time required for dissolution of Zn and Cs in the bath and subsequent volatilization. The isokinetic samples did not capture all the zinc and cesium added to the bath due to insufficient volatilization time.

The relatively small magnitude of the loading values calculated for both zinc and cesium indicate deposition of significant quantities of these elements in the off-gas piping upstream of the hot dust port. When samples were scraped off the piping surface and analyzed, only small concentrations of zinc and cesium were detected. It was postulated that the observed loading was affected by the amount of time required for dissolution of Zn and Cs in the bath before subsequent volatilization. The rates of

VHMs incorporation and volatilization are normally determined by the operating conditions such as bath temperature and the components' vapor pressures. The lower than predicted loadings were derived from the on-line isokinetic samples, which did not capture all the zinc and the cesium added to the bath due to insufficient volatilization time.

To compare with the actual amount of post-run dust collected, the total amount of dust predicted to be generated was calculated using average dust loadings, VHMs concentrations in the dust, and feed injection times. The predictions reflected dust and VHMs generation during feed injection only, and did not account for volatilization occurring during inerts injection or during post-injection operations. Therefore, it was believed that the amount of dust calculated would underestimate the actual amount of dust expected to accumulate in the gas handling train, assuming that dust collection was complete. Estimated dust and VHMs generation for runs R005-95-006 and R005-95-007 are shown in Table 2.63 and Table 2.64. The amount of material collected in the gas cooler was based on the difference between the dust loading entering the gas cooler and the dust loading entering the baghouse.

Table 2.63
R005-95-006: Estimated Dust Generation and VHMs Recovery

	Gas Cooler	Baghouse
Average off-gas rate (scfm)	161	161
Total injection time (min)	820	820
Total dust collected (lb)	11.85	62.17
Avg Cs concentration (Wt%)	7.30	7.46
Avg Zn concentration (Wt%)	8.03	8.21
Wt% Cs recovery (based on dust generated)	6.18	33.11
Wt% Zn recovery (based on dust generated)	6.80	36.48

Table 2.64
R005-95-007: Estimated Dust Generation and VHMs Recovery

	Gas Cooler	Baghouse
Average off-gas rate (scfm)	146	146
Total injection time (min)	1764	1764
Total dust collected (lb)	20.3	117.2
Avg Cs concentration (Wt%)	7.65	7.13
Avg Zn concentration (Wt%)	8.71	10.58
Wt% Cs recovery (based on dust generated)	5.11	27.51
Wt% Zn recovery (based on dust generated)	5.71	40.01

[1] Problems with sample equipment prevented isokinetic sampling. This number was generated assuming a similar difference in dust loading between hot dust port and baghouse inlet as observed in run R005-95-006.

The projected recovery values for zinc and cesium in run R005-95-006 were significantly higher than the actual recoveries (see Table 2.64) calculated based on the amount of dust collected. In addition, the projected dust generation during feed injection was 50% higher than the actual amount of dust recovered from the process baghouse. These findings are consistent with the conclusion that post-run dust collection was incomplete. In run R005-95-007, the projected recovery values for Zn and Cs were less than the actual recoveries by approximately 50%, and the projected dust generation was one third that of the actual dust removed from the process baghouse. The dust loading projections were based on isokinetic dust samples taken during feed injection only, and did not account for dust and VHMs generation during inert injection.

2.7.9. Conclusions

- Volatile heavy metals (Pb, Zn, and Cs) partitioned almost completely to the gas phase, with very little retained in the tapped metal or ceramic phase;
- Mass balance closure for VHM compounds varied significantly with the extent of post-run dust removal from the process baghouse. Materials mass balance closure approached 100 wt% for Pb and Zn in some experiments. The highest Cs recovery was 68 wt%;
- VHM loadings typically varied between 0.3-0.5 g/g fed at both the hot dust port and the baghouse inlet, based on isokinetic dual sampling. There was only a

slight drop in dust loading observed between the two locations, indicating that deposition of VHMs in the gas cooler was much less than in the baghouse;

- Calculations of projected dust and VHMs generation was consistent with the fact that the majority of dust accumulation occurred in the process baghouse. The projections also confirmed that the mass balance closure was strongly dependent on the extent of dust collection;

- Thermodynamic analysis predicted a large degree of VHM deposition in the off-gas duct between the CPU and the gas cooler. However, sampling analysis showed very little VHM concentration in the line, primarily due to entrainment by the high gas velocities exiting the CPU;

- Impinger sampling indicated that the quantity of VHMs present downstream of the baghouse was negligible.

2.7.10. Addition of Lead Chromate - Part 1

2.7.11. Objective

In earlier volatile heavy metal partitioning studies, VHMs were injected through the bottom tuyere in a fine solid form and in a dissolved liquid form. The amount of VHMs injected comprised 1-3 wt% of the total feed stream. Processing of waste feed materials can also be accomplished by top addition of materials on the metal bath surface. In this experiment, lead-containing feed was top-added below the surface of a molten metal bath, and data was collected on the partitioning of its elemental components.

2.7.12. Experimental Set-up

The test material for the trial consisted of lead chromate contained in 2 ½"x 2 ½"x 7.25" ceramic shell. Each shell, containing 1 lb of lead chromate powder, was packed in an open ended 3 ½" x 3 ½" x 8" metal container made from 1/16" steel plate. Steel balls were used to fill up some of the enclosed spare volume of the container and the contents were held in place by expanded metal mesh tacked over the open end. Vent holes near the closed end of the container were covered with mineral wool to prevent the lead chromate powder from being ejected by gases vented from the container. A 2" diameter solid steel bar 24" long was welded to the closed end of each container to counter buoyancy forces from the submerged container. The overall length, 32", was chosen to prevent the container assembly from lying horizontally in the metal bath.

A 36" long feeding pipe 6" in diameter was mounted on a pneumatically actuated gate valve sighted immediately above the molten metal bath of the CEP reactor. An isolating valve on top of the pipe allowed loading of individual shell container assemblies. Nitrogen purge and vent connections on the pipe enabled air and furnace gases to be swept from the loading tube as required.

The ceramic shells were enclosed in steel containers in order to force the containers to be submerged beneath the metal bath, hence ensuring that disposal of the powder over the bath and its possible entrainment in the off-gas was effectively minimized. This procedure was deemed necessary because the CEP demonstration unit used for this experiment consists of one chamber only and, therefore, does not facilitate pre-processing of the feed while maintaining the quality of the off-gas.

2.7.13. Method of Approach

Prior to lead chromate addition, five metal samples were taken in quick succession to determine average chromium and lead baseline concentrations in the metal bath. An isokinetic gas probe was operated for 30 minutes at the baghouse inlet in order to collect a baseline dust sample.

One shell-container assembly was loaded into the feeding tube which was then isolated and purged. The lower gate valve was activated and the assembly with the round bar uppermost was dropped vertically into the bath. A slight darkening of the TV monitor display provided visual evidence of the container's drop into the bath. Five more markers were loaded and dropped in succession over a period of 21 minutes.

Dust sampling at the baghouse inlet was initiated at the start of feed addition and was continued for 30 minutes after the last shell was added. Five more post-injection metal samples were taken 60 minutes after the last shell was added to the bath to determine metals' retention in the bath. In addition, post-run metal and dust samples were taken from the tapped metal and the GHT, respectively, for analysis. The metal and dust samples were analyzed by an independent third party laboratory. Table 2.65 shows the sampling protocol followed during the experiment.

Table 2.66 shows chromium and lead levels detected in the metal samples during the experiment.

Table 2.65
Sampling Protocol

Timing	Sample Type	Purpose
Baseline (prior to lead chromate addition)	Metal samples (5)	Obtain average Cr and Pb baseline concentrations in the metal
Baseline (prior to lead chromate addition)	Isokinetic dust at the baghouse inlet port	Determine Cr and Pb baseline concentrations in the dust
During addition of lead chromate (start 5 minutes before first addition and finish 30 minutes after final addition)	Isokinetic dust at the baghouse inlet port	Determine Cr and Pb concentrations and loading in the dust during injection
30 minutes after final addition	Isokinetic dust at the baghouse inlet port	Determine residual Cr and Pb concentrations in the dust
60 minutes after final addition	Metal samples (5)	Obtain average final Cr and Pb concentrations in the metal
Post-run (after metal tapping)	Tapped metal sample	Obtain post-run Cr and Pb concentrations in the metal
Post-run	Collected dust from GHT	Obtain post-run Cr and Pb amounts in the GHT

Table 2.66 Concentration of Cr and Pb in the Metal Bath

Sample	Pb (ppm)	Cr (ppm)
Pre-Injection Metal (Avg)	< 25	380±11
Post-Injection Metal (Avg)	1264±80	692±43
Post-Run Metal	< 25	830

2.7.14. Discussion

In a CEP system, reaction thermodynamics and solution equilibria drive feed conversion and product synthesis. When a feed is injected into the CEP reactor, it dissociates into its elemental constituents. Reducible metals will readily dissolve in the molten metal solvent, as predicted by the Gibbs Free Energy diagram (Figure 2.107),

under the given reaction conditions. Therefore, at a reaction temperature of 1260-1345 °C, chromium will be recovered as an alloy in the iron solvent.

Figure 2.107
Gibbs Free Energies of Oxidation

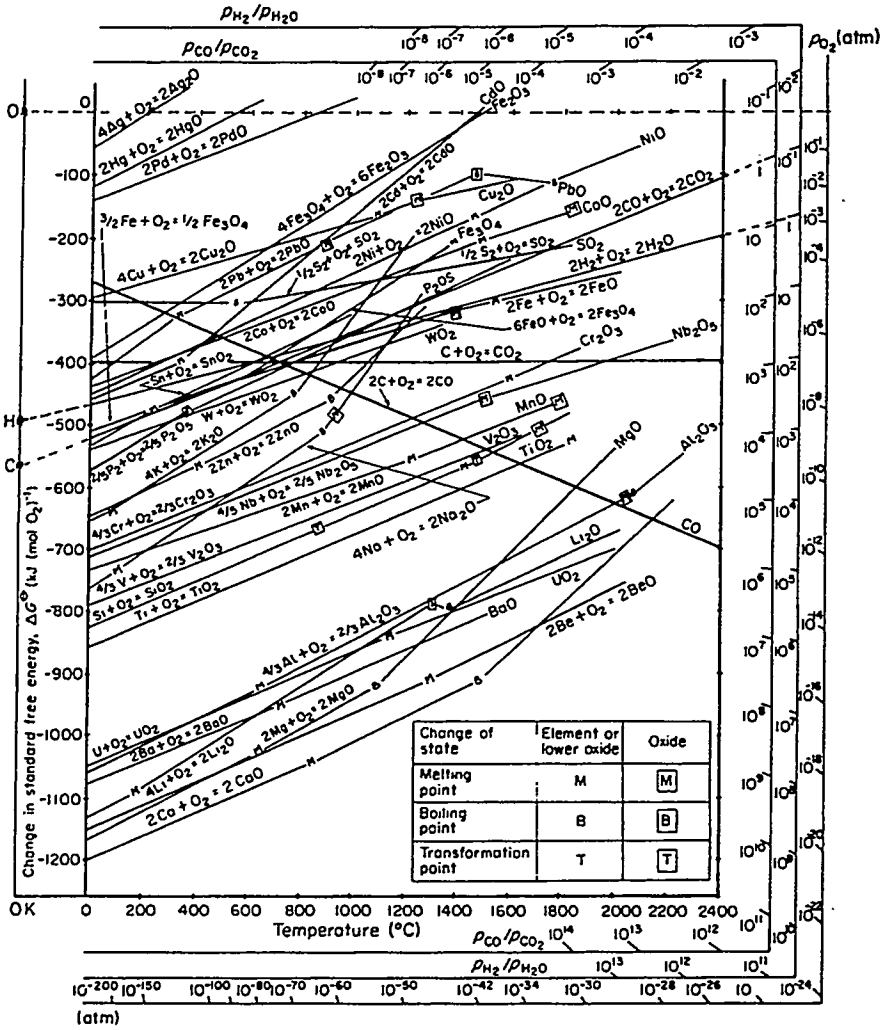

Source: Moore, J.J., Chemical Metallurgy, 2nd Edition Butterworth & Co., London, 1990

Lead partitioning, on the other hand, is dependent on a number of factors and hence cannot be predicted simply. Although the boiling point of lead (1740 °C) is higher than normal CEP operating temperatures, the vapor pressure of lead is high enough that it can severely limit the capture of lead in the metal phase. When lead (or lead compounds) is added to the metal bath, it will dissolve until it reaches its solubility limit as determined thermodynamically. The amount of time needed for lead concentration in the bath to reach steady-state depends on the operating conditions. In

addition, the stripping action of the evolving gas stream can also cause entrainment of lead into the gas handling train. Earlier work (see 3.7.1) had suggested that at temperatures of 1480-1540 °C, less than 15% of the lead was recovered in the metal phase indicating significant lead volatility.

Post-run partitioning data for chromium and lead were calculated. In order to maximize the amount of Cr and Pb accounted for, post-run dust and liquid samples were collected from the various process units in the gas handling train including the process baghouse, the gas cooler, the quencher, the scrubber, and the tap/ceramic baghouse. Mass balance closure data and recovery values for Cr and Pb are summarized in Table 2.67.

Table 2.67 Post-run Partitioning and Recovery data for Cr and Pb

	Qty (lbs)	Pb (ppm)	Cr (ppm)	Pb (lbs)	Cr (lbs)	Pb (% recovery)	Cr (% recovery)
Gas cooler average	31	1920	163	0.060	0.005	1.575	0.6737
Tap/ceramic baghouse	28	760	510	0.021	0.014	0.563	1.904
Process baghouse	426	3888	140	1.656	0.060	43.817	7.952
Scrubber (gals)	100	92	6	0.077	0.005	2.031	0.668
Quencher (gals)	100	32	14	0.027	0.012	0.706	1.558
Metal (post-addition sample)	2000	1239[1]	312[2]	2.478	0.624	65.556[3]	83.20[4]
Metal[5] (tapped sample)	2000	25	450[6]	0.050	0.900	1.323[7]	120[8]
Total recovery (based on tapped metal samples)						50.02	132.76

[1,2] (post-addition concentration) - (pre-addition concentration)
[3,4] Recovery % values in the metal bath based on post-addition samples
[5] Post-run sample
[6] (post-run concentration) - (pre-addition concentration)
[7,8] Recovery % values in the metal bath based on post-run samples

Recovery in the metal phase was calculated from the difference in average initial and final concentrations, based on a bath weight of 2,000 lb. This bath weight was determined as the average of the initial pre-melting metal charge to the reactor and the amount of metal tapped out (rather than just using the final tap weight). The lead chromate powder material was determined to contain 63 wt% Pb and 12.5 wt% Cr. The weight of the powder material was approximately 1 lb per shell.

As predicted, chromium was almost completely partitioned to the metal phase. Only trace levels were detected throughout the gas handling train, as shown in Table 2.68. The high chromium recovery (greater than 100%) was due to uncertainty in estimating the final metal bath weight and to the fact that the total amount of chromium (0.75 lb) added to the reactor was small relative to the total bath weight (2,000 lb).

Post-run analysis of the tapped metal samples (see Table 2.66) shows that changes in pre- and post-run lead levels were not detectable, indicating complete partitioning of lead to the gas phase. These results are consistent with data observed during earlier lead partitioning experiments. The partitioning of significant quantity of Pb to the metal phase observed shortly after lead chromate addition was due to insufficient volatilization time.

Volatilization rates for lead were calculated during different time periods in order to compare with the known quantities of Pb collected in the dust. A summary of these calculations is shown in Table 2.68.

Table 2.68
Pb Volatilization Calculations

	During markers addition	Post markers addition (1 hour)	Inert injection prior to tapping	Total Pb (lbs)
Initial Pb in bath (lbs)	3.78	2.52[1]	2.06	
Total Off-gas flow (scfm)	90	85	100	
Time (min)	102	60	160	
Total Pb volatilized (lbs)	0.47	0.18	0.46	1.11
[1] based on post-addition metal samples				

Based on the amount of volatilized Pb calculated for each time period, the high concentration of Pb in the metal bath analytically observed 60 minutes after the last feed addition is reasonable. The total amount removed from the bath based on the volatilization calculations was less than observed by the tapped metal analysis. However, these calculations did not include any removal by entrainment, which can be quite significant at the observed off-gas rates. The combination of the volatilization and the entrainment over a sufficient time period resulted in approximately 100% partitioning of Pb to the gas phase.

The majority of lead was collected from the process baghouse dust. The overall recovery of Pb was 50%, which is slightly higher than typical Pb recovery data from previous experimental runs on the demonstration unit. The incomplete closure is attributed to difficulty in accounting for the small amounts of lead injected and to the incomplete recovery of dust from the gas handling train.

2.7.15. Conclusions

- The injection method ensured dissolution of the marine markers in the bath without allowing bypassing of lead chromate;
- Chromium partitioned almost completely to the metal bath. Only trace levels were detected in the dust entering the baghouse;
- Based on post-run samples, lead partitioned almost completely to the gas phase and was condensed and captured in the GHT. Volatilization calculations supported the higher Pb concentrations observed shortly following lead chromate addition.

2.7.16. Addition of Lead Chromate - Part 2

2.7.17. Objective

During an earlier experiment, ceramic containers of lead chromate were added to the top of the metal surface. To ensure complete submersion upon addition, the ceramic shells were enclosed in steel containers. The metal components (Cr and Pb) partitioning was evaluated and documented (see 3.7.2). The primary goal of this experiment was to examine the metals' dissolution and partitioning patterns through addition of lead chromate shells on top of the metal bath without submerging. In addition, comparisons were made with submerged top addition of the feed material.

2.7.18. Experimental Procedure

Prior to lead chromate addition, the CEP demonstration unit was maintained at steady-state conditions during inert gas injection through the tuyere to induce bath agitation. The liquid metal temperature was 2,750 °F. The metal bath carbon content was 3 wt%.

2.7.18.1.1. Base Line

Five metal samples were taken in quick succession prior to feed addition to provide a base line metal analysis in the bath. Fifteen pounds of nickel was added as a tracer so that a more accurate determination of the metal bath weight could be calculated through subsequent bath meta sampling. Off-gas dust sample were also taken prior to lead chromate charging to determine base line conditions.

2.7.18.1.2. Single Addition of Containers

Twenty ceramic shell containers were added individually through the double lock and hopper system to the bath over a period of 40 minutes. Off-gas dust sampling was performed throughout the addition period and was concluded only 30 minutes after the last container was added. Five metal samples were taken from the bath after addition was completed.

2.7.18.1.3. Multiple Addition of Containers

An additional twelve lead chromate containers were added to the bath in quick succession. Two batches each containing five shells and one batch of two shells were all added through the double lock and hopper feeding system within three minutes. Five metal samples were taken from the bath 10 minutes after the bulk addition of markers was completed. Samples were taken at an approximately two minute intervals. Single metal samples were taken at hourly intervals for another three hours to examine short and long term bath compositions.

2.7.19. Results And Discussion

2.7.19.1.1. Base Case

The initial five metal samples were analyzed by X-ray fluorescence (XRF) in house. A summary of metal sampling analysis is shown in Table 2.69. Prior to lead chromate addition, bath chromium, lead, and nickel content was 0.0435 wt%, < 0.003 wt%, and 0.032 wt%, respectively. The lead content was picked up merely as a trace. Fifteen pounds of nickel were added to the bath. The nickel content rose to 0.480 wt% indicating a bath weight of 3,330 lb.

Table 2.69
Metal Sampling Analysis: Base Case

Sample No	Concentration Cr (Wt%)	Pb (Wt%)	Ni (Wt%)
M1	0.042	<0.001	0.033
M3	0.043	<0.004	0.034
M4	0.043	<0.001	0.030
M5	0.044	<0.004	0.030
M7	0.044	<0.001	0.033
Average	**0.0435**	**<0.003**	**0.032**

2.7.19.1.2. Single Additions

Five samples (M9 through M13) were taken after the sequential addition of 20 individual ceramic containers of lead chromate. The average chromium content of the bath rose to 0.14 wt%. The bath nickel content of 0.488 wt% indicated a bath weight of 3,290 lb. Based on this close correspondence, a bath weight of 3330 pounds was used throughout the analysis.

Lead remained at a trace level in the bath despite the addition of approximately 13.8 lb Pb contained in the 20 containers, indicating complete partitioning to the gas phase. The average bath concentration of chromium was 0.14 wt%, resulting in an overall recovery of 127 wt% (mass Cr out/mass Cr in).

Table 2.70
Single Additions of Lead Chromate Ceramic Containers

Sample No	Concentration Cr (Wt%)	Pb (Wt%)	Ni (Wt%)
M9	0.13	<0.001	0.50
M10	0.18	<0.001	0.49
M11	0.13	<0.001	0.49
M12	0.13	<0.001	0.49
M13	0.13	<0.004	0.49
Average	**0.14**	**<0.002**	**0.049**

2.7.19.1.3. Multiple Additions

Twelve lead chromate containers were added batchwise (batches of 5, 5, and 2 containers). Samples M14 through M18 were taken at timed intervals of approximately 2 minutes. Sampling began ten minutes after the last batch was added.

It was observed that dust loading in the off-gas stream increased shortly after the addition of the containers before gradually declining. Lead volatilization from the bath occurred upon addition which diminished as the lead content in the bath was reduced. The bath lead content remained at trace levels throughout the sampling period, indicating rapid dissolution in the bath followed by evaporation into the gas phase. Alternatively, lead sublimation could have occurred without dissolution in the metal bath prior to departing the CPU.

Bath metal sampling revealed an average chromium content of 0.176 wt%, resulting in a recovery value of 77 wt%. The overall (single and multiple addition sequences) mass balance closure for chromium was 107.5 wt%. Table 2.71 is a summary of metal sampling analysis.

Table 2.71
Multiple Additions of Lead Chromate Ceramic Containers

Sample No	Concentration Cr (Wt%)	Pb (Wt%)	Ni (Wt%)
M14	0.16	<0.001	0.51
M15	0.17	<0.001	0.50
M16	0.18	<0.004	0.50
M17	0.20	<0.004	0.49
M18	0.17	<0.004	0.51
Average	**0.18**	**<0.003**	**0.502**

2.7.19.1.4. Isokinetic Sampling

Isokinetic dust sampling was performed at the baghouse inlet prior to, during, and after lead chromate containers were added. Pre-addition samples were taken to determine baseline Pb and Cr concentrations. Post-addition samples were taken to determine if lead volatilization was complete. Both the pre- and post-addition samples showed negligible accumulation of dust. The samples taken during feed addition were analyzed for Pb and Cr by an independent third party laboratory. Lead and chromium loadings in the process off-gas measured at the hot dust port and the process baghouse inlet are shown in Table 4.

Table 2.72
Pb and Cr Loading in the Off-gas during Lead Chromate Addition

Baghouse Inlet Samples	Addition Sequence	Pb Wt%	Cr Wt%	Pb Loading (g/scf)	Cr Loading (g/scf)
Hot dust port	Single	90.69	0.14	0.059	9.14E-05
Baghouse inlet	Single	9.38	0.07	0.238	1.78E-03
Hot dust port	Multiple	69.59	0.15	0.291	6.27E-05
Baghouse inlet	Multiple	3.96	0.01	0.004	1.0E-05
Run R005-95-007		1.40	0.07	0.0018	8.8E-05

During the addition of multiple containers, lead and chromium component loading decreased from the hot dust port to the baghouse inlet, due to condensation. The baghouse inlet loading during the single addition sequence appeared unreasonably high compared to the loading calculated during multiple additions. Moreover, the loading observed at the baghouse inlet was higher than that calculated at the hot dust port. It is most likely high due to inaccuracies with the sample weight or a large amount of dust clogging the filter and reducing the flow, resulting in non-isokinetic flows through the sample device. The loading values for Pb and Cr at the baghouse inlet were comparable to those calculated during the submerged addition of lead chromate. There was not an appreciable effect of using different charging methods on Cr and Pb concentration in the off-gas.

A standard EPA Method 5 impinger train was used to sample the process off-gas at the baghouse outlet (upstream of scrubber), to determine the amount of Pb remaining in the gas during lead chromate addition. No visible particulates accumulated on the filter, and Pb levels were non-detectable in the impinger solutions. This result is consistent with earlier findings indicating that very little, if any, VHMs existed downstream of the process baghouse.

2.7.20. Conclusions

- Top addition of lead chromate contained in ceramic shells to the metal bath achieved complete decomposition of the compound into its elemental components;

- Chromium partitioned to the metal bath, with negligible amounts detected in the gas phase. Lead was not retained in the metal phase leading to complete separation of the two metals;

- The method of feed addition (submerged, top-charging, singly, or batchwise) did not have an appreciable effect on the ability to effectively separate and recover chromium and lead metals.

3. Task 1.2: Experimental Test Plan

MMT developed and executed a comprehensive experimental test plan that was designed to provide performance data on the application of the Catalytic Extraction Process to DOE wastes. The test plan was developed to demonstrate selective radionuclide partitioning and immobilization using surrogates; destruction of hazardous organic constituents; partitioning of non-radioactive recyclable metals, and processing of bulk solids. These experiments also addressed waste feed management, safety management, general operations management, and off gas management. The results of this experimental test plan, which are used throughout this final report, have successfully demonstrated the versatility of CEP to process a broad spectrum of waste materials in the DOE complex. A listing of the experiments performed under this contract have been categorized by major tasks in the statement of work and are presented in Table 3.1 through Table 3.4. In the numerous cases where experiments addressed more than one major task, the experiment has been listed under the task that was the primary focus of the experiment. It should also be noted that experiments addressing the partitioning of actual radionuclides were not funded by the current contract; therefore, they have not been included in these tables.

Table 3.1
Task 1.1 - Design CEP System

Run#	Date	Title
CTP-94-001		**Bulk Solids Injection Water Model**
WM-94-002		Investigation of Different Lance Designs
WM-94-003		Characterize Bubbles and Flow Patterns While Simulating Bulk solids Injection Through a Lance; nitrogen injection
WM-94-004		Back Attack Video Studies
WM-94-005		Bulk Solids Injection Studies - Ammonia Trials Week of 2/21/94 Ammonia Trials - 2" Lances
WM-94-006		Ammonia Trials - 2" Lances
WM-94-007		Bulk Solids Water Model Studies
WM-94-008		Bulk Solids Lance Injection Studies CO_2 Trials 2" Lances
WM-94-010		Bulk Solids Water Model Tuyere Placement Studies
WM-94-012		Bulk Solids Water Model Reinjection Studies
WM-94-015		Bulk Solids Water Model, Ceramic Studies
WM-94-017		Bulk Solids Water Model, Ceramic Studies
WM-94-020		Ceramic Studies Bulk Solids Water Model
R012-95-003	3/14/95	Lance Studies on the Bulk Solids Water Model
CTP-04-025		**Test Protocol for Evaluation of Alternative Metal/Alloy Systems for CEP**
10-94-049		Chlorinated Hydrocarbon Injection Into A Nickel Bath: Product Quality Studies; Evaluate CO_2 reduction in the metal bath
10-94-050		Blank test of CO_2 injection in non-metallic bath to investigate reducing potential of CO_2 with graphite susceptor.
10-94-052		CO injection in copper bath with graphite susceptor
10-94-059		Injection of CO to determine dust formation
10-94-062		Injection of CO to determine dust formation
10-94-064		Determine dust formation via syngas shift reaction in a copper bath
10-94-066		Injection of Hydrocarbon
10-94-070	10/25/94	Co-injection of ethylene and CO_2 through four hole lance
10-94-072	10/27/94	Injection of ethylene through a four hole lance
10-94-074	10/31/94	Injection of ethylene with and without CO_2
05-94-084	11/7/94	Evaluation of alumina crucible with SiC coated graphite
05-94-085	11/10/94	Evaluation of alumina crucible using steel ball as susceptor
05-94-085	11/29/94	Evaluation of alumina crucible using steel ball as susceptor
05-95-086	11/30/94	Evaluation of alumina crucible without susceptor
10-94-087	12/2/94	Injection of ethylene through four hole lance

Table 3.1 (Continued)

Run#	Date	Title
CTP-04-025		**Test Protocol for Evaluation of Alternative Metal/Alloy Systems for CEP (continued)**
10-94-089	1/4/95	Evaluate low carbon steel pipe as induction heating susceptor
R003-95-001	1/9/95	CO-injection of ethylene and CO_2 in a metal Bath
R003-95-002	1/11/95	Repeat of CO-injection of ethylene and CO_2 in a metal bath
R003-95-003	1/16/95	Injection of ethylene in a metal bath
R003-95-004	1/19/95	CO-injection of Ethylene with CO_2 in a metal bath
R003-95-005	1/23/95	Injection of ethylene in a metal bath
R003-95-006	1/25/95	Injection of ethylene in a metal bath
R003-95-007	1/27/95	CO_2 injection in metal bath
R003-95-008	1/31/95	Hydrocarbon injection with and without CO2
R003-95-009	2/3/95	Hydrocarbon injection with and without CO2
R003-95-010	2/8/95	Hydrocarbon injection with and without CO2
R003-95-011	2/13/95	Partial oxidation of ethylene with CO_2
R003-95-012	2/15/95	Injection of ethylene in a metal bath
R003-95-015	3/21/95	Ethylene in Oxygen-rich Bath
R003-95-016	3/24/95	Ethylene Injection Studies
R003-95-017	3/28/95	Conversion of Ethylene at Different Reactor Conditions
R003-95-018	3/29/95	Ethylene Injection in a Binary Molten Metal System
R003-95-019	4/3/95	Ethylene Injection in a Binary Molten Metal System
R003-95-020	4/5/95	Conversion of Ethylene in a Binary Molten Metal System

Table 3.1 (Continued)

Run#	Date	Title
CTP-95-008		Particulate Characterization and Control, and Capture of VHMs
R003-95-021	5/23/95	Processing of feed containing volatile heavy metals
R003-95-022	5/31/95	Processing of feed containing volatile heavy metals
R003-95-023	6/7/95	Processing of feed containing volatile heavy metals (alkali-3)
R003-95-024	6/9/95	Processing of feed containing volatile heavy metals (alkali-4)
R003-95-025	6/13/95	Processing of feed containing volatile heavy metals (alkali-5)
R003-95-026	6/15/95	Processing of feed containing volatile heavy metals (alkali-6)
R003-95-028	6/27/95	Processing of feed containing volatile heavy metals (alkali-8)
R003-95-033	7/26/95	Feasibility of Processing Group I, Chlorinated Materials (Alkali-11)
R003-95-034	7/28/95	Feasibility of Processing Group I, Chlorinated Materials (Alkali-12)
R003-95-036	8/15/95	Feasibility of processing Group I, chlorinated materials (Alkali-14)
R003-95-037	8/21/95	Feasibility of processing Group I, chlorinated materials (Alkali-15)
R003-95-038	9/1/95	Feasibility of processing Group I, chlorinated materials (Alkali-16)
R003-95-039	9/7/95	Feasibility of processing Group I, chlorinated materials (Alkali-17)
R003-95-042	10/17/95	Feasibility of processing Group I, chlorinated metals
R003-95-043	10/24/95	Feasibility of processing Group I, chlorinated metals (Alkali-19)
R003-95-044	10/31/95	Feasibility of processing Group I, chlorinated metals (Alkali-20)
R003-95-045	11/01/95	Feasibility of processing Group I, chlorinated metals (Alkali-21)
R013-95-079	11/09/95	Melt down of ceramic phase in a Crucible
R013-95-080	11/15/95	Feasibility of processing Group I, chlorinated metals (Alkali-22)
R003-95-049	11/29/95	Feasibility of processing Group I, chlorinated metals (Alkali-23)
R014-95-086	12/6/95	Feasibility of processing Group I, chlorinated metals
R009-95-016	12/8/95	Feasibility of processing Group I, chlorinated metals
R013-95-082	12/13/95	Feasibility of processing Group I, chlorinated metals
R009-95-017	12/14/95	Feasibility of processing Group I, chlorinated metals
R014-95-087	12/18/95	Feasibility of processing Group I, chlorinated metals

Table 3.1 (Continued)

Run#	Date	Title
CTP-95-010		**Feed Dissolution Studies during Lance Injection**
R014-95-048	6/1/95	Injection of methane/argon
R014-95-049	6/9/95	Injection of toluene/argon
R014-95-050	6/19/95	Injection of ethylene/argon
R014-95-052	6/23/95	Injection of C_2H_4/H_2/argon
R014-95-053	6/27/95	Injection of C_3H_8/H_2/argon
R014-95-056	7/25/95	Injection of $C_7H_8/H_2/Ar$
R014-95-057	7/25/95	Injection of $C_7H_8/H_2/Ar$: effect of alumina chips
R014-95-058	7/31/95	Injection of $C_7H_8/H_2/Ar$: effect of alumina chips
R014-95-059	8/2/95	Injection of $CH_4/H_2/Ar$
R014-95-060	8/8/95	Injection of $CH_3Cl/H_2/Ar$
R014-95-061	8/11/95	Injection of $CH_4/Cl/H_2/Ar$
R014-95-062	8/16/95	Injection of $CH_2Cl_2/H_2/Ar$
R014-95-063	8/22/95	Injection of $CH_2Cl_2/H_2/Ar$
R014-95-064	8/31/95	Injection of $CH_2Cl_2/H_2/Ar$
R014-95-065	9/1/95	Injection of $C_3H_8/H_2/Ar$
R014-95-066	9/7/95	Injection of $CH_3Cl/H_2/Ar$
R014-95-067	9/11/95	Injection of $CH_3Cl/H_2/Ar$
R014-95-077	9/19/95	Injection of $C_7H_8/H_2/Ar$
R014-95-080	10/30/95	Injection of CH_4, $C_7H_8/H_2/Ar$
R014-95-082	11/08/95	Injection of CH_4, $C_7H_8/H_2/Ar$
CTP-95-020		**Bulk Solids Volatilization/Dissolution Zone Investigation**
R014-95-084	11/14/95	Processing of large batch of ceramic material
CTP-95-022		**Off-gas Duct Studies**
R026-95-003	12/8/95	Dust characterization in off-gas stream
R026-95-004	12/11/95	Dust characterization in off-gas stream
R026-95-005	12/12/95	Dust characterization in off-gas stream
R026-95-006	12/20/95	Dust characterization in off-gas stream
CTP-95-028		**Plasma Torch Operations Studies**
R028-95-001	11/27/95	Initial plasma torch test series
CTP-95-029		**Characterization of Bulk Solids Polishing Zone**
R030-95-001	12/15/95	Physical model evaluation of Zone 2 concept

Table 3.1 (Continued)

Run#	Date	Title
R005-95-004/007		**Experimental Campaign on the Demonstration Unit**
R005-95-004/7	5-7/95	Establish partitioning of VHMs at low bath carbon
R005-95-008		**Experimental Campaign on the Demonstration Unit**
R005-95-008	8/95	Establish partitioning of VHMs at saturated bath carbon
R005-95-009/010		**Experimental Campaign on the Demonstration Unit**
R005-95-009/10	9/95	Establish partitioning of VHMs
R005-95-011		**Experimental Campaign on the Demonstration Unit**
R005-95-011	10/95	Study partitioning and capture of VHMs (Zn, Cs) and Hg in GHT
R005-95-011	10/95	Perform bulk solids addition experiments
		Experimental Campaign on the Advanced Processing Unit (APU)
R007-95-013	10/11/95	Multi-zone reactor characterization pilot studies
R007-95-013	10/19/95	Multi-zone reactor characterization pilot studies

Table 3.2 Task 1.4 - Optimization of the Vitreous Phase for Stabilization of Radioactive Species

Run#	Date	Title
CTP-94-009		Optimization of the Vitreous Phase for Stabilization of Radioactive Species
10-94-001		Demonstrate selective partitioning of radionuclide surrogate hafnium from the metal phase (Fe) to the oxide phase.
10-94-002		Demonstrate selective partitioning of radionuclide surrogate hafnium from the metal phase (Fe) to the oxide phase.
10-94-004		Demonstrate selective partitioning of radionuclide surrogate hafnium from metal phase (Fe) to the oxide phase.
10-94-005		Demonstrate selective partitioning of radionuclide surrogate hafnium from metal phase (Fe) to the oxide phase.
10-94-007		Perform temperature gradient measurements with metal bath.
10-94-008		Reactor Characterization
10-94-009		Reactor Characterization
10-94-010		Reactor Characterization
10-94-011		Reactor Characterization
10-94-012		Reactor Characterization
10-94-013		Testing of a 4-hole lance
10-94-014		Reactor between Co and H_2
10-94-015		Refractory/ceramic test experiment
10-94-019	10/25/94	Initial evaluation of refractory-ceramic interaction
10-94-022	10/25/94	Initial evaluation of refractory-ceramic interaction
10-94-026	10/27/94	Initial evaluation of refractory-ceramic interaction
10-94-029	10/28/94	Initial evaluation of refractory-ceramic interaction
10-94-032	10/28/94	Initial evaluation of refractory-ceramic interaction
10-94-035	10/29/94	Initial evaluation of refractory-ceramic interaction
10-94-037	11/1/94	Initial evaluation of refractory-ceramic interaction
10-94-039	11/1/94	Initial evaluation of refractory-ceramic interaction
05-94-029		Demonstrate selective partitioning of radionuclide surrogate hafnium form the metal phase (Fe) to the oxide (borosilicate) phase.
05-94-037		Demonstrate better material balance closure, a non-porous 99.8% alumina crucible will be used.
05-94-074	11/3/94	Calcium aluminosilicate glass will be evaluated for operability in a partitioning experiment conducted with a nickel bath
05-94-076	11/5/94	Evaluate glass operability, demonstrate and quantify selective partitioning of surrogates from metal phase to oxide phase
05-94-077	11/13/94	Evaluate glass operability, demonstrate and quantify selective partitioning of surrogates from metal phase to oxide phase

Table 3.2 Continued

Run#	Date	Title
CTP-94-009		**Optimization of the Vitreous Phase for Stabilization of Radioactive Species (continued)**
05-94-078	11/18/94	Evaluate different glasses when used in a nickel bath
05-94-080	11/21/94	Evaluate effect of using a basic glass in a nickel bath on ceramic foaming
CTP-94-013		**Development of Integrated Containment System Testing Unit Applicable to CEP**
WM-95-001	1/11/95	Refractory Longevity Studies
R013-95-002	1/10/95	Penetration of FeS through a Sintered Al2O3 Dry-vibe for Containment
R006-95-001	1/13/95	Containment Test to Evaluate Penetration of FeS through a Sintered Al_2O_3 Dry-vibe
R006-95-003	1/25/95	Extended Compatibility Test with HCl
R006-95-004	2/9/95	Extended Compatibility Test with HCl
R019-95-001	2/27/95	Hot Check of ICTF
R019-95-002	4/24/95	Verify ICTF Functionality and Generate Corrosion Data
20-94-023		Establish wear rate of NARCO K85C material in metal/ceramic
20-94-024		Wear Rate of NARCO K85C Material
20-94-025		Wear Rate of NARCO K85C Material
20-94-026		Hot Check of APU Coil
20-94-027		Wear Rate of NARCO Spinal Material
20-94-028		Wear Rate of NARCO Spinal Material
20-94-028A		Test Proper Operation of 20-lb Coil
20-94-032		Establish Wear Rate of NARCO Spinal Material
CTP-94-014		**Bottom Tapping Pilot Studies**
R007-95-010	7/24/95	APU-1 commissioning, sintering and bottom tapping

Table 3.2 Continued

Run#	Date	Title
CTP-94-019		**Electrochemical Study on Ceramic/Refractory/Metal Interface Reactions**
10-94-041		Electrochemical Study on Ceramic/Refractory/Metal Interface Reactions
10-94-043		Electrochemical Study on Ceramic/Refractory/Metal Interface Reactions
10-94-045		Electrochemical Study on Ceramic/Refractory/Metal Interface Reactions
10-94-058		Electrochemical Study on Ceramic/Refractory/Metal Interface Reactions
10-94-060		Electrochemical Study on Ceramic/Refractory/Metal Interface Reactions
10-94-066		Electrochemical Study on Ceramic/Refractory/Metal Interface Reactions
10-94-076	11/01/94	Electrochemical study on ceramic/refractory/metal interface reactions (7th experiment)
10-94-078	11/09/94	Electrochemical study on ceramic/refractory/metal interface reactions (8th experiment)
R013-95-010	1/23/95	Testing of Zircoa electrodes
R013-95-012	1/24/95	Testing of Zircoa electrodes
CTP-94-020		**Relative Performance of Several Refractory Bricks With a CaO-Al_2O_3-SiO_2 Ceramic Phase and Carbon-Saturated Iron**
20-94-044		Spin Tests on Refractory Brick in contact with C-saturated Fe and CAS ceramic
20-94-046		Spin Tests on Refractory Bricks
20-94-047		Spin Tests on Refractory Bricks
20-94-049		Spin Tests on Refractory Bricks
20-94-051		Spin Tests on Refractory Bricks in Contact with C-saturated Fe and CAS ceramic
20-94-052		Final Planned Spin Test
R006-95-008	3/21/95	Spin Tests on Refractory Bricks in Contact with Low Carbon Fe
R006-95-009	3/27/95	Spin Tests on Refractory Bricks in Contact with Low Carbon Fe
R006-95-010	3/31/95	Spin Tests on Refractory Bricks in Contact with Low Carbon Fe

Table 3.2 Continued

Run#	Date	Title
CTP-94-022		**Chemical Skulling**
R013-95-021	2/7/95	Chemical Skulling
R013-95-023	2/9/95	Chemical Skulling
R013-95-024	2/14/95	Chemical Skulling
R013-95-025	2/22/95	Chemical Skulling
R013-95-026	2/16/95	Chemical Skulling
R013-95-028	2/28/95	Chemical Skulling
R013-95-029	3/2/95	Chemical Skulling
R013-95-030	3/6/95	Chemical Skulling
R013-95-031	3/7/95	Chemical Skulling
R013-95-036	3/31/95	Chemical Skulling
R013-95-044	4/28/95	Chemical Skulling
R013-95-049	5/8/95	Chemical Skulling
R013-95-050	5/16/95	Chemical Skulling
R013-95-051	5/24/95	Chemical Skulling
R013-95-052	6/2/95	Chemical Skulling
CTP-94-024		**Study of Relation between Electrical Resistivity and Viscosity of the Ceramic Phase**
R013-95-056	6/20/95	Run #1, base line resistivity measurements
R013-95-057	6/27/95	Run #2, reproducibility run
R013-95-058	7/6/95	Reproducibility Run, Run #3
R013-95-059	7/10/95	Cell Constant Variation Run #4
R013-95-060	7/19/95	Cell constant Variation Run #5
R013-95-061	7/24/95	Cell constant Variation Run #6
R013-95-062	7/28/95	Test of two single piece electrode configurations, Run #7
R013-95-064	8/8/95	Test of two single-piece electrode configurations, run #8
R013-95-069	9/6/95	Reproducibility of resistivity measurement with single piece electrode configurations, run #9
R013-95-074	10/26/95	Reproducibility of resistivity measurement with single piece electrode configurations, run #10
R013-95-075	10/31/95	Reproducibility of resistivity measurement with single piece electrode configurations, run #11

Table 3.2 Continued

Run#	Date	Title
CTP-94-027		**Relative Performance of Selected Refractory Bricks**
20-94-056	10/31/94	Gas Injection System and GHT for CTP-94-027.
20-94-057	11/1/94	Compatibility Test with HCl Contacting 4 Refractory Bricks in a Carbon-Saturated Nickel Environment.
20-94-059	11/14/94	Compatibility Test with HCl Contacting 4 Refractory Bricks in a Carbon-Saturated Nickel Environment.
20-94-060	11/17/94	Compatibility Test with HCl Contacting 4 Refractory Bricks in a Carbon-Saturated Nickel Environment.
20-94-062	11/30/94	Compatibility Test with HCl Contacting 4 Refractory Bricks in a Carbon-Saturated Nickel Environment.
20-94-063	12/7/94	Compatibility Test with HCl Contacting 4 Refractory Bricks in a Carbon-free Copper Environment.
R006-95-005	2/28/95	Perform a Corrosion Test for a Nickel Bath at Minimal Molten Temp.
R006-95-006	3/3/95	Perform a Corrosion Test
R006-95-011	4/7/95	Compatibility Test Experiments
CTP-95-004		**Impermeable Composite Coatings**
R013-95-033	3/20/95	RX-36 Baseline Coating
R013-95-034	3/22/95	RX-36 Baseline Coating
R013-95-035	3/27/95	Composite Coatings Experiments
R013-95-037	4/3/95	Composite Coatings Experiments
R013-95-038	4/5/95	Composite Coatings, #5
R014-95-042	4/12/95	Composite Coatings,#6
R013-95-044	4/25/95	Composite Coatings,#7
R013-95-047	5/4/95	Composite coating #7
R006-95-012	5/12/95	Coated coupon test
R013-95-047	5/4/95	Composite coating #7
R006-95-012	5/12/95	Coated coupon test

Table 3.2 Continued

Run#	Date	Title
CTP-95-006		**Solid Precipitation from Fe-C-X-Y Melt and Theoretical Comparison**
R013-95-039	4/7/95	Study the Solid Precipitation from Fe-C-X-Y Melt
R013-95-040	4/11/95	Study the Solid Precipitation from Fe-C-X-Y Melt
R013-95-041	4/13/95	Study the Solid Precipitation from Fe-C-X-Y Melt
R013-95-042	4/17/95	Re-run of R013-95-041
R013-95-043	4/29/95	Study of Preferential Reactions in Fe-C-X-Y Melt
R013-95-046	5/2/95	Study the solid precipitation from Fe-C-X-Y melt
R013-95-049	5/11/95	Study the solid precipitation from Fe-C-X-Y melt
CTP-95-012		**Development of a Quantitative Corrosion Test Protocol for Gas/Liquid/Refractory Interface Reactions**
R006-95-013	6/5/95	Corrosion test for refractory samples
R006-95-014	6/20/95	Corrosion test for refractory samples
R006-95-015	6/23/95	Corrosion test for refractory samples
R006-95-017	8/22/95	Test the ICTF/20-lb inductotherm power supply
CTP-95-016		**Behavior of Refractory Lining materials in Contact with different Melt Compositions**
R019-95-004	8/23/95	Dry-vibratable refractory lining test
CTP-95-018		**Effect of Bath Chemistry on Refractory Integrity**
R013-95-063	8/1/95	Determine effect of carbon concentration on refractory performance
R013-95-065	8/15/95	Determine effect of carbon concentration on refractory performance
R014-95-075	10/16/95	Determine effect of carbon concentration on refractory performance
R014-95-076	10/18/95	Determine effect of carbon concentration on refractory performance
R014-95-078	10/25/95	Determine effect of carbon concentration on refractory performance
R014-95-078a	11/21/95	Effect of bath carbon concentration on refractory performance
CTP-95-023		**Relative Performance of Selective Refractory Materials**
R006-95-018	10/6/95	Test of mullite/alumina refractories
R006-95-019	10/13/95	Test of mullite/alumina refractories
R006-95-020	10/18/95	Test of mullite/alumina refractories
R006-95-022	12/8/95	Test of mullite/alumina refractories
R006-95-021	11/27/95	Test of mullite/alumina refractories

Table 3.2 Continued

Run#	Date	Title
CTP-95-027		**Effect of Melt Composition on Candidate Refractory Systems**
R019-95-05	11/06/95	Refractory system behavior studies, #1
R019-95-06	11/16/95	Refractory system behavior studies
R005-95-004/007		**Experimental Campaign on the Demonstration Unit**
R005-95-004/7	5-7/95	Evaluate containment system at low bath carbon
R005-95-008		**Experimental Campaign on the Demonstration Unit**
R005-95-008	8/95	Evaluate containment system at saturated bath carbon
R005-95-009/010		**Experimental Campaign on the Demonstration Unit**
R005-95-009/10	9/95	Evaluate containment system
R005-95-011		**Experimental Campaign on the Demonstration Unit**
R005-95-011	10/95	Evaluate containment system

Table 3.3
Task 1.5 - Experimental Testing of RCRA Wastes[1]

Run#	Date	Title
CTP-94-004		**Part II Thermochemistry of Chloride/Iron/Nickel and Ceramic Phase**
05-94-035		Thermochemistry of HCL/Fe/Ni
05-94-050		Thermochemistry of HCL/Fe/Ni
05-94-051		Thermochemistry of HCL/Fe/Ni
05-94-052		Thermochemistry of HCL/Fe/Ni
05-94-053		Thermochemistry of HCL/Fe/Ni
05-94-054		Thermochemistry of HCL/Fe/Ni
05-94-055		Thermochemistry of HCL/Fe/Ni
05-94-057		Thermochemistry of HCL/Fe/Ni
05-94-058		Thermochemistry of HCL/Fe/Ni
05-94-059		Thermochemistry of HCL/Fe/Ni
05-94-065		Thermochemistry of HCL/Fe/Ni
05-94-066		Thermochemistry of HCL/Fe/Ni
05-94-067		Thermochemistry of HCL/Fe/Ni
05-94-068		Thermochemistry of HCL/Fe/Ni
05-94-069		Thermochemistry of HCL/Fe/Ni
05-94-071		Thermochemistry of HCL/Fe/Ni
05-94-072		Thermochemistry of HCL/Fe/Ni
05-94-073		Thermochemistry of HCL/Fe/Ni
R003-94-083	11/2/94	Part II Thermochemistry of HCl/Fe/Ni
R003-94-087	12/14/94	Part II Thermochemistry of HCl/Fe/Ni
R003-94-088	12/14/94	Part II Thermochemistry of HCl/Fe/Ni
R003-94-089	12/19/94	Part II Thermochemistry of HCl/Fe/Ni

[1] This table list experiments whose primary focus was testing of RCRA Wastes. It should be noted that RCRA wastes were also processed during testing that focused on other technical areas (e.g. refractory materials).

Table 3.3 (Continued)

Run#	Date	Title
CTP-94-010		**Formation and Destruction of Trace Components in Catalytic Extraction Process**
10-94-018		Reaction between CO and H_2
10-94-020		Reaction between CO and H_2
10-94-023		Reaction between CO and H_2
10-94-028		Reaction between CO and H_2
10-94-034		Reaction between CO and H_2
10-94-036		Reaction between CO and H_2
10-94-040		Reaction between CO and H_2
10-94-042		Reaction between CO and H_2
10-94-044		Reaction between CO and H_2
10-94-048		Reaction between CO and H_2
10-94-051		Reaction between CO and H_2
10-94-053		Reaction between CO and H_2
10-94-056		Reaction between CO and H_2
10-94-057		Reaction between CO_2 and Propane
10-94-061		Reaction between CO_2 and Propane
10-94-063		Reaction between CO_2 and Hydrocarbon
10-94-065		Reaction between CO_2 and Hydrocarbon
10-94-067	10/24/94	Reaction between CO_2 and ethylene
10-94-069	10/24/94	Reaction between CO_2 and ethylene
10-94-071	10/26/94	Reaction between CO_2 and ethylene
10-94-073	10/27/94	Reaction between CO_2 and ethylene
10-94-075	11/1/94	Reaction between CO_2 and propane
10-94-079	11/14/94	Reaction between CO_2 and ethylene
10-94-080	11/16/94	Reaction between CO_2 and ethylene
10-94-081	11/30/94	Reaction between CO_2 and ethylene
10-94-082	11/30/94	Reaction between CO_2 and ethylene
10-95-003	1/11/95	Argon gas jet impinging on molten metal surface
10-95-005	1/13/95	Hydrocarbon gas jet impinging on molten metal surface
10-95-006	1/16/95	Hydrocarbon gas jet impinging on molten metal surface
10-95-008	1/19/95	Hydrocarbon gas jet impinging on molten metal surface
10-95-011	1/24/95	Hydrocarbon gas jet impinging on molten metal surface
R013-95-014	1/30/95	Hydrocarbon gas jet impinging on molten metal surface
R013-95-017	1/31/95	Hydrocarbon gas jet impinging on molten metal surface

Table 3.3 (Continued)

Run#	Date	Title
R013-95-019	2/3/95	Hydrocarbon gas jet impinging on molten metal surface
R014-95-027	2/8/95	Hydrocarbon gas jet impinging on molten metal surface
R014-95-029	2/21/95	Hydrocarbon gas jet impinging on molten metal surface
CTP-94-028		**Chlorinated Hydrocarbon Studies**
R007-94-29 to 36	10/25/94	Continuation of Work on Injection of Chlorinated Hydrocarbon into a Nickel Bath.
R007-94-029	11/2/94	Melt Iron and Sinter New Type of Dry Vibratable in APU Furnace
R007-94-030-037	11/2/94	Continuation of Work on Injection of Chlorinated Hydrocarbon into a Nickel Bath.
R018-94-006-08	11/22/94	Reconstruction of the Gas Handling Train and Cold Testing (APU-10)
R018-94-029-044	12/20/94	Continued Testing of Injection
R007-95-001 through 009	1/9/95	Continuation of Chlorinated Hydrocarbon Studies
R018-95-001 through 012	1/27/95	Dust Data for Comparison of Dust Generation with Gaseous and Liquid Feeds
R018-95-005 through 011	2/22/95	Continuation of Chlorinated Hydrocarbon

Table 3.4
Task 1.6 - Conceptual Design for a CEP Radioactive Scrap Metal Processing Facility

Run#	Date	Title
CTP-94-017		**Investigation of Tapping on 100-lb. Reactor**
WM-94-030		Compare Conditions for Sculling Inside Tapping Sleeve
BTU-94-001		Tapping Study
BTU-94-004		Tapping Study
BTU-94-005	12/2/94	Feasibility study and investigation of tapping
R017-95-001	1/24/95	Feasibility studies
R017-95-002	2/21/95	Investigation of tapping
R017-95-004	4/11/95	Investigation of Tapping
R017-95-005	5/8/95	Cold test on the bottom tuyere unit
CTP-94-024		**Study of Relation between Electrical Resistivity and Viscosity of the Ceramic Phase**
R013-95-077	11/06/95	Reproducibility of resistivity measurement with single piece electrode configurations, Run #12
R003-95-046	11/27/95	Reproducibility of resistivity measurement with multiple-sheath electrode probe configurations, Run #13
CTP-95-003		**Tuyere Testing Unit**
R020-95-004	3/16/95	Operability Test Runs
R020-95-007	4/6/95	Operability Test Runs
R020-95-008	4/11/95	Operability Test Runs(argon as carrier gas)
R020-95-009	4/11/95	Operability Test Runs(argon as carrier gas)
R020-95-012	5/8/95	Test run on the tuyere testing unit
R020-95-013	5/9/95	Test run on the tuyere testing unit
R020-95-014	5/9/95	Test run on the tuyere testing unit
R020-95-015	5/12/95	Test run on the tuyere testing unit
R020-95-016	5/15/95	Test run on the tuyere testing unit
R020-95-011&018	5/22/95	Test run on the tuyere testing unit
R020-95-019	6/9/95	Test run on the tuyere testing unit
R020-95-020	6/13/95	Test run on the tuyere testing unit
R020-95-021	6/21/95	Test run on the tuyere testing unit
CTP-95-007		**Capture of Volatile Radionuclide Species**
R021-95-001	4/17/95	Test of Equipment for Radionuclide Removal
R021-95-002	4/26/95	Capture Mechanism Performance Tests
R021-95-003	5/2/95	Capture mechanism performance tests
R021-95-004	5/25/95	Capture mechanism performance tests

Table 3.4 Continued

Run#	Date	Title
CTP-95-014		**Bottom Tapping Pilot Studies**
R007-95-012	10/3/95	Bottom tapping tests
R007-95-013	10/3/95	Bottom tapping tests
CTP-95-022		**Off-gas Duct Studies**
R026-95-001	11/9/95	Zinc dust characterization study in a 10 ft duct
R026-95-002	11/14/95	Zinc dust characterization study in a 10 ft duct
R005-95-004/007		**Experimental Campaign on the Demonstration Unit**
R005-95-004/7	5-7/95	Establish reliability of CO/CO_2 ratio for control of O_2 activity
R005-95-004/7	5-7/95	Test reliability of bath oxygen sensor
R005-95-004/7	5-7/95	Evaluate utility of lightpipe devices
R005-95-008		**Experimental Campaign on the Demonstration Unit**
R005-95-008	8/95	Establish reliability of methods for bath chemistry control
R005-95-008	8/95	Test reliability of on-line control modules
R005-95-008	8/95	Evaluate utility of lightpipe temperature measuring devices
R005-95-009/010		**Experimental Campaign on the Demonstration Unit**
R005-95-009/10	9/95	Establish reliability of methods for bath chemistry control
R005-95-009/10	9/95	Test reliability of on-line control modules
R005-95-009/10	9/95	Evaluate utility of lightpipe temperature measuring devices
R005-95-011		**Experimental Campaign on the Demonstration Unit**
R005-95-011	10/95	Test automatic bath temperature control
R005-95-011	10/95	Evaluate operator on-line control interfaces
Misc.		**Development of Instrumentation and Sensing Devices**
R013-95-070	9/1/95	IR lightpipe for measuring the level of molten metal bath
R003-95-040	9/22/95	IR lightpipe for measuring the level of molten metal bath

4. Task 1.3: Experimental Testing

A substantial amount of theoretical work has been performed on the separation of chemically similar metals such as technetium (Tc), uranium (U), and nickel (Ni). It is clearly desirable to separate these long half-life contaminants from short half-life and nonradioactive constituents of the waste material and contaminated metals. With uranium this is more readily accomplished due to the ease of oxidizing its oxide (UO_2) into its dication (UO_2^{2+}). Technetium also forms a dioxide (TcO_2) and it is also possible to form a similar dication (TcO_2^{2+}). If TcO_2^{2+} forms readily, technology can be developed to effect a phase transfer of technetium from its metallic state to an ionic or vitreous phase. High level non-empirical quantum calculations on Tc- and Ni-oxides were performed to derive estimates of the energetics of reactions which can potentially be used for the separation of technetium from nuclear waste or metal surfaces. Theoretical results suggest that oxidation and subsequent migration from the metal phase to the ceramic phase should have a much more favorable equilibrium constant for extraction of technetium oxides (TcO and TcO_2) than for the nickel oxides. Given that the oxidation potential for the uranium oxides (UO and UO_2) are significantly lower than those of technetium, the oxidation of technetium metal into its oxide in the presence of nickel and its subsequent transfer from the metal phase to the ceramic phase is considered to be feasible. The calculated value of the Gibbs Free Energy for oxidation of technetium suggests that the reaction is thermodynamically favorable; however, additional work is required to assess the accuracy of the computational data and to estimate the free energy of the TcO_2 phase transition from available experimental data. This important theoretical work will provide the foundation for a future experimental program which may lead to the ability to recycle and reuse the approximately $1.5 billion of radioactive contaminated nickel in the DOE inventory.

A series of experiments was performed with a divinyl benzene organic combined with either surrogate or actual radionuclides to measure the partitioning of radionuclides in the metallic, ceramic, and gas phases. The radioactive portion of these experiments was not performed under this contract; however, the data has been included in this final report because it is known to be a major DOE interest item. The focus of these experiments was to establish operating requirements to partition radionuclides to the desired phase. MMT has successfully demonstrated that CEP can substantially reduce the volume of radioactive wastes while producing a highly stable waste form for eventual disposal. As predicted, processing conditions enabled complete capture of non-volatile radionuclides into the metallic and ceramic phase. Further, MMT has successfully demonstrated the ability of CEP to control partitioning of radionuclides to either the metal phase which provides a stable waste form with significant self-shielding (the self-absorption of radiation-reducing radiation levels), or to the ceramic phase which also provides a stable waste form and achieves substantial volume reduction. Volatile radionuclides were captured from the gas phase with measured decontamination factors in excess of 10^4. These experiments clearly demonstrate CEP's ability to recycle and reuse radioactive contaminated wastes, effectively control

partitioning to the desired product phase, substantially reduce the volume of radioactive wastes, and produce a highly stable waste form for eventual disposal.

Experiments were also performed to measure sulfur capture in the metal phase, determine trace sulfur off-gas species, and to evaluate refractory containment material to identify potential boundaries on feed composition for processing mixed wastes. Sulfur partitioning experiments were performed using FeS and H_2S with sulfur levels ranging from 0 to 37 wt%. Partitioning data indicates that greater than 97% of the injected sulfur was captured in the metal phase as FeS. It was also confirmed that the use of a high sulfur bath results in trace sulfur species in the off-gas. The production of H_2S as a function of crucible temperature was concordant with the Fe-S system transition from beta-FeS to gamma-FeS. The relationship between sulfur concentration in the bath and carbon activity in the bath was also confirmed using a total hydrocarbon (THC) monitor to measure trace organic species in the off-gas during feed injection. Carbon solubility in the bath decreases as sulfur concentration increases, which results in increased carbon activity.

4.1. A Combined Theoretical and Experimental Approach to the Separation of Similar Metals Such as Technetium, Nickel, and Uranium

4.1.1. Introduction

Uranium and technetium are both important constituents of nuclear waste. Both elements have isotopes with half-lives of over one million years. It is desirable to separate these long half-life contaminants from short half-life and nonradioactive constituents of the waste material and contaminated metals. With uranium this is more readily accomplished due to the ease of oxidizing its oxide, UO_2, into its dication, UO_2^{2+}. Technetium also forms a dioxide and it is possible that TcO_2 can also form a TcO_2^{2+} dication. Although the most common oxidation states for Tc are +4 and +7, the +6 oxidation state is represented by TcF_6. If TcO_2^{2+} forms readily, technology can be developed to effect a phase transfer of technetium from its metallic state in an ionic or vitreous phase.

There are few relevant experimental data on technetium-containing species[1] because of the scarcity of the metal and the problems associated with the handling of radioactive materials. Some of the experimental data are, in fact, just estimates based on similarities in chemistry of manganese, technetium and rhenium. Thus, it is not possible to study this problem using only the available experimental data because of their incompleteness and insufficient accuracy. Therefore, quantum chemical calculations provide an appealing alternative to explore the chemistry of technetium. Further, the results of these calculations can serve as a source of data on properties of technetium compounds if the experimental data are not currently available.

Our approach is to perform a high level non-empirical calculations on Tc- and Ni-oxides as the initial stage of this project in order to derive estimates of energetics of

reactions which can be used potentially for the separation of techenetium from nuclear waste or metal surfaces. Where the accurate experimental data on Ni- and Tc-containing species are available, they have been used in this study in combination with the computational results.

4.1.2. Computational Methodology

Calculations of transition metal compounds have been a challenging problem in theoretical chemistry. Recent years have witnessed encouraging results of applications of density functional theory (DFT)[2] methods to metal complexes, employing both "gradient-corrected"[3] and hybrid approaches[4] in which the Hartree-Fock "exact exchange" is also included in the functional.[5-8] Among various proposed functionals the Becke's three-parameter hybrid functional[3a,4a] combined with the Lee, Yang and Parr (LYP) correlation functional[3b] and denoted as B3-LYP,[4b] appears to be the functional form which yields good results in calculations of atomization energies,[9] proton affinities,[10] harmonic frequencies of polyatomic molecules[11] and binding energies of species containing first-row transition metals.[6a,e,7b]

Effective core potentials (ECP)[12] provide a way to reduce difficulties in calculations of species containing heavy atoms, which are caused by a large number of two electron integrals.[1,13] It is also important that relativistic or quasirelativistic ECPs can reflect (to some extent) relativistic effects upon geometries and bond energies.[12-14] Quasirelativistic ECP parameters are derived, as a rule, from quasirelativistic calculations for atoms and monoatomic ions, in which the mass-velocity term and the averaged Darwin-spin-orbit term are taken into account as the most important relativistic terms of the Dirac-Fock Hamiltonian.[15] ECP calculations can achieve nearly the same or sometimes even better accuracy as the all-electron calculations with large basis sets at the same level of theory used to describe correlation effects.[16-18]

Therefore, for calculations of Ni- and Tc-containing species as well as of other transition-metal species we have developed an approach which combines advantages of using both DFT and ECP (denoted as B3LYP/ECP(S)).

Ab initio molecular orbital calculations[20] were performed with the GAUSSIAN 94 system of programs.[21] The Becke's three-parameter hybrid functional combined with the Lee, Yang and Parr (LYP) correlation functional, denoted B3-LYP, was employed in the calculations using density functional theory (DFT). For iron the energy-adjusted quasirelativistic effective core potential (ECP) developed by the Stuttgart group[22] was used (denoted further as ECP(S)). This ECP simulating the influence of the Ne-like core, Fe^{16+}, on the $3s^23p^63d^64s^2$ ($3d^74s^1$) valence shell was derived using atomic excitation and ionization energies.[22a] Applicability of the ECPs generated from Hartree-Fock atomic calculations to DFT-calculations has been shown recently.[23] Geometries were optimized[24] at the B3LYP level using the 6-311G(d) basis set[20] for O and the (14s11p6d)/[6s6p3d] valence basis set for Ni. The final energies were obtained by single

point calculations using the (14s11p6d1f)/[6s6p4d1f] valence basis set and the 6-311+G(3df) basis set for for Ni and O, respectively. The (8s7p6d)/[6s5p4d] valence basis set was used for Tc in single point calculations and the geometry optimization was carried out using the (8s7p6d)/[6s5p3d] valence basis set for Tc and the 6-311G(d) basis set for O. We also carried out calculations with the basis set for Tc, which was augemented by polarization f functions. The f function exponent (1.98) was optimized for the ground ^6S state of Tc. The test calculations have shown that including the f functions results in insignificant changes of excitation and ionization energies. Thus, we used mainly (8s7p6d)/[6s5p4d] valence basis set for Tc. The stationary points on the potential energy surfaces were characterized by calculations of vibrational frequencies, which were done numerically in the ECP calculations of iron-containing species at the B3LYP level. Enthalpy temperature corrections were derived using harmonic frequencies which were computed at the B3LYP/6-311G(d,p) level, and standard statistical thermodynamics formulas.[20,25] Theoretical enthalpies of formation at 0 K and 298 K, $\Delta H_{f\ 0}$ and $\Delta H_{f\ 298}$ respectively, were derived from calculated B3LYP atomization energies for the species at 0 K or 298 K and standard experimental enthalpies of formation for the atoms at 0 K or 298 K, respectively. The compendium of Lias et al.[26] was used as the source of thermodynamical data unless stated otherwise.

4.1.2.1. Test Calculations for Ni-Containing Species

A fundamental requirement which a computational scheme applied to calculations of transition-metal species should fulfill is its ability to correctly reproduce atomic excitation and ionization energies. We have chosen the energy-adjusted effective core potentials which were optimized to reproduce these energies, therefore we anticipated good agreement beween the calculated and experimental values. Indeed, the data given below show that in some cases our computational estimates are the best when compared with the results of previous calculations.

Atomic excitation energy ($Ni^+ d^9(^2D) \rightarrow Ni^+ d^8s^1 (^4F)$) is

0.72 eV (B3LYP/ECP)

0.57 eV (MCPF; Pettersson, L. G. M.; Bauschlcher, C. W.; Langhoff, S. R.; Partridge, H. *J. Chem Phys.* **1987**, *87*, 481)

1.08 eV (Exptl.; taken from the Moore tables, ref 27)

2.71 eV (B3LYP/Wachters basis set; Holthausen, M. C.; Mohr, M.; Koch, W. *Chem. Phys. Lett.* **1995**, *240*, 245)

-0.24 eV (B3LYP/Hay-Wadt ECP)

Ionization energy ($Ni\ d^8s^2 (^3F) \rightarrow Ni^+ d^8s^1 (^5D)$) is

8.9 eV (B3LYP/ECP)

8.73 eV (B-LYP/Wachters basis set; Russo, T. V.; Martin, R. L.; Hay, P. J. *J. Chem. Phys.* **1994**, *101*, 7729).

8.67 eV (Exptl, ref 27)

Table 4.1
Computational Results for NiO

NiO $^3\Sigma^-$	ICAPF[a]	CI[b]	QCISD/ECP[c]	B3LYP/ECP[d]	Exptl
R (Å)	1.626	1.693	1.591	1.620	1.627
ν (cm^{-1})	850	754	848	854	838
D_0 (eV)	3.75	3.04	2.33	3.50 (D_e = 3.55)	3.87 ± 0.03[e] 3.6 ± 0.3[f]

a Bauschlicher, C. W.; Maitre, P. Theor. Chim. Acta 1995, 90, 189.
b Panas, I.; Schüle, J.; Brandemark, U.; Siebahn, P.; Wahlgen, U. J. Phys. Chem. 1988, 92, 3079.
c Dolg, M.; Wedig, U.; Stoll, H.; Preuss, H. J. Chem. Phys. 1987, 86, 2123.
d (14s11p6d1f)/[6s6p4d1f] valence basis set for Ni and the 6-311+G(3df) basis set for O, the geometry optimization was carried out using the (14s11p6d)/[6s6p3d] valence basis set for Ni and the 6-311G(d) basis set for O.
e The value cited in Bauschlicher, C. W.; Maitre, P. Theor. Chim. Acta 1995, 90, 189.
f Radzig, A. A.; Smirnov, B. M. Reference Data on Atoms, Molecules, and Ions, Springer: Berlin, 1985.

The data given in Table 4.1 indicate that the B3LYP/ECP scheme underestimates the bonding energy (D_o) in NiO by 0.37 eV (8.5 kcal/mol). As shown later, it will result in an overestimated enthalpy of formation of NiO (Table 4.8), although the difference between the calculated and experimental values of $\Delta H_{f\,298}$ is only 5.6 kcal/mol. The calculated exaltation energy of 0.72 eV is closer to the experimental value of 1.08 eV than the result of the MCPF calculations, which required significantly greater computer time. The B3LYP/ECP ionization energy is in quite good agreement with experiment.

4.1.2.2. Test Calculations for Tc-Containing Species

Atomic excitation energy ($Tc^+ d^5s^1 (^7S) \rightarrow Tc^+ d^6(^5D)$) is

0.41 eV (B3LYP/ECP with the (8s7p6d)/[6s5p4d] basis set)

0.39 eV (B3LYP/ECP with the (8s7p6df)/[6s5p4df] basis set, the f exponent is 1.98 (optimized for $Tc(^6S)$)

0.89 eV (MCPF; Pettersson, L. G. M.; Bauschlicher, C. W.; Langhoff, S. R.; Partridge, H. *J. Chem Phys.* **1987**, *87*, 481); see also Bauschlicher, C. W. et al., ibid, **1989**, *91*, 2399.

Our B3LYP/ECP calculations give the best estimate of this excitation energy, which is very close to the experimental value of 0.52 eV 27, in contrast to the MCPF calculations of Bauschlicher.

Atomic excitation energy (Tc d^5s^2 (^6S) → Tc d^6s^1 (^4D)) is

0.98 eV (B3LYP/ECP)

1.81 (MCPF, Blomberg, M. R. A.; Siegbahn, P. E. M.; Svensson, M. *J. Am. Chem. Soc.* **1992**, *114*, 6095).

1.37 eV (Exptl, ref 27).

Atomic excitation energy (Tc d^5s^2 (^6S) → Tc d^6s^1 (^6D)) is

0.20 eV (B3LYP/ECP)

0.72 eV (MCPF, Langhoff, S. R., et al., *J. Chem. Phys.* **1986**, *86*, 268)

0.41 eV (Exptl, ref 27).

Ionization energy (Tc d^5s^2 (^6S) → Tc^+ d^6(^5D)) is

7.26 eV (B3LYP/ECP with the (8s7p6d)/[6s5p4d] basis set)

7.27 eV (B3LYP/ECP with the (8s7p6df)/[6s5p4df] basis set, the f exponent is 1.98 (optimized for Tc(^{6}S))

7.28 eV (*j*-averaged value (see Martin, R. L.; Hay, P. J. *J. Chem. Phys.* **1981**, *75*, 4539) taken from the Moore Tables, ref 27)

The computational data on TcO in Table 4.2 show that the B3LYP/ECP scheme gives the dissociation energy of TcO (D_o), which is close to the MCPF computed value (Langhoff, S. R.; Bauschlicher, C. W.; Pettersson, L. G. M. *Chem. Phys.* **1989**, *132*, 49.). However, the latter requires correction using the ratio of the experimental to MCPF calculated D_o values for MoO.

Table 4.2
Table 2. Computational Results for TcO

TcO $^6\Sigma^+$	MCPF[a]	B3LYP/ECP[b]
R (Å)	1.775	1.749
ν (cm^{-1})	766	3406
D_0 (eV)	4.35[c] (3.55)	4.97 (D_e = 5.17)[d]

a Langhoff, S. R.; Bauschlicher, C. W.; Pettersson, L. G. M. *Chem. Phys.* **1989**, *132*, 49.
b (8s7p6d)/[6s5p4d] valence basis set for Tc and the 6-311+G(3df) basis set for O, the geometry optimization was carried out using the (8s7p6d)/[6s5p3d] valence basis set for Tc and the 6-311G(d) basis set for O.
c The D_0 value was scaled by the ratio of the experimental to theoretical D_0 values for MoO. The unscaled D_0 value is given in parentheses.
d ZPE(B3LYP) value is unscaled.

4.1.2.3. Conclusion on the Computational Methodology

The results presented above have shown that the B3LYP/ECP scheme can provide quite reliable results which are, in some cases, the best reported to date. Therefore, it gives us confidence to apply this computational scheme to calculations of Ni- and Tc- containing species. However, the bonding energy for NiO is underestimated by 8.5 kcal/mol (Table 4.1). It means that properties relevant to the NiO bonding can exhibit similar error too. Nevertheless, if this error shows a systematic behavior, it can be corrected empirically.

4.1.3. Results and Discussion

Computational results for the cation and dication for TcO, TcO_2, and NiO including their ionization energies are presented in Table 4.3 through Table 4.6.

Table 4.3
Computational Results for TcO, its Cation and Dication

Species	$-E_{tot}$(hartrees)	R(Tc-O) Å	ZPE (kcal/mol)	ν (cm^{-1})
TcO $^6\Sigma^+$	155.99271 (155.98366)[a]	1.749	4.87	3406
TcO^+ $^5\Sigma^-$	155.67174 (155.66169)	1.711	4.42	3089
TcO^+ $^3\Sigma^-$	155.61386 (155.60371)	1.725	5.05	3534
TcO^{2+} $^2\Sigma^+$	155.06397 (154.83032)	1.692	5.00	3499
TcO^{2+} $^4\Sigma^+$	155.065233 (155.05090)	1.657	5.11	3576

a (8s7p6d)/[6s5p4d] valence basis set for Tc and the 6-311+G(3df) basis set for O, the geometry optimization was carried out using the (8s7p6d)/[6s5p3d] valence basis set for Tc and the 6-311G(d) basis set for O (these total energies are given in parentheses).

Table 4.4
Total energies, geometrical parameters, zero point vibrational energies and the lowest harmonic frequencies for the neutral TcO_2 and its cation and dication calculated at the B3LYP/ECP level

Species	$-E_{tot}$(hartrees)	R(Tc-O)Å	<OTcO	ZPE (kcal/mol)	$\nu_{min}(cm^{-1})$
TcO_2 $^4B_1$	231.28786 (231.26828)[a,b,c]	1.711	129.1°	11.03	(a_1) 461
TcO_2^+ $^3B_1$	230.94817 (230.92517)	1.669	117.0°	11.61	(a_1) 450
TcO_2^{2+} $^2A_1$	230.29829[d] (230.26956)	1.645	105.9°	11.93	(a_1) 527

a (8s7p6d)/[6s5p4d] valence basis set for Tc and the 6-311+G(3df) basis set for O, the geometry optimization was carried out using the (8s7p6d)/[6s5p3d] valence basis set for Tc and the 6-311G(d) basis set for O (these total energies are given in parentheses).

b The TcO_2 C_{2v} structure of $^4B_2$ state has a higher energy (-231.14361 hartrees ((8s7p6d)/[6s5p3d]; 6-311G(d)); R(Tc-O) = 1.806 Å, <OTcO = 126.8°).

c A linear structure of TcO_2 (a doublet state) has a higher energy (-230.19845 hartrees using the (8s7p6d)/[6s5p4d] valence basis set and the 6-311+G(3df) basis set for Tc and O, respectively, and does not correspond to a minimum (one imaginary frequency, 916 *i* cm^{-1}, R(Tc-O) = 1.925 Å).

d The TcO_2^{2+} C_{2v} structure of $^2B_1$ state has higher energy (-230.26177 hartrees using the (8s7p6d)/[6s5p3d] valence basis set for Tc and the 6-311G(d) basis set for O).

Table 4.5
Computational Results for NiO, its Cation and Dication

Species	$-E_{tot}$(hartrees)	R(Ni-O) Å	ZPE (kcal/mol)	ν (cm^{-1})
NiO $^3\Sigma^-$	246.12970 (246.11236)[a]	1.620	1.22	854
NiO^+ $^2\Sigma^+$	245.75438 (245.73855)[b]	1.798	0.67	468
NiO^{2+} $^1\Sigma^+$	244.95316 (244.93002)	1.606	1.18	825

a (14s11p6d1f)/[6s6p4d1f] valence basis set for Ni and the 6-311+G(3df) basis set for O, the geometry optimization was carried out using the (14s11p6d)/[6s6p3d] valence basis set for Ni and the 6-311G(d) basis set for O (these total energies are given in parentheses).
b For NiO^+ at the UCISD/ECP level, R(NiO) = 2.1531 Å; ν = 212 cm^{-1} ; ZPE = 0.30 kcal/mol, E_{tot} = -244.80706 hartrees. No SCF convergence was found in the BD(T)/ECP calculations at this geometry.

Table 4.6
Calculated Ionization Energies (in eV) for NiO, TcO and TcO_2

Species	IE_1	IE_2[a]
NiO	10.21 (9.5 ± 0.2 Exptl, ref 28)	32.02
TcO	8.73	25.24
TcO_2	9.24 [9.20][b]	26.93 [26.88][b]

a Ionization of a neutral molecule into its dication.
b Values obained using the (8s7p6df)/[6s5p4df] basis set with the f exponent of 1.98 (optimized for Tc(^{6}S)) are gven in square brackets.

The calculated ionization energy (10.21 eV) for NiO shows an acceptable agreement with the experimental value (9.5 ± 0.2 eV). It would be reasonable to compare the ionization energies of TcO and TcO_2 with those for UO and UO_2. The first ionization energies of UO and UO_2 have not been accurately determined. Values of 5.6 ± 0.1 and 5.4 ± 0.1 eV, as measured by electron impact mass spectrometry (Rauh, E. G.; Ackerman, R. J. *J. Chem. Phys.* **1974**, *60*, 1396), appear to be the most reliable for the first adiabatic ionization energies of UO and UO_2, respectively.

It is significant that both the ionization energy for oxidation of TcO (IE_1) and TcO (IE_2) are lower than that of the corresponding nickel oxides. This suggests that oxidation and subsequent migration from the metal to the ceramic phase should have a much more favorable equilibrium constant for extraction of TcO and TcO_2 than for the nickel oxides. It should, however, be noted that the oxidation potential for the uranium oxides (UO and UO_2) are both considerably lower than those of technetium. Nevertheless, we feel that oxidation of Tc metal into its oxide in the presence of Ni should be feasible (see below) and its oxidation from the metal to the ceramic phase, by analogy with oxidation of UO_2, should also be feasible. The calculated gas-phase enthalpies of formation for NiO, TcO, and TcO_2 are presented in Table 4.7.

Table 4.7
Calculated Gas-phase Enthalpies of Formation (in kcal/mol) for NiO, TcO and TcO_2

Species	$\Delta H_{f\,0}$	$\Delta H_{f\,298}$
NiO	80.6	79.6[a,b]
TcO	-	101.5
TcO_2	-	32.0

a Experimental values of $\Delta H_{f\,298}$ (NiO (g)) are 74. 0 (ref 1) and 71 ± 4 (ref 26) kcal/mol.
b At 1800 K ΔH_f (NiO (g)) = 72.5 kcal/mol (the experimental $\Delta H_{f\,1800}$ value is 66 kcal/mol (see ref 1).

Table 4.8
Calculated and Experimental Enthalpies, Entropies and Gibbs Free Energies of Formation for NiO(g) (ΔH and ΔG are in kcal/mol, ΔS is in cal/mol K) [a,b,c]

T	ΔH_f calc.	ΔH_f exptl.	ΔS_f calc.	ΔS_f exptl	ΔG_f calc.	ΔG_f exptl
0	80.6	-	-	-	-	-
298	79.6	74.0	23.46	26.04	72.61	66.25
1800	72.5	66.0	15.29	19.54	44.98	30.85

a Calculated for the $Ni(s) + 1/2O_2 \rightarrow NiO(g)$ reaction. At 1800 K, Ni is liquid, Ni(l).
b Experimental values cited in ref 1 were taken from Pankratz, L. B. Thermodynamic Properties of Elements and Oxides, US Buro of Mines, Bulletin 672, Supt. of Docs., Washington, D.C., 1982.
c Experimental values of entropy for Ni(g) (43.54 and 54.0 cal/mol K at 298 K and 1800K, respectively; taken from ref 1) and for the phase transitions, $Ni(g) \rightarrow Ni(s)$ (-36.41 cal/mol K at 298 K) and $Ni(g) \rightarrow Ni(l)$ (-30.58 cal/mol K at 1800 K) were used.

Table 4.9
Calculated and Experimental Entropies for NiO, Ni and O_2 (S is in cal/mol K)

Species	T	S calc.	S exptl
NiO(g)	298	55.08	57.69
NiO(g)	1800	70.26	74.60
Ni(g)	298		43.54
Ni(g)	1800		54.00
O_2(g)	298	48.98	49.04
O_2(g)	1800	63.10	63.28

The calculated enthalpy of formation of NiO agrees with the experimental estimates ($\Delta H_{f\,298}$ (NiO (g)) are 74. 0 (ref 1) and 71 ± 4 (ref 26) kcal/mol).

As seen in Table 4.8 and Table 4.9, the difference between calculated and experimental values of ΔG_f is a result of the differences in calculated and experimental ΔS_f values. The differences in the latter apparently stems from the fact that thermal occupancies have not been taken into account in calculations of the entropy for NiO because there are no experimental data on energies of the lowest electronic states of NiO.

In an effort to predict the energetics for the reaction of Tc with dioxygen in presence of a large excess of Ni, we have examined computationally the reaction of NiO with Tc metal. All such calculations are by definition at 0 K and relate to the gas phase.

For the reaction:

$2NiO(g) + Tc(g) \rightarrow 2Ni(g) + TcO_2(g)$,

the calculated ΔE and $\Delta H(0\ K)$ values are -83.4 and -75.8 kcal/mol.

The experimental data on the enthalpies of formation for NiO(s) and TcO_2(s) (s stands for the solid state) lead to the estimates for the reaction, $2NiO(s) + Tc(s) \rightarrow 2Ni(s) + TcO_2(s)$, which are listed in Table 4.10.

Table 4.10
Experimental Thermochemistry for $2NiO + Tc \rightarrow 2Ni + TcO_2$ Reaction
(ΔH and ΔG are in kcal/mol, ΔS is in cal/mol K)[a]

T (K)	ΔH	ΔS	ΔG
300	11.08	1.11	10.74
1000	10.79	0.04	10.75
1800	20.19	5.65	10.02
2200	21.42	6.27	7.63
2300	-3.96	-5.12	7.83
2500	-8.15	-6.8	8.85
3000	-3.89	-5.25	11.86

a Phase transition, Ni(solid) → Ni(liquid) occurs at 1726 K.

For comparison, the experimental data for the analogous oxidation of U with NiO are given in Table 4.11.

Table 4.11
Experimental Thermochemistry for $2NiO + U \rightarrow 2Ni + UO_2$ Reaction
(ΔH and ΔG are in kcal/mol, ΔS is in cal/mol K)

T (K)	ΔH	ΔS	ΔG
298	-144.7	2.70	-145.5
1000	-145.9	0.89	-146.8
1800	-140.7	3.33	-146.7
2500	-161.9	-6.22	-146.3
3000	-151.9	-2.61	-144.1

These data show that oxidizing U is highly favorable reaction relative to Tc. However, it should be taken into account that the experimental data on Gibbs free energy of formation for TcO_2 (s) are not well established. In fact, the ΔG value is based on the entropy of TcO_2 (s) estimated by the additivity method. This is the only estimate of thermodynamical functions for TcO_2 reported in the literature and these data are subsequently cited in various handbooks. It is based on the early work[29] of 1953. In the

case of Tc_2O_7 (s), this additivity scheme gives the entropy value for Tc_2O_7 to be 43.9 cal/mol K (entropy units), whereas the entropy estimate from the experimental entropy of dehydration (1/2 Tc_2O_7 (s) + 1/2 H_2O (l) → $HTcO_4$(s)) leads to the value of 45.8 cal/mol K. This difference becomes particularly important for estimates of ΔG at higher temperatures where the $T\Delta S$ term becomes very important. The entropy value for TcO_2 determined by this method is also dependent upon the TcO_2 - TcO_4^- couple potential. Consequently, the ΔS term for TcO_2 may not be sufficiently reliable to estimate ΔG values at high temperature. It was this potential discrepancy in the experimental entropy that prompted us to reexamine the possibility of oxidative separation of Tc from Ni.

It should be also noted that the experimental data on ΔH_f and ΔG_f for TcO_2 (s) are available only up to T = 1200 K. Therefore, the estimates at T = 1800 K are extrapolated from the experimental data at lower temperatures. Thus we can conclude only quite approximate experimental estimates for the enthalpy and free energy of the 2NiO + Tc → 2Ni + TcO_2 reaction are available at present.

The B3LYP/ECP calculations give for the 2NiO(g) + Tc(g) → 2Ni(g) + TcO_2(g) reaction at 1800 K

ΔE = -77.4 kcal/mol; ΔH = -66.7 kcal/mol; ΔS = -4.7 cal/mol K and ΔG = -69.0 kcal/mol.

Using the calculated ΔG (= -69.0 kcal/mol) value for the 2NiO(g) + Tc(g) → 2Ni(g) + TcO_2(g) reaction and the experimental free energies for the phase transition (Tc(s) → Tc(g), 94.95 kcal/mol; Ni(l) → Ni(g), 40.19 kcal/mol; NiO(s) → NiO(g), 50.18 kcal/mol; all these data were taken from ref 1), the free energy of the 2NiO(s) + Tc(s) → 2Ni(l) + TcO_2(g) reaction is + 45.9 kcal/mol at 1800 K.

The main problem here is an absence of the experimental data on the TcO2 gas phase→solid phase transition. In fact, there are no gas-phase experimental data on TcO_2. This value could be estimated using the data on analogous oxides in the gas-phase and solid state. However, these data for the analogous oxides are incomplete. For example, MnO_2 decomposes at 1120 K. MoO_2(l) does not form MoO_2 (g) and decomposes at 2250 K.

We have tried to estimate the free energy (ΔG) of the gas-phase → solid phase transition for TcO_2 at 1800 K.

Its estimate can be derived from the enthalpy and entropy values for the phase transitions at the corresponding temperatures (when ΔG(phase transition) = 0).

The corresponding data can be taken from ref 30:

T		ΔH (kcal/mol)	ΔS (cal/mol K)
TcO_2 (s) → TcO_2 (l)	2400	18	7.5
TcO_2 (l) → TcO_2 (g)	4000	105	26

Using T = 1800 K instead of the temperatures at which these phase transitions occur, we obtain an estimate for ΔG_{1800} TcO2 (g→s), which is -62.7 kcal/mol as shown in Table 4.12. Therefore, for the 2NiO(s) + Tc(s)→2Ni(l) + TcO_2(s) reaction ΔG is -16.8 kcal/mol at 1800 K. However, it should be recognized that these estimates of the enthalpy and entropy for the phase transition at the temperatures which differ from 1800 K, are only approximate values.

Table 4.12
Thermochemistry for NiO(g) + C(g) → Ni (g) + CO (g), TcO_2(g) + C(g) → TcO(g) + CO (g), and TcO(g) + C(g) → Tc(g) + CO(g) Reactions at 1800 K, Calculated at the B3LYP/ECP Level (ΔH and ΔG are in kcal/mol, ΔS is in cal/mol K)

Reaction	ΔH	ΔS	ΔG
NiO(g) + C(g) →Ni (g) + CO (g)	-173.6 (-170.3)[a]	-7.12 (-6.38)[a]	-160.7 (-158.8)[a]
TcO_2(g) + C(g) →TcO(g) + CO (g)	-131.6	-12.81	-108.5
TcO(g) + C(g) →Tc(g) + CO(g)	-138.1	+3.29	-144.0
a Experimental estimates are given in parentheses. At 298 K, the experimental estimates for this reaction are as follows: ΔH = -168.9 kcal/mol, ΔS = -4.66 cal/mol K, ΔG = -167.52 kcal/mol.			

The data presented in Table 4.13 show a good agreement with the experimental data on the NiO(g) + C(g) →Ni (g) + CO (g) reaction.

Table 4.13
Experimental Thermochemistry for $NiO + C \rightarrow Ni + CO$, $TcO_2 + 2C \rightarrow Tc + 2CO$, $TcO_2 + 2Fe \rightarrow Tc + 2FeO$, $TcO_2 + 2Mn \rightarrow Tc + 2MnO$, $3TcO_2 + 4Cr \rightarrow 3Tc + 2Cr_2O_3$ (ΔH and ΔG are in kcal/mol, ΔS is in cal/mol K)

Reaction	T (K)	ΔH	ΔS	ΔG
$NiO(s) + C(gr) \rightarrow Ni(s) + CO(g)$	300	30.87	43.93	17.69
$NiO(s) + C(gr) \rightarrow Ni(l) + CO(g)$	1800	31.37	42.39	-44.92
$TcO_2(s) + 2C(gr) \rightarrow Tc(s) + 2CO(g)$	300	50.66	85.76	24.64
$TcO_2(s) + 2C(gr) \rightarrow Tc(s) + 2CO(g)$	1800[a]	42.56	79.12	-99.86
$TcO_2(s) + 2Fe(s) \rightarrow Tc(s) + 2FeO(s)$	300	-26.53	11.03	-29.84
$TcO_2(s) + 2Fe(l) \rightarrow Tc(s) + 2FeO(s)$	1800	-17.20	-16.81	-47.46
$TcO_2(s) + 2Mn(s) \rightarrow Tc(s) + 2MnO(s)$	300	-80.64	8.25	-83.11
$TcO_2(s) + 2Mn(l) \rightarrow Tc(s) + 2MnO(s)$	1800	-94.58	-2.45	-90.17
$3TcO_2(s) + 4Cr(s) \rightarrow 3Tc(s) + 2Cr_2O_3(s)$	300	-234.27	1.29	-234.65
$3TcO_2(s) + 4Cr(s) \rightarrow 3Tc(s) + 2Cr_2O_3(s)$	1800	-243.33	-3.82	-236.46

a Estimates for TcO_2 at 1800 K were extrapolated from those at 1200 K. The experimental data were taken from ref 1.

Conclusions

1. Our best estimate of the ΔG_{1800} value for the $2NiO(s) + Tc(s) \rightarrow TcO_2(s) + 2Ni(l)$ reaction is -16.8 kcal/mol. The experimental estimate which is, in fact, an extrapolation and maybe not that accurate, as shown above, is +10.02 kcal/mol. It should be noted that for the gas-phase reaction, $2NiO + Tc \rightarrow TcO_2 + 2Ni$, the calculated ΔG_{1800} value is -69.0 kcal/mol. Consequently, any estimates of the free energy of the $2NiO(s) + Tc(s) \rightarrow TcO_2(s) + 2Ni(l)$ reaction is highly dependant upon the accuracy of the estimated enthalpy and entropy of vaporization of TcO_2.

2. The calculated ΔG_{1800} value of -16.8 kcal/mol suggests the possibility that the $2NiO(s) + Tc(s) \rightarrow TcO_2(s) + 2Ni(l)$ reaction is thermodynamically favorable. However, an error in the range of 20 kcal/mol maybe involved and one should view this conclusion with caution. If we can successfully remove TcO_2 from the metal phase by oxidative extraction into the ceramic phase, then it is not essential that the concentration of TcO_2 at equilibrium be high as the equilibrium can be shifted.

3. Further work will address the assessment of the accuracy of the computational data for Tc-containing species. We plan to carry out calculations of Tc_2O_7 for which gas-

phase experimental data on enthalpy of formation are available. We will also study the way to estimate free energy of the TcO2 (g→s) phase transition from the available experimental data, which is now a point of continuation for this project.

References

(1) Barin, I. *Thermochemical Data of Pure Substances,* VCH: Weinheim, 1993.

(2) (a) Labanowski, J. K.; Andzelm, J. W. (Eds.) *Density Functional Methods in Chemistry,* Springer: New York, 1991. (b) Ellis, D. E. (Ed.) *Density Functional Theory of Molecules, Clusters, and Solids,* Kluwer: Dodrecht, 1995.

(3) (a) Becke, A. D. *Phys. Rev. A* **1988**, *37*, 785. (b) Lee, C.; Yang, W.; Parr, R. G. *Phys. Rev.* **1988**, *B41*, 785.

(4) (a) Becke, A. D. *J. Chem. Phys.* **1993**, *98*, 5648. (b) Stevens, P. J.; Devlin, F. J.; Chablowski, C. F.; Frisch, M. J. *J. Phys. Chem.* **1994**, *80*, 11623.

(5) (a) Ziegler, T. *Chem. Rev.* **1991**, *91*, 651. (b) Ziegler, T.; Li, J. *Can. J. Chem.* **1994**, *72*, 783. (c) Li, J.; Schreckenbach, G.; Ziegler, T. *J. Phys. Chem.* **1994**, *98*, 4838.

(6) (a) Ricca, A.; Bauschlicher, C. W. *J. Phys. Chem.* **1994**, *98*, 12899. (b) Ricca, A.; Bauschlicher, C. W. *Theor. Chim. Acta* **1995**, *92*, 123. (c) Ricca, A.; Bauschlicher, C. W. *Chem. Phys. Lett.* **1995**, *245*, 150. (d) Bauschlicher, C. W.; Sodupe, M. *Chem. Phys. Lett.* **1995**, *240*, 526. (e) Xu, Y. C.; Lee, S. A.; Freiser, B. S.; Bauschlicher, C. W. *J. Am. Chem. Soc.* **1995**, *117*, 5413.

(7) (a) Holthausen, M. C.; Heinemann, C.; Cornehl, H.; Koch, W.; Schwarz, H. *J. Chem. Phys.* **1995**, *102*, 4931. (b) Holhausen, M. C.; Mohr, M.; Koch, W. *Chem. Phys. Lett.* **1995**, *240*, 245. (c) Holthausen, M. C.; Fiedler, A.; Schwarz, H.; Koch, W. *Angew. Chem.* **1995**, *107*, 2430. (d) Schröder, D.; Fiedler, A.; Schwarz, H. *Int. J. Mass Spectrom. Ion Processes* **1994**, *134*, 239. (e) Fiedler, A.; Schröder, D.; Shaik, S.; Schwarz, H. *J. Am. Chem. Soc.* **1994**, *116*, 10734.

(8) (a) Russo, T. V.; Martin, R. L.; Hay, P. J. *J. Chem. Phys.* **1994**, *101*, 7729. (b) Fournier, R. *J. Chem. Phys.* **1993**, *99*, 1801. (c) Castro, M.; Salahub, D. R.; Fournier, R. *J. Chem. Phys.* **1994**, *100*, 8233. (d) Wu, Y.-D.; Lai, D. K. W. *J. Am. Chem. Soc.* **1995**, *117*, 11327. (e) Harada, M.; Dexpert, H. *J. Phys. Chem.* **1996**, *100*, 565.

(9) (a) Bauschlicher, C. W.; Partridge, H. *Chem. Phys. Lett.* **1995**, *240*, 533. (b) Bauschlicher, C. W.; Partridge, H. *J. Chem. Phys.* **1995**, *103*, 1788. (c) Hertwig, R. H.; Koch, W. *J.*

Comput. Chem. **1995**, *16*, 576. (d) Mebel, A. M.; Morokuma, K.; Lin, M. C. *J. Chem. Phys.* **1995**, *103*, 7414. (e) Hay, P. J. *J. Phys. Chem.* **1996**, *100*, 5.

(10) Smith, B. J.; Radom, L. *Chem. Phys. Lett.* **1994**, *231*, 345.

(11) Rauhut, G.; Pulay, P. *J. Phys. Chem.* **1995**, *99*, 3093.

(12) (a) Krauss, M.; Stevens, W. J. *Ann. Rev. Phys. Chem.* **1984**, *35*, 357. (b) Christiansen, P. A.; Ermler, W. C.; Pitzer, K. S. *Ann. Rev. Phys. Chem.* **1985**, *36*, 407. (c) Gropen, O. In: *Methods in Computational Chemistry*, Wilson, S. (Ed.), Plenum: New York, 1988, Vol. 2, p. 109.

(13) (a) Frenking, G.; Antes, I.; Böhme, M.; Dapprich, S.; Ehlers, A. W.; Jonas, V.; Neuhaus, A.; Otto, M.; Stegmann, R.; Veldkamp, A.; Vyboishchikov, S. F. In *Reviews in Computational Chemistry*, Lipkowitz, K. B.; Boyd, D./. B. (Eds.), Vol. VII; VCH: Weinheim, 1995.

(14) (a) Pyykkö, P. *Adv. Quantum. Chem.* **1978**, *11*, 353. (b) Pyykkö, P. *Acc. Chem. Res.* **1979**, *12*, 276. (c) Pitzer, K. S. *Acc. Chem. Res.* **1979**, *12*, 271. (d) Pyykkö, P. *Chem. Rev.* **1988**, *88*, 563. (e) Wilson, S. (Ed.) *Relativistic Effects in Atoms and Molecules*, Methods in Computational Chemistry; Vol. 2, Plenum: New York, 1989.

(15) (a) Golding, R. M. *Applied Wave Mechanics,* Van Nostrand: New York, 1969. (b) Szasz, L. *The Electronic Structures of Atoms,* Wiley: New York, 1992.

(16) Veldkamp, A.; Frenking, G. *J. Comput. Chem.* **1992**, *13*, 1184.

(17) Chen, H.; Krasowski, M.; Fitzgerald, G. *J. Chem. Phys.* **1993**, *98*, 8710.

(18) Glukhovtsev, M. N.; Pross, A.; McGraw, M. P.; Radom, L. *J. Chem. Phys.* **1995**, *103*, 1878.

(19) Salahub, D. R. In: *Ab Initio Methods in Quantum Chemistry. Part II,* Lawley, K. P. (Ed.), Wiley: New York, 1987, p:447.

(20) Hehre, W. J.; Radom, L.; Schleyer, P. v. R.; Pople, J. A. *Ab Initio Molecular Orbital Theory*; Wiley: New York, 1986.

(21) Frisch, M. J; Trucks, G. W.; Head-Gordon, M.; Gill, P. M. W.; Wong, M. W.; Foresman, J. B.; Johnson, B. G.; Schlegel, H. B.; Robb, M. A.; Replogle, E. S.; Gomperts, R.; Andres, J. L.; Raghavachari, K.; Binkley, J. S.; Gonzalèz, C.; Martin, R. L.; Fox, D. J.; DeFrees, D. J.; Baker, J.; Stewart, J. J. P.; Pople, J. A. **GAUSSIAN-92**, Gaussian Inc., Pittsburg PA, 1992.

(22) (a) Dolg, M.; Wedig, U.; Stoll, H.; Preuss, H. *J. Chem. Phys.* **1987**, *86*, 866. (b) Dolg, M.; Wedig, U.; Stoll, H.; Preuss, H. *J. Chem. Phys.* **1987**, *86*, 2123. (c) Andrae, D.; Dolg, M.; Stoll, H.; Ermler, W. C. *Chem. Phys. Lett.* **1994**, *220*, 341.

(23) Russo, T. V.; Martin, R. L.; Hay, P. J. *J. Phys. Chem.* **1995**, *99*, 17085.

(24) (a) Schlegel, H. B. *J. Comput. Chem.* **1982**, *3*, 214. (b) Schlegel, H. B. *Adv. Chem. Phys.* **1987**, *67*, 249.

(25) McQuarrie, D. A. *Statistical Thermodynamics.* University Science Books: Mill Valley, 1973.

(26) Lias, S. G.; Bartmess, J. E.; Liebman, J. F.; Holmes, J. L.; Levin, R. D.; Mallard, W. G. *J. Phys. Chem. Ref. Data* **1988**, *17*, Suppl.1.

(27) Moore, C. E. *Atomic Energy Levels.* US National Bureau of Standards: Washington, DC; Circ. no 467.

(28) Radzig, A. A.; Smirnov, B. M. *Reference Data on Atoms, Molecules, and Ions*, Springer: Berlin, 1985.

(29) Smith, W. T.; Cobble, J. W.; Boyd, G. E. *J. Am. Chem. Soc.* **1953**, *75*, 5773.

(30) *CRC Handbook of Chemistry and Physics*, 52nd Edition, CRC: Cleveland, 1972.

4.2. Radionuclide Partitioning

4.2.1. Overview

In order to confirm theoretical predictions and surrogate studies, a series of experiments were conducted to measure the partitioning of radionuclides in the metallic, ceramic, and gas phase.

The experiments were conducted with a divinyl benzene organic combined with either surrogate or actual radionuclides. Testing was also performed with hydrogen sulfide and iron sulfide during specific sulfur studies. Injections were performed into an iron bath with various levels of carbon and sulfur. Metallic, ceramic, and gas phase partitioning were determined by post-run gamma analysis.

This series of experiments focused on establishing operating requirements to partition radionuclides to the desired phase. In general, the results for the experiments showed that Q-CEP™ can substantially reduce the volume of radioactive wastes while producing a stable waste form for eventual disposal. As predicted, processing conditions enabled complete capture of non-volatile radionuclides into the metallic and ceramic phase. Volatile radionuclides were captured from the gas phase with measured decontamination factors in excess of 10^4 while not including the baghouse HEPA

filtration in the calculation. Sulfur studies have been conducted with FeS_2, and H_2S injections with sulfur levels ranging from 0 to 37 wt.%. Partitioning indicates greater than 97% of the injected sulfur is captured in the metal phase as FeS. Metal phase separation occurs as expected, without adversely impacting bath catalytic performance.

Table 4.14
Radiological Properties Of The Major Radionuclides Tested

Isotope	Half Life (years)	Beta Energy (KeV)	Gamma Energy (KeV)
Cesium-134	2.06	89.0	563.3
Cesium-137	30.30	514.0	661.6
Chromium-51	0.08	--	320.0
Cobalt-58	0.19	--	810.8
Cobalt-60	5.27	315.0	1,173.2
Iron-55	2.73	Orbital Electron Capture	
Manganese-54	0.86	--	834.0
Nickel (59 & 63)	100.0	65.0	--
Zinc (65)	0.68	325.0	1,115.5

4.2.2. Partitioning

4.2.2.1. Thermodynamics of metal oxidation in an Fe-C system

A summary of thermodynamic data associated with the partitioning of the radionuclides listed in Table 4.14 is presented in Figure 4.1. The free energy of formation of the common oxides as a function of temperature spanning the entire operating range of Q-CEP™ is presented. Figure 4.1 shows the relative stability of iron, cobalt, and manganese in the metal phase. The stability of zinc, sodium, and cesium is dependent on vapor pressure due to the relatively low boiling points of these metals at Q-CEP™ operating temperatures. The metal vapor pressures of cesium, zinc, and iron (and other elements) are presented in Figure 4.2. Under Q-CEP™ operating temperatures and thermodynamic control (without a ceramic layer), vapor pressure and free energy calculations show Co, Fe, and Mn will remain in the metal phase while Cs, Na, and Zn are released to the gas phase.

A summary of the thermodynamic data associated with the formation of simple sulfide-containing compounds in the bath, along with sulfur-containing compounds found in the off-gas is presented in Figure 4.3. The free energy of formation of common sulfides shows the propensity of sulfur to remain in the metallic phase as FeS. Thus, one would expect little of the injected sulfur to partition to the gas phase, provided the bath is not yet saturated with sulfur.

Figure 4.1
The Free Energy of Formation of Metallic Oxides

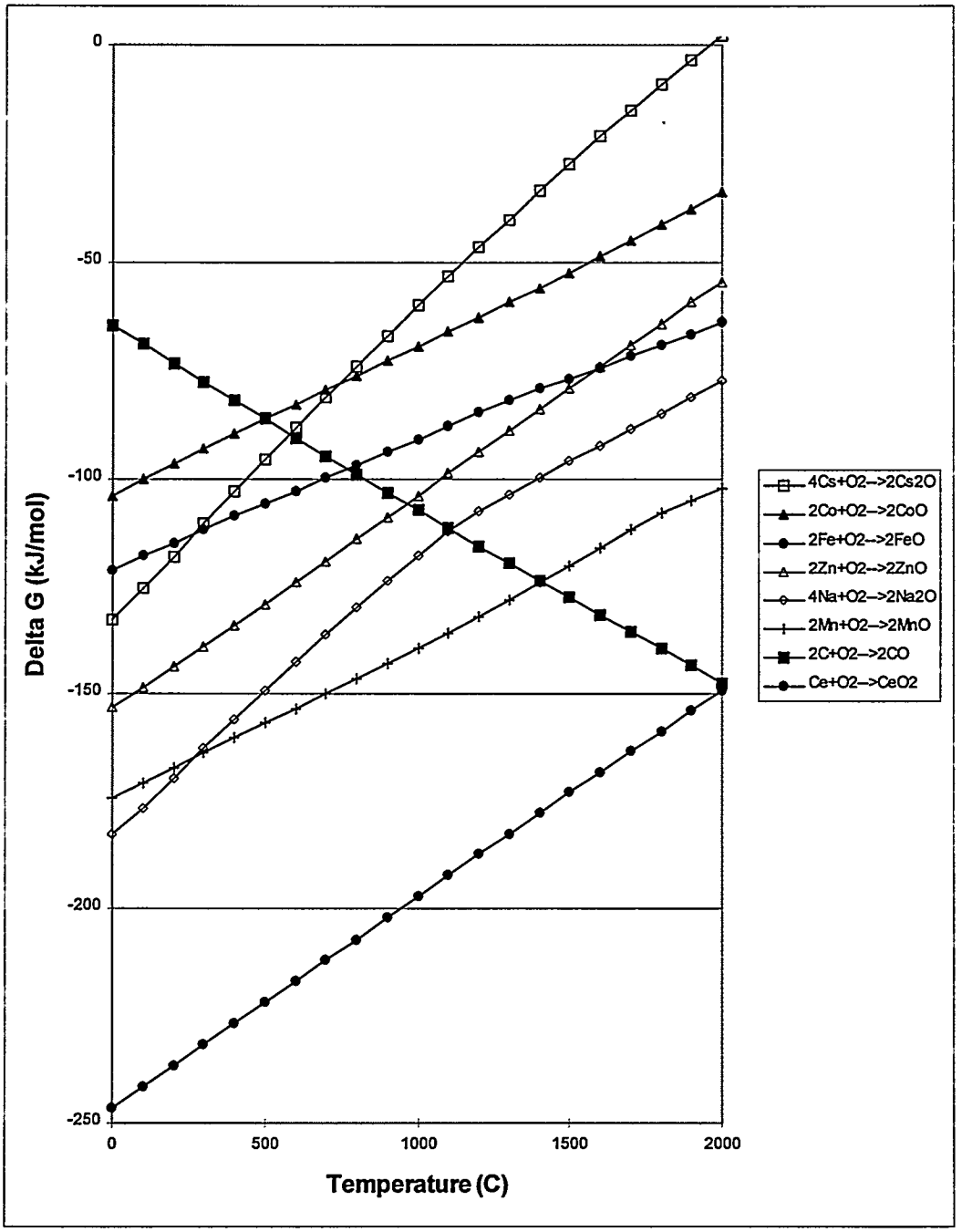

Figure 4.2
Metal Vapor Pressure Diagram

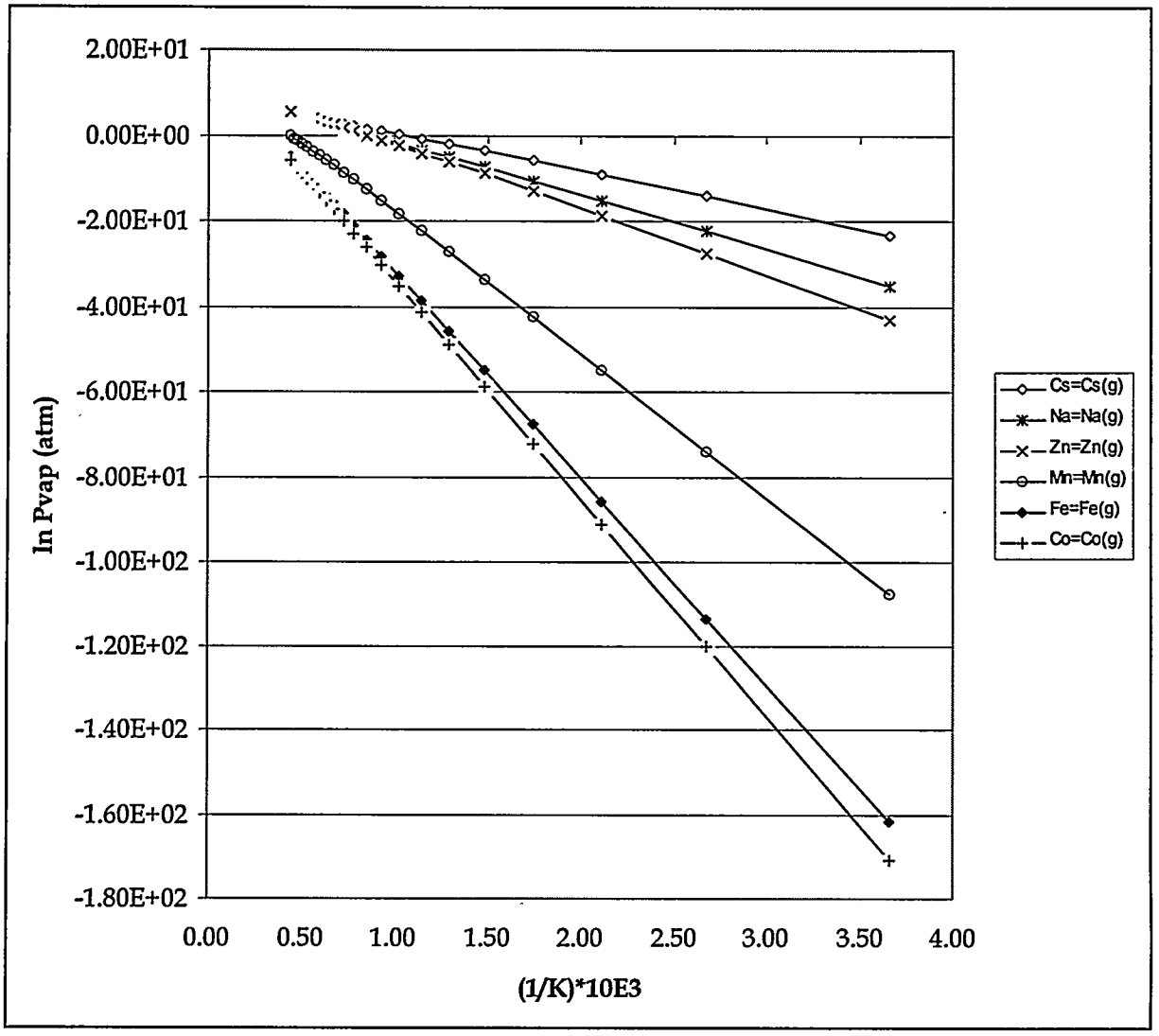

Figure 4.3
Sulfur Free Energy Diagram

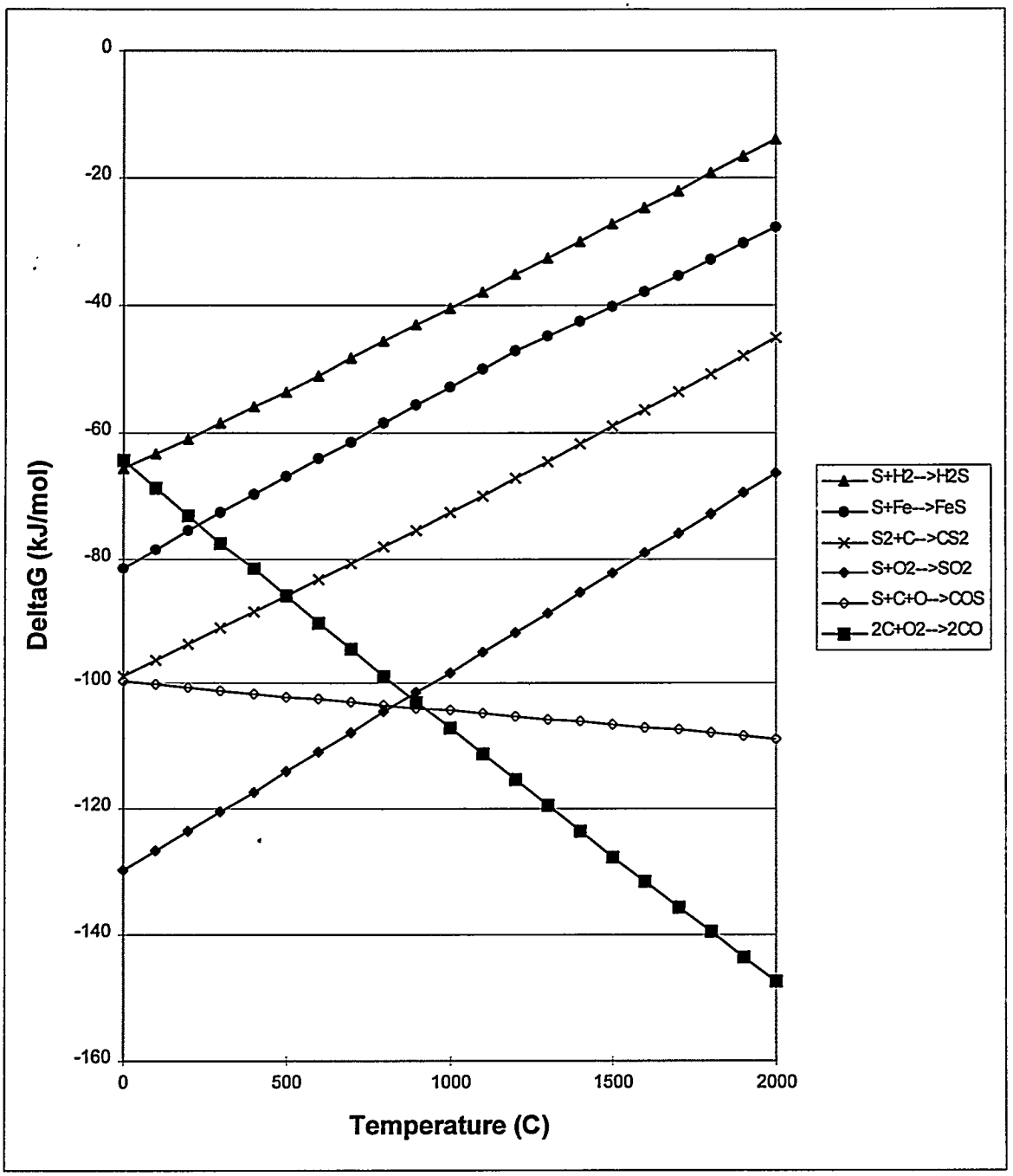

4.2.2.2. Metal Phase

From the experiments conducted, metal phase partitioning data is available from three different systems. These compositions were chosen to partition more of the radionuclides to the metal phase. Capture in the metal phase provides a stable waste form with significant self-shielding (the self-absorption of radiation-reducing radiation levels). Table 4.15 gives the specific compositions used.

Table 4.15
Bath Compositions For Metal Phase Capture Of Radioactive Metal.

	Composition	Temperature (°C)
Iron-carbon	Carbon: 0.1 to 3.2 wt.%	1575 - 1700
Iron-carbon-sulfur	Carbon: 0.1 to 3.2 wt.% Sulfur: 0 to 37 wt.%	1575 - 1700
Copper-zinc	50% copper 50% zinc	900

In the iron-carbon system, radioactive cobalt, manganese, and iron partitioned to the metal phase. Appendices A and B present the Curie balance for the injection of radioactive feed into a molten bath. As shown in Figure 4.1 the partitioning of these three radioactive metals is controlled by thermodynamics. Therefore, the radioactive metals remain in their reduced states, inside the metal phase. The metal phase capture of Co, Mn, and Fe remained unchanged for varied temperature and carbon levels.

The partitioning of sodium was altered significantly in the ternary system in the presence of sulfur due to the formation of sodium sulfide. In the Fe-C system sodium concentration was below detectable levels. Capture of the sodium in the sulfide/matte phase, instead of the gas phase, is advantageous in some off-gas capture scenarios.

The partitioning of sodium in the iron-carbon-sulfur system was investigated in more detail by injecting Na_2CO_3 into the molten iron system containing both 5 and 15 wt.% sulfur. Subsequent neutron activation analysis (NAA) on post-run samples provided sodium partitioning data. Of the sodium recovered (total closure of 90±4%), 58% was found in the metal, 36% in the crucible (averaged over the entire crucible above and below the metal line), and 6% in the headspace. Only 0.1% of the measured sodium was detected in the GHT. The presence of sodium in the metal phase indicates the formation of the non-volatile sodium sulfide compound as shown in Figure 4.3., since the Fe-C system resulted in no sodium capture in the metal phase. Furthermore, the sodium which partitioned to the charge formed a concentration gradient concordant with the measured sulfur gradient as presented in Table 4.16.

Table 4.16
Sodium Concentration Versus Location In Charge.

Sample	Location	Sodium (ppm)	Sulfur (wt.%)
M1	0" Down from top (top surface)	22,100	7.73
M2	1" Down from top	6,700	5.27
M3	2" Down from top	138	2.60
M4	3.24" Down from top	77	2.75
M5	4" Down from top (bottom surface)	88	2.50

The observation that sodium partitions preferentially to regions of high sulfur supports the argument that stable, non-volatile sodium sulfide (MP 1180°C) is formed in the molten bath. Using HSC™, two thermodynamically favorable reactions were identified.

$$2Na + S \rightarrow Na_2S \qquad \Delta G = -59 kcal/mol\ (1500°C)$$

$$2Na + FeS \rightarrow Na_2S + Fe \qquad \Delta G = -35 kcal/mol\ (1500°C)$$

Thus, based solely on thermodynamic data, the formation of Na_2S is favorable at process bath temperatures (Figure 4.4).

Figure 4.4
Free Energies For Competing Reactions In Sodium/Sulfur Bath

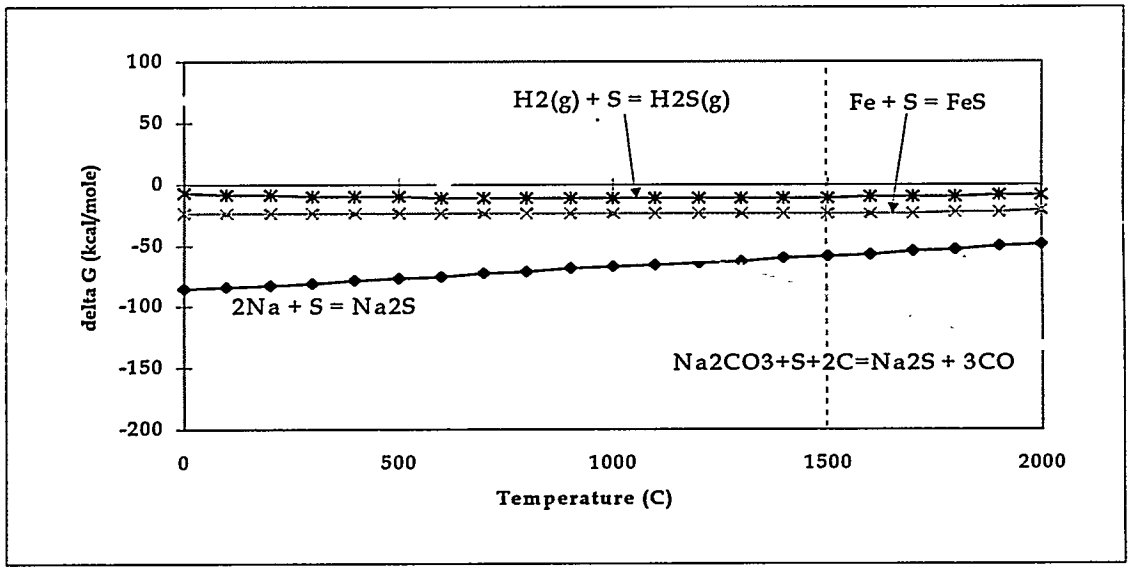

A large fraction of the sodium injected in this experiment partitioned to the metal phase (~50%). Nearly 90% of the injected sodium remained in the reactor system, including the charge, crucible, headspace, and insulation. The remaining 10% was unaccounted for in the sodium balance. Sodium did not partition to the off-gas system above measured background concentrations. (See Appendix C for sodium mass balances.)

4.2.2.3. Ceramic Phase

From the conducted experiments, ceramic phase partitioning data are available from two different systems. These compositions were chosen to partition more of the radionuclides to the ceramic phase and improve bath performance (better injection reliability and reduced splashing).

Of the compositions tested, the high-alumina layer that floated on the bath surface produced the most interesting results. First, the high-alumina layer on top of the bath mitigates surface splashing during lance injection (and also dampens lance vibrations which cause mechanical stress in the lance) increasing lance injection life.

Another result associated with the high-alumina ceramic layer was the preferential capture of cesium and cerium and the complete passthrough of zinc. The amount of capture of cesium and cerium appears to be a function of oxidation or surface "Redox" reaction with the alumina. Appendix D is a representative Curie balance for an alumina covered bath. This data shows 53% of the cerium, 18% of the cesium, and 1% of the zinc was captured in the high-alumina layer. Virtually no capture of these metals (Cs, Ce, and Zn) occurred in the metal phase. Since cesium vaporizes from the bath and enters the ceramic layer that is above its boiling point, simple physical adsorption onto the alumina is not expected as a significant capture mechanism. Nevertheless, capture of up to 40% of the injected cesium has been observed using alumina as the main constituents of the ceramic layer. Investigation of an oxidative or surface reaction (Redox) with the alumina was studied as a possible mechanism of capture. See Table 4.17 for relevant physical properties of the four metals.

Table 4.17
Some Physical Properties Of Al, Ce, Cs And Zn[3]

Metal	M.P.(°C)	B.P. (°C)	Valence State	Ionic Radius (Å)
Al	660	2520	3	0 .54
Al_2O_3	2115	2980	3	-
Ce	799	3424	3 or 4	1.14 (+3)
Cs	28	671	1	1.74
Zn	419	907	2	0.74

Using HSC™, the thermodynamically favorable oxidation reactions were identified. The oxygen source during injection is CO_2, used as carrier gas.

$$Zn + O_2 \rightarrow ZnO + 1/2O_2$$

$$2Cs + O_2 \rightarrow Cs_2O + 1/2O_2$$

$$Ce + O_2 \rightarrow CeO_2$$

See Table 4.18 for the free energy of formation of these reactions. As expected, cerium, a member of the lanthanide series, is easily oxidized. Oxidation of both cesium and zinc is favorable thermodynamically. The complete absence of zinc in the high-alumina layer suggests oxidative capture of zinc is not occurring, however, the capture of cesium in the alumina layer suggests oxidative capture.

A surface Redox reaction with the alumina was explored as another mechanism of capture. The oxidation-reduction equilibria for the following reactions were calculated.

$$2Al^{+3} + 3Zn + \rightarrow 2Al + 3Zn^{+2} + 6e$$

$$Al^{+3} + 3Cs + 3e \rightarrow Al + 3Cs^{+1} + 3e$$

$$Al^{+3} + Ce + 3e \rightarrow Al + Ce^{+3} + 3e$$

The cell emf values for each reaction were related to the free energy of reaction by the following relationship,

$$\Delta G = nFE$$

where n is the moles of electrons transferred, F is the charge of one mole of electrons, and E is the potential increase. The calculated values of the free energy of formation for the three Redox reactions are also presented in Table 4.18.

Table 4.18
Free Energy Oxidation And Surface Redox Reactions With The Alumina.

Element	Oxidation* (Kcal/mol)	Redox (Kcal/mol
Zinc	-39	+124
Cesium	-13	-87
Cerium	-172	-46
*at 1500°C		

Under free energy control, the dominant capture mechanism for cerium is oxidation from the CO_2 present. For cesium, on the other hand, the surface Redox reaction with the alumina is more favorable. Zinc, experimentally, had complete passthrough through the high-alumina layer even though the oxide reaction is favorable. Capture of zinc in either the metal or ceramic layer requires an alternative metal and ceramic system if capture other than in the gas phase is desired.

A liquid calcium-alumina-silicate ceramic layer was also tested to measure the partitioning of Cs, Ce and Zn. Initially two surrogate runs using a liquid calcium-alumina-silicate ceramic layer were performed to determine the best capture composition for cesium. The best composition was used in a subsequent radioactive feed injection (see Appendix C for the Curie balance). The results for all of these experiments are presented in Table 4.19.

Table 4.19
Cesium Capture With Calcium-Alumina-Silicate. Cesium Capture With Metal To Ceramic Ratio Of 5.7, Operating Temperature Of 1575°C.

Composition	Injection	Quenched Ceramic Description	Total Capture
A	CsCl	Two phase: pale blue and yellow	12.5% (Cs)
B	CsCl	Single phase: bluish	5.0% (Cs)
A	Radioactive	Three phase: gray crystallized, blue-gray glassy, and yellow-brown rim. (slow cooled)	0.6% (Ce, Co, Cs, Mn) of all activity injected*

* % capture for individual radionuclides: ^{141}Ce 44%; ^{60}Co 0.4%; $^{134\&137}Cs$ 2%; ^{54}Mn 1.5%, and ^{65}Zn <MDA.

4.2.2.4. Gas Phase

The previous section showed lack of cesium and zinc capture in the bath. Development of a dry cold trap (refer back to Figure 4.2) proved effective in complete capture of cesium and zinc. Gas phase radionuclide capture experiments were performed with two different media (glass wool and activated alumina) on the bench scale. The capture efficiency of the high-alumina ceramic phase was evaluated over a temperature range of 29°C to 316°C.

The volatile radioactive capture experiments were carried out differently from the metal or ceramic phase studies, in that the feed was injected on top of the bath surface. This injection procedure was used to simulate a worst case scenario, namely lance breakage with feed injection into the headspace. These challenging experimental conditions produced the greatest amount of activity in the off-gas. A second lance injected additional CO_2 into the headspace to minimize off-gas sooting. During these experiments it was discovered that a significant portion (greater than 60%) of the Co and Mn partitioned to the molten bath during surface injection.

While maintaining a constant cold trap volume, but replacing the glass wool with high-alumina ceramic, experiments were conducted to determine capture media efficiency. Decontamination Factors (DF) of headspace radioactive feed injection using both glass wool and alumina are compared in Table 4.20. The Curie balance for RPU2-94-057 is presented in Appendix E.

Table 4.20
DF Comparisons Between Glass Wool And Alumina Media. Cold Trap Media Volume Was Held Constant

Nuclide	Feed	
	RPU2-94-011; Glass Wool	RPU2-94-057; Alumina
Ce-141	4.01E+03	1.92E+02
Co-58	7.04E+03	1.26E+03
Co-60	2.28E+04	5.00E+04
Cr-51	1.65E+03	<MDA
Cs-134	9.07E+03	1.18E+04
Cs-137	2.57E+04	2.50E+04
Mn-54	2.41E+04	2.58E+04
Zn-65	3.68E+04	2.00E+04
Average	1.64 E + 04	1.92 E + 04

The DFs show that there was very little difference in capture ability between cold trap media. Neither packing material allowed any detectable radioactive passthrough into the GHT. A measure of the performance of the bed type is to compare how much of the activity passed through the bed (glass wool or alumina) and was trapped on the cold trap HEPA (preceding the GHT). Glass wool had 1.2% of the total activity (strictly cesium) collected in the cold trap passthrough to the cold trap HEPA, compared to the alumina bed where approximately 0.5% of the total activity passed through, consisting of Cs, Co and Zn.

Another measure of the media performance is the number of mCi collected in the cold trap media divided by the number of mCi collected in the cold trap HEPA. These ratios were 25.6 and 83.3 for glass wool and alumina, respectively. The lower value for the glass wool set-up indicates a higher percentage of the radionuclides passing through the glass wool.

4.2.3. Sulfur Studies

Experiments to measure sulfur capture in the metal phase, determine trace sulfur off-gas species, and primary work on refractory containment material were designed to identify some potential boundaries to feed composition for processing mixed waste.

4.2.3.1. Overall Partitioning

The partitioning of sulfur has been determined at four different bath carbon levels (0.1, 1.0, 2.0 and 3.0 wt.% C), using two different sulfur sources (hydrogen sulfide and iron sulfide). It was confirmed that over 97% of the injected sulfur resides in the metal phase at bath sulfur concentrations ranging from 0 to 37 wt.%.

In the Fe-S-C ternary system, an amicability gap occurs. For example, at 1500 °C an Fe-S-C melt separates into two liquids containing 1.8 wt% sulfur and 4.2 wt% carbon in the bottom layer and 26.5 wt% sulfur and 0.9 wt% carbon in the top layer[4]. Experimentally, upon solidification, phase separations similar to this were observed. See Table 4.21 for the carbon and sulfur distributions for several experiments.

Table 4.21
Distributions Of Sulfur And Carbon In Fe-S-C Ternary Alloys

Exp.	Sulfur*	Sample Locations**					
		Bottom		Middle		Top	
		Sulfur	Carbon	Sulfur	Carbon	Sulfur	Carbon
-037	6.1%	1.6%	NM	5%	NM	20%	NM
-049	8.1%	3.44%	3.22%	4.60%	3.20%	28.90%	0.54
-051	13.0%	3.48%	1.18%	12.9%	0.76%	18.10%	0.57%
-053	22.5%	23.0%	NM	24.60%	NM	28.20%	NM
-060A	30.1%	25.43%	0.03%	30.54%	0.08%	30.55%	0.05%

*Final bath sulfur content calculated by volume averaging.
**Bottom: 1/4" from surface; Middle: observable miscibility gap location; Top: 1/4" from surface.
NM: not measured

Two trends are apparent in the Table 4.21 data. First, at low sulfur concentrations (<10 wt%) there exists a definitive phase separation. Second, at higher sulfur levels (>20 wt%) the sulfur concentration profile from top to bottom becomes flatter. The high sulfur charges (above 30 wt%) were in a single crystalline phase (metal sponge). The color of the charges were dull golden black. They were also brittle, shattering when the alumina crucible was broken open.

These trends indicate that carbon control at high bath levels will be different from previous work due to the reduced solubility of carbon in the bath. For a quiescent bath sampling, results need to be corrected due to phase separation. For a well mixed bath, carbon solubility is reduced (since a high carbon layer cannot exist).

4.2.3.2. Containment Issues

The successful completion of the sulfur studies could not have been possible without a workable refractory system. The successful system used for all the high-sulfur experiments is a 97% alumina crucible with an HY-Wash coating (alumina suspended in phosphoric acid, locally applied). In parallel with these studies separate refractory evaluation experiments were performed with replicate conditions. A series of tests were undertaken to evaluate a number of candidate crucible materials in order to determine a material and vendor for the commercial plant. Detailed results from these crucible studies of the specific mechanisms controlling containment performance are presented in Section 5.

Appendix A: Curie Balance Of Radioactive Feed Injection Into A Liquid Ceramic Layer Bath

Conditions: Iron 4600g;
Feed injected: 40g activity: 1.07 μC;
Operating temperature 1500°C;
Carbon content: 2.0 wt.%;
Experiment: RPU2-94-028;

Ceramic Layer: Calcium - Alumina - Silicate
Ceramic Layer: Mass 800 grams

SAMPLE		Ce-151	Co-58	Co-60	Cs-134	Cs-137	Mn-54	Zn-65	Total Activity	%
	Mass (g)	%	%	%	%	%	%	%	SUM	%
Recovered Resin	3.92	23.44%	14.88%	15.46%	13.50%	14.09%	17.54%	14.39%	1.74E-01	15.02%
Metal	4601.00	<MDA	78.19%	76.33%	<MDA	<MDA	71.99%	1.95%	4.14E-01	35.85%
Ceramic Layer	744.37	43.79%	<MDA	0.43%	1.13%	0.85%	1.46%	<MDA	7.15E-03	0.62%
Crucible	3245.00	43.79%	<MDA	1.05%	10.72%	9.81%	2.53%	13.43%	8.32E-02	7.2%
Injection Lance	299.65	11.98%	2.35%	1.77%	1.63%	1.41%	4.17%	0.43%	9.24E-02	1.54%
Cold Trap	142.43	20.80%	4.58%	5.37%	74.15%	74.69%	3.78%	69.80%	4.67E-01	40.39%
Wet Scrubber	500.00	<MDA	<MDA	<MDA	<MDA	<MDA	<MDA	<MDA	<MDA	---
Coarse Filter	20.00	<MDA	<MDA	<MDA	<MDA	<MDA	<MDA	<MDA	<MDA	---
HEPA Filter	13.50	<MDA	<MDA	<MDA	<MDA	<MDA	<MDA	<MDA	<MDA	---
Total Measured: uCi		3.65E-03	1.70E-02	4.11E-01	5.95E-02	1.74E-01	1.11E-01	3.80E-01	1.16E+00	
Total Injected: uCi		4.99E-03	1.37E-02	3.23E-01	5.22E-02	1.50E-01	1.11E-01	4.16E-01	1.07E+00	
% Recovered		73.08%	124.00%	127.04%	113.99%	115.94%	100.31%	91.30%	**107.91%**	100.00%

Appendix B: Curie Balance Of Radioactive Feed Injection Into A High Sulfur Bath (20 Wt.% Sulfur)

Conditions: Iron 1,721 g, FeS_2 2,879 g; organic feed injected 44.96g;
Activity: 1.98 μCi, operating temperature 1575°C
Carbon Content: 1.0 wt.%, sulfur content 20 wt.%.
Experiment: RPU2-94-073.

SAMPLE		Ce-151	Co-58	Co-60	Cs-134	Cs-137	Mn-54	Zn-65	Total Activity	%
	Mass (g)	%	%	%	%	%	%	SUM	%	%
Metal	3900.00		54.05%	74.91%	19.69%	11.32%	84.52%	<MDA	7.04E-01	41.70%
Ceramic Layer	3498.00		<MDA	0.70%	10.52%	10.53%	<MDA	<MDA	6.28E-02	3.72%
Crucible	502.00		38.21%	7.45%	42.90%	48.57%	9.42%	<MDA	3.30E-01	19.54%
Injection Lance	336.57		7.74%	2.35%	13.16%	14.23%	1.32%	68.07%	3.07E-01	18.2%
Cold Trap	50.75		<MDA	14.60%	13.73%	15.36%	4.73%	31.93%	2.84E-01	16.84%
Wet Scrubber	515.60		<MDA	<MDA	<MDA	<MDA	<MDA	<MDA	<MDA	0.00%
Coarse Filter	18.60		<MDA	<MDA	<MDA	<MDA	<MDA	<MDA	<MDA	0.00%
HEPA Filter	5.05		<MDA	<MDA	<MDA	<MDA	<MDA	<MDA	<MDA	0.00%
Total Measured: uCi			9.53E-03	6.45E-01	1.22E-01	4.32E-01	1.69E-01	3.11E-01	1.69E+00	
Total Injected: uCi			7.45E-03	6.58E-01	1.16E-01	4.50E-01	1.52E-01	5.98E-01	1.98E+00	
% Recovered			127.90%	97.93%	105.57%	95.94%	111.13%	51.97%	**85.19%**	100.00%

Appendix C: Sodium Mass Balance In A 5 Wt.% Sulfur Bath

Conditions: Iron 3,786 g; FeS_2 813g;
Injected 126g Sodium Carbonate;
Operating temperature 1575°C;
Carbon Content: 1.0 wt.%;
Sulfur content 5 wt.%;
Experiment: R010-95-016.

Input	Injected wt. (g)	wt. uncert. (grams)	Na wt.% (%)	uncrt. (%)	Na grams	uncert. (grams)	% of Total	uncrt. (%)
Sodium Carbonate	126.0	2.0	43.4%	0.50%	54.68	1.07	100.0%	2.0%
Total Inputs	126.0	2.0	-----	-----	**54.68**	**1.07**	100.0%	2.0%

Output	Sample wt.	wt. uncert. (grams)	Na wt.% (%)	uncrt. (%)	Na grams	uncert. (grams)	% of Total	uncertainty (%)
Charge: M1	941.0	50.0	2.21%	0.014%	20.80	1.11	38.0%	2.2%
Charge: M2	941.0	50.0	0.67%	0.003%	6.30	0.34	11.5%	0.7%
Charge: M3	941.0	50.0	0.01%	0.001%	0.13	0.01	0.2%	0.0%
Charge: M4	941.0	50.0	0.01%	0.001%	0.07	0.01	0.1%	0.0%
Charge: M5	941.0	50.0	0.01%	0.001%	0.08	0.01	0.2%	0.0%
Charge: Total	4705.0	-----	-----	-----	27.38	1.16	50.1%	2.1%
Crucible: Total	3800.0	-----	-----	-----	17.78	1.66	32.5%	3.0%
Total Headspace, GHT	310.3	-----	-----	-----	3.81	0.21	7.0%	0.4%
Total Outputs	**8815.3**	-----	-----	-----	48.97	2.04	89.6%	4.1%
Percent Closure	-----		-----	-----	-----	-----	**89.6%**	**4.1%**

Appendix D: Curie Closure For A Radioactive Injection Into A High-Alumina Ceramic Covered Bath

Conditions: Iron 4600g;
Feed Inserted 30.3g;
Activity: 0.7 mci;
Operating temperature 1575°C;
Carbon Content: 2.0 wt.%.

Alumina: 650 grams;
Experiment RPU2-94-022;

SAMPLE	Mass (g)	Ce-151 %	Co-58 %	Co-60 %	Cs-134 %	Cs-137 %	Mn-54 %	Zn-65 %	Total Activity SUM	% %
Metal	4834.1	<MDA	90.71%	92.73%	1.04%	1.15%	95.13%	<MDA	3.69E-01	58.35%
Ceramic Layer	454.1	76.74%	0.30%	0.29%	29.83%	27.4%	0.24%	1.03%	2.32E-02	3.67%
Crucible	3206.0	<MDA	<MDA	<MDA	24.41%	29.02%	<MDA	<MDA	3.43E-02	5.41%
Injection Lance		23.26	8.37%	6.67%	11.64%	10.58%	4.39%	41.89%	1.14E-01	18.01%
Cold Trap	22.4	<MDA	0.31%	0.31%	33.08%	31.85%	<MDA	57.08%	9.29E-02	14.68%
Wet Scrubber	250.0	<MDA	<MDA	<MDA	<MDA	<MDA	<MDA	<MDA		
Coarse Filter	13.7	<MDA	<MDA	<MDA	<MDA	<MDA	<MDA	<MDA		
HEPA Filter	5.8	<MDA	<MDA	<MDA	<MDA	<MDA	<MDA	<MDA		
Total Measured: µCi		4.34E-03	1.68E-02	2.91E-01	3.08E-02	9.22E-02	1.11E-01	9.18E-02	6.33E-01	
Total Injected: µCi		7.10E-03	1.24E-02	2.19E-01	3.34E-02	9.18E-02	7.47E-02	2.82E-01	7.12E-01	
% Recovered		61.07%	135.15%	132.94%	92.17%	100.44%	148.54%	32.62%	88.87%	100%

Appendix E: Curie Balance For A Headspace Radioactive Feed Injection Using A High-alumina Ceramic Layer

SAMPLE	Mass (g)	Ce-141 %	Co-58 %	Co-60 %	Cs-134 %	Cs-137 %	Mn-54 %	Zn-65 %	Total Act. SUM	Percent %
METAL	4600.90	<MDA	95.11%	87.39%	<MDA	8.64%	90.09%	1.05%	9.79E-01	41.51%
Crucible	3444.69	<MDA	<MDA	1.52%	25.34%	21.26%	1.34%	67.18%	6.22E-01	26.37%
Injection Lance	17.85	24.76%	2.11%	1.92%	13.72%	12.88%	4.34%	0.61%	1.08E-01	4.56%
Ceramic Layer	400.00	75.24%	<MDA	0.12%	0.28%	0.17%	0.40%	<MDA	4.25E-03	0.18%
Cold Trap	558.41	<MDA	2.78%	9.05%	60.66%	57.05%	3.83%	31.16%	6.46E-01	27.38%
Wet Scrubber	500.00	<MDA	<MDA	<MDA	<MDA	<MDA	<MDA	<MDA	-----	0.00%
Coarse Filter	15.64	<MDA	<MDA	<MDA	<MDA	<MDA	<MDA	<MDA	-----	0.00%
HEPA Filter	10.08	<MDA	<MDA	<MDA	<MDA	<MDA	<MDA	<MDA	-----	0.00%
Total Measured: µCi		1.69E-03	1.40E-02	8.27E-01	1.27E-01	4.63E-01	2.17E-01	7.08E-01	2.36E+00	
Total Injected: µCi		1.81E-03	1.61E-02	8.83E-01	1.43E-01	4.76E-01	2.37E-01	8.63E-01	2.62E+00	
% Recovered		93.36%	86.91%	93.66%	89.32%	97.29%	91.56%	82.00%	**90.01%**	100.00%

The results of this Curie balance show a large concentration (>40%) of the activity in the metal, which is somewhat surprising considering the headspace injection. The cold trap collected 27.4% of the activity, mainly in the form of Cs-134, Cs-137, and Zn-65, as expected. A large portion of the injected Zn-65 (39.5%) deposited on the top plate, the first available cooled surface encountered by the process gases and other materials, and the Kaowool insulation. Due to the nature of these samples, thin dust coating over large surface area, it is possible a significant portion of the material went unaccounted for, resulting in the relatively poor closure of the Zinc-65 activity balance (82%). No activity was detected beyond the cold trap HEPA.

4.3. Physical Behavior Of Sulfur-Containing Compounds Injected Into A Molten Iron-Carbon System II

4.3.1. Introduction

For background purposes, previous sulfur-related experiments were conducted with bath sulfur levels that ranged from 0 to 20 wt%. In the 0 to 20 wt% sulfur range over 97% present in incoming feed of the sulfur partitioned to the metal phase, regardless of bath carbon level and the sulfur source. Testing was performed at four different bath carbon levels (0.1, 1.0, 2.0 and 3.0 wt% C) using two different sulfur sources (hydrogen sulfide and iron sulfide). Sulfur was also removed from the bath using hydrogen and methane gas injection. An issue that surfaced in these initial experiments was containment of the high-sulfur phase -- FeS. Successful containment was accomplished by coating the 97% alumina crucible (3% is a silica binder) with an HY-wash coating composed of alumina suspended in phosphoric acid

4.3.2. Apparatus and Procedure

To conduct the sulfur experiments, the Gas Handling Train (GHT) underwent slight changes to better facilitate passthrough of sulfur during heat-up and provide off-gas sulfur capture for multiple injections. The GHT used during these experiments is shown in Figure 4.5.

Figure 4.5
The GHT Set-up for the Sulfur Off-gas Experiments

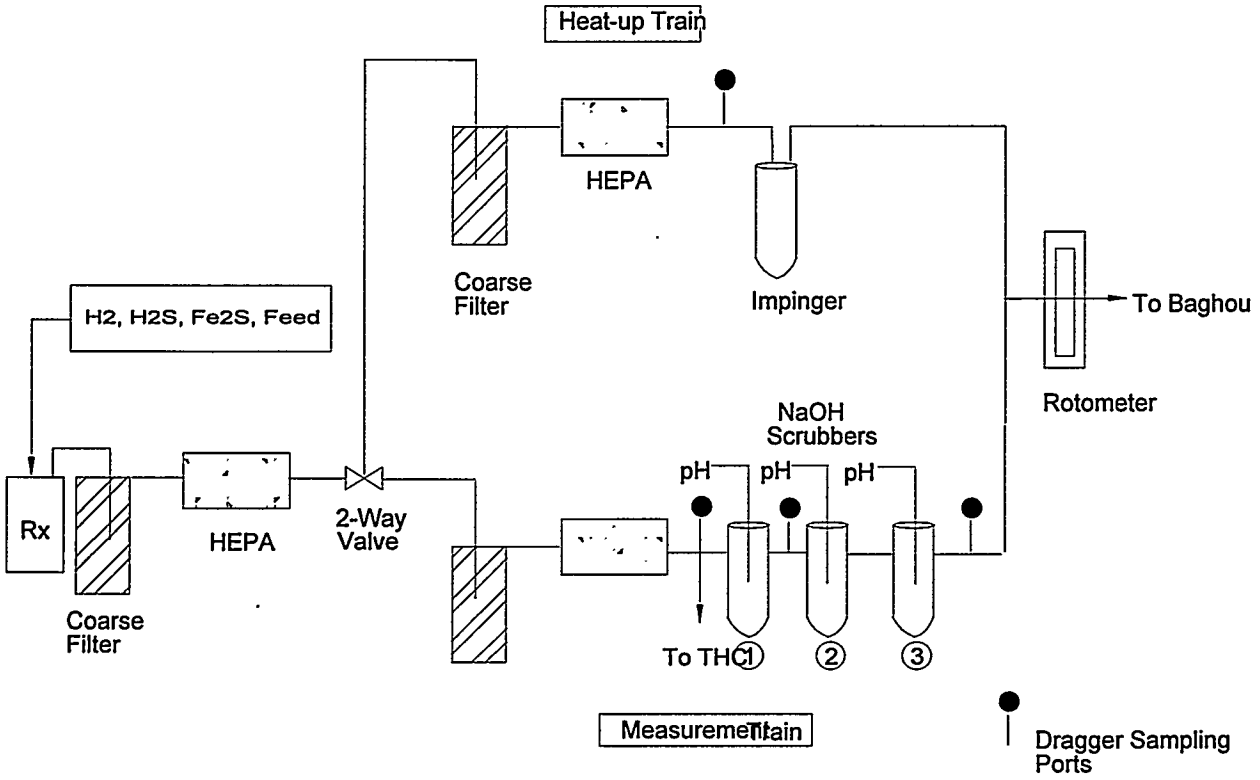

For high sulfur control the off-gas consisted of two trains: one for heat-up and the other for measurements. The heat-up GHT was required to reach the high sulfur levels without exhausting the measurement train caustic scrubbers. To reach the high sulfur levels, FeS_2 was added to the iron charge. When heated the FeS_2 produces sulfur gas (S_2) starting at 200°C. The production of H_2S, plotted against the crucible temperature for a 100% pyrite charge, is shown in Figure 4.6.

Figure 4.6
H_2S generation and crucible temperature as a function of time. The charge of 100% FeS_2 was heated in a hydrogen-rich environment.

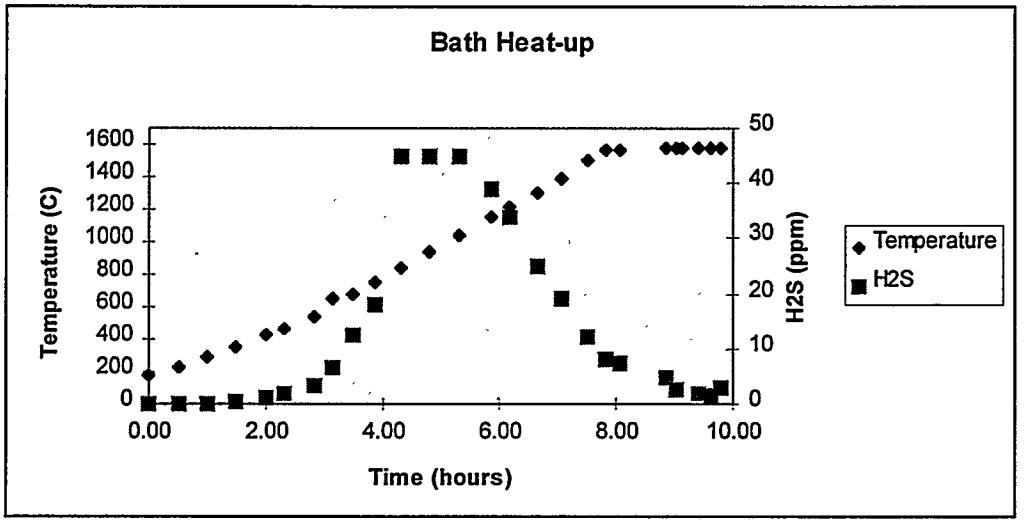

The peak H_2S levels occur between 800 and 1200°C which is concordant with the Fe-S system transition from beta-FeS_2 to gamma-FeS.

The measurement GHT consisted of a coarse filter, HEPA, and three caustic scrubbers (with pH probes) and was put on-line once the bath was fully molten. The GHT set-up pictured in Figure 4.5 allowed us to perform injections to collect the off-gassing sulfur, stop injection, switch to the heat-up train to collect samples, then replace the caustic scrubber back in the measurement train. This allowed several different injection experiments with the same molten bath.

Headspace injections were performed in several experiments with the lance positioned 6" above the metal surface at a temperature of ~400 to 800°C. The data was then used to quantify headspace reactions and provide an upper bound with which to compare submerged lance data (with the lance positioned 6" below the metal surface).

Containment control was refined in the previous sulfur experiments, in which it was found that the 97% alumina crucible, with an HY-wash coating maintained integrity at extreme bath sulfur levels. HY-wash is a liquid slurry of alumina in phosphoric acid. The coating is applied by dipping the entire crucible into a container of HY-wash, pouring out the excess, and heating the crucible to 200°C for three hours to remove the excess moisture. The coating proved successful in all experiments, with the pinnacle experiment holding 37 wt% sulfur bath for over 12 hours.

4.3.3. Total Hydrocarbon (THC) Generation

The THC monitor was used to indirectly measure the carbon activity in the bath during resin injection. As the sulfur concentration increases in the bath the carbon solubility decreases, hence the carbon activity increases. The increase in carbon activity results in higher THC readings, as observed experimentally. This trend was found in several experiments (as annotated) and is shown in Figure 4.7.

Figure 4.7
Off-Gas Total Hydrocarbon Content as a function of Bath Sulfur Levels.

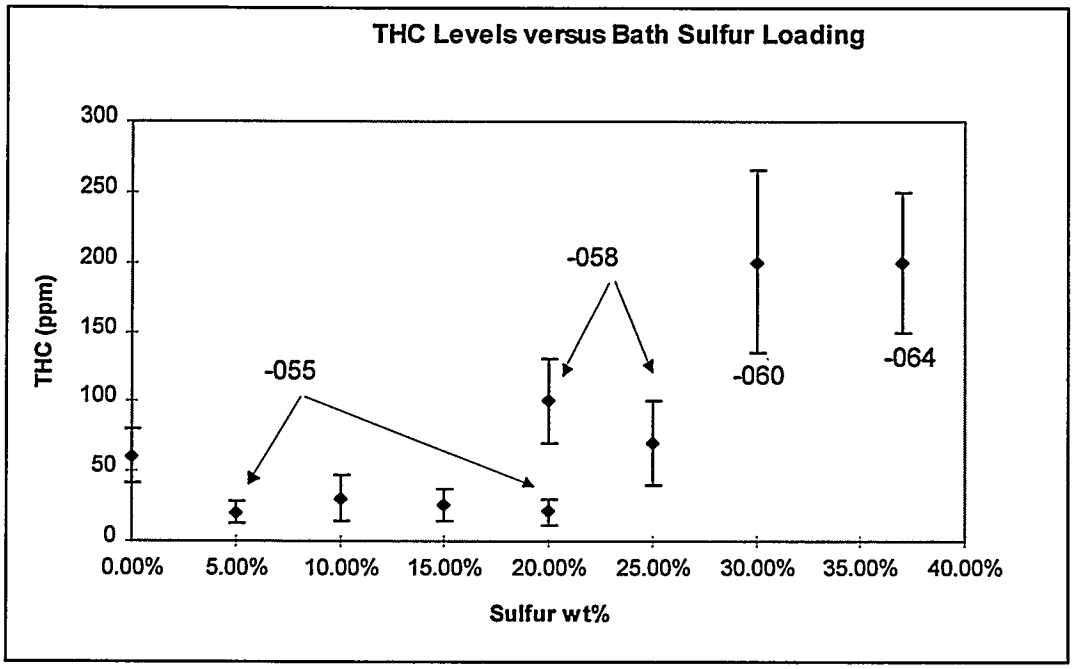

The combined results show off-gas THC concentration increases with bath sulfur levels; however, this increase is considered insignificant.

A more detailed look at the THC data for experiment -064 (see Figure 4.7), in which organic feed was injected into a bath with a theoretical sulfur level of 37 wt%, is shown in Figure 4.8. These THC data for three separate injections (overlaid for comparison) show the submerged injection had the highest THC values.

Figure 4.8
THC Concentration vs. Time (30 wt. % Sulfur)

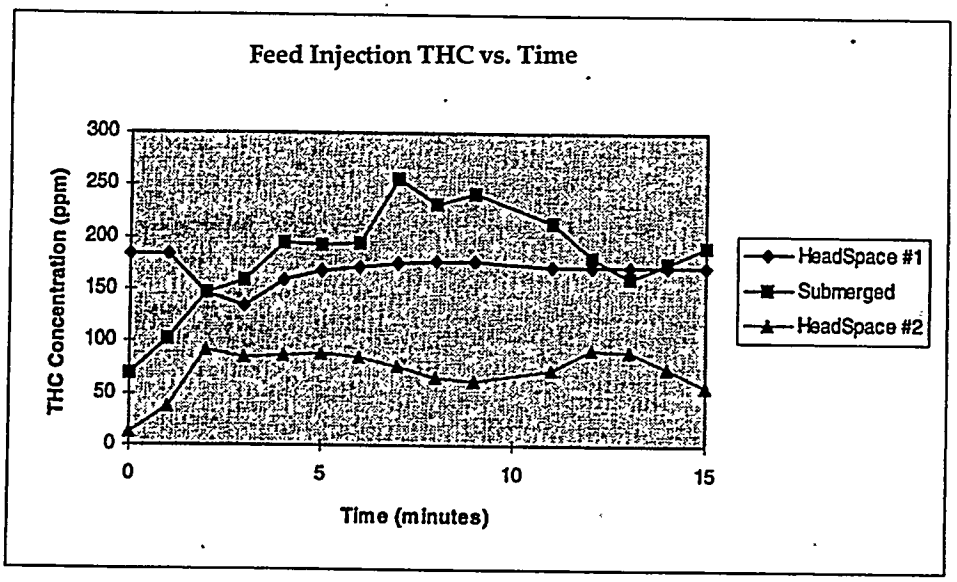

Figure 4: THC Concentration vs. Time (30 wt.% Sulfur)

The lower THC values during headspace injections are attributed to partial feed melting with subsequent particulate deposition in the reactor and GHT. Whereas the submerged injection resulted in full conversion of the organics to the gas phase. This theory could be easily validated by headspace injections closer to the metal surface.

The sulfur escaping to the off-gas was collected for each of the sulfur and organics injections shown above. The sulfur capture for each separate injection is shown in Table 4.22. For comparison, the sulfur captures during hydrogen and hydrogen sulfide injections are also shown. This set of injections had a higher H_2S concentration than all previous experiments.

Table 4.22
Molten FeS (37 wt% sulfur) bath injection data

Feed	Loc.	Flow/Feed Rate	Max. H_2S	Injected Sulfur	Scrubber S Capture	% to Of-Gas (Inj.S/Cap.S)
H_2	H	0.5 SLPM	2.5%	0	0.62g	-----
Organics & Sulfur	H	~lg/min	5.0%	0.75(g)	2.94g	392%*
H_2S	H	0.5 SLPM	4.4%	11.0(g)	0.64g	5.8%
H_2S	S	0.5 SLPM	2.7%	10.7(g)	0.45g	4.2%
H_2	S	0.5 SLPM	6.5%	0	0.70g	-----
Organics & Sulfur	S	~lg/min	3.5%	0.55(g)	0.81g	148%*
Organics & Sulfur	H	~lg/min	3.5%	0.35(g)	0.308g	88%*

*Unreliable closure during resin injection is attributed to resin feed rate is estimated (+ 30%)
H: Headspace injection

S: Submerged injection

Note: Between each injection the GHT was purged and caustic scrubbers replaced.

For clarity the interpretation of Table 4.22, "Injected Sulfur," refers to the feed rate multiplied by time; "Scrubber S Capture," in the amount of sulfur captured in the scrubber during the injection; "% to Off-Gas," is the captured sulfur divided by the injected sulfur.

The immediately noticeable discrepancy of these results are off-gas sulfur captures greater than 100% during injection of organics with sulfur. During these injections, CO_2 was used as a carrier gas, increasing the oxygen availability in the metal. The oxygen, therefore, removes additional sulfur from the bath, perhaps as SOx or COS. The small fraction of sulfur collected in the off-gas during hydrogen sulfide injection validates the bath's ability to absorb sulfur. Another trend shown in Table 4.22 is, for the same injected flow rate of H_2 and H_2S into the bath, hydrogen gas produces twice as much H_2S in the off-gas.

4.3.4. H_2S Bath Injections

Hydrogen sulfide injections have been performed at varying bath temperatures, carbon levels, and sulfur levels. In all of these injections there was a significant sulfur partitioning to the metal phase (greater than 98%). Initial experiments established that

the physical passthrough of H_2S was negligible at the experimental flow rates. Thus, this study reflects actual partitioning, of sulfur to the metal phase.

In this set of experiments, injections of H_2S into high sulfur baths (> 30 wt% S) were performed to determine the steady state generation rate of sulfur in the gas phase, following sulfur saturation of the metal phase. Figure 4.9 shows Ar, H_2S, and H_2 injections in both the headspace and the high sulfur metal (at 30 and 37 wt% in experiments -060A and -064 respectively). The large differences between the submerged and headspace injections show the metal phase was not completely saturated with sulfur. In the ten separate injections shown, injection time, bath temperature, and gas flow rate were held constant.

Figure 4.9
Off-gas H_2S levels versus different injection gases, bath sulfur levels and injection locations

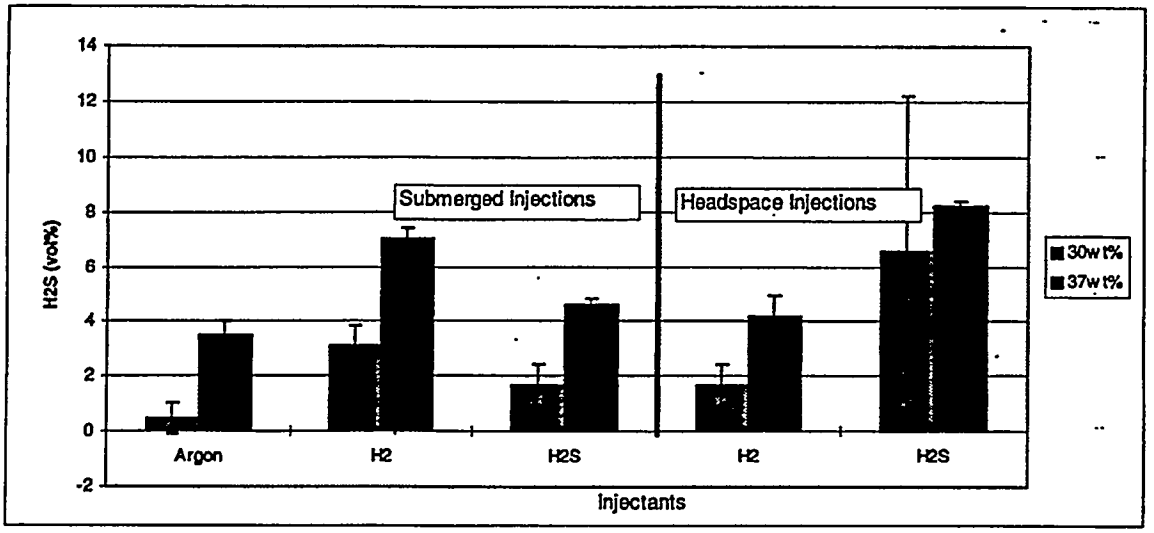

The submerged injections of hydrogen and hydrogen sulfide had almost the same off-gas levels of H_2S. This shows the dominance of thermodynamic control where the bath continues to absorb sulfur by the following reaction:

$$H_2S + Fe \text{ ---> } FeS + H_2 \qquad \text{(delta G @ 1500°C is -13 kcal/mol)}$$

and H_2 combines with sulfur to produce H_2S by the following reaction:

$$H_2 + S \text{ ---> } H_2S \qquad \text{(delta G @ 1500°C is -27kcal/mol)}$$

As expected, hydrogen sulfide gas injection into the headspace resulted in considerably higher H_2S levels, 9.5 vol%. However, the calculated "passthrough" H_2S levels should

have been 40 vol%, indicating some bath sulfur capture and/or sulfur deposition in the GHT during H_2S injection.

4.3.5. Immiscibilities in Solidified Melts

In the Fe-S-C ternary system, immiscibility gaps occur. For example, at 1500°C a Fe-S-C melt separates into two liquids containing 1.8 wt% sulfur and 4.2 wt% carbon in the bottom layer and 26.5 wt% sulfur and 0.9 wt% carbon in the top layer. Experimentally, upon solidification, immiscibility gaps similar to this were observed after solidification (see Table 4.23).

Table 4.23
Distributions of sulfur and carbon in Fe-S-C ternary alloys.

Exp #	Sulfur*	Sample Locations**					
		Bottom		Middle		Top	
		Sulfur	Carbon	Sulfur	Carbon	Sulfur	Carbon
-037	6.1%	1.6%	NM	5%	NM	20%	NM
-049	8.1%	3.44%	3.22%	4.60%	3.20%	28.90%	0.54
-051	13.0%	3.48%	1.18%	12.9%	0.76%	18.10%	0.57%
-053	22.5%	23.0%	NM	24.60%	NM	28.20%	NM
-060A	30.1%	25.43%	0.03%	30.54%	0.08%	30.55%	0.05%

*Final bath sulfur content calculated by volume averaging.
**Bottom: 1/4" from surface; Middle: observable miscibility gap location; Top: 1/4" from surface.
NM: not measured

There are two trends shown in the Table 4.23 data. First, at low sulfur concentrations (<10 wt%) there exists a definitive phase separation. Second, at higher sulfur levels (>20 wt%) the sulfur concentration profile from top to bottom becomes flatter. Carbon control at high bath sulfur levels will be difficult due to the reduced solubility of carbon in the bath. The high sulfur charges (above 30 wt%) were in a single crystalline phase (metal sponge).

4.3.6. Containment

The successful completion of these runs, however, could not have been possible without a workable refractory system. The successful system used for all the high-sulfur experiments is a 97% alumina crucible from Engineered Ceramics, HY-wash (alumina suspended in phosphoric acid) coated (locally applied), and dried at 200°C. Ongoing in

parallel with these studies are separate refractory evaluation experiments with replicate conditions. These detailed refractory studies are addressed in a separate report.

After all four experiments the HY-wash coating was a thin dark layer inside the crucible, while the interior of the crucible was light gray. Analysis of the crucible surfaces and cross sections are given below. Chemical analysis of the HY-wash coating surfaces (both inside and outside) shows that during processing, the refractory coating loses the phosphorous that is present in the unfired material and increases considerably in both sulfur and iron content. The presence of both sulfur and iron in the outside surface of the containment crucible indicates penetration of the material through the entire crucible. Analysis of the crucible cross sections for 30 and 37 wt% sulfur runs also shows elevated sulfur (~0.8 wt%) and iron contents; however, these values are much lower than those measured for the HY-wash coat (4.22 wt%). Table 4.24 provides the results from Uniquant XRF analysis.

Table 4.24
MMT Uniquant XRF Analysis for sulfur containment crucibles*

Sample ID	Sample Description	Na20	MgO	Al2O3	SiO 2	P20s	S	K20	CaO	FeO
HY-wash	unfired	0.20	—	91.5	0 66	4.36	0.01	—	0.12	2.67
RPUI-94-058-R3	HY-wash out-side surface	0.44	—	74.6	0.71	0.05	3.26	—	0.13	20.4
RPUI-94-058-R3	HY-wash inside surface	0.08	—	71.7	0.72	0.02	4.22	—	0.17	22.4
RPU1-94-058-R4	crucible cross-section	0.22	—	93.0	4.9	0.009	0.56	—	0.09	0.80
R010-94-60A-R2-R1	crucible cross-section	0.13	0.13	89.0	7.8	0.05	0.69	0.04	0.38	1.05
R010-94-60A-R2-R2	crucible cross-section	0.16	0.07	90.1	6.8	0.06	0.84	0.03	0.25	1.3
R010-94-60A-R2-C	biack slag layer	0.89	1.73	21.7	62.8	0.31	1.40	0.89	6.2	3.4
R010-94-64-R2-C2A	black slag layer	0.85	1.75	13.5	74.7	0.99	0.74	1.06	4.36	1.63
Sample ID	**Sample Description**	**Na**	**Mg**	**Al**	**Si**	**P**	**S**	**K**	**Ca**	**Fe**
R010-94--60A-R1-M3	metal phase	0.04	0.06	0.08	0.02	0.09	33.3	0.01	0~	65 5
FeS2 Raw Material		0.095	0.27	0.64	2.52	0.026	43.4	0.15	0.97	50.8
*Analysis reported as wt.%										

4.3.7. Reference

1. Loewen, Eric, Interim Progress Report (IPR), IPR-94-023, "Physical Behavior of Sulfur Containin Compounds Injected into a Molten Iron-Carbon System", (September 23, 1994).

2. Lenkford, P., "The Making, Shaping and Treating of Steel" 10th edition, page 124.

3. Shaw, Cathy, "Diarnonite Al_2O_3 Dry Slag SEM/EDX Analysis." InterOffice Memo, 10/21/94.